Aviral Shrot

Inverse identification of material parameters from machining processes

Inverse identification of material
parameters from machining processes

Inverse identification of material parameters from machining processes

Von der Fakultät für Maschinenbau
der Technischen Universität Carolo-Wilhelmina zu
Braunschweig

zur Erlangung der Würde

eines Doktor-Ingenieurs (Dr.-Ing.)

genehmigte Dissertation

von: **Aviral Shrot**
aus: Ranchi, Indien

eingereicht am: 12.10.2012
mündliche Prüfung am: 25.01.2013
Gutachter: Priv.-Doz Dr. Martin Bäker
           Prof. Dr.-Ing. Peter Horst
           Prof. Dr. rer. nat. Joachim Rösler (Vorsitzender)

2013

To my mother

Acknowledgements

I would like to take this opportunity to thank everyone whose contributions have made this work possible. First of all, I would like to express my sincere gratitude to my supervisor Dr. Martin Bäker, whose valuable advice and constant encouragement helped me develop as a researcher. His willingness to share his insight regarding the chip formation process and its numerical modelling assisted me at every stage of the work. I also acknowledge the academic freedom which was given to me so that I could approach the problem from different perspectives. It was a great pleasure working with him and his help in writing this thesis was invaluable.

The work presented in this thesis has been carried out within the 7th Framework Programme of the Commission of the European Community; section PEOPLE, Marie Curie Actions, Initial Training Networks, Project "MaMiNa", Grant Agreement PITN-GA-2008-211536. The aim of the EU-project "Macro, Micro and Nano aspects of machining (MaMiNa)" was to improve the machinability of difficult to machine materials such as Titanium alloys and Nickel-base superalloys. Collaborative work with nine network partners consisting of universities and research institutions provided an excellent opportunity to learn and share research expertise. I gratefully acknowledge the generous financial support provided by the European Commission during the project which allowed me to conduct research and travel to conferences and partner institutions. As the coordinator of the MaMiNa project and the head of the Institut für Werkstoffe, Prof. Joachim Rösler actively supported my work and encouraged my research endeavours.

I would like to thank my colleague Carsten Siemers, who not only managed the MaMiNa project with great enthusiasm and efficiency but also shared with me his deep knowledge regarding the Titanium alloys. I would like to thank Tatiana Sazonova, who helped me in the administrative matters. My colleague Philipp Seiler and student assistants Dmitrij Menschikow and Peter Harrass provided an excellent

IT support which was necessary in a computationally intensive project like this.

I would like to thank the project partners and Early Stage Researchers (ESRs) with whom I actively collaborated during this work. Dr. Mikko Hokka, Tonu Leemet and Dmitri Gomon from the Tampere University of Technology provided me with the flow stress data obtained from Split Hopkinson Bar testing. I am thankful to Dr. Hans-Werner Hoffmeister and ESRs Dawid Ksiezyk and Jarkko Metsäjoki from the Institut für Werkzeugmaschinen und Fertigungstechnik who kindly shared with me the quick-stop results. I am obliged to Prof. Vadim Silberschmidt who as the head of the simulations group in the MaMiNa project helped me with the issues related to computational modelling. I had a number of constructive discussions with ESRs Murat Demiral and Riaz Muhammad regarding the finite element simulation of machining. I had the pleasure of working with ESRs Badya Zahra, Mohammad Sajid Hussain, Seda Erbas and Kai Nowag, all of whom I also got to know personally and were a great source of personal support. Kai Nowag very kindly helped me with the german translation of the thesis abstract.

Finally, I would like to express my eternal gratitude to my family for the trust they have placed in me. I would especially like to thank my mother who been a source of inspiration for me all my life. I would also like to thank my wife who supported me throughout my endeavours and could help me with proof-reading and correcting this thesis.

Abstract

Finite element simulation has become an important tool in understanding the chip formation process. Complex machining processes with complex chip morphologies have been simulated this way. An important challenge in the modelling of machining processes is that material parameters are not available which can robustly predict the material behaviour at large ranges of strains, strain rates and temperatures. During a continuous chip formation process, strains can reach up to 200%, strain rates can be of the order of 10^5 s^{-1} and temperature variation can be in the order of hundreds of degrees. In comparison, state-of-the-art experimental methods such as the Split Hopkinson Pressure Bar (SHPB) tests can usually reach strains of up to 50% and strain rates of the order of 10^3 s^{-1}. Data fitting techniques are then used to identify material parameters from the experimental data. Due to the large extrapolations involved, the machining simulation results do not robustly match the experimental results.

The difficulty of using the material parameters determined from standard experiments for machining simulations is first shown for three different materials. The Johnson-Cook material parameters are obtained for Ti-15-3-3-3, Ti-6246 and Alloy 625 from SHPB experiments. These are then used to simulate the chip formation using the finite element method. For Ti-15-3-3-3 and Ti-6246, segmented chip formation is observed. For Alloy 625, the Johnson-Cook model overestimates the material strength at high strains and the resulting machining simulation gives rise to a continuous chip. Therefore a modified Johnson-Cook model is used for machining simulations which forms segmented chip. The average cutting force in the three cases are predicted within 20% of the experimentally obtained values. There are significant differences in the predicted chip shapes and the experimentally obtained chip shapes. These differences can be attributed to the difficulty of predicting the material behaviour at conditions prevailing during machining.

An inverse identification method is used to identify material parameters directly from machining processes to resolve this problem. The chip shapes and the cutting forces are matched to a standard by systematically varying the material parameters. The robustness of the method is tested by identifying parameters for two different materials and conducting optimisations from different starting points. Studies are also conducted to improve the convergence and reduce the computational expense. The knowledge of the effect of stress-strain curves on the chip shapes and the cutting forces can also be used to improve the optimised solution predicted by the inverse identification algorithm. This can lead to reduction in the computational expense.

It is observed during the identification process that a number of parameter sets can be found which give rise to similar chips and cutting forces. This is because all the different parameter sets represent the same flow stress curve in the domain of machining. In order that the identified parameters are valid over a large machining domain, widely varying cutting conditions are chosen for the identification process.

Zusammenfassung

Die Finite-Elemente-Simulation ist ein wichtiges numerisches Werkzeug zur Verbesserung des Verständnisses des Spanbildungsprozesses. Mit dieser Methode können komplexe Bearbeitungsprozesse mit komplexen Span-Morphologien simuliert werden. Eine wichtige Herausforderung bei der Modellierung spanender Bearbeitungsverfahren ist, dass keine Materialparameter bekannt sind, die das Werkstoffverhalten unter stark variierenden Dehnungen, Dehnungsgeschwindigkeiten und Temperaturen vorhersagen können. Während eines Fließspanbildungsprozesses können Dehnungen von bis zu 200%, sowie Dehnungsgeschwindigkeiten in der Größenordnung von 10^5 s^{-1} und Temperaturerhöhungen im Bereich von mehreren 100 °C auftreten. Im Vergleich dazu können experimentelle Methoden wie der Split-Hopkinson-Pressure-Bar-Test (SHPB) in der Regel Dehnungen von bis zu 50% und Dehnungsgeschwindigkeiten in der Größenordnung von 10^3 s^{-1} erreichen. Diese Tests können dazu genutzt werden, um mittels Datenanpassungsmethoden die Materialparameter aus den experimentellen Daten zu bestimmen. Aufgrund der großen Extrapolationsbereiche stimmen die Ergebnisse der Zerspanungssimulationen in der Regel nicht besonders gut mit den experimentellen Ergebnissen überein.

Zuerst werden die Schwierigkeiten der Verwendung der Materialparameter, die aus Standard-Experimenten bestimmt werden, für die Zerspanungssimulationen von drei verschiedenen Werkstoffen aufgezeigt. Die Johnson-Cook-Parameter werden für Ti-15-3-3-3, Ti-6246 und Alloy 625 aus SHPB-Experimenten bestimmt. Diese werden anschließend verwendet, um die Spanbildung mit Hilfe der Finite-Elemente-Methode zu simulieren. Für Ti-15-3-3-3 und Ti-6246 wird die Bildung eines segmentierten Spans beobachtet. Für Alloy 625 wird die Materialfestigkeit bei hohen Dehnungen vom Johnson-Cook-Modell überschätzt, wodurch in der Simulation die Bildung eines Fließspans vorhergesagt wird. Daher wird ein modifiziertes Johnson-Cook-Modell für die Zerspanungssimulationen verwendet, resultierend in einer segmentierten Spanform. Die

durchschnittlichen Schnittkräfte werden in den drei Fällen im Rahmen von 20% der experimentell erhaltenen Werte vorhergesagt. Es gibt deutliche Unterschiede in den vorhergesagten und den experimentell ermittelten Spanformen. Diese Unterschiede können auf die Schwierigkeit der Vorhersage des Materialverhaltens unter den während spanender Bearbeitung vorherrschenden Bedingungen zurückgeführt werden.

Dieses Problem wird durch die Verwendung einer inversen Parameterbestimmungsmethode beseitigt, da auf diese Weise die Materialparameter direkt aus den Zerspanungsprozessen identifiziert werden. Die Spanformen und die Schnittkräfte der Simulation werden durch die systematische Variation der Materialparameter mit den entsprechenden Werten aus den Standardexperimenten abgestimmt. Die Robustheit des Verfahrens wird durch die Identifizierung von Parametern für zwei verschiedene Materialien, sowie die Durchführung von Optimierungen von verschiedenen Ausgangspunkten getestet. Ebenfalls werden Studien durchgeführt, um die Konvergenz zu verbessern, und um den Berechnungsaufwand zu reduzieren. Die Lösung, die aus dem inversen Identifikationsalgorithmus vorhergesagt wird, kann ebenfalls durch die Kenntnis des Einflusses der Spannungs-Dehnungs-Kurven auf die Spanformen und die Schnittkräfte verbessert werden, was auch den Berechnungsaufwand verringern kann.

Es hat sich gezeigt, dass viele Parametersätze identifiziert werden können, die ähnliche Spanformen und Schnittkräfte zur Folge haben. Dies ist darin begründet, dass alle Parametersätze im Gebiet der Zerspanungverfahren die gleiche Fließspannungskurve wiedergeben. Um Parameter zu bestimmen, die über einen möglichst großen Bereich gültig sind, werden sich stark unterscheidende Schneidbedingungen für den Identifikationsprozess gewählt.

Contents

List of Figures

List of Tables

Chapter 1

Introduction

1.1 Motivation

Machining is a widely used manufacturing process in which a workpiece material is progressively given a complex shape by material removal using a tool (Childs *et al.* (2000); Shaw (1984)). The relative motion between a tool and a workpiece is used to remove material in the form of chips. This technique has been used for a wide variety of materials such as metals (Childs *et al.* (2000); Shaw (1984)), non-metals (Alauddin *et al.* (1995); Koch (1964)) and composites (Ferreira *et al.* (1999); Komanduri *et al.* (1991)). Even though this idea of material removal is very simple, the physical understanding of the process is complicated by the complex interactions between the tool and the workpiece. High stresses, strains, strain rates and temperature variations are encountered during the process which have a direct bearing on the energy consumption, tool wear, workpiece surface finish *etc.* A better understanding of the machining process is therefore necessary in order to optimise the process parameters so as to make it more efficient and reduce the wastage of resources.

The mechanics of machining has been studied for more than 100 years (Childs *et al.* (2000)). Early studies of the chip formation process were based on the analytical modelling of the idealised orthogonal chip formation process (see Section 1.5). The analytical modelling was however only useful for analysing very simple cases of chip formation. High speed machining, segmented chip formation, complex machining processes such as milling, drilling, grinding, *etc.* could not be readily modelled using analytical techniques. With the advent of powerful computers and the development of robust numerical algorithms, the simulation of the chip

formation process has become an important tool for understanding the mechanics of machining and has also been successfully used for simulating complex cutting processes.

Finite element simulation of the chip formation process is however challenging. The material behaviour under the conditions prevailing during machining is not well-known. Apart from this, the tool and the chip interaction is complex, due to the extreme conditions prevailing near the tool tip. The interaction is also extremely sensitive to the application of external elements such as lubricants and coolants. Both the material properties and the interaction properties are coupled; for instance a change in temperature can lead to a change in the frictional properties. Chemical reactions can also take place between the newly formed surface and the surrounding environment, changing the physical property. All this prevents the modelling of machining processes from being robust.

In the absence of robust cutting models, the manufacturing industry has resorted to creating large machining databases in which machining parameters are recommended for various workpiece material and tool combinations. This approach is not only expensive and time taking, it is also very unreliable. The machining parameters often have to be further tuned by trial and error to achieve the best results. On top of this, new workpiece and tool materials are frequently developed and such databases are rarely available for all possible combinations. Without a robust predictive machining model, a lot of time, money and efforts are thus being spent to determine the optimal machining parameters.

During continuous chip formation at high cutting speeds, in regions near the tool tip, the average strain in the chip can reach up to 200%, strain rates can reach up to the order of 10^5 s^{-1} and a temperature rise of several hundreds of degrees can take place. In Figure 1.1, D$_1$ schematically represents the domain of state variables - strains, strain rates and temperatures during a machining experiment. For a finite element model of machining, the flow stress as a function of these state variables is required. Phenomenological material models, such as the Johnson-Cook model (see Section 2.2.3), are parametric models which can predict the flow stress as a function these state variables. The main challenge lies in obtaining these parameters at the correct range of state variables. Experimental methods, such as the Split Hopkinson Pressure Bar (SHPB) test, can be used to obtain the flow stress at strains up to 50%, strain rates of the order of 10^4 s^{-1} and temperature rise of hundreds of degrees. In Figure 1.1, D$_2$ schematically represents the domain of state variables during a typical SHPB test. Using data fitting techniques, the material parameters are obtained from the experimental data. In

this case, the material parameters are optimised for predicting the flow stress values in the domain of the state variables reached during the SHPB test. On using these material parameters for high speed machining simulations, extrapolations over several orders of magnitude of strains and strain rates are expected to occur. The material model provides a way for extrapolating the flow stress curves outside the domain at which the parameters are obtained. Since the material parameters are not optimised for the machining conditions, the extrapolated flow stress values in the domain of machining are expected to be inaccurate.
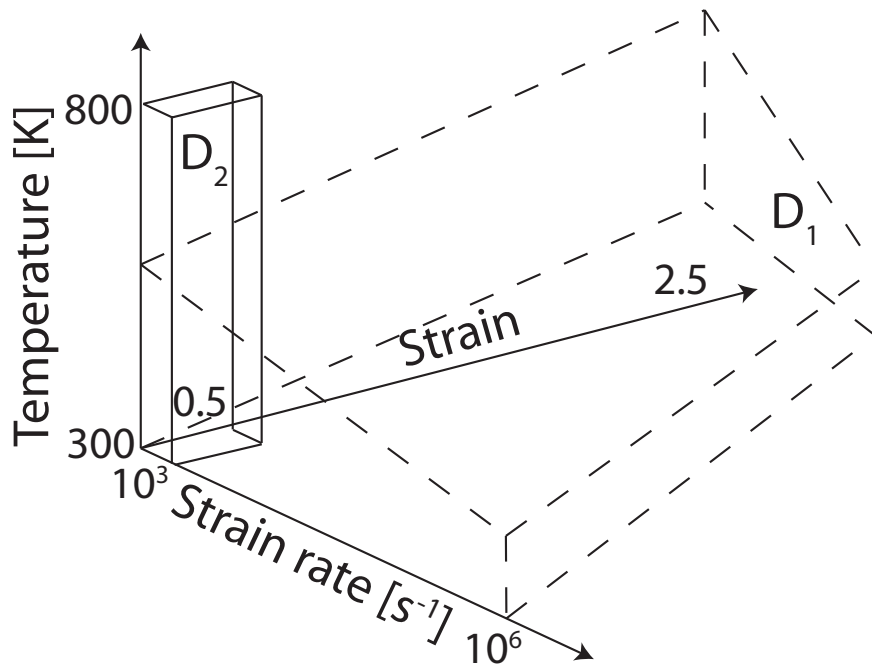
Figure 1.1: The domain D_1 schematically represents the range of strain, strain rate and temperature a typical high speed machining experiment where continuous chips are formed and D_2 schematically represents their range during a typical SHPB test.

To obtain material parameters valid in the domain of machining, parameters can be identified directly from the machining process itself using the inverse identification process. In this method, simulations are conducted with a set of material parameters and the resulting chip shapes and cutting forces are compared to those from the experiments. If the experimental and the simulation results do not match, the material parameters in the simulations are methodically varied until the match occurs. The use of a material model makes the inverse identification process feasible. If the flow stress were to be found as a set of values for different combinations of state variables, inverse identification would have been impossible as a large number of parameters would have to be

identified. In a parametric material model like the Johnson-Cook model, the different material parameters can be adjusted in a way that a number of parameter sets give rise to similar flow curves (see Chapter 4). If these parameter sets are optimised over the domain of machining for a given set of cutting condition, similar chips and cutting forces are expected to be formed, as long as the state variables reached are within this domain. If the cutting conditions were changed in such a way that state variables are obtained outside the domain in which the material parameters are determined, extrapolations would occur, making the simulation results unreliable. A robust material parameter set should be optimised for a large range of cutting conditions so that the flow stress can be predicted correctly over a large domain. If the same flow stress curve is correctly represented in a given domain by more than one parameter set, the resulting observables would also be similar. Consequently it should not matter what is the numerical value of the parameter to represent a given stress-strain curve. Even though in this work the inverse identification method is used for identifying parameters for the Johnson-Cook model, this technique can be used for any other material model.

1.2   Overview

The next sections in this chapter give a background to machining and cutting mechanics. In Section 1.3, the orthogonal cutting process is explained along with the associated terminology. The different chip shapes which can be formed during machining and the basics of their characterisation are also discussed. In Section 1.5, the different analytical models of the orthogonal chip formation process are given. Oxley's predictive cutting model (Section 1.5.2) has not only been used for machining predictions, but has also been used for understanding material behaviour at high cutting speeds.

In Chapter 2, the finite element modelling of chip formation has been discussed. A number of modelling issues such as meshing, the choice of material models, the difficulty in modelling material separation, and computational expense are considered here. During the simulation of segmented chip formation, the problem of hourglassing may occur which can destabilise the simulation. Therefore, a detailed study of hourglassing is also discussed in this chapter.

In Chapter 3, the problem of using material parameters obtained from experimental methods is shown with examples. For two alloys of Titanium (Ti-15-3-3-3 and Ti-6246) and a nickel-based superalloy (Alloy 625), Johnson-Cook parameters are obtained from SHPB experiments.

Machining simulations are then conducted using these parameters, and the chip shapes and the cutting forces obtained from simulations are compared to experiments. The limitations of this method are then discussed in detail. The Johnson-Cook model is also modified for simulating chip formation in Alloy 625.

In Chapter 4, the problem of the non-uniqueness of parameter sets arising from the use of the Johnson-Cook model is studied. The Johnson-Cook model is analysed to understand under what conditions the different parameter sets give rise to similar chips and cutting forces. Finally, recommendations are made to choose the cutting conditions during the inverse identification process in order to identify material parameters which are optimised over a large machining domain.

In Chapter 5, the inverse identification method is discussed. The chip shapes and the cutting forces from standard numerical machining experiments and test simulations are matched to inversely identify the parameters. An error function is created which takes into account the chip shape and the cutting force mismatch. The error function is then minmised using different optimisation strategies. After verifying that this method works for simple cases, a number of identification studies are done to understand the effects of optimisation parameters on convergence and how to improve it. Identification studies are conducted for different cutting conditions and different parameter sets to test the robustness of the method. Finally, using the knowledge of the stress-strain curves, a method of solution improvement is proposed which leads to savings in the computational expense.

In this work, the state-of-the-art and the related previous works are discussed in each chapter. The results in Chapter 3 are a part of a collaborative work. Furthermore, parts of this work have been previously published in international conferences and journals. The publications associated with different chapters are listed below:

Chapter 3: Hokka *et al.* (2012a), Hokka *et al.* (2012b), Hokka *et al.* (2012c)
Chapter 4: Shrot & Bäker (2010), Shrot & Bäker (2012b)
Chapter 5: Shrot & Bäker (2011a), Shrot & Bäker (2011c), Shrot & Bäker (2011b), Shrot & Bäker (2011d), Shrot & Bäker (2012a)

1.3   Basics of Machining

The machining processes can be divided into two broad categories (DIN 8589): ones in which the cutting edges are geometrically well defined, such as turning, milling, drilling, shaping *etc.* and ones in which the cutting edges are geometrically undefined, such as grinding, honing, lapping etc. The processes of the first type are often called "cutting processes" and those of the second type are called "abrasive processes" or "grinding processes". The focus of this work is the study of a simplified cutting process with geometrically defined edge called the orthogonal cutting process, in which the cutting edge is perpendicular to the workpiece motion. A schematic diagram of the orthogonal cutting process has been shown in Figure 1.2.
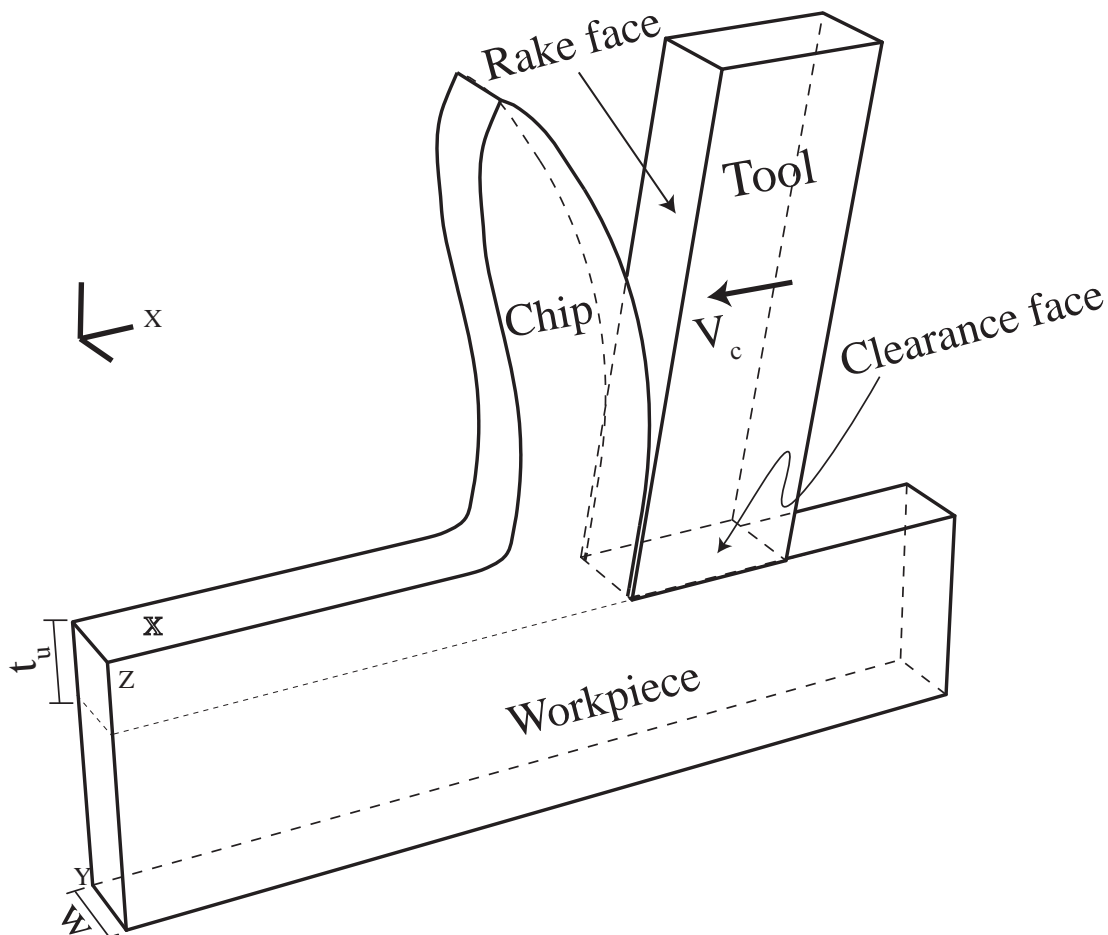
Figure 1.2: A schematic diagram of orthogonal cutting. The cutting edge is perpendicular to the cutting velocity and the chip slides across the rake face.

During this idealised cutting process, the cutting edge is perpendicular to the cutting velocity and the chip slides across the rake face, without
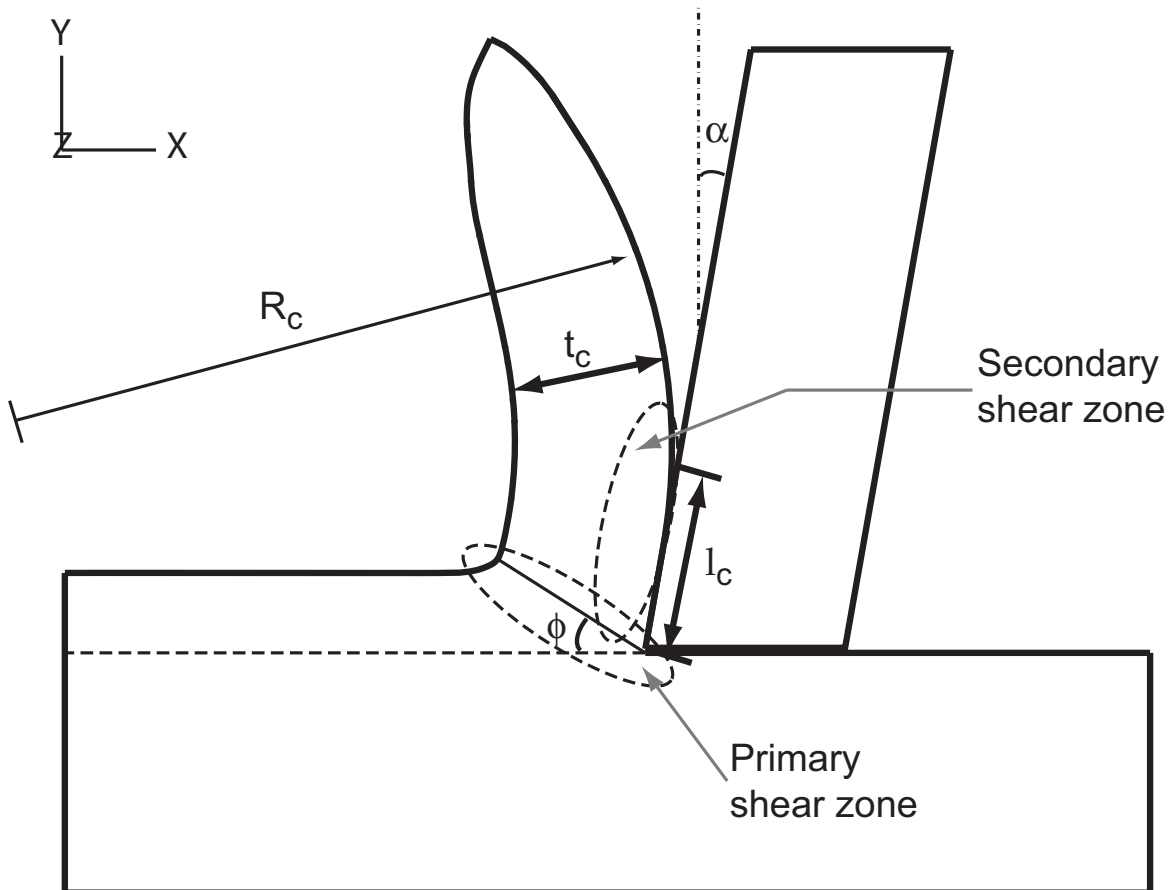
Figure 1.3: A two dimensional representation of orthogonal cutting showing the notable dimensions in a continuous chip.

any curl (Figure 1.2). If the cutting depth is much smaller than the width of cut, then the width of the chip is almost equal to the width of cut. This simplification leads to the assumption of plane strain conditions during the chip formation process: the cutting process can be analysed in two dimensions only, and the physical parameters such as stress, strain, temperature *etc.* are assumed not to vary along the *z*-direction. In a realistic situation, some increase in the chip width is expected (Lee & Shaffer (1951)), and the stress and temperature distributions in the outer surfaces must be different from those of the interior due to the difference in the heat dissipation. Due to some stochastic instabilities in the material, some chip curl can also occur.

The speed of the tool with respect to the workpiece is called the cutting speed (V_c) and the depth of cut is the same as the uncut chip thickness (t_u). In this case the feed is also the same as the depth of cut since, after each pass, the tool will move down by a distance equal to the depth of cut. The chip has some measurable dimensions (Figure 1.3) such as the chip thickness (t_c), the chip curvature (R_c) and the chip

contact length (l_c). The chip thickness is easy to define in a continuous chip (see Section 1.4) where it is more or less constant. However, in non-continuous chips, an average chip thickness can be defined (Cotterell & Byrne (2008)).

(a)	(b)
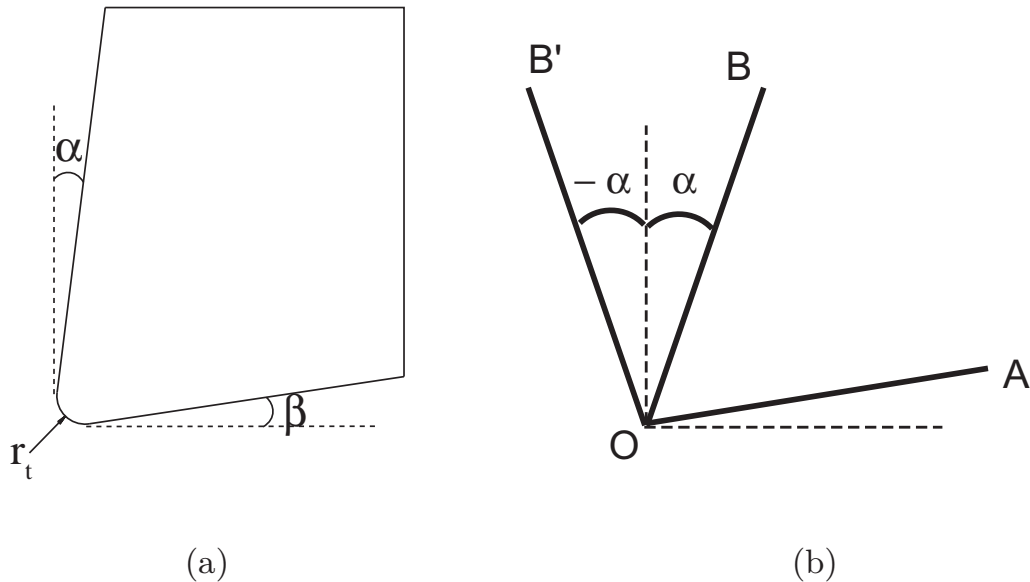
Figure 1.4: a) A schematic representation of the tool showing the rake angle (α), the clearance angle (β) and the tool tip radius (r_t). b) Convention adopted for measuring positive and negative rake angles.

The tool geometry (Figure 1.4a) has a pronounced effect on the chip formation. The rake angle (α) is defined as the angle between the vertical and the rake face. The convention for measuring positive and negative rake angles are shown in Figure 1.4b. Surfaces OB or OB$'$ represent the rake face of the tool and the surface OA represents the flank face of the tool. Cutting experiments and simulations (Ceretti *et al.* (1999); Günay *et al.* (2004); Lo (2000); Shih (1995); Worthington (1975)) have shown that the rake angle variation affects the observables such as the chip shape and the cutting force profoundly. The clearance angle (β) is defined as the angle between the horizontal and the flank face. The clearance angle has a relatively smaller influence on the cutting mechanics, it is however important for the quality of the machined surface: a positive clearance angle is necessary, so as to allow the tool to clear the machined surface without any interference. This interference can be caused by the spring back of the workpiece or the vibrations of the tool and the workpiece. However, if the clearance angle is too large, the tool tip's strength may be reduced and it will be prone to breakage. It has also been shown that the clearance angle has a bearing upon the

flank face wear; an optimum clearance angle of about 6° is recommended so as to balance the flank wear and workpiece surface quality (Moneim *et al.* (1981)). The tool nose radius has also been shown (Chou & Song (2004); Liu *et al.* (2004); Yen *et al.* (2004)) to have a significant influence on the chip shape, cutting forces, surface roughness, residual stresses etc.

The tool advance which causes the material deformation and overcomes the frictional force between the tool and the workpiece results in a force on the tool. In orthogonal cutting, the force acting on the tool can be resolved into two components, one in the cutting direction which is called the cutting force (F_c) and the second in the vertical direction called the passive or the thrust force (F_t). When comparing cutting force measurements from different experiments, it is reasonable to compare the specific cutting force, *i.e.* the cutting force divided by the product of the uncut chip thickness and the cutting width, which has the units of pressure or energy density.

Large plastic deformations occur during the chip formation process. In early chip formation theories (Ernst & Merchant (1941); Merchant (1945a); Piispanen (1948)), it was assumed that most of the deformation takes place in an infinitesimally thin plane called the shear plane. The angle at which this plane is inclined to the horizontal is called the shear angle (ϕ) (Figure 1.3). It has been later shown (Oxley & Welsh (1963)) that this is an idealisation and that the workpiece material is gradually deformed over a zone called the primary shear zone. The chip and the tool interact to cause further plastic deformation called the secondary shear zone.

1.4   Chip Morphology

Based on the chip morphology, the chip shapes can be divided into the following broad categories (shown in Figure 1.5):

Continuous chip: Continuous chips can be characterised by their practically smooth surface with a constant chip thickness. These chips are formed in a stationary process and the deformation in the chip is more or less uniform. Such chips are often associated with ductile materials. The resulting surface roughness is good as the tool vibration is reduced due to a stable chip formation process. However, this is bad for the automation of the process since long ribbon-like chips can get entangled around the tool holder and the cutting process has to be interrupted to remove the chips from the process zone.

(a) Continuous chip

(b) Segmented chip

(c) Separated chip

(d) Built-up edge (BUE) chip
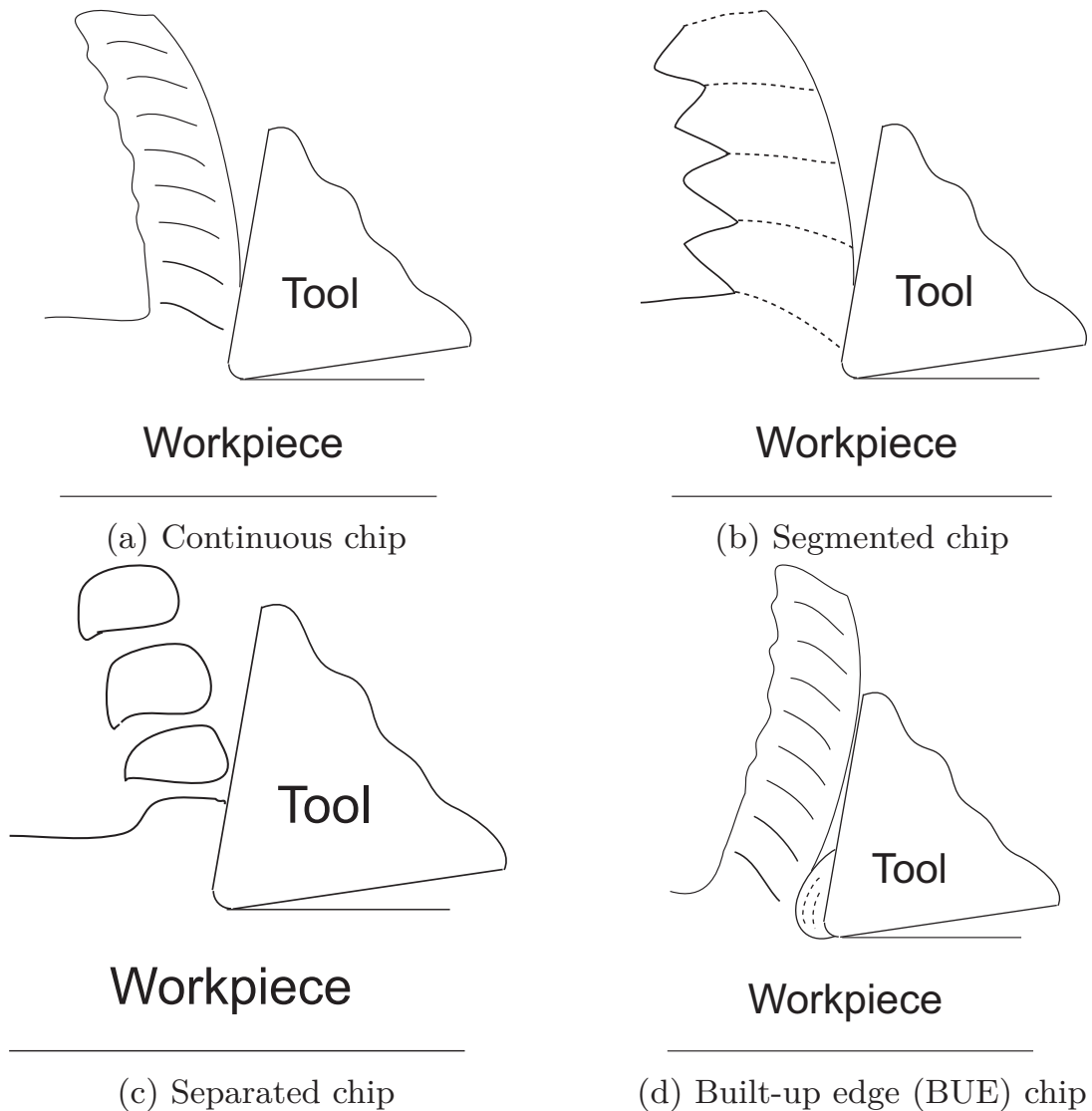
Figure 1.5: Different chip morphologies

Segmented chip: Segmented chips, also called serrated chips or saw tooth chips are characterised by a series of peaks and valleys in the chip thickness. The region between two valleys, called a segment, is weakly deformed and most of the large deformation concentrates in a narrow region, called the shear band. Such chips are often formed under high cutting speeds and materials with low thermal conductivity are prone to form such chips. The geometrical parameters used to characterise a segmented chip are shown in Figure 1.6. An average chip thickness may be defined for the segmented chips as

$$t_c^{av} = \frac{h_{max} + h_{min}}{2} . \tag{1.1}$$
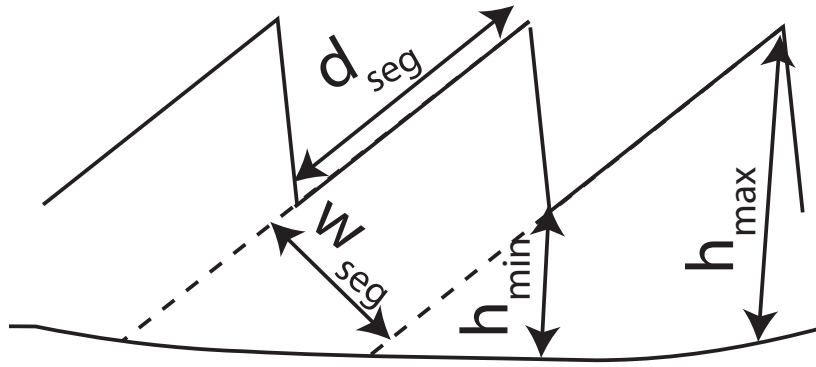
Figure 1.6: Geometrical parameters used for characterising segmented chips. h_{max} is the maximal segment height, h_{min} is the minimal segment height, w_{seg} is the segment width and d_{seg} is the sheared distance.

Average chip compression factor for a segmented chip is given by

$$\lambda_c^{av} \quad = \quad \frac{t_c^{av}}{t_u} \,. \tag{1.2}$$

The degree of segmentation is defined as

$$g_{seg} \quad = \quad \frac{h_{max} - h_{min}}{h_{max}} \,. \tag{1.3}$$

The value for g_{seg} is 0 for a continuous chip and 1 for a separated chip.

Separated chip: Separated chips or discontinuous chips are formed when the chip segments get completely separated. The cutting force varies rapidly when the segments break away, leading to tool vibrations and increased surface roughness in the case of ductile materials. However, the machining of such materials can be readily automated since short breaking chips are formed.

Built-up edge chip: Built-up edge (BUE) chips are formed due to the adherence of the workpiece material onto the tool surface, often due to extreme conditions of high temperature and pressure existing near the tool tip. Chemical interaction between the workpiece material and the tool material is also one of the factors which leads to its formation. The built up chips grow in size gradually, accumulating more and more material, until they become unstable and break away. Built up edge chips are detrimental to the surface roughness and also lead to faster tool wear.

1.5 Analytical description of cutting mechanics

In this section, some major results from analytical models of the chip formation process will be discussed in brief. An in-depth analysis of the methods can be found in (Childs *et al.* (2000); Oxley (1989); Shaw (1984)). The most important parameters of interest which can be found by such models are usually the cutting force, average strain, average strain rate and average temperature. Out of these, the cutting force prediction is especially important in industrial settings since it gives the process designer some idea about the input power requirements. The cutting force is also an important criterion to help in tool design and selection, as are parameters such as the rake angle and the clearance angle. Strain, strain rate and temperature predictions are of a greater interest to the material scientist, who can better understand the material behaviour at these conditions and help in the development of new materials and processes (Rösler *et al.* (2005)).

1.5.1 Shear plane model

One of the earliest analytical models was the shear plane model (Ernst & Merchant (1941)) for orthogonal cutting. One of the most important assumptions in this theory was that all the shear deformation took place in a single shear plane. This assumption was based on Ernst's (Ernst (1938)) observations that the continuous chip are formed with most of the deformation taking place in a very thin zone going from the tool to the chip top surface.

Assumptions used in the shear plane model are (also summarised in Shaw (1984)):

1. The material is ideally rigid and perfectly plastic.

2. The tool is perfectly sharp and there is no interaction between the flank face and the workpiece.

3. The shear occurs along a plane called the shear plane

4. The cutting velocity is uniform.

5. The cutting edge is perpendicular to the cutting velocity.

6. The uncut chip thickness is constant.

7. The tool width is greater than the width of cut.

8. A continuous chip forms without a built up edge

9. Plane strain conditions exist.

10. The stresses on the shear plane and the tool are uniform.
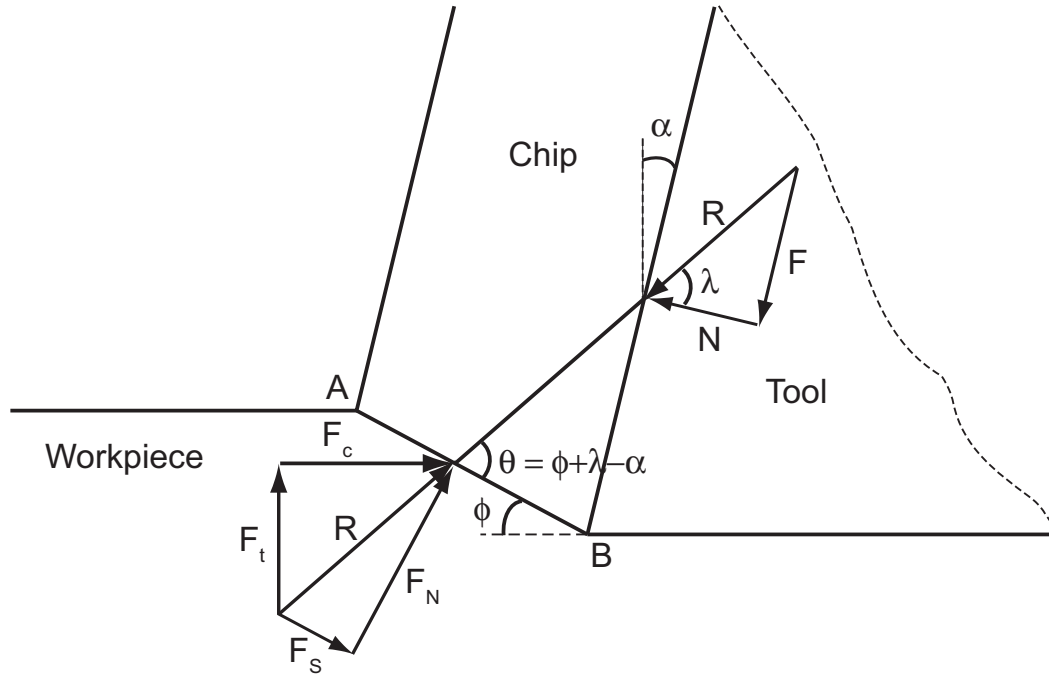
Figure 1.7: The shear plane model along with the associated forces.

Figure 1.7 shows a schematic diagram of the shear plane model. The cutting speed is V_c, the chip speed is v, the uncut chip thickness is t_u, the chip thickness is t_c, the rake angle is α and the shear angle is ϕ. The length of the shear plane AB is l. The chip speed is related to the cutting speed by

$$v \quad = \quad \frac{V_c \sin \phi}{\cos(\phi - \alpha)} \,. \tag{1.4}$$

The velocities along (v_S) and normal (v_N) to the shear plane can also be related to the cutting speed using

$$v_S \quad = \quad \frac{V_c \cos \alpha}{\cos(\phi - \alpha)} \,, \tag{1.5}$$

$$v_N \quad = \quad V_c \sin \phi \,. \tag{1.6}$$

The shear strain undergone by the material across the shear plane is given by

$$\gamma_S \quad = \quad \frac{v_S}{v_N} \tag{1.7}$$

$$= \quad \frac{\cos \alpha}{\sin \phi \cos(\phi - \alpha)} \,. \tag{1.8}$$

Due to the assumption that all the shear occurs across an infinitely thin shear plane, the strain rate is infinite. Using the constancy of volume, a relation between the chip thickness and the uncut chip thickness can be obtained:

$$V_c t_u = v t_c, \tag{1.9}$$

or

$$\frac{t_u}{t_c} = \frac{v}{V_c} \tag{1.10}$$

$$= \frac{\sin\phi}{\cos(\phi - \alpha)}. \tag{1.11}$$

The cutting force (F_c) and the thrust force (F_t) can be expressed in terms of R which is the resultant force transmitted across the tool-chip interface and λ which is the mean angle of friction (Figure 1.7):

$$F_c = R\cos(\lambda - \alpha), \tag{1.12}$$
$$F_t = R\sin(\lambda - \alpha). \tag{1.13}$$

The resultant force R can also be expressed in terms of F_S, the shear force along the shear plane as:

$$R = \frac{F_S}{\cos\theta} \tag{1.14}$$

$$= \frac{k_S t_u w}{\sin\phi \cos\theta}, \tag{1.15}$$

where θ is the angle made by the resultant R with the shear plane and k_S is the shear flow stress along the shear plane. The resultant force can be resolved along the rake face as:

$$F = R\sin\lambda, \tag{1.16}$$

and normal to the rake face as

$$N = R\cos\lambda. \tag{1.17}$$

The shear angle (ϕ) is an unknown quantity which is required in calculating the cutting force as well as the parameters which determine the chip geometry. Therefore it is important to have an analytical estimate of the shear angle. By choosing ϕ so that the expenditure of work is minimised (Ernst & Merchant (1941); Merchant (1945a,b)), the shear angle is given by:

$$\phi = \frac{\pi}{4} + \frac{\alpha}{2} - \frac{\lambda}{2}. \tag{1.18}$$

Using a similar argument for the minimisation of energy, but for a material whose shear flow stress increased linearly with the increase in the normal stress in the shear plane (Merchant (1945a,b)), the shear angle was predicted to be

$$\phi \;=\; \frac{\cot^{-1} s_f}{2} + \frac{\alpha}{2} - \frac{\lambda}{2}, \tag{1.19}$$

where s_f is the slope of the shear flow stress against the normal flow stress relation.

The shear plane theory was the first analytical method to study the chip formation process. However, there were a number of weaknesses in this model. Most significantly, a realistic material behaviour was not considered and the assumption that all deformation took place in a shear plane was an approximation. It has been seen (Oxley (1989)) that the deformation takes place in a zone called the shear zone where the workpiece material gets gradually deformed into the chip. This zone may be thick or thin, based on parameters such as the material plasticity, cutting speed, heat conductivity etc. At higher cutting speeds, where the shear zones are expected to be thinner, there is a greater likelihood of saw tooth chip formation, which is not handled by this model. The dependence of this model on the *a priori* knowledge of the shear angle makes it difficult to make accurate predictions since the shear angle relation is not well known at a wide range of cutting parameters. The minimum work assumption used in the model is also shown to be incorrect by Bäker (2005).

1.5.2   Oxley's predictive machining theory

Oxley and his co-workers have worked extensively in developing an analytical theory for predicting the cutting force and the shear angle during continuous chip formation. The assumption that most of the plastic deformation occurred gradually over a parallel sided shear zone instead of occurring on a single shear plane allowed for the estimation of the strain rates in the shear zone (Oxley & Welsh (1963)). The shear strain rate along AB is given by:

$$\dot{\gamma}_{AB} \;=\; C_{ox}\frac{v_S}{l}, \tag{1.20}$$

where C_{ox} is a dimensionless constant and l is the length of AB with

$$l \;=\; \frac{t_u}{\sin \phi}. \tag{1.21}$$

A simple material hardening model was considered such that the flow stress

$$\sigma_p = \sigma_1 \varepsilon_p^n \,, \tag{1.22}$$

where σ_1 and n are material constants and ε_p is the plastic strain. It is related to the shear strain using the relation:

$$\varepsilon = \frac{\gamma}{\sqrt{3}} \,, \tag{1.23}$$

and consequently the plastic strain rate is related to the shear strain rate

$$\dot{\varepsilon} = \frac{\dot{\gamma}}{\sqrt{3}} \,. \tag{1.24}$$

The angle θ which the resultant R makes with the shear plane is given by:

$$\tan \theta = 1 + 2\left(\frac{\pi}{4} - \phi\right) - C_{ox} n \,, \tag{1.25}$$

which from geometry is also equal to

$$\theta = \phi + \lambda - \alpha \,. \tag{1.26}$$

The strain at AB is given by:

$$\gamma_{AB} = \frac{1}{2} \frac{\cos \alpha}{\sin \phi \cos(\phi - \alpha)} \,, \tag{1.27}$$

which is half of what is predicted by the shear plane theory. The temperature at AB is given by:

$$T_{AB} = T_w + \eta \Delta T_{SZ} \,, \tag{1.28}$$

where T_w is the initial workpiece temperature, ΔT_{SZ} is the temperature rise in the shear zone and η is a factor ($0 < \eta \leq 1$) to account for the fact that not all of the plastic deformation occurs at AB. The temperature rise in the shear zone can be calculated by considering the plastic work done.

To calculate the flow stress using the Equation 1.22 at given temperature and plastic strain rate, a velocity modified temperature term is introduced which is used to find the values of σ_1 and n at the given conditions (Oxley (1989)). The velocity modified temperature term is given by:

$$T_{mod} = T\left[1 - \kappa_{ox} \ln \frac{\dot{\varepsilon}_p}{\dot{\varepsilon}_{p0}}\right] \,, \tag{1.29}$$

κ_{ox} is a constant and $\dot{\varepsilon}_{p0}$ is the reference plastic strain rate ($\kappa_{ox} = 0.09$ and $\dot{\varepsilon}_{p0} = 1\mathrm{s}^{-1}$ for plain carbon steels in the works of Oxley (Oxley (1989))).

Further analytical equations were developed to estimate the shear zone temperature, temparature at the tool-chip interface, the chip contact length *etc.*, the details of which can be found in Oxley (1989).

1.5.3 Algorithm for machining calculations using Oxley's theory

Oxley's predictive machining theory can be used to calculate the shear angle and the cutting forces given the cutting conditions and the material properties. The cutting force is calculated so that the work is minimised. The assumption of work minimisation during chip formation has later been shown to be incorrect (Bäker (2005)). Oxley's predictive machining theory is however useful as it provides an analytical method for estimating the cutting forces, which is required to find the power requirements for the machining process. This method has also been used by a number of researchers to estimate the flow stress at machining conditions and finding the corresponding material parameters (discussed in Section 5.1). Whereas Oxley used the Power law material model for machining predictions, some researchers extended his theory also for the Johnson and Cook model (Lalwani *et al.* (2009)). Oxley's theory has thus proved to be a useful analytical tool for machining predictions.

One of the major limitations of this method is that segmented chip and separated chip formation cannot be studied with it. Another disadvantage is that only average estimates are available for a number of physical quantities, which is insufficient. For example, chips with completely different shapes can be formed with similar average cutting force values (Bäker (2003a)). In recent times, numerical techniques such as the finite element method are used to study the chip formation process. They provide a better understanding of the physics of the chip formation process. The use of the finite element method for the chip formation process is described in Chapter 2.

Chapter 2

Finite Element Model

Finite element modelling of the machining process is challenging. Two major problems are associated with it:

Numerical issue: Since large strains are involved, the finite element mesh can get highly deformed, which affects the simulation accuracy. Moreover, a highly deformed mesh poses convergence issues that can make the simulation unstable. Another challenge is contact modelling, since complex conditions of high stress, strains and temperature gradients exist near the tool tip. This leads to convergence difficulties in some modelling techniques. The simulation of unstable chip formation, where chip segmentation occurs, can also be difficult: here again, the mesh can get highly deformed in the shear bands.

Material modelling issue: The second issue pertains to our limited knowledge of material behaviour at extreme conditions. The material in the shear zone experiences strains of more than 200%, strain rates of the order of 10^6 s^{-1} and a local temperature rise of hundreds of degrees. Using existing experimental methods, only limited strains at high strain rates can be reached. Typically, at strain rates of the order of 10^3 to 10^4 s^{-1}, a 50% strain can be reliably achieved in a Hopkinson split bar test. Experimentally testing material behaviour outside this range is difficult using the current methods. Contact modelling suffers from a similar difficulty as the friction parameters are not well known in these conditions. The issue of obtaining material parameters at the conditions of interest is gaining more and more relevance now, due to a tremendous advance in the numerical modelling methods and computational

speeds. Machining simulations which were prohibitively expensive, time taking or difficult to perform due to numerical limitations can now be accomplished in desktop PCs in a reasonable amount of time.

In the next section (Section 2.1), the numerical and the modelling aspects of machining will be explained in brief. Some relevant modelling details will also be discussed in order to give an idea of available numerical methods and their challenges. A review of different material models which can be used for machining simulations is given in Section 2.2.3. In Section 2.3, the finite element model used in this work will be explained in detail. The problem of hourglassing is considered in Section 2.4. The different strategies used to reduce the computational expense are discussed in Section 2.5. Finally, in Section 2.6, methods for comparing two chip shapes and cutting forces are described.

2.1 Finite Element modelling

Modern computers are becoming more powerful and the computational costs are declining. Consequently, numerical techniques have become more and more attractive for studying the chip formation process. The finite element method is one of the most popular, due to a strong theoretical basis (Zienkiewicz & Taylor (2005)) and easy to use commercial software packages which have been extensively validated for various engineering problems. The advent of commercial software packages has coincided with the development of more robust and efficient algorithms and improved computational speeds. This has enabled engineers and scientists to concentrate on physical problem modelling and analysis. Some of the earliest works in machining simulations using the finite element method were done in the early 1970's (Kakino (1971); Zienkiewicz (1971)). In these, the chip shape was presumed, the material model was assumed to be independent of strain rate and temperature and the tool-chip interface was frictionless. The work by Shirakashi and Usui in 1976 (Shirakashi & Usui (1976)) was one of the earliest works in which the chip shape was predicted, the chip-tool friction was considered and the material model was more realistic: the strain, strain rate and temperature effects were taken into account. Since then a large body of work has been performed in the chip formation simulation using the finite element method. A comprehensive review of these methods can be found in literature (Mackerle (1998, 2003)).

A number of commercial and open source finite element software packages are available for *e.g.* DEFORM-2D (Fluhrer (2004)), ADVANT-

EDGE (AdvantEdge (2007)), Code Aster (Proix *et al.* (2000)). In this work, the commercial finite element simulation software Abaqus (Abaqus Analysis User's Manual, V. 6.9) has been used for simulating the chip formation process. Since this work aims at creating a model for cutting simulations and understanding the effect of material parameters in the results, rather than the inner workings of the software, Abaqus software package was found to be sufficient. It is well documented, validated and is easy to use. It also provides for flexibility as new material behaviours, element types, friction behaviour *etc.* can be programmed as FORTRAN subroutines. It has also been used by a large number of researchers for machining simulations (*e.g.* Arrazola *et al.* (2005); Bäker (2004); Mabrouki *et al.* (2008); Ng & Aspinwall (2002); Ramesh & Melkote (2008)), making it easy to find relevant literature discussing the pros and cons of certain techniques.

2.2 Components of an FE Model

In this section, the major components of a finite element model of chip formation simulation will be discussed.

2.2.1 Geometric description

A simplified model, obtained through a judicious choice of geometric description, can drastically reduce the simulation times and computational costs, although it is often associated with a number of idealisations and assumptions that can reduce the accuracy of the solutions.

A geometrically simple machining process such as orthogonal cutting is essentially three dimensional. The simplifying assumption of plane strain conditions renders it a two dimensional problem, thereby leading to large savings in the computational costs. Due to this assumption, the stress, strain and temperature distributions are assumed not to change in the z-direction. In all the simulations in this work, only 2D models have been considered for the orthogonal cutting process.

2.2.2 Choice of solution methods

Finite element modelling methods can be divided into two broad categories: based on the frame of description of the problem and based on the type of solver.

Problem description methods

Lagrangian Description: In this description of the physical problem, the mesh is associated with the material and gets distorted along with the deformation of the material. The large deformations of the mesh during machining might not only cause the simulation time to be very high, but due to the deteriorating mesh quality, the solution can be inaccurate. One solution to this problem is to use a very fine mesh so that high stress, strain and temperature gradients can be locally resolved.

Another challenge in this description is modelling the chip separation from the workpiece. Due to the tool motion, the material should deform to separate the chip from the workpiece. However, the mechanism of this separation is not clear. One of the two possible mechanisms is a crack propagation mechanism where the atomic bonds are broken and material separation takes place on an atomic scale. The second is the continuous deformation of the material as an extreme case of a forging process. Two different methods approximating these two mechanisms are used so that the elements near the tool tip are not excessively deformed, crashing the simulation. Element deletion based on physical criteria can be used to recreate the first mechanism, and a remeshing technique can be employed to recreate the second mechanism, for which the distorted mesh is replaced with a better quality mesh.

Eulerian Description: This description is often used in Computational Fluid Dynamics problems. The material can flow through a control volume and the mesh is fixed at all times. The advantage of this formulation is that in cases in which complex flow patterns such as eddies or vortices are involved, there is no distortion of the mesh as it is fixed. For machining problems, a similar approach can be devised, in which the viscoplastic workpiece material can be modelled to be flowing around the tool (Leopold (1999); Leopold *et al.* (2001)). This is an attractive option, in contrast to the Lagrangian description. Since the mesh is fixed and the region with high strain gradients is known, a finer mesh can be used near the tool tip and the workpiece material can flow in and out of it. This method does not require a special chip separation criterion as new surfaces can be easily created due to the flow of the material around the tool. As the material boundary is not the same as the meshed region, it should be tracked at all times during the computations, because some mesh elements can have either the

tool material, the workpiece material, both or none. However, this approach has not yet been used for segmented chip formation.

In iterative methods such as Leopold (1999); Leopold *et al.* (2001), the chip boundaries are the free surfaces whose location is iteratively determined so that the velocity vectors are tangential to the free surface and no normal force acts on the surface, thus determining the chip shape. To obtain the final chip shape, a preliminary chip shape is assumed which is then iteratively updated till the velocity vectors are tangential to the free surface. Due to the dependency of the material properties on variables such as strain, strain rate and temperature, an iterative procedure is necessary for the simulation.

The Eulerian description has been used before for the simulation of the continuous chip formation process, for instance in the work of Strenkowski and Moon (Strenkowski & Moon (1990)) for simulating the orthogonal cutting of an Aluminium alloy 6061-T6. When comparing the simulation results to the cutting experiments, the cutting force and average temperatures matched well. However, no comparison was made between the experimental and predicted chip geometries in this paper.

Mixed approach: There have been a few approaches which use the advantages of the Lagrangian and the Eulerian descriptions. Two notable examples will be described here. The Arbitrary Lagrangian Eulerian (ALE) method (Rakotomalala *et al.* (1993)) has gained recent popularity in the simulation of machining. In this method, the solution is achieved using the Lagrangian description and, once the mesh deforms strongly, the nodes are shifted to improve the mesh quality. The solution from the old mesh is interpolated to the new mesh. The mesh topology does not change, meaning that the connectivity of nodes and elements remains the same. Since the mesh can move independently of the material, the mesh does not distort severely even though the material itself might undergo large strains. Another important aspect is that the material and the mesh boundaries coincide and each mesh element contains only a single material, clearly defining the material boundaries and allowing for more complex contact interactions.

In another mixed approach, proposed by Benson and Okazawa (Benson & Okazawa (2004)), the basic mass, momentum and energy equations are split into Eulerian and Lagrangian descriptions. After this, the Lagrangian step is solved which leads to the defor-

mation of the mesh along with that of the material. During the Eulerian step, the deformed mesh is moved back to the original fixed mesh and the material transport between the adjacent elements is calculated. Finally, the Lagrangian solution variables are recalculated taking into account the material flow into adjacent elements using transport algorithms. This formulation is also known as "Lagrange-plus-remap" (Abaqus Analysis User's Manual, V. 6.9) due to the staggered approach in which the solution is first found by the Lagrangian method and then is mapped back to the old fixed mesh. In the work of Benson and Okazawa (Benson & Okazawa (2004)), continuous, segmented and discontinuous chips were successfully simulated using this method. A mixed approach like this shows a lot of promise for simulating complex machining processes such as milling and turning in which the chip separation can be automatically taken care of.

Iterative convergence method: This method is similar to the Eulerian approach in the idea that an initially assumed chip shape is updated until the plastic flow is fully developed, *i.e.* when the tool load has achieved a stationary value or when the volume of material flowing in and out of the zone is conserved. This method differs from the Eulerian approach in the sense that the chip separation criterion must be devised and the material does not automatically flow around the tool. In order to do this, a small crack ($\sim 5\%$ of the uncut chip thickness) is introduced in front of the tool tip and the tool is advanced further. Another possibility is to have twin node elements near the tool tip so that, on the advancement of the tool, one node moves up the tool rake face and the other moves to form the cut surface. This method seems to give reasonable results (Childs *et al.* (2000); Maekawa *et al.* (1996); Shirakashi & Usui (1976)) for simulating stationary problems, however, it cannot be used for simulating segmented chip formation.

Solver types

Implicit Solver: Abaqus Standard implements the implicit integration scheme for solving the non-linear finite element equation, which is of the form $\mathbf{F}(\mathbf{u}_n) = 0$ where $\mathbf{u}_n$ represents the nodal displacements (Abaqus Analysis User's Manual, V. 6.9). In an implicit method, this equation is solved using iterative methods such as the Newton-Raphson method (Zienkiewicz & Taylor (2005)). An initial guess, sufficiently close to the actual solution is made, and the solution is

iteratively improved until a predetermined convergence criterion is met. As long as the initial guess is indeed close to the actual solution, something which is difficult to ascertain beforehand, the convergence is expected to be quadratic. As a consequence, the application of the force or the displacement boundary condition is done in a series of time steps so that the converged solution at each time step acts as a starting guess for the subsequent time step. A detailed explanation of the implicit method can be found in the literature (Zienkiewicz & Taylor (2005)).

Abaqus Standard has previously been used for machining simulations, most prominently in the work of Bäker (Bäker (2004)) in which a simple two dimensional cutting model with very simple contact conditions was created. Either low coefficients of friction were used or the effect of friction was neglected.

One of the major advantages of Abaqus standard is that it allows for adaptive remeshing and mesh refinement. During the machining process, large deformation of elements can take place near the tool tip and in the shear bands, which affects the solution accuracy. Badly deformed elements can lead to convergence difficulties. Adaptive remeshing can be helpful in eliminating this problem. Moreover, using mesh refinement techniques, the simulation can proceed with a relatively coarse mesh which can be selectively refined in the areas where large stress or strain gradients are expected.

One of the difficulties of Abaqus Standard in machining simulations is the handling the complex contact conditions between the tool and the workpiece. The contact acts as a discontinuity in the finite element scheme and the iterative method of the implicit solver may not converge in case of complex contact if the solution of one time step is not a good initial guess for the next one. Therefore Abaqus Standard is not widely used for more realistic machining simulations.

Explicit Solver: Abaqus Explicit implements the explicit integration scheme for solving the non-linear finite element equations (Abaqus Analysis User's Manual, V. 6.9). In the case of dynamic problems, the finite element equation can be recast into a system of equations, making a direct solution possible (Zienkiewicz & Taylor (2005)). However the solution to these equations is conditionally stable and is guaranteed to converge only if the time increments are

sufficiently small. The stable time increment limit is dependent on the highest eigenfrequency (ω_{max}) of the system. It is given by

$$\delta t \quad \leq \quad \frac{2}{\omega_{max}} \, . \tag{2.1}$$

In the case of Abaqus Explicit, some damping is added in order to control the high frequency oscillations. In this case the stable time increment limit is given by

$$\delta t \quad \leq \quad \frac{2}{\omega_{max}} (\sqrt{1 + \zeta^2} - \zeta) \, , \tag{2.2}$$

where ζ is the fraction of critical damping in the highest mode.

The highest eigenfrequency of the system is unknown and another method is used to estimate a conservative value for the stable time increment. This value is estimated by finding the maximum elemental eigenfrequency $\omega_{max}^{element}$. This is a conservative estimate of the stable time increment, smaller than the true stable time increment obtained by using the highest eigenfrequency of the model. It is determined by the time required by a dilatational wave to traverse an element (Abaqus Analysis User's Manual, V. 6.9). This is given by

$$\delta t \quad = \quad min \left(\frac{L_e}{v_w} \right) , \tag{2.3}$$

where L_e is the characteristic element dimension and v_w is the dilatational wave speed. Equation 2.3 can be rewritten in the form (ignoring damping)

$$\delta t \quad \leq \quad min \left(L_e \sqrt{\frac{\rho}{\hat{\lambda} + 2\hat{\mu}}} \right) . \tag{2.4}$$

Here ρ is the material density. $\hat{\lambda}$ and $\hat{\mu}$ are Lamé's constants and they are given by

$$\hat{\lambda} = \frac{E\nu}{(1 + \nu)(1 - 2\nu)} \, , \tag{2.5}$$

$$\hat{\mu} = \frac{E}{2(1 + \nu)} \, , \tag{2.6}$$

where E is the Young's Modulus and ν is the Poisson's ratio of the material. Equation 2.4 clearly shows that the computational time is dependent on the characteristic element dimension and the material density. In Sections 2.3.1 and 2.5, it will be shown how this relation can be used to reduce the simulation time for machining.

Solution method used in the work

In this work, an explicit solution method based on the Lagrangian description was chosen for simulating machining, as a wide range of cutting conditions can be modelled this way. It does not suffer from the limitations of resolving complex contact conditions as is the case for implicit methods. The issue of chip separation is handled by having a layer of sacrificial elements which are deleted when a physically defined criteria is attained. Deleting elements from the simulation can severely affect the residual stress values in the workpiece. However, as it was not relevant to this work, no attempt has been made to analyse this here. The separation layer has been kept as thin as possible, along with a fine mesh, so that its effect on the chip shape and cutting forces is minimised.

The Lagrangian description can also be used for simulating both continuous and segmented chips. In such cases, using a fine mesh is necessary but time consuming. However, improvements in computational speed have made getting a solution in a reasonable amount of time possible.

2.2.3 Material Models

Material models are required for the machining simulations to describe the inelastic material behaviour. A table of plastic stress values can be obtained from experiments in which strains, strain rates and temperatures are varied. Such a table can be directly taken as an input to describe the material behaviour in a finite element software. However, when the conditions are outside the experimental range, the plastic stress value has to be obtained by extrapolation. A material model is expected to have an ability to reasonably predict the material behaviour at given physical conditions even outside the range where it has been calibrated. When extrapolation takes place over several orders of magnitude, as is the case during machining simulations, resulting material parameters cannot be reliably used.

In the finite element softwares, the deformation in the material is separated into elastic and inelastic parts. The elastic deformation is recoverable and is not affected by the inelastic deformations[1]. The separation of the elastic and inelastic part is based on an assumption that the elastic ($\dot{\varepsilon}_E$) and plastic ($\dot{\varepsilon}_P$) strain rate tensors can be added to give the total strain rate tensor ($\dot{\varepsilon}_T$) *i.e.*

$$\dot{\varepsilon}_T = \dot{\varepsilon}_E + \dot{\varepsilon}_P \, . \tag{2.7}$$

In case of isotropic yielding, the uniaxial equivalent yield stress (σ_p) is given in terms of the uniaxial equivalent plastic strain (ε_p), uniaxial equivalent plastic strain rate ($\dot{\varepsilon}_p$), temperature (T) and other state variables. The equivalent plastic strain can be calculated from the plastic strain rate tensor by:

$$\varepsilon_p = \int_0^t \sqrt{\frac{2}{3}\dot{\varepsilon}_P : \dot{\varepsilon}_P} \, dt \, , \tag{2.8}$$

and equivalent plastic strain rate is give by:

$$\dot{\varepsilon}_p = \sqrt{\frac{2}{3}\dot{\varepsilon}_P : \dot{\varepsilon}_P} \, . \tag{2.9}$$

Further details regarding the numerical implementation of isotropic elasto-plastic material models can be found in Abaqus Analysis User's Manual, V. 6.9. From the next chapter, the subscript p will be dropped from these quantities for the sake of clarity.

The material models can be classified into two broad categories: phenomenological models or empirical models and physically based models.

a) Phenomenological models or empirical models : They describe the observed material flow stress behaviour in terms of input parameters without attempting to describe the underlying physics. Often these models contain a number of free parameters which are found from calibration tests using parameter fitting methods.

The physical quantities which are used for correlation are often chosen empirically from experimental tests. For example, with increasing deformation (strain) the stress increases. At higher rates of deformation (strain rates) the stresses are found to be higher as compared to the quasi-static cases. Finally at higher temperatures the stress values are lower than those at lower temperatures. This means that there is a dependence of the flow stress on those physical quantities. This is of course a very simplistic explanation of material behaviour since the flow stress also

---

[1]Damage models consider degradation of elasticity due to severe loading.

depends on heat treatment, the presence of alloying elements, phase transformations, grain size, grain orientation *etc.* Complex material behaviour taking these effects into account has, however, not been discussed in this work.

Some of the simplest and earliest empirical models relating the flow stress to the strain have been the Hollomon's equation (Hollomon (1945)) and the Ludwik's equation (Ludwik (1909)). The Hollomon's equation, also known as the power law, relates the plastic strain (ε_p) to the flow stress (σ_p):

$$\sigma_p = K_H \varepsilon_p^{n_H} .\tag{2.10}$$

Similarly the Ludwik's equation relates the flow stress to the plastic strain by:

$$\sigma_p = \sigma_y + K_L \varepsilon_p^{n_L} .\tag{2.11}$$

These early attempts at relating the stress to strain were extremely simple and did a very good job of approximating the material behaviour at a constant strain rate and a constant temperature. Even early on, there was a general understanding that the material hardens with increasing strain, roughly in the form of a power law. In case of machining, this material model is found to be inadequate as the effect of strain rate and temperature is not considered.

Taking into account the effects of plastic strain, plastic strain rate and temperature, the Johnson-Cook model (Johnson & Cook (1983)) is a relatively simple model, with five free parameters, which is very popular in simulating machining. The flow stress is given by:

$$\sigma_p = \underbrace{\left(A + B\varepsilon_p^n\right)}_{Elasto-Plastic\ term} \underbrace{\left[1 + C\ln\left(\frac{\dot{\tilde{\varepsilon}}}{\dot{\varepsilon}_0}\right)\right]}_{Viscosity\ term} \underbrace{\left[1 - \tilde{T}_h^m\right]}_{Thermal\ softening\ term} \tag{2.12}$$

The elasto-plastic term in equation 2.12 is the same as the Ludwik's equation 2.11. A viscosity term and a thermal softening term modify the equation 2.11 to take into account the strain rate and temperature effects. The parameter A gives the yield strength at the reference strain rate and temperature. The parameters B is the pre-exponential factor and n is the hardening exponent. C is the strain rate sensitivity factor and m is the thermal sensitivity exponent. All the parameters must be positive.

The strain rate hardening has a logarithmic dependence on the plastic strain rate. The plastic strain rate values below the reference plastic

strain rate value ($\dot{\varepsilon}_0$) are assumed not to have any influence on the flow stress. Therefore, the constrained plastic strain rate ($\dot{\tilde{\varepsilon}}$) is given by:

$$\dot{\tilde{\varepsilon}} = \begin{cases} \dot{\varepsilon}_0, & \text{if } \dot{\varepsilon} < \dot{\varepsilon}_0 \\ \dot{\varepsilon}, & \text{otherwise} . \end{cases} \tag{2.13}$$

The constrained homologous temperature term ($\tilde{T}_h$) is given by:

$$\tilde{T}_h = \begin{cases} 0, & \text{if } T_h < 0 \\ T_h, & \text{if } 0 \le T_h \le 1 \\ 1, & \text{if } T_h > 1 , \end{cases} \tag{2.14}$$

where T_h is the homologous temperature and is given by:

$$T_h = \frac{T - T_{room}}{T_{melt} - T_{room}} . \tag{2.15}$$

The homologous temperature expresses the material temperature as a fraction of its melting temperature (both the numerator and the denominator terms are considered as a temperature rise from a fixed temperature, here the room temperature). This model has been implemented in most of the commercial Finite Element software packages and will be analysed in detail in Section 4.1.

A number of modified Johnson-Cook type models have also been created for use in machining simulations, with reasonable success in predicting the chip shapes and cutting forces. In the work of Calamaz et al (Calamaz *et al.* (2008)), the Johnson-Cook model was modified to take into account the dynamic recrystallisation which causes microstructural softening. The modified material model is given by

$$\begin{aligned} \sigma_p = \quad & \left(A + \frac{B\varepsilon_p^n}{\exp \varepsilon_p^a} \right) \left[1 + C \ln \left(\frac{\dot{\tilde{\varepsilon}}}{\dot{\varepsilon}_0} \right) \right] \left[1 - \tilde{T}_h^m \right] \\ & \left[D(T) + (1 - D(T)) \tanh \left(\frac{1}{(\varepsilon_p + S(T))^c} \right) \right] \end{aligned} \tag{2.16}$$

with

$$D(T) = 1 - \left(\frac{T}{T_{melt}} \right)^d \tag{2.17}$$

and

$$S(T) = \left(\frac{T}{T_{melt}} \right)^b . \tag{2.18}$$

a, b, c and d are new material parameters in addition to the usual parameters of A, B, n, C and m, giving a total of nine free parameters.

Two different modified models, taking into account the strain softening were proposed by Sima and Özel (Sima & Özel (2010)) and were used for machining simulations. The first modified model is given by:

$$\sigma_p = \left(A + B\varepsilon_p^n\right)\left[1 + C\ln\left(\frac{\dot{\varepsilon}}{\dot{\varepsilon}_0}\right)\right]\left[1 - \left(\frac{T - T_{room}}{T_{melt} - T_{room}}\right)^m\right] \\ \left[D + (1 - D)\left[\tanh\left(\frac{1}{(\varepsilon_p + S)^c}\right)\right]^N\right], \quad (2.19)$$

which is a slightly modified version of the equation 2.16 with temperature independent parameters. Here A, B, n, C, m, c, D, S and N are nine free parameters. The second modified model has temperature dependent parameters and is given by:

$$\sigma_p = \left(A + B\varepsilon_p^n\right)\left[1 + C\ln\left(\frac{\dot{\varepsilon}}{\dot{\varepsilon}_0}\right)\right]\left[1 - \left(\frac{T - T_{room}}{T_{melt} - T_{room}}\right)^m\right] \\ \left[D(T) + (1 - D(T))\left[\tanh\left(\frac{1}{(\varepsilon_p + S(T))^c}\right)\right]^N\right], \quad (2.20)$$

with $D(T)$ and $S(T)$ given by equations 2.17 and 2.18 respectively. Here A, B, n, C, m, b, c, d and N are nine free parameters.

A material model taking the Rockwell hardness (H_{RC}) of AISI 52100 bearing steel into account was developed by Umbrello et al (Umbrello *et al.* (2004)). This model provides a systematic way of accounting for the changes in the material hardness following heat treatments. The downside of having such a model is the large number of free parameters which have to be determined experimentally. This model is given by:

$$\sigma_p = B(T)(C\varepsilon_p^n + G\varepsilon_p + F)\left[1 + (ln(\dot{\varepsilon})^m - A)\right] \quad (2.21)$$

with

$$B(T) = \exp(aT^5 + bT^4 + cT^3 + dT^2 + eT + f) \quad (2.22)$$

$$F(H_{RC}) = gH_{RC} + h \quad (2.23)$$

$$G(H_{RC}) = iH_{RC} + j. \quad (2.24)$$

Here the free parameters a-j, A, C, n and m are fitted from experiments.

Another material model, taking into account the strain history of the material was created by Shirakashi, Maekawa and Usui (Shirakashi

et al. (1983), Maekawa *et al.* (1983), Childs (1998)) for machining. This material model is as follows:

$$\sigma_p = A\left(\frac{\dot{\varepsilon}_p}{\dot{\varepsilon}_{p0}}\right)^B e^{CT}\left(\frac{\dot{\varepsilon}_p}{\dot{\varepsilon}_{p0}}\right)^D$$

$$\left[E+\left\{F+\int_{strain\ path} e^{-CT/G}\left(\frac{\dot{\varepsilon}_p}{\dot{\varepsilon}_{p0}}\right)^{-D/G} d\varepsilon_p\right\}^G\right]. \quad (2.25)$$

Here A-G are free parameters which can be temperature dependent.

In recent times, a number of parameter-rich material models have proliferated, aiming to model the material behaviour in great detail. However, large progress has not been seen in identifying material parameters in the relevant domain of strains, strain rates and temperatures for machining, mostly due to difficulties in reliably testing the material behaviour in these extreme conditions. This problem will be considered in Chapter 3.

b) Physically based model: A number of material models have been proposed based on the dislocation mechanics to describe the material behaviour (Xu & Huang (2012)). The flow stress is assumed to depend on dislocation density, dislocation movement and interaction, thermal activation of dislocation movement, grain size, crystal structure *etc.* Theoretical models are used to relate the flow stress to the physical parameters. However, the difficulty in these models comes from the lack of understanding of material behaviour at high strain rates and high temperatures. Therefore to make effective predictions, these models have to be calibrated and the material parameter values have to be found out from experiments. Such models are also sometimes called semi-empirical models.

Zerilli-Armstrong model (Zerilli & Armstrong (1987)) is one such model, based on simplified dislocation mechanics. The flow stress according to this model is given by:

$$\sigma_p = \Delta\sigma_G + [C_1 + C_2\sqrt{\varepsilon}]e^{(-C_3+C_4\ln\dot{\varepsilon})T} + \quad (2.26)$$
$$C_5\varepsilon^{n_{ZA}} + \frac{k_{ZA}}{\sqrt{l_G}},$$

where $\Delta\sigma_G$ is a stress component occurring due to the solute and initial dislocation density, k_{ZA} is the microstructural stress intensity, l_G is the average grain diameter, n_{ZA} is the strain hardening exponent and C_1-C_5 are the material constants which depend on the crystal structure of the material. For face centered cubic metals $C_1 = C_5 = 0$ and for body

centered cubic metals $C_2 = 0$. The athermal component of the flow stress $\sigma_a := \Delta\sigma_G + {} + C_5\varepsilon^{n_{ZA}} + \dfrac{k}{\sqrt{l_G}}$ is independent of thermal effects, as the name suggests.

For hexagonal close packed metals showing dynamic recovery, Equation 2.26 is modified (Zerilli & Armstrong (1997)) to give

$$\sigma = \Delta\sigma_G + \frac{k_{ZA}}{\sqrt{l_G}} + C_1 e^{-\beta T} + C_2\sqrt{\varepsilon_r(1 - e^{-\varepsilon/\varepsilon_r})}e^{-\alpha T}, \quad (2.27)$$

where C_1 and C_2 are material constants, α and β are functions of strain rate given in terms of material constants α_0, α_1, β_0 and β_1 by:

$$\alpha = \alpha_0 - \alpha_1 \ln\dot\varepsilon, \qquad\qquad\qquad\qquad (2.28)$$
$$\beta = \beta_0 - \beta_1 \ln\dot\varepsilon. \qquad\qquad\qquad\qquad (2.29)$$

The strain rate and the thermal effects are coupled together in the exponential term. In Equation 2.27, ε_r is a characteristic strain for dynamic recovery and for large strains the term inside the square root sign converges to ε_r, leading to a saturation of the flow stress.

In Jaspers (1999), material parameters for the Zerilli-Armstrong model have been found using Split Hopkinson Bar tests. It was shown that the Zerilli-Armstrong model described the material behaviour correctly for AISI 1045 which is a bcc alloy and AA-6082-O which is an fcc alloy. However for fcc alloy AA-6082-T6, the Zerilli-Armstrong model is found to be inadequate. The Zerilli-Armstrong model has also been used in machining simulations with varying success (Halle & Meyer (2004); Kiliçaslan (2009)).

Material parameters used in this work

In this work, the material parameters of two different materials are used for standard continuous chip formation simulations during the inverse identification process. The material parameters for HY-100 steel and AISI 52100, 62 HRC steel are taken from literature. The material parameters for HY-100 steel are listed in Tables 2.1 and 2.2. The temperature dependent thermal parameters for HY-100 steel are given in Figures 2.1 and 2.2. Material parameters for AISI 52100, 62 HRC steel are listed in Tables 2.3 and 2.4.

2.3   FE Model description and issues

In this work, a two dimensional explicit finite element model of orthogonal machining in Lagrangian description (Section 2.2.2) is created using the

Density [$\mathrm{kg\,m^{-3}}$]	7860
Young's Modulus [GPa]	205
Poisson's Ratio	0.28
$C_p = 92.78 + 0.7454T + \dfrac{12404 \times 10^3}{T^2}\ \mathrm{J\,kg^{-1}\,K^{-1}}$	
Element failure criterion:	
Equivalent plastic strain at failure ($\bar{\varepsilon}_f^{pl}$)	2.0

Table 2.1: Material properties for HY-100 steel. Taken from Batra & Kim (1990); Durrenberger & Molinari (2009); Goto *et al.* (2000)

A [MPa]	B [MPa]	n	C	m	T_{melt} [K]	T_{room} [K]	$\dot{\varepsilon}_0$ [$\mathrm{s^{-1}}$]
316	1067	0.107	0.0277	0.7	1500	300	3300

Table 2.2: Johnson-Cook parameters for HY-100 steel. Taken from Batra & Kim (1990); Durrenberger & Molinari (2009); Goto *et al.* (2000)
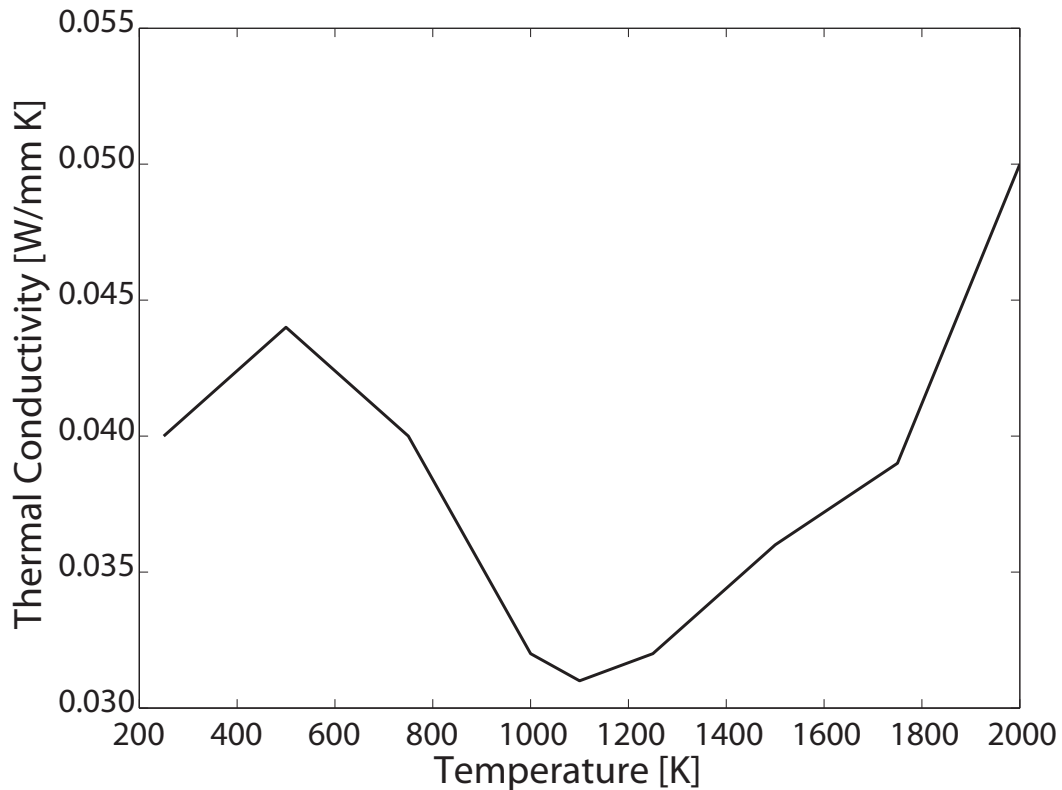
Figure 2.1: Temperature dependent thermal conductivity for HY-100 steel. Taken from Taljat *et al.* (1998)
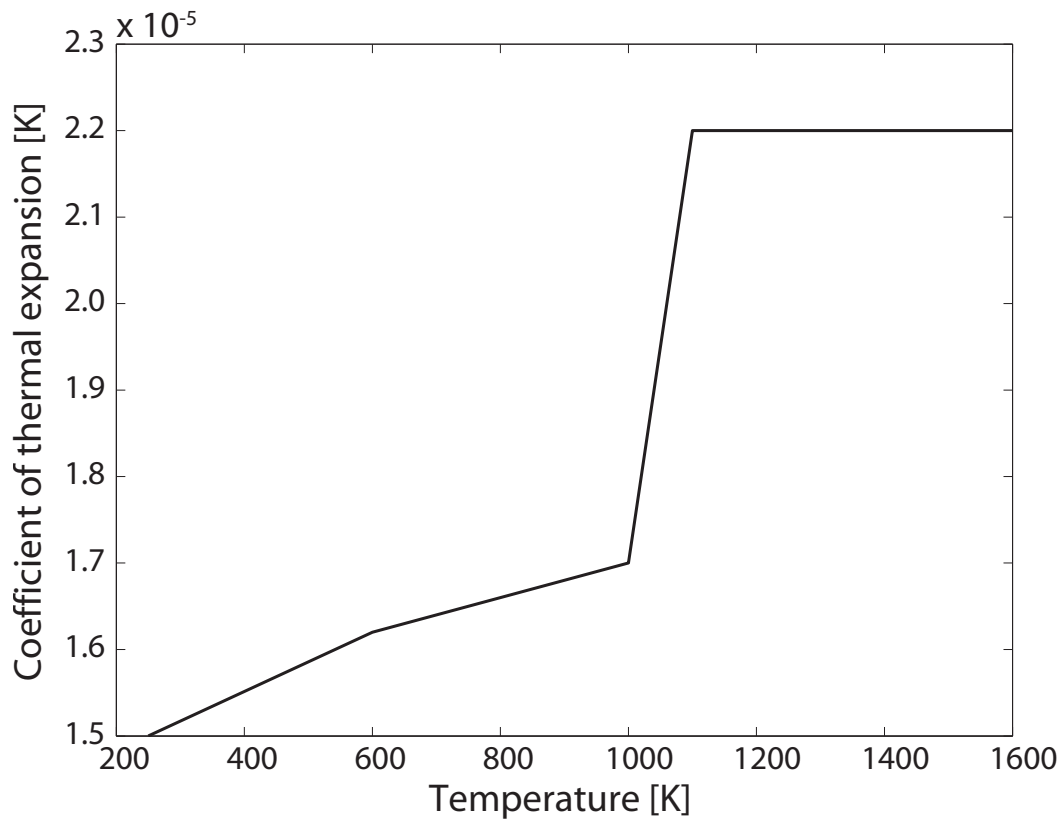
Figure 2.2: Temperature dependent coefficient of thermal expansion for HY-100 steel. Taken from Taljat *et al.* (1998)

Density [kg m^{-3}]	7827
Young's Modulus [GPa]	210
Poisson's Ratio	0.277
Specific Heat Capacity [J kg^{-1} K^{-1}]	693.6
Coefficient of thermal expansion [K^{-1}]	13.5×10^{-6}
Thermal Conductivity[W m^{-1} K^{-1}]	46.6

Table 2.3: Material properties for AISI 52100, 62 HRC steel (from Ramesh & Melkote (2008)).

A [MPa]	B [MPa]	n	C	m	T_{melt} [K]	T_{room} [K]	$\dot{\varepsilon}_0$ [s^{-1}]
688.17	150.82	0.3362	0.04279	2.7786	1643	298	0.001

Table 2.4: Johnson-Cook parameters for AISI 52100, 62 HRC steel (from Ramesh & Melkote (2008)).
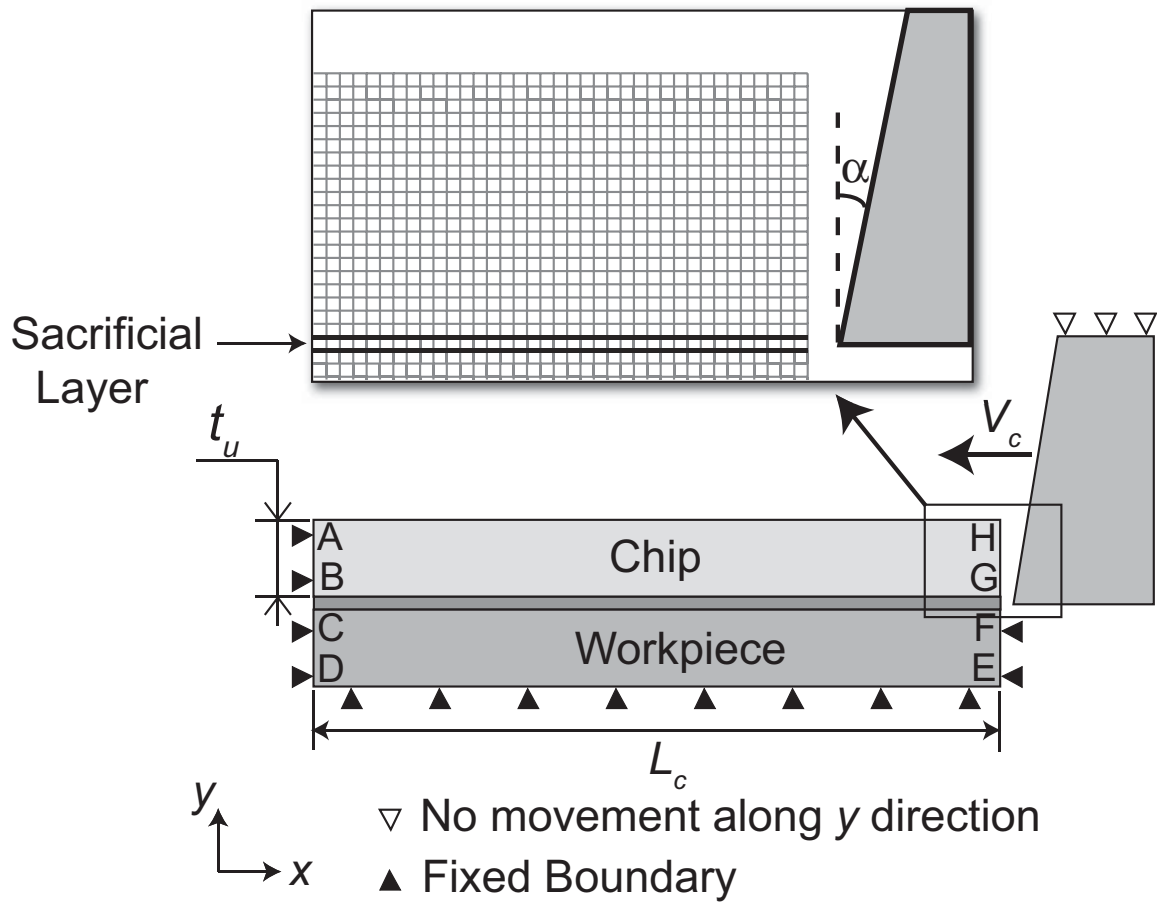
Figure 2.3: A schematic diagram of the finite element model

commercial software Abaqus (Abaqus Analysis User's Manual, V. 6.9). A schematic diagram of the model is shown in Figure 2.3. The workpiece is partitioned into three regions so that the top region (A-B-G-H) forms the chip, the bottom region (C-D-E-F) forms the machined workpiece and the intermediate region (B-C-F-G) forms the sacrificial layer. The sacrificial layer allows the chip to separate from the workpiece by deleting the elements when a pre-defined physical criterion is reached. The tool is considered to be rigid and is meshed using R2D2 elements (Abaqus Analysis User's Manual, V. 6.9). No heat conduction is allowed into the tool from the workpiece. The workpiece is held stationary and the tool moves in the negative x direction with a constant velocity (V_c). The cutting force (F_c) has a negative sign, implying that the cutting force vector points towards the negative x direction. For convenience only the magnitude of the cutting force has been reported in this work. The interaction between the tool and the workpiece is assumed to be frictionless in the inverse identification simulations (in Chapter 5). In machining simulations for Ti-15-3-3-3, Ti-6246 and Nickel based

superalloy 625 (in Chapter 3), a Coulombian friction is assumed for the tool chip interaction.

The simulated workpiece is assumed to be a small part which is being machined. The "Encastre" type boundary condition is applied to the boundaries AB, BC, CD, DE and EF. This simply means that the nodes on this boundary do not have any displacement or moment degrees of freedom. A boundary condition is also enforced on the tool, so that it is not allowed to move in the y-direction. The tool tip is placed such a way that at the start of the machining process it touches the workpiece at the mid point of FG of the sacrificial layer.

In high speed machining, chip formation is associated with material deformation taking place at a very high rate and localised heat generation due to plastic work. If the machining speed is high, the generated heat does not have enough time to escape the process zone, leading to approximately adiabatic conditions there. This kind of high speed machining process can be modelled using an adiabatic simulation. In lower speed machining, the process is not completely adiabatic and heat transfer around the process zone is possible. Such processes can be modelled using non-adiabatic simulations. For adiabatic simulations, the workpiece is meshed using CPE4R elements (Abaqus Analysis User's Manual, V. 6.9) and for non-adiabatic simulations CPE4RT elements are used.

The Johnson-Cook material model has been used for describing the material behaviour in most parts of this work. However, a modified Johnson-Cook type model has been used for the simulations of Alloy 625 (details can be found in Chapter 3).

A simple chip separation criterion is used for allowing the chip to separate from the workpiece. The elements in the sacrificial layer are deleted when a critical plastic strain is reached. If the critical plastic strain value is too small, a crack leads the tool tip as the elements get deleted too soon. On the other hand, if the critical plastic strain value is too large, the elements in the sacrificial layer can get highly deformed. This can also deform the "machined workpiece" surface and sometimes crash the simulation due to excessive element distortion. Figure 2.4 shows the two extreme cases for the high speed machining simulation of HY-100 steel (model discussed in detail in Section 2.5). In Figure 2.4a a crack runs in front of the tool tip when an extremely low critical plastic strain value of 0.25 is used. By opposition, in Figure 2.4b a set of highly deformed but undeleted elements near the tool tip can be seen when a large critical shear strain value of 4.0 is used. The value for the critical plastic strain, estimated from experience, is typically between 1.0 and 2.0 and depends on the material and the cutting conditions. For instance,

(a) critical plastic strain = 0.25   (b) critical plastic strain = 4.0
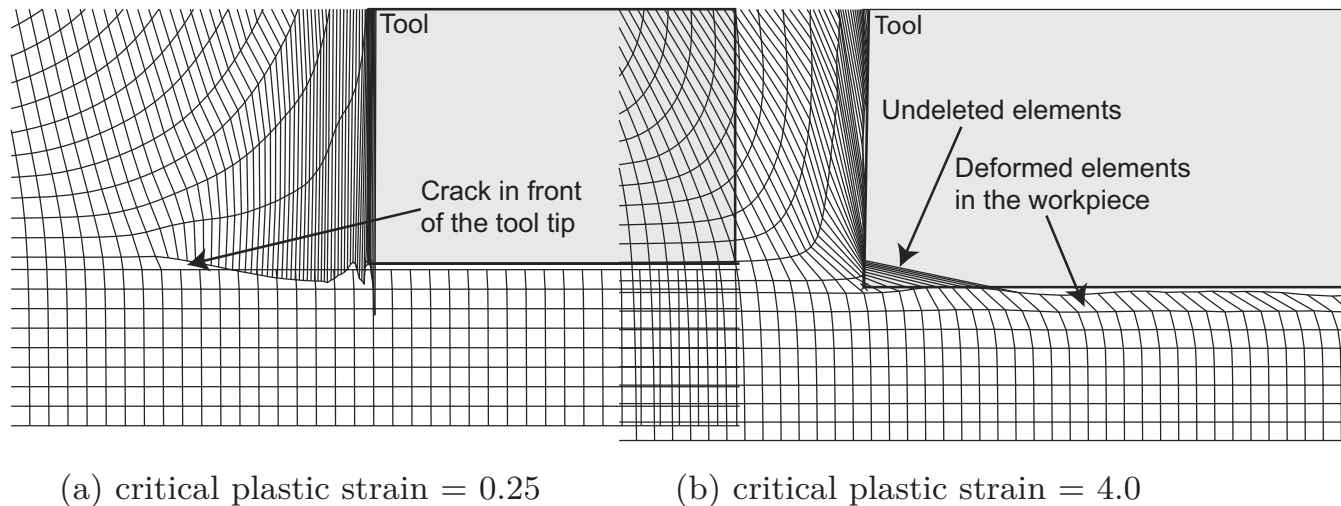
Figure 2.4: Effect of extreme values of the critical plastic strain on the simulation of chip formation

for HY-100 steel, a critical plastic strain value of 1.0 does not lead to a crack before the tool tip at rake angles of +1° or -5°. However at a more negative rake angle of -10°, a crack forms in front of the tool tip. A critical plastic strain value of 2.0 is therefore used for this material so that chip separation can take place without the above mentioned problems for rake angles in the range of -10° to +10°.

In the case of AISI 52100, 62 HRC steel, the chip formation simulations at a rake angle of 0° in Section 4.2 are done with a critical plastic strain of 1.0. This value was also sufficient for modelling chip separation in simulations with a positive rake angle. However, in Section 4.4, simulations are done with a rake angle of -10° where crack formation before the tool tip is found when the critical plastic strain is 1.0. A higher critical plastic strain value of 1.5 resolved this problem. Later in Chapter 5, the critical plastic strain of 2.0 is used as it is more robust for large variations of material parameters and cutting conditions. The chip shape and the cutting force were minimally influenced (less than 1% change in observables) when the critical plastic strain was varied between 1.0 and 2.0 at a rake angle of 0°.

In Chapter 3, chip formation is simulated for Ti-15-3-3-3, Alloy 625 and Ti-6246 which form segmented chips. During the chip separation, the elements in the separation layer in front of the tool tip get thermally softened which causes more than one element to have a reduced load bearing capacity at the same time. Thus more than one element can fail simultaneously. Due to this the chip material in front of the tool tip, flows downwards towards the machined surface (Figure 2.5). The nodes of some of these elements can get trapped underneath the lower

surface of the tool, causing extreme distortion of the element leading the simulation to crash. In order to resolve this problem, an auxiliary surface is created in front of the tool tip (Figure 2.6) so that it can only interact with the chip and not the sacrificial layer or the workpiece layer. The purpose of this surface is to prevent the chip nodes from coming underneath the tool. The surface is placed close to the tool tip so that elements from the chip do not normally interact with it, unless they are flowing downwards. In the case of Ti-15-3-3-3 and Ti-6246 simulations, the auxiliary surface IJKL is sufficient to prevent the elements from flowing downwards. In the case of Alloy 625, an additional surface JM is added to further aid the chip elements to climb up the tool surface. Since this material shows a large initial hardening before softening, the chip elements in front of the tool tip can buckle and flow downwards without this extra surface (Figure 2.7) just before the shear banding starts. The buckling occurs even if the critical failure strain is increased to a value as high as 8.0. In Figure 2.8, the region in front of the tool tip is shown in a greater detail. The surface IJKL is inclined at an angle of 20° to the horizontal. a-b-c-d is an element from the sacrificial layer, the length c-K is 0.25·b-c and the length e-b is approximately 0.5·a-b.
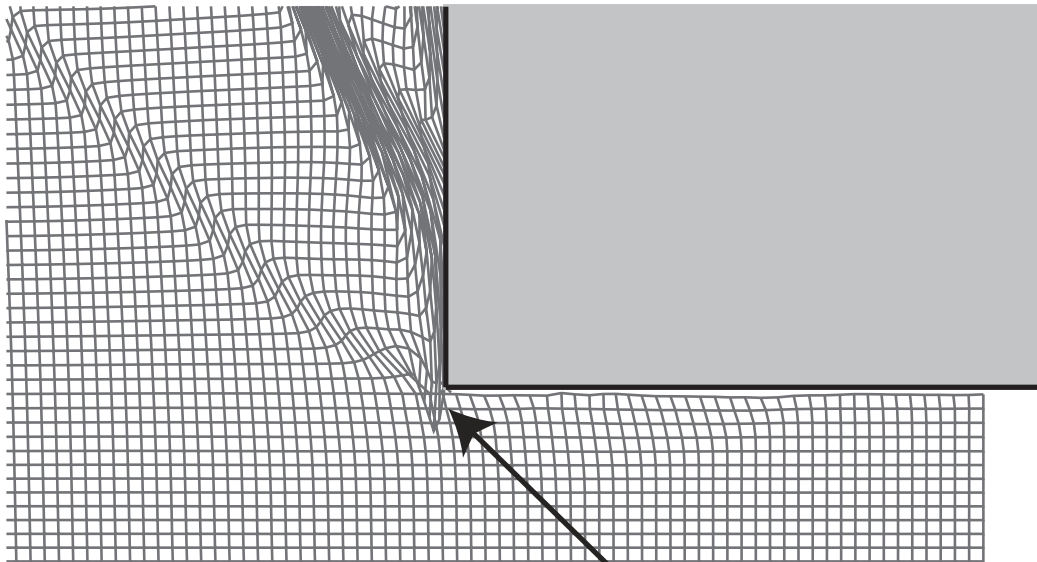
Downward flow of elements

Figure 2.5: Softened elements in front of the tool tip can flow downward towards the machined surface.

In some of the published literature (Mabrouki *et al.* (2008); Ramesh & Melkote (2008)), the sacrificial layer thickness has been kept approxi-
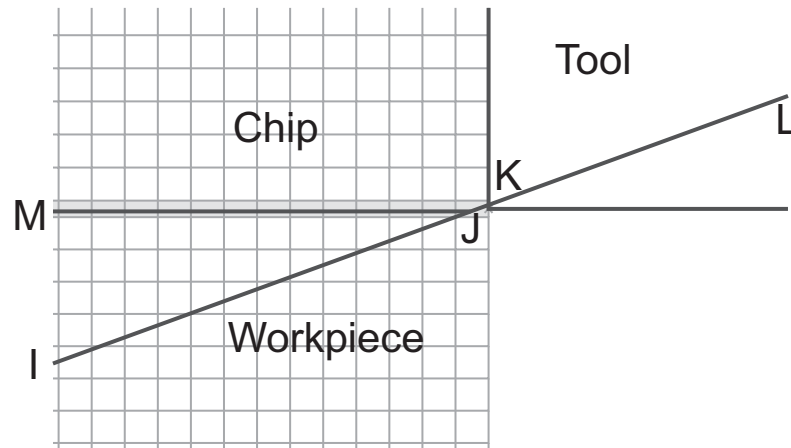
Figure 2.6: Auxiliary surface used in segmented chip formation simulations. Surface JM has been used only in the simulations for Alloy 625. The shaded elements belong to the sacrificial layer.

mately $1/20^{th}$ of the uncut chip thickness and the chip shapes and the cutting forces are shown to match with the experiments. In this work, the sacrificial layer thickness is kept as thin as possible (at the most $1/20^{th}$ of the uncut chip thickness [1]) to keep its effect low on the chip formation simulation. For the simulations in Chapter 3, at least 44 elements are there in the chip thickness direction and the sacrificial layer thickness is $1/44^{th}$ of the uncut chip thickness. It is assumed that when using a fine mesh, the effects of the chip separation criterion and the sacrificial layer thickness are reduced. The value of the critical plastic strain can also affect the chip curvature, but has not been studied in Chapter 3 due to this assumption.

The chip shapes and cutting forces in machining simulations have been found to be sensitive not only to the material parameters but also to the friction parameters (Özel (2006)), mesh density and orientation (Hortig & Svendsen (2007)), heat conduction between the tool and chip (Maekawa & Ohhata (1997)). The focus of this work is on the inverse identification material parameters from machining processes. Therefore a simple machining model is used which does not take the friction or tool-chip heat conduction into account as an extra deformation process along with heat generation and conduction will make the analysis more difficult. In this work, having a more complex finite element model is not expected to influence the identification process.

---

[1]In Section 5.3, to save computational time, a coarse mesh is used to validate the parameter identification process where the sacrificial layer thickness is $1/8^{th}$ of the uncut chip thickness. However it is later shown (Section 5.5) that this does not affect the parameter identification results.

(a) Without extra auxiliary surface

(b) With extra auxiliary surface
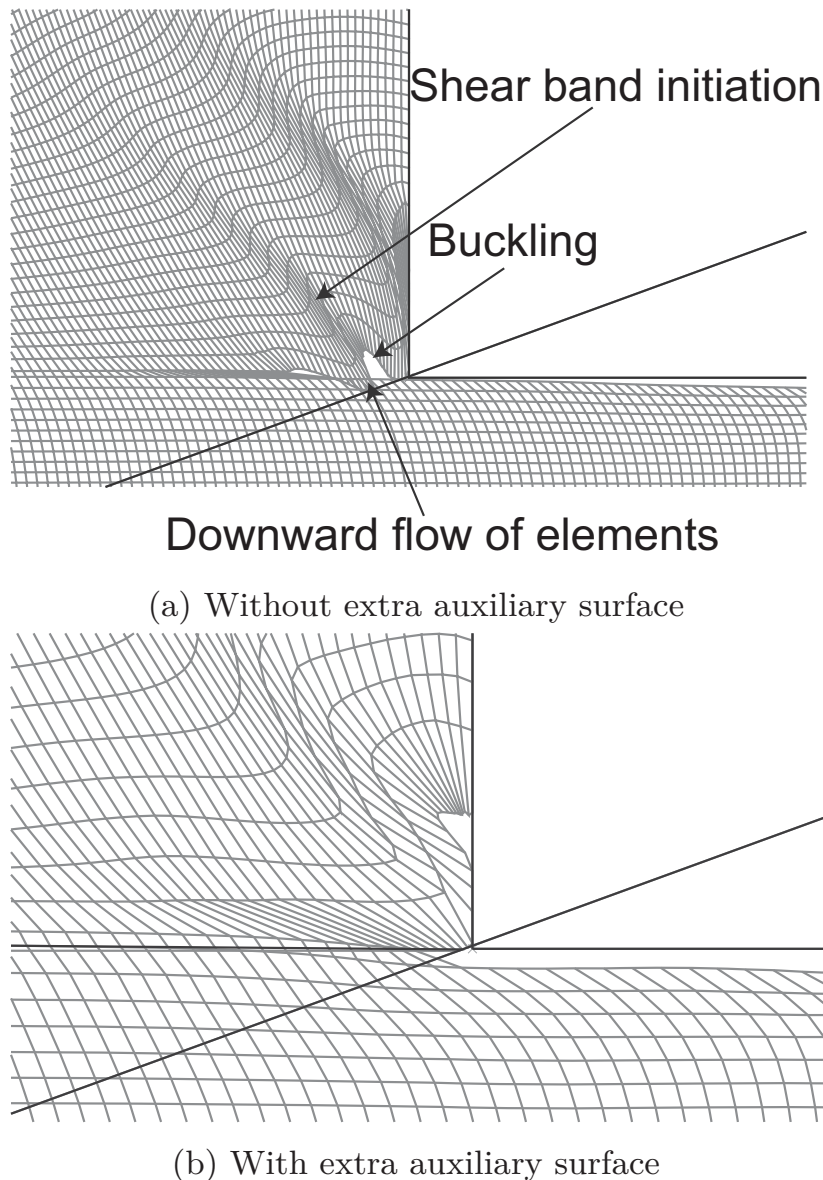
Figure 2.7: The extra auxiliary surface JM (see Figure 2.6) used in simulations for Alloy 625 prevent the elements from flowing downwards.

2.3.1 Meshing

The workpiece is meshed using the CPE4R or CPE4RT elements if the simulation is adiabatic or non-adiabatic, respectively. However, it is important to understand the advantages and the disadvantages of these element types. In Abaqus (Abaqus Analysis User's Manual, V. 6.9) CPE4R element refers to a 4 noded bilinear continuum element with plane strain assumption. It is a reduced integration type element with hourglass control. This type of element can be used in an adiabatic dynamic explicit analysis. For non-adiabatic simulations with coupled temperature-displacement, the CPE4RT element, a counterpart of the
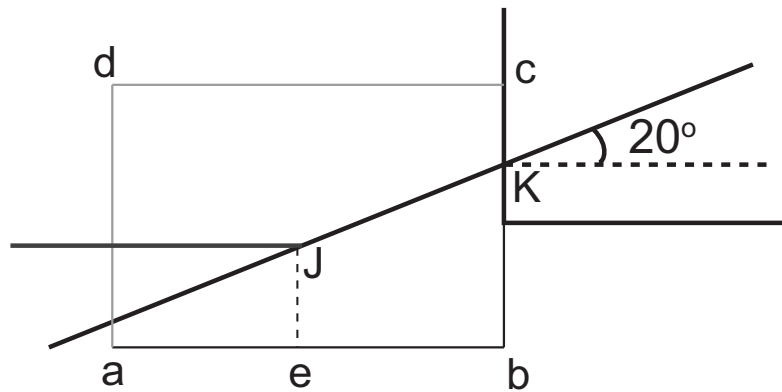
Figure 2.8: Zoom of the auxiliary surface near the tool tip. a-b-c-d is an element from the sacrificial layer.

CPE4R element with an additionally active temperature degree of freedom, is used. For CPE4R elements, only x and y displacement degrees of freedom are active.

The reduced integration elements employ a numerical integration scheme one order lower than a full integration scheme during the evaluation of the stiffness matrices in finite element calculations (Flanagan & Belytschko (1981)). In the CPE4R and CPE4RT elements, there is only one integration point called the Gauss point, and the numerically calculated values of the field variables such as the strain, strain rate and temperature exists only at this point. The whole element is therefore deemed to have the same value of the field variable as calculated at the integration point. Using the reduced integration elements has many advantages, first because these elements do not "shear lock", a phenomenon in which the response of the elements can be too stiff. Another advantage of the reduced integration scheme is that it is computationally less expensive than the full integration scheme. Its disadvantage is that the elements can show the "hourglass" mode of deformation, the mode in which the element shows no stiffness. Figure 2.9 shows the possible modes of deformation in a quadrilateral element. Mode Σ_I is the translational mode and does not cause a strain. Mode Λ_{1I} is the normal strain mode and Mode Λ_{2I} is the shear strain mode. Mode Γ_I is the hourglass mode of deformation in a first order reduced integration element, since there is no corresponding strain at the integration point which is at the centroid of the element, even though the element deforms. The problem in first order 4 node quadrilateral elements can be severe as this mode can propagate through the mesh, making it unusable. Therefore, some

artificial stiffness has to be introduced in the elements to control the hourglass modes. This is discussed in Section 2.4. The effect of meshing on the computational expense is studied in Section 2.5.
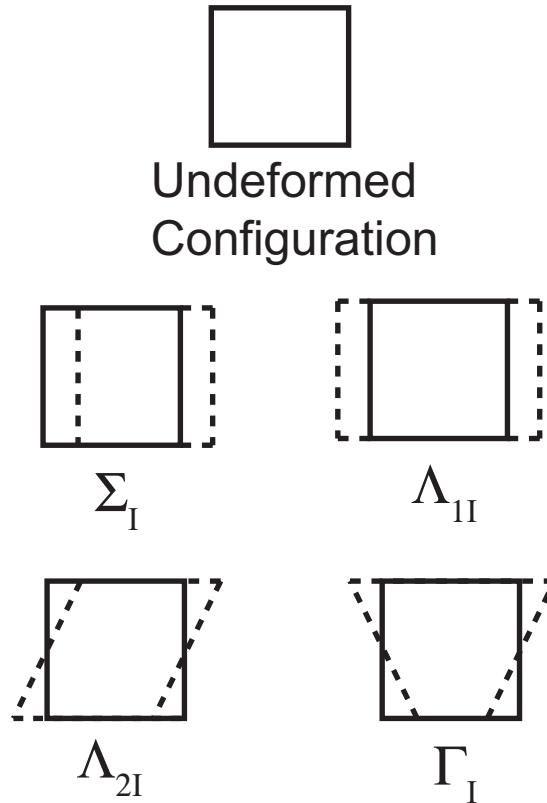
Figure 2.9: Modes of deformation of a quadrilateral element. Mode Γ_I is the hourglass mode of deformation in a first order reduced integration element.

2.4 Hourglass Control

To understand the occurrence of hourglassing in the machining simulations using reduced integration elements CPE4R, a machining simulation was done using the default hourglass controls. The cutting parameters and the material parameters used in the simulation are shown in Tables 2.5 and 2.6. The material parameters are that of an Aluminium alloy (A2024-T351) and are taken from literature (Bauccio & American Society for Metals (1993); Mabrouki *et al.* (2008)). Segmented chips are expected to be formed, even though no damage parameters have been used to enhance the material softening, which would have lead to a more pronounced segmentation.

Density [$\mathrm{kg\,m^{-3}}$]	270
Young's Modulus [GPa]	73
Poisson's Ratio	0.3
Specific Heat Capacity [$\mathrm{J\,kg^{-1}\,K^{-1}}$]	892
Coefficient of thermal expansion [$\mathrm{K^{-1}}$]	2.34×10^{-5}
Thermal Conductivity [$\mathrm{W\,m^{-1}\,K^{-1}}$]	122
Element failure criterion:	
Equivalent plastic strain at failure ($\bar{\varepsilon}_f^{pl}$)	1.3

Table 2.5: Material properties for A2024-T351 alloy.

A [MPa]	B [MPa]	n	C	m	T_{melt} [K]	T_{room} [K]	$\dot{\varepsilon}_0$ [$\mathrm{s^{-1}}$]
352	440	0.42	0.0083	1.0	793	300	0.001

Table 2.6: Johnson-Cook parameters for A2024-T351 alloy.

A relatively coarse mesh of 20 elements in the chip thickness direction is used with the default settings for hourglassing in Abaqus. The simulation result shows hourglassing inside the shear bands. In extreme cases, especially near the underside of the chip, the elements invert (Figure 2.10).

To reduce hourglassing, two solutions are possible in this case. One is to have a finer mesh, which would increase the simulation time. The other is to change the hourglass control method and the hourglass stiffness values. The first method is recommended by the developers of the Abaqus software (Abaqus Analysis User's Manual, V. 6.9). As a first step, the mesh is refined by doubling the number of elements which existed in the uncut chip thickness direction. The inversion of elements can still be observed in the shear band (Figure 2.11a). Strong hourglassing is observed in the shear bands and the chip underside (Figure 2.11b) even after nearly tripling the elements in the uncut chip thickness direction (57 elements).

The default hourglass control in Abaqus/Explicit is the integral viscoplastic control. If q is the hourglass mode magnitude and Q is the force or moment conjugate to q to suppress the mode, the Q value according to this approach is given by:

$$Q = \int_0^t sK(t - t')\frac{dq}{dt}dt' . \tag{2.30}$$
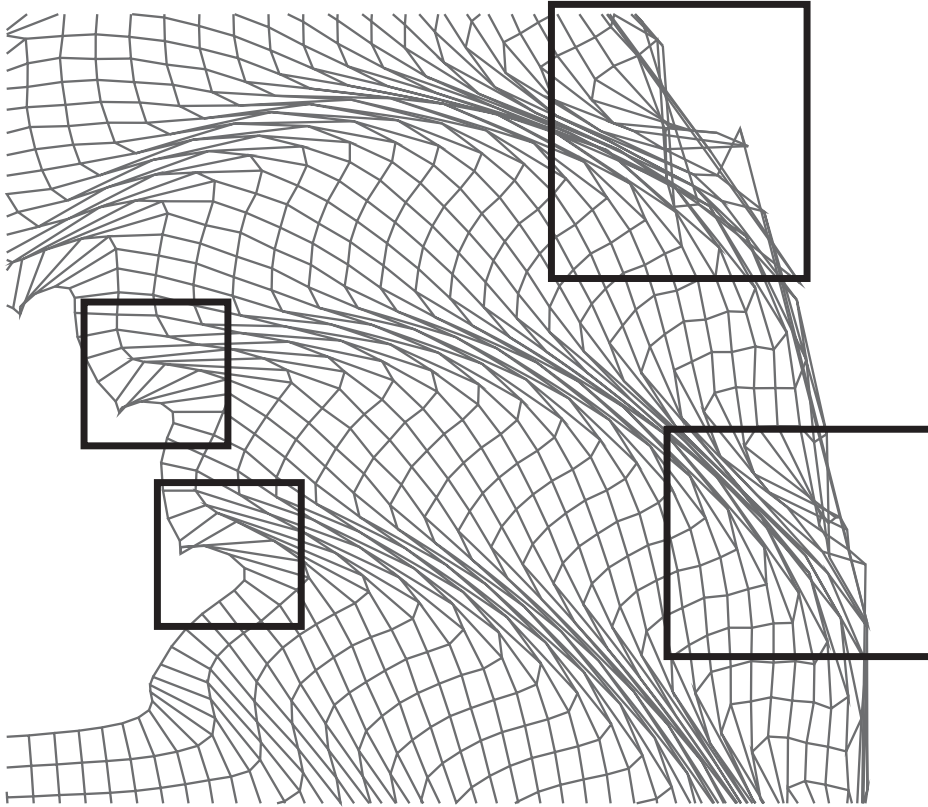
Figure 2.10: Problem of hourglassing in simulations with a coarse mesh (20 elements in the chip thickness direction) when using the default hourglass control settings. Hourglassed and inverted elements are shown inside boxes.

Here K is the hourglass stiffness ($= 0.005G$ for solid element where G is the material shear modulus) and s is a scale factor. By default, s is 1. This hourglass control resists the hourglassing early on in the analysis step, when sudden dynamic loading is expected to occur. In machining, dynamic loading occurs at all times during which the cutting is taking place, making the default control insufficient.

Instead of the default controls, a stiffness type hourglass control is used. This type of control uses a constant stiffness scaling throughout the analysis. The governing equation is given by:

$$Q = sKq. \tag{2.31}$$

The choice of the scaling factor s is important as a small value will not suppress the hourglass modes and a large value can adversely affect the shear banding.

A number of researchers (Nagaraj *et al.* (1999); Westerberg (2002)) have suggested that the ratio of artificial energy (ALLAE) to the total
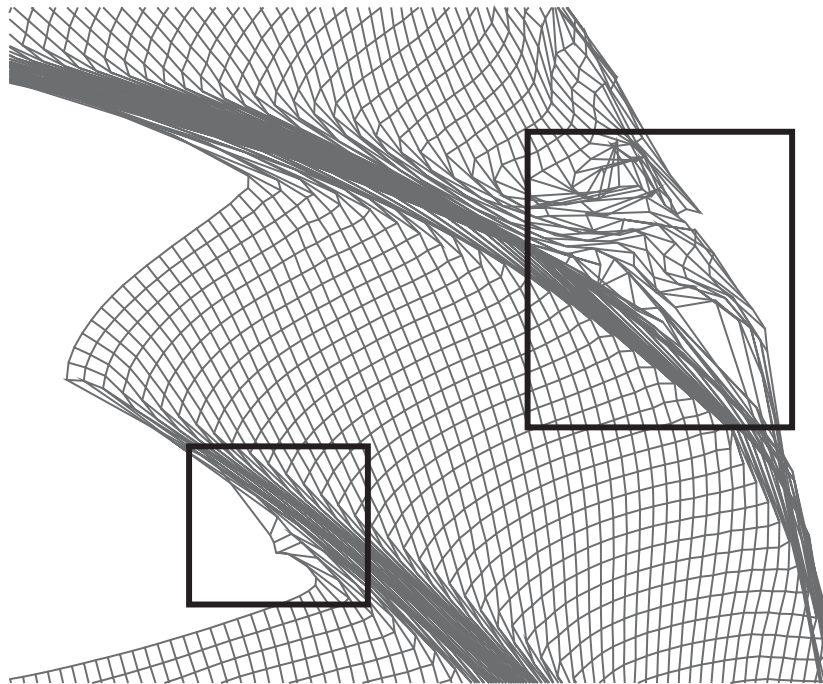
(a) 40 elements in the chip thickness direction
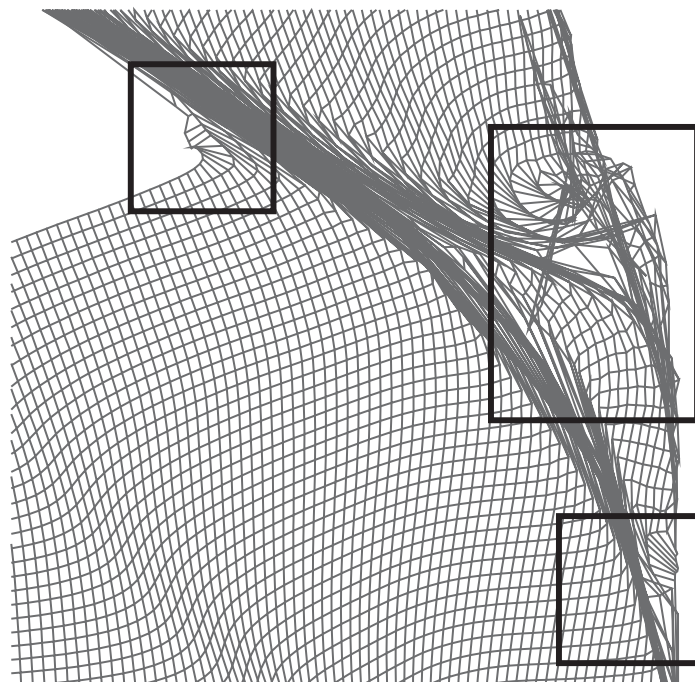
(b) 57 elements in the chip thickness direction

Figure 2.11: Problem of hourglassing in simulations with a finer mesh when using the default hourglass control settings. Hourglassed and inverted elements are shown inside boxes.

internal energy (ALLIE) should be as small as possible (typically 5-10%). The artificial energy term contains the energy dissipated to suppress the hourglass modes. However, in Abaqus, a particular mode of deformation is determined to be an hourglassing mode or not using a local criterion (Abaqus Analysis User's Manual, V. 6.9). An hourglassing mode and a pure bending mode cannot be differentiated from each other this way, as locally these modes look similar. As a result, the artificial energy term contains contributions from both modes. A high artificial energy value does not imply hourglassing. Regions where the artificial energy value is high must therefore be further inspected to check for signs of hourglassing.

ALLAE and ALLIE are calculated over the whole model, and do not provide information about the artificial and internal energy in an element. In Abaqus, it is possible to obtain elemental values of artificial energy dissipation (ELASE), plastic dissipation (ELPD), creep dissipation (ELCD) and strain energy (ELSE). The global internal energy (ALLIE) is given by:

$$\text{ALLIE} \quad = \quad \text{ALLSE} + \text{ALLPD} + \text{ALLCD} + \text{ALLAE} \,, \qquad (2.32)$$

where ALLSE, ALLPD, ALLCD and ALLAE are strain energy, plastic dissipated energy, creep dissipated energy and artificial energy respectively, for the whole model. An equivalent elemental quantity is not available in Abaqus, but can be calculated using:

$$\text{ELIE} \quad = \quad \text{ELSE} + \text{ELPD} + \text{ELCD} + \text{ELASE} \,. \qquad (2.33)$$

In the current problem, as there is no creep dissipation, ELCD is neglected.

The ratio of ELASE to ELIE, calculated as a percentage value, is plotted for simulations with different values of s (Figure 2.12). It can be observed that the degree of segmentation of the chip decreases with an increasing value of s. However, for low values of s, hourglassing is still present in the shear bands. Therefore an intermediate value of s has to be chosen.

Most of the hourglassing occurs in the region inside or near the shear bands. In this region, the ELASE to ELIE ratio is 10% or higher. A closer look at the elements near the shear band (Figure 2.13) shows that the elements deform primarily by shear within the shear band. Within the segment, the elements are weakly deformed. However, in the transition zone between the segment and the shear band, large bending deformations can be observed, which also contribute to the artificial energy value.

(a) $s = 0.5$

(b) $s = 1$

(c) $s = 2$

(d) $s = 5$
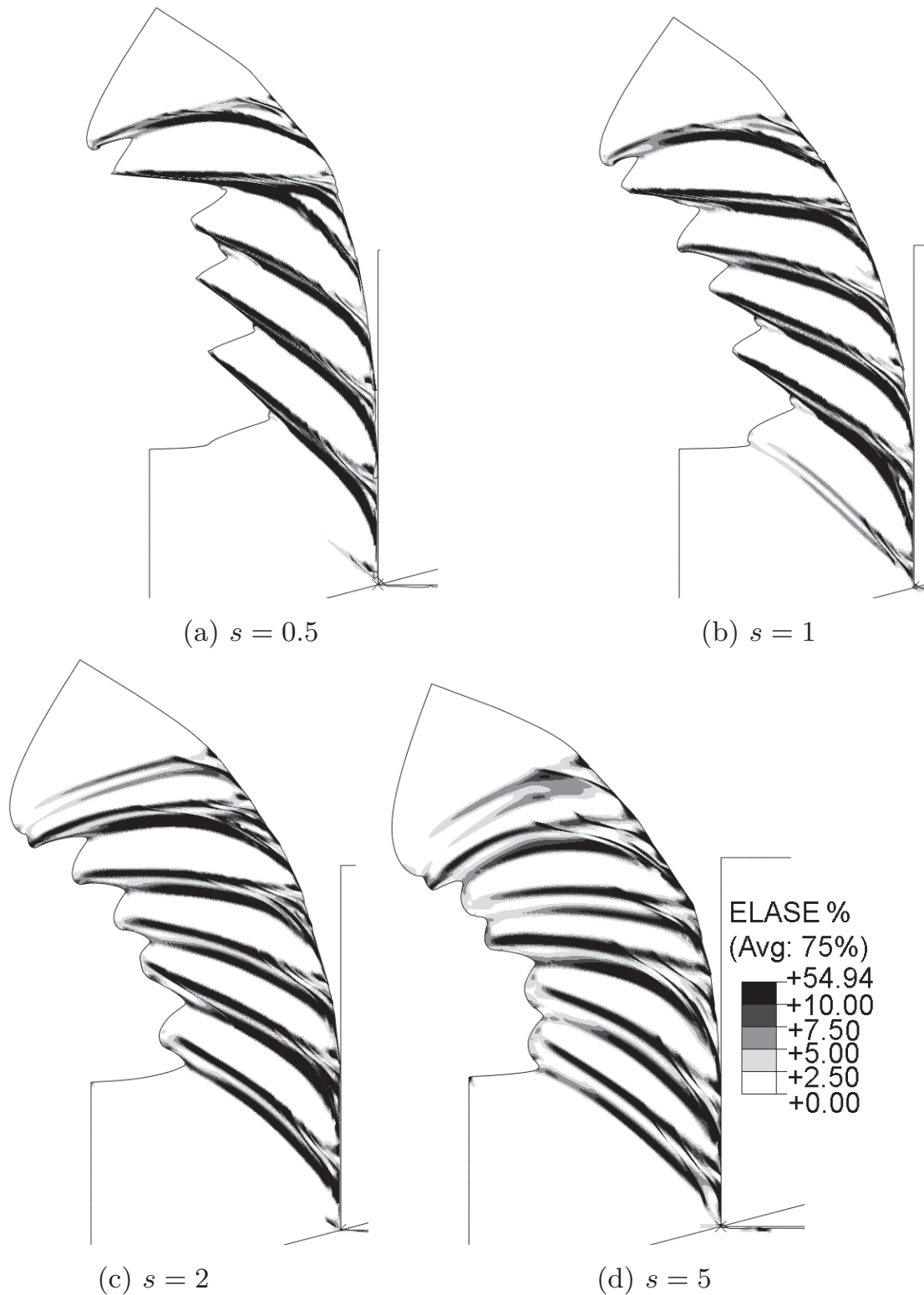
Figure 2.12: Distribution of the ratio of ELASE to ELIE expressed as a percentage in the chip for different values of s.
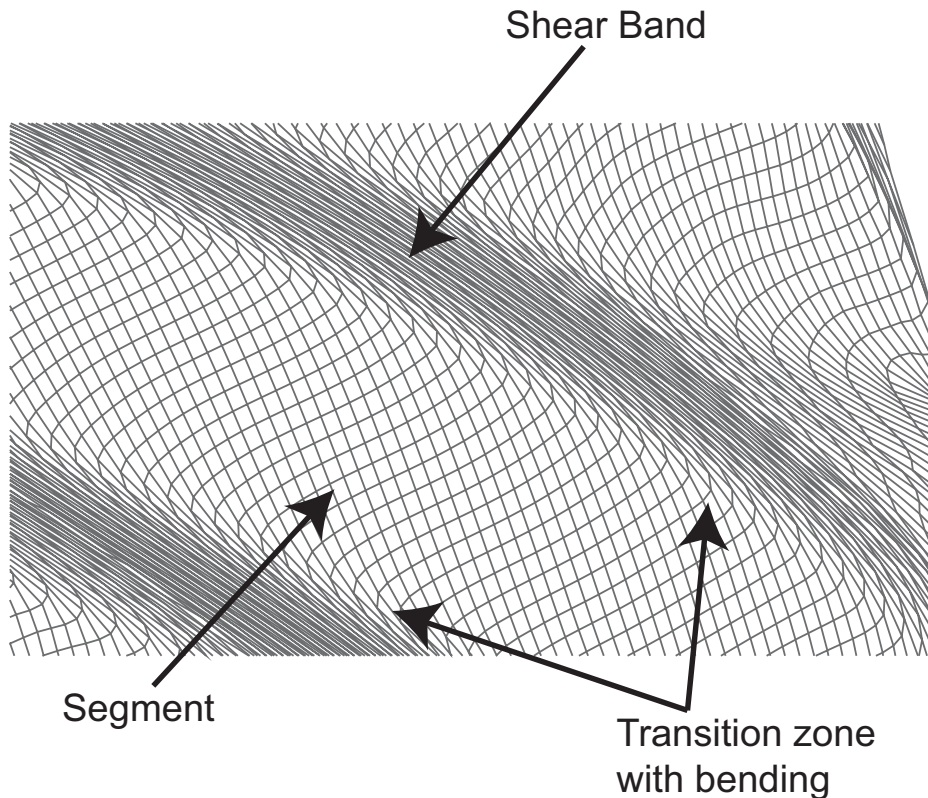
Figure 2.13: Zoom of the deformed mesh near a shear band, showing a weakly deformed segment and the highly deformed shear band. Most of the deformation in the shear band is due to shear, but bending deformations can be observed in the transition zone between the shear band and the segment.

The mesh near the shear band for $s = 1$ and $s = 2$ is plotted with its deformation scaled by a factor of 0.1, to visually inspect for signs of hourglassing. For $s = 1$, hourglassing can be observed near the shear bands but for $s = 2$, the hourglassing is reduced (Figure 2.14). The value of $s = 2$ has been used for all the simulations in this work. This is a conservative value as far as suppressing hourglassing is concerned, but this also means that chip segmentation will be reduced. Damage models can be used to further enhance the segmentation.

The identification of material parameters where continuous chip formation takes place is not expected to be affected by the choice of the hourglass control as it will be a constant during the identification process.

This problem clearly illustrates the need for development of better element types which do not hourglass. Global hourglass detection schemes might also improve the use of the stiffness hourglass control method, so that it is used only for elements which are actually hourglassing.
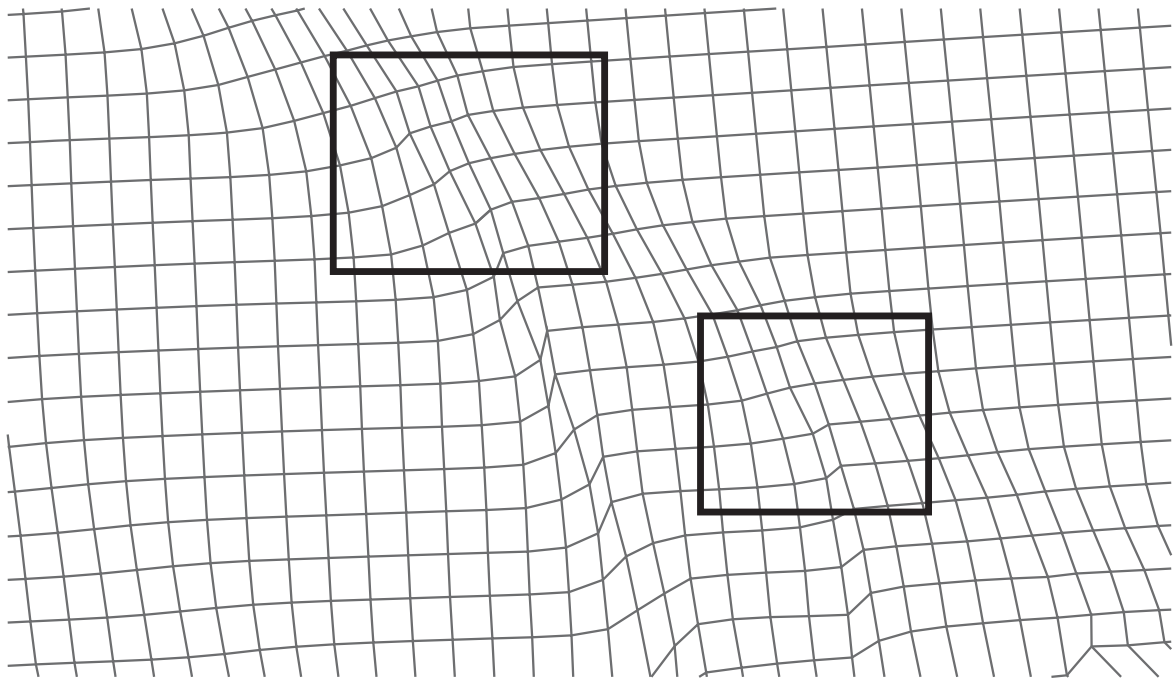
(a) $s = 1$
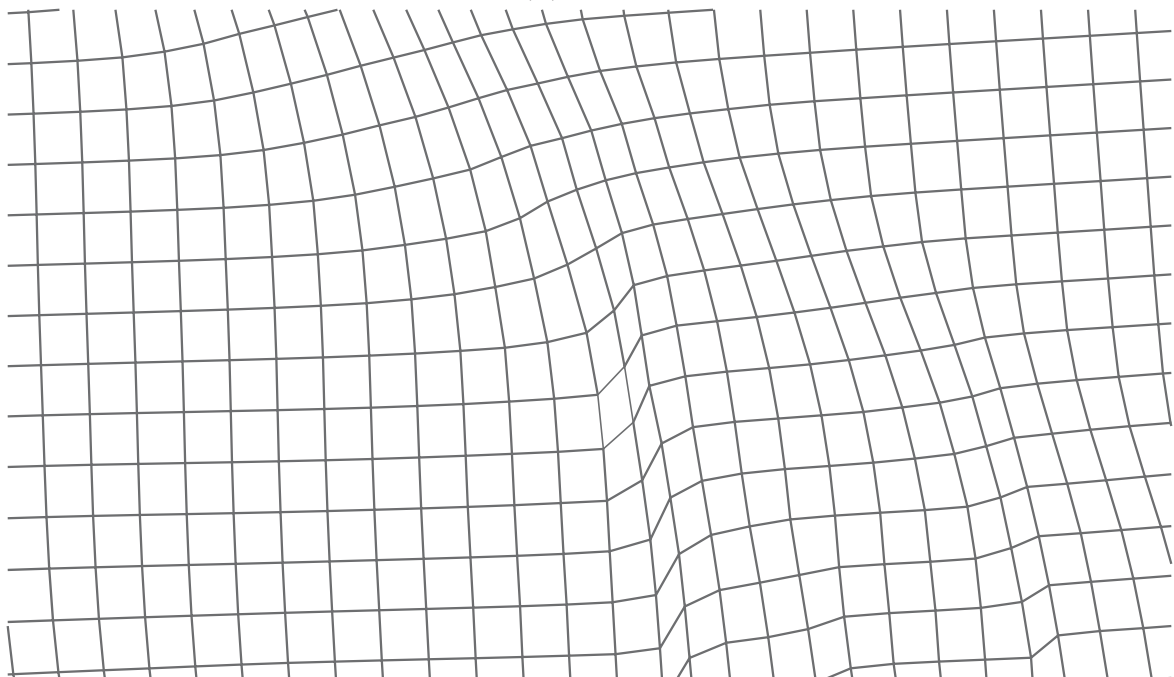
(b) $s = 2$

Figure 2.14: Mesh deformation, scaled by a factor of 0.1, near a shear band is analysed for hourglassing. For $s = 1$, hourglassing can be observed within the boxes.

2.5   Computational expense

Machining simulations can take a long time. A fine mesh used when simulating segmented chip formation reduces hourglassing and aids the formation of the shear band. A coarse mesh can average out the instabilities in the material, preventing the shear band formation. A fine mesh, however, increases the simulation time. By refining the mesh by a factor of two in each direction in a two dimensional simulation, the simulation time is expected to increase roughly by a factor of 8 – the number of elements will be four times as many as the coarser mesh and the stable time increment will be half of the coarser mesh.

At the start of the simulation, the workpiece elements adjacent to the sacrificial layer get severely crushed on coming in contact with the tool, especially in the simulation of continuous chip formation. Once the separation of the chip from the workpiece takes place and the chip starts flowing over the tool rake face, the elements do not get crushed as badly as they did initially. Most of the stable time increment is therefore determined in the initial part of the simulation, which affects the overall simulation time.

If continuous chip formation is expected, as is the case in this work during the inverse identification problem, certain tricks can be used to reduce the simulation time. In the case of HY-100 steel, a comparison was made between the computational expenses of two simulations, one using a uniformly meshed workpiece and the other using a non-uniformly meshed workpiece. The material parameters for HY-100 are given in Tables 2.1 and 2.2. The cutting parameters used in the simulations are listed in Table 2.7. Continuous chips are formed using the given material parameters in both the cases.

The mesh for the non-uniformly meshed workpiece has been shown in Figure 2.15 where the first 10% length of the workpiece contains rectangular elements of dimensions $8.5 \times 6.25~\mu$m and rest of the length contains elements of dimensions $6.25 \times 6.25~\mu$m (except in the separation layer). In the separation layer, the first 10% length has elements of dimension $8.5 \times 4.0~\mu$m and in the rest of the length $6.25 \times 4.0~\mu$m. In case of the uniformly meshed workpiece, the element dimensions are $6.25 \times 6.25~\mu$m in the whole of the workpiece except in the separation layer where it is $6.25 \times 4.0~\mu$m. There are 32 elements in the uncut chip thickness direction in both the cases. The simulation using the non-uniform mesh takes approximately 30 minutes on Intel™Core™2

Quad CPU Q9400@2.66GHz with 3.9 GB Memory and an operating system of SUSE Linux release 11.2. The same simulation with a uniform mesh takes roughly 41 minutes: using a non-uniform mesh can reduce the simulation time by around 25%. The chip shapes and cutting forces are found to match extremely well. Overlays of the chip shapes and the cutting forces have been shown in Figures 2.16 and 2.17. However using a non-uniform mesh is only advantageous in case of continuous chip formation: when segmented chips form, the elements in the shear band will deform strongly anyway, losing the advantage of a larger stable time increment gained using a non-uniform mesh.

Cutting Speed [$\mathrm{m\,s^{-1}}$]	33.3
Uncut chip thickness [µm]	200
Co-efficient of friction	0
Rake angle	0°
Mesh element type for Workpiece	CPE4R
Mesh element type for Tool	R2D2
Uniform mesh (chip)	6.25×6.25 μm
Non-uniform mesh (chip)	6.25×6.25 μm; 8.5×4.0 μm

Table 2.7: Cutting conditions for uniform and non-uniform meshing.

As the stable time increment depends only on the mesh size and the material properties, simulations at high cutting speed need less computing time. The use of mass scaling has been found to be very useful for lower speed non-adiabatic simulations.

In an explicit analysis the stable time increment (Abaqus Analysis User's Manual, V. 6.9) is also dependent on the material density (Equation 2.4). By artificially increasing the material density ρ by a factor of f^2, the stable time increment can be increased by a factor of f, thereby reducing the simulation time by a factor of f. This is called the mass scaling technique. This way the simulation time can be reduced while the cutting speed is still slow. The rate-dependent behaviour of the material is not affected and the conduction of heat within the chip can also be taken into account in a non-adiabatic simulation. In case of low speed non-adiabatic simulations, the mass scaling factor is determined by gradually increasing it until it affects the chip shapes and cutting forces. Despite its benefits, the mass scaling technique must only be used as long as the inertia forces do not dominate and change the solution, as is the case in high speed machining simulations.
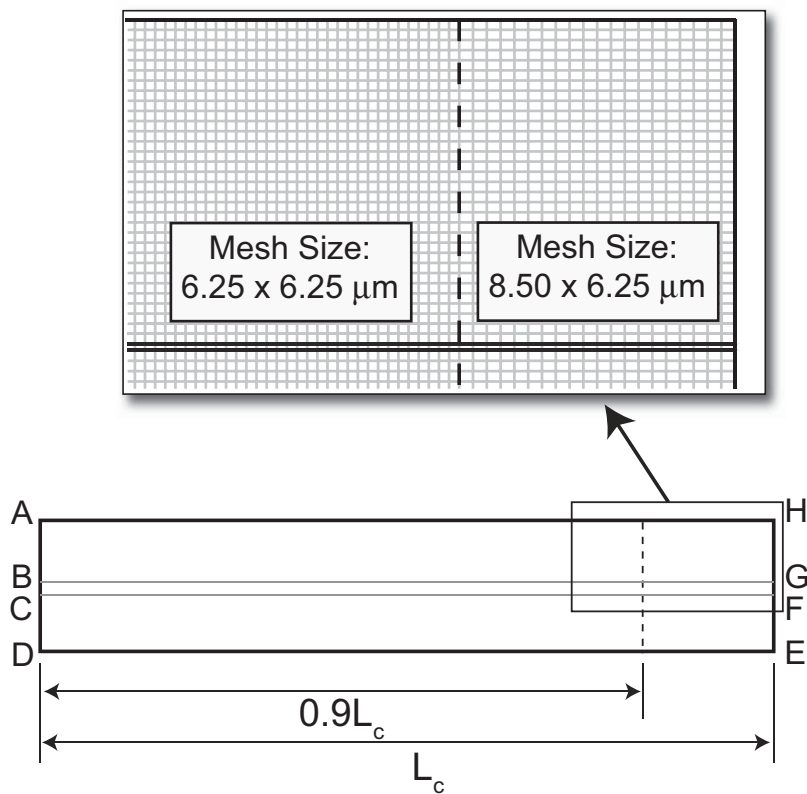
Figure 2.15: Non-uniform meshing used for HY-100 steel simulations
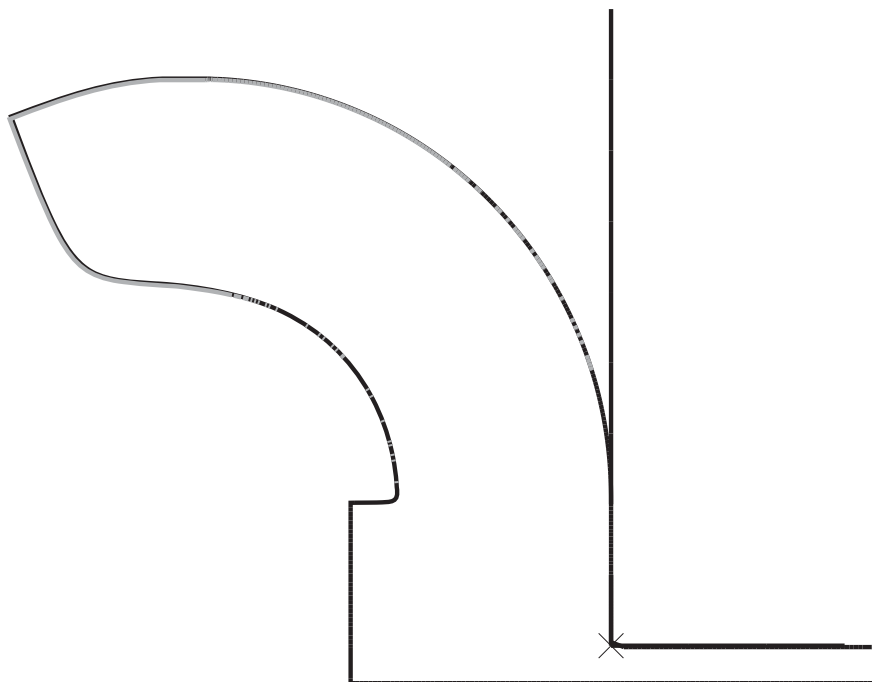
Figure 2.16: Overlay of chip shapes
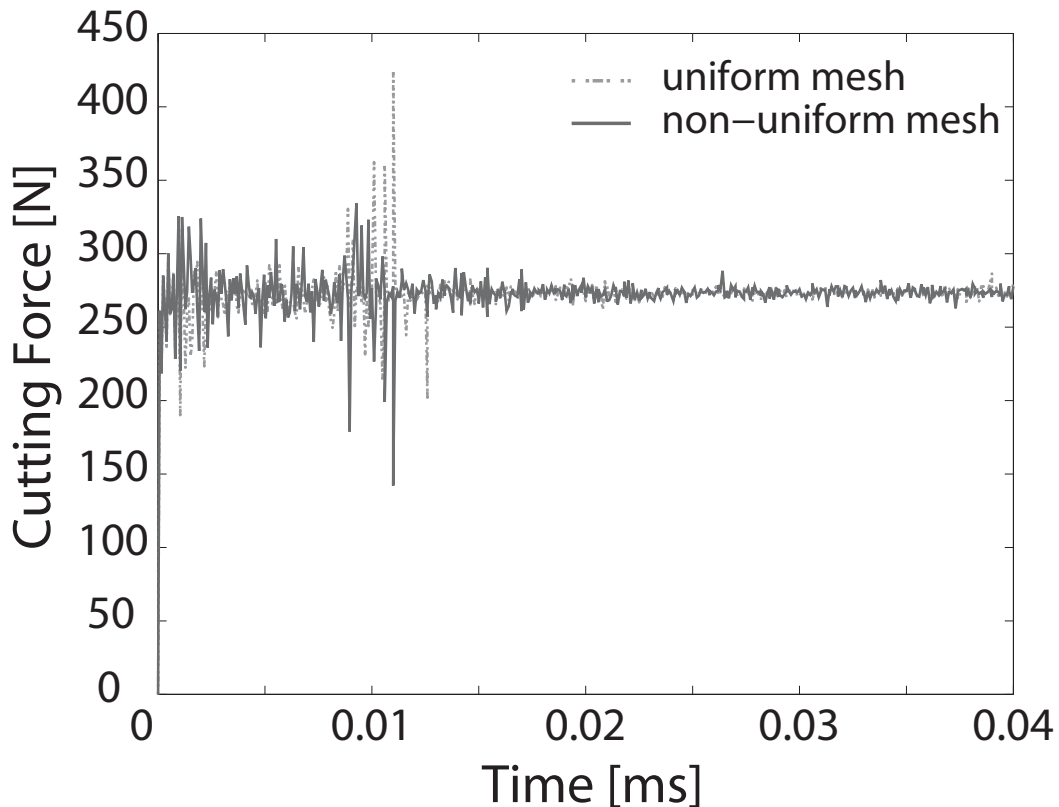
Figure 2.17: Overlay of cutting forces

2.6 Comparison of results

The results of two experiments are compared using the chip shapes and the cutting forces. The experiments can either be real machining experiments or virtual ones, *i.e.* simulations. To compare the chip shapes, the chip shape outlines are overlaid and the area of non-overlap is calculated (Shrot & Bäker (2011a)). The region of interest on the overlaid chips is bound by a window. It is discretised by a number of horizontal lines. The intersections of the horizontal lines with the chip outlines are found out, and the length of the line intercepted between the chip outlines can be obtained. Using the distance between the discretising lines and the intercepted length, the elemental area of non-overlap is calculated. It is summed over all the elemental areas to give the area of non-overlap (Figure 2.18). For two chip shapes which match exactly, the area of non-overlap should be zero.

When two chips are obtained at different cutting conditions and are to be compared with the standard chips obtained at the respective cutting conditions, the absolute value of the area of non-overlap is not a good metric for comparison. Since the chip shapes change significantly
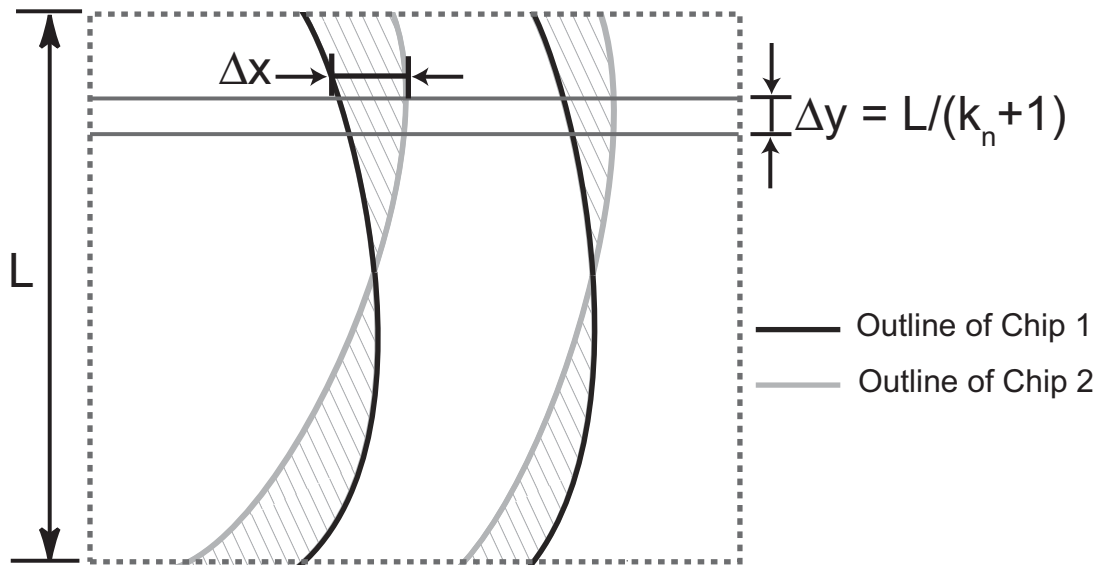
Figure 2.18: Estimation of the area of non-overlap. The region of interest is discretised by k_n lines. (Shrot & Bäker (2011a))

under different cutting conditions, the area of non-overlap magnitude also differs. A better metric is to normalise the area of non-overlap by the total area of the standard chip. Expressed as a percentage, it is given by:

$$\Delta A_C\% \quad = \quad \frac{\text{non-overlap area}}{\text{area of the standard chip}} \cdot 100 \,. \tag{2.34}$$

Using the normalised area of non-overlap as a metric, the following observations are made:

1. When $\Delta A_C\%$ is less than 1%, then the chip shapes match almost perfectly.

2. When $\Delta A_C\%$ is between 1% and 3%, then the chip shapes are visually indistinguishable and the match is considered very good.

3. When $\Delta A_C\%$ is between 3% and 5%, then the chip shape match is fairly good but the chips can be visually distinguished when overlaid. When comparing chips obtained from real machining experiments to chips from simulations, this kind of a match will be acceptable. However, in the inverse identification study in Chapter 5, in which all the chips are obtained from simulations at known cutting conditions, this match is not sufficient for claiming that the material parameters have been correctly identified.

4. When $\Delta A_C\%$ is more than 5%, then the chip shape match is considered bad.

The cutting force evolution is given by the finite element software at the reference node on the rigid tool. For a continuous chip, the cutting force stabilises once the cutting is stationary. The average value can then be used for comparisons. To compare two cutting forces from continuous chip formation, the normalised cutting force difference expressed as a percentage is given by

$$\Delta F_C\% \quad = \quad \frac{\text{difference of average cutting force}}{\text{average standard cutting force}} \cdot 100 \,. \qquad (2.35)$$

However, for segmented chip formation, the cutting force evolution must be taken into account. In case of explicit simulations, the cutting force evolution is noisy due to the presence of elastic waves in the workpiece. A way to measure the cutting force, without noise, from the simulations is to use the external work evolution with respect to time (ALLWK in Abaqus). The cutting force can be calculated using

$$F_c \quad = \quad \frac{1}{V_c} \frac{dW_{\text{ALLWK}}}{dt} \,. \qquad (2.36)$$

This approach has however not been used in this work.

Chapter 3

Parameter identification from standard experiments

In this chapter, the identification of the Johnson-Cook parameters from state-of-the-art experiments is described. Flow stress curves are obtained using the Split Hopkinson Pressure Bar (SHPB) tests at different temperatures and strain rates. These data are used to fit a constitutive material model, in this case the Johnson-Cook material model. Using the Johnson-Cook material parameters, chip formation simulations are performed and the results are compared to experiments. These experiments and simulations are conducted for three different materials in this work *viz.* Ti-15-3-3-3, Ti-6246 and Alloy 625 (see Section 3.4).

The research work described in this chapter is a result of a collaboration undertaken within the MaMiNa Project. All the SHPB testing in this work has been performed in the Tampere University of Technology (TUT) by Mikko Hokka, Tonu Leemet and Dmitri Gomon. The Johnson-Cook parameter identification for Ti-15-3-3-3 has also been performed in the TUT (Section 3.5.1). The Johnson-Cook parameter identification for Alloy 625 has been done by the author from the SHPB data (Section 3.5.3). The parameter identification code written by the author has been used to identify the Johnson-Cook parameters for Ti-6246 in the TUT from the SHPB data (Section 3.5.6). The modification of the material model for Alloy 625 has been done in close collaboration between Mikko Hokka and the author (Section 3.5.4). All the machining simulations have been performed by the author, including the writing of

the VUHARD routine for implementing the modified material model for Alloy 625 (Section 3.5.5). The U-type specimen testing has also been performed at TUT. The quick-stop experiments have been performed by Dawid Ksiezyk (Ti-15-3-3-3 and Alloy 625) and Jarkko Metsäjoki (Ti-6246) in the Institut für Werkzeugmaschinen und Fertigungstechnik at the TU Braunschweig, from which all the quick-stop images used in this chapter have been obtained.

3.1   Material state during machining

A number of researchers have tried to identify the range of values for strains, strain rates and temperatures which might be attained during machining. According to the analytical techniques presented in Chapter 1, the average plastic equivalent strain in case of continuous chip is expected to be between 1 and 3, depending on the rake angle and friction condition (Hastings *et al.* (1980)). Similar average strain values are predicted using the finite element methods (Marusich & Ortiz (1995); Sekhon & Chenot (1993); Strenkowski & Carroll (1985)). A larger strain value is usually found in the tool side of the chip, where there can be an interaction between the newly formed chip surface and the tool. Evidence of such large strain values is also found using experimental techniques such as visioplasticity: a grid is created using mechanical scratching or etching on the workpiece surface. During machining, the grid deforms along with the workpiece material, thus enabling the strains and strain rates to be measured. This method has been used by several researchers (among which Brown (1987); Pujana *et al.* (2008)) and the average strain in a continuous chip is found to be between 1 and 2. In the thin layer adjacent to the tool, strains as high as 20 can be found (Madhavan *et al.* (2000); Marusich & Ortiz (1995); Mathew & Oxley (1982)). In segmented chip formation, the material in the shear band is sheared very strongly and a plastic equivalent strain of over 3 is predicted (Bäker (2003b); Marusich & Ortiz (1995)).

Strain rates of the order of 10^4-10^6 s^{-1} are predicted in the primary shear zone using the analytical techniques (Mathew & Oxley (1982); Oxley (1989)), and the finite element method indicates similar values for conventional cutting speeds (Bäker (2004); Davim & Maranhão (2009)). Direct experimental verification of such high strain rate deformation is challenging, yet the strain rate values can be estimated using indirect means. Particle Image Velocimetry (PIV) and Particle Tracking Velocimetry (PTV) techniques have been used more recently to estimate the strain rates occurring in the primary shear zone (Gnanamanickam

et al. (2009); Lee *et al.* (2006); Sevier *et al.* (2007)). Such methods consist in introducing asperities on the workpiece by abrasion or sand blasting, which can be tracked during a deformation process. Subsequently, the strain and strain rate measurements are made by taking images at uniform intervals. In PIV techniques, the movement of a group of particles gives information about the local strains and strain rates averaged over an interrogation window. In PTV, each of the particles is individually tracked to give the local strain and strain rate values. The difficulties in taking images of the deforming workpiece fast enough and at a sufficiently high quality limit the range of these methods. At the extremely low cutting speeds of 10 mm s^{-1}, a strain rate of approximately 100 s^{-1} is measured in the shear zone. Lee *et al.* (2006) suggested that, by assuming that the strain rate varies nearly linearly with the cutting speed, the strain rate in the cutting speed range of 1 to 100 m s^{-1} would be of the order of 10^4 to 10^6 s^{-1}. Using high speed photography, Pujana *et al.* (2008) also estimated the strain rate in the primary shear zone to be of the order of 10^4 s^{-1} for cutting speeds ranging from 2 to 5 m s^{-1}. Finite element simulations such as Bäker (2003b); Marusich & Ortiz (1995) place the strain rate in the primary shear zone in a similar range. Moreover, when shear band formation takes place, the strain rate in the narrow shear band is expected to be of the order of 10^7 s^{-1} or even more (Bäker (2004)).

During machining, plastic work is constantly done on the workpiece to form the chip. A large proportion of the plastic work transforms to heat, leading to a local rise in temperature near the tool tip, of the order of hundreds of degrees. At lower cutting speeds, heat conduction is possible within the chip, between the chip and the tool and between the chip and the surrounding workpiece material, assuming dry cutting conditions. At higher cutting speeds, the process is close to adiabatic and the plastic heat generated near the tool tip is not conducted away. Heat is also generated due to friction between the tool and the chip which can have detrimental effects on the tool wear. One of the earliest experimental measurements of the chip temperature distribution was done by Boothroyd (1963), who used infrared photography to estimate the temperature distribution in the chip and the tool tip for mild steel and brass for different cutting conditions. A maximum homologous temperature (see Equation 2.15) of approximately 0.48 is reached for relatively low cutting speeds below 0.5 m s^{-1}. With consistent developments in digital photography and high speed cameras over a period of time, high speed processes like machining can also be captured accurately. In Sutter & Ranc (2007), the chip temperatures for high speed cutting of a low carbon steel (C15) and a low alloyed medium carbon steel (42CrMo4) are recorded in real time for

cutting speeds between 20 and 60 m s^{-1}. For a cutting speed of around 22 m s^{-1}, a homologous temperature of approximately 0.4 is reached for low carbon steel (C15) and approximately 0.55 for 42CrMo4 steel. At an increased cutting speed of 60 m s^{-1}, a homologous temperature of 0.46 is obtained for low carbon steel (C15). It is important to note while analysing these results that there are a lot of uncertainties in the measurements since the actual emissivity of the material is not known. These numbers only provide an estimate of the temperatures achieved during machining. In all the above quoted values, the temperature rise in the shear zone is in between 600 °C - 750 °C. A similar range of temperature rise is also predicted by finite element simulations such as Mamalis *et al.* (2001); Marusich & Ortiz (1995).

3.2 Experimental determination of material parameters

In section 3.1, it was seen that during machining the material undergoes large strains of the order of 200% or more, at strain rates of the order of 10^5 s^{-1} or more and a temperature rise of several hundreds of degrees Celsius. In order to obtain material parameters which are valid over such a large range of strains and strain rates, experimental techniques are needed to achieve similar conditions in controlled experiments where measurements can be made.

Low strain rate compression tests are relatively easy to perform on servo-hydraulic testing machines, on which a specimen can be deformed at a given strain rate. Temperature controlled compression tests are also possible at low strain rates: the specimen can then be heated with attachments such as a high power induction heater. However, with increasing strain rates, more and more sophisticated machines are needed so that the actuating cross-head stops before damaging the machine parts. The sudden starting and stopping of the actuating cross-heads requires the hydraulic pumps and parts to be larger so that high rate shocks can be sustained. Higher strain rates can also lead to higher vibrations, which can affect the experimental results. Due to all these reasons there is a physical constraint on the maximum strain rates which can be achieved safely on servo hydraulic testing machines. Strain rates up to 100 s^{-1} are achievable using advanced servo-hydraulic systems which are equipped with high capacity servo-hydraulic valves and speed control equipments.

The Split Hopkinson pressure bar (SHPB) apparatus is a widely used setup for achieving higher strain rates . Conventional SHPB setups are

capable of achieving strain rates of up to 10^4 s^{-1} and miniaturised SHPB apparatus can achieve as much as 10^5 s^{-1}. Usually strain rates of the order of 10^3 s^{-1} are reliably and consistently attained in experiments using conventional SHPB setups. A strain of up to 1 is possible in such setups, yet it is limited to 0.5 in usual experiments. The next section will describe the setup in detail and discuss its limitations.

3.2.1   Split Hopkinson bar testing

A split Hopkinson pressure bar setup consists of two long symmetric bars which are accurately aligned axially using bearings so that the bars are free to move in the horizontal direction (Figure 3.1). The length of the bars is chosen so that one dimensional wave propagation can be assumed in the bars (Gray (2000)). A striker bar is launched using a controlled release of pressurised gas which gives it a known initial velocity. On hitting the *incident* (or *input*) bar, a stress wave is generated which propagates through it and is partly transmitted on to the specimen. The remaining part of the stress wave is reflected from the input bar/specimen interface back into the input bar as a tension wave. The wave transmitted to the specimen is further transmitted to the *transmitted* (or *output*) bar and finally to a momentum trap through which the kinetic energy is finally dissipated. The propagation of the stress wave in the Split Hopkinson Bar setup has been shown by means of a Lagrangian diagram in Figure 3.2. The strain gages are affixed on the bars in such a position that the incident and the reflected stress waves do not overlap. In practice, the strain gages are often fixed in the middle of the bars. The incident stress wave reaches the strain gage in the incident bar with a delay of τ_i, the reflected stress wave reaches the same strain gage with a delay of τ_r and the transmitted stress wave reaches the strain gage in the transmitted bar with a delay of τ_t. The strain signal resulting from the stress wave are captured by the strain gages. It is then recorded by data acquisition equipment for further processing. At all times the incident and the transmitted bars deform only elastically. The strain signals from the strain gages are then separated into the incident strain wave ($\varepsilon_i(t + \tau_i)$), the reflected strain wave ($\varepsilon_r(t + \tau_r)$) and the transmitted strain wave ($\varepsilon_t(t + \tau_t)$). This information can be used to find the plastic stress, strain and strain rate in the specimen.

Material testing at higher temperatures is enabled by the attachment for manipulating hot specimen: the specimen is held in a ring, surrounded by ceramic wool so that only its ends are exposed. The ring is affixed
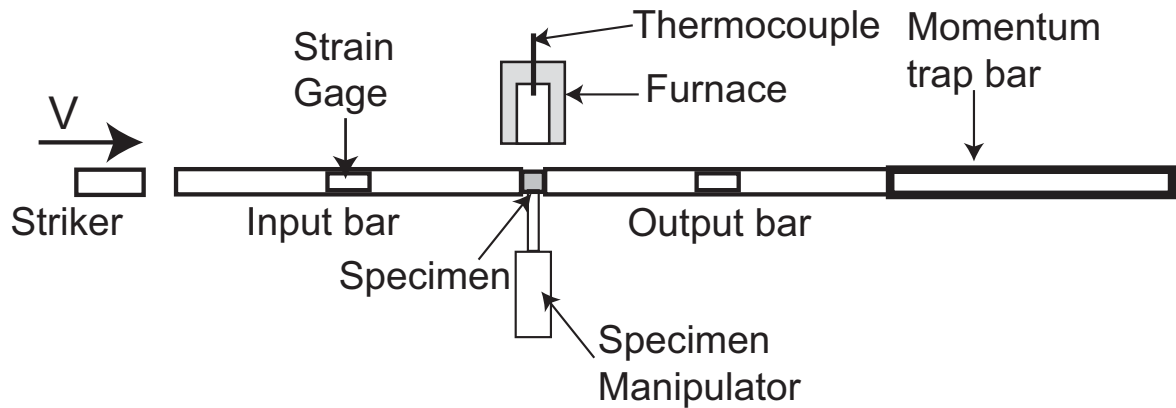
Figure 3.1: A schematic diagram of the Split Hopkinson Pressure Bar setup
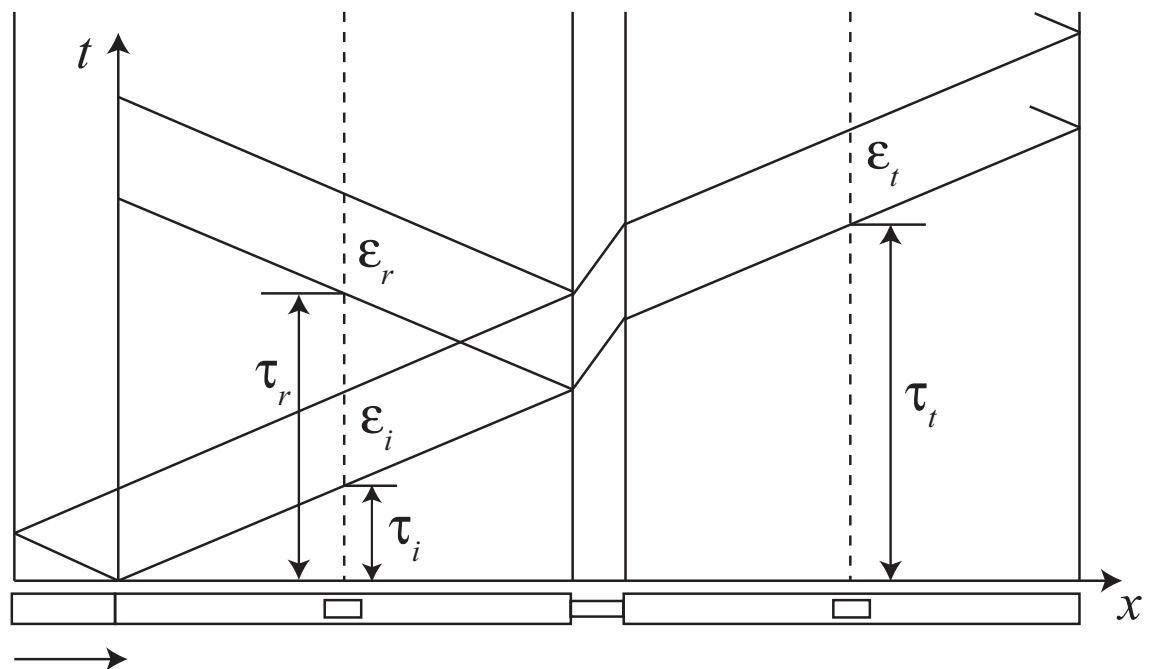
Figure 3.2: A Lagrangian diagram showing the propagation of the stress wave in the Split Hopkinson Bar setup (redrawn from Ramesh (2008)). The size of the specimen has been exaggerated in the diagram for clarity.

on to a manipulator arm, which is used to place the specimen in a furnace where it is heated to a uniform temperature. Once the desired temperature is reached, the manipulator arm quickly retracts and the specimen is placed in the centerline of the input and the output bars. At this point, the striker bar is launched and the bars are brought in contact with the hot specimen by another manipulator only a fraction of a second before the impact. This ensures that the input and the output bars remain at room temperature and the specimen does not conduct away significant heat into the bars before impact.

The average strain rate of the specimen can be given in terms of the reflected strain wave ($\varepsilon_r(t + \tau_r)$) as:

$$\dot{\varepsilon}(t) = \frac{2V_b \varepsilon_r(t + \tau_r)}{L_s}, \tag{3.1}$$

where V_b is the sound velocity in the bar and L_s is the specimen length. Integrating the strain rate in Equation 3.1, the average strain in the specimen is given by:

$$\varepsilon(t) = \frac{2V_b}{L_s} \int_0^t \varepsilon_r(t + \tau_r) dt. \tag{3.2}$$

The normal forces in the input (F_I) and the output bars (F_O) are given by:

$$F_I = EA_b(\varepsilon_i(t + \tau_i) + \varepsilon_r(t + \tau_r)) \tag{3.3}$$

and

$$F_O = EA_b \varepsilon_t(t + \tau_t), \tag{3.4}$$

where A_b is the cross sectional area of the bars and E is their elastic modulus. Therefore, the mean axial stress in the specimen is given by:

$$\sigma(t) = \frac{F_I + F_O}{2A_s} \tag{3.5}$$

$$= \frac{EA_b}{2A_s}(\varepsilon_i(t + \tau_i) + \varepsilon_r(t + \tau_r) + \varepsilon_t(t + \tau_t)), \tag{3.6}$$

where and A_s is the instantaneous cross sectional area of the specimen. From the initial specimen length (l_{s0}) and cross sectional area A_{s0}, the instantaneous cross sectional area can be calculated using the volume constancy relationship $A_{s0} l_{s0} = A_s l_s$ where the instantaneous specimen length (l_s) can be deduced from the strain values. Finally, when dynamic equilibrium is attained, the normal forces in the input and the output bar are equal, leading to:

$$\varepsilon_i(t + \tau_i) + \varepsilon_r(t + \tau_r) = \varepsilon_t(t + \tau_t) \tag{3.7}$$

and the mean axial stress Equation 3.5 is reduced to:

$$\sigma(t) \quad = \quad \frac{EA_b\varepsilon_t(t+\tau_t)}{A_s}\,. \tag{3.8}$$

The volume conservation is required if true stress in the specimen has to be obtained using the Equations 3.5 or 3.8. Therefore materials which undergo compaction during compression require additional methods to evaluate the stress values. The analysis represented by Equations 3.1, 3.2 and 3.8 is also called "1 wave" analysis: only the reflected wave is required to calculate the strain and the strain rate in the sample, and only the transmitted wave is required to calculate the stress in the sample. The additional assumption in this analysis is that the stress and the strain remain uniform along the length of the specimen during the experiment. At the start of the compression, there is a finite time required for the stress wave to propagate through the sample, during which the sample face in contact with the incident bar is loading while the other face stays at rest. The results given by this analysis during this finite time are inaccurate; one reason why the high rate elastic modulus of the sample cannot be measured using the SHPB setup. It was shown by Davies & Hunter (1963) that for ductile metal specimen, approximately 3 reverberations of the stress wave in the specimen are needed for the condition of dynamic equilibrium to be fulfilled.A detailed description of the SHPB technique can be found in literature (Gray (2000); Ramesh (2008)).

3.2.2 Limitations

In Equations 3.1 - 3.5, it is implicitly assumed that the strains measured at the strain gages are exactly the same as those occurring at the bar-specimen interface. In reality, this is not the case as the loading at the bar ends is not uniform, due to the mismatch in the diameters of the bar and the specimen. Due to the Poisson's effect, the bars also expand radially when compressed longitudinally. Consequently, waves of different frequencies are produced in the bars which propagate at different velocities. Thus the waveform measured at the strain gage location is different from the ones at the bar ends. It is possible to numerically correct for moderate wave dispersion (Gorham & Wu (1996)). To limit dispersion, the difference in the bar and the specimen diameters is therefore kept as small as possible. Typically, the specimen diameter $d_s \approx 0.8D$ where D is the bar diameter (Gray (2000)). Thus a plastic strain of 20-30% can be imparted to the specimen, before the diameter of the deformed specimen exceeds that of the bar. Despite these precautions,

at high strain rates the problem of dispersion causes the superimposition of high frequency oscillations which further load the specimen (Ramesh (2008)) and cannot be corrected. A pulse has a greater high-frequency component at high strain rates, since the pulse duration is short with sharp rise times. To avoid this problem, pulse shaping techniques are available (Gray (2000)) but at high strain rates of the order of 10^4 s^{-1}, their usefulness is limited.

Friction effects are also responsible for non-uniform stress distribution in the specimen. If there is significant friction at the ends of the specimen, additional work has to be done to overcome it. The friction may lead to non-uniform deformation of the specimen: the specimen diameter in the middle is greater than at the ends (barreling of specimen). To reduce friction, the specimen and the bar ends are manufactured with low roughness and are kept well lubricated prior to the experiment. Another way to limit the friction effect is to limit the strains in the specimen to less than 20-25% in a single test (Gray (2000)). Specimens with larger diameters, when deformed at same strain rates, have larger radial displacements than smaller specimens (Gorham (1991)). At larger displacements, there is a greater probability that lubricant breakdown will occur (Pearsall & Backofen (1963)). The lubricant may also be lost due to jetting at high velocities (Gorham (1991)).

Due to inertia effect, there is an upper limit to the strain in the specimen. At high strain rates, the force required to accelerate the material can be high, which can lead to inaccuracies in the measurements. This effect, also called the inertia effect, has been mathematically modelled (Gorham (1989)) to estimate the stress due to inertia, given by

$$\sigma_i \approx \rho_s d_s^2 \left[\frac{1}{64} + \frac{1}{6} \left(\frac{l_s}{d_s} \right)^2 \right] \dot{\varepsilon}^2 + \rho_s d_s^2 \left[\frac{1}{6} \left(\frac{l_s}{d_s} \right)^2 - \frac{1}{32} \right] \ddot{\varepsilon}, \quad (3.9)$$

where l_s is the specimen length, d_s is the specimen diameter and ρ_s is the specimen density. Typically, the $\frac{l_s}{d_s} \approx 1$ during the start of the SHPB tests and this ratio decreases during compression. Terms in the square brackets thus have their maximum values at the start of the experiment. However, the inertia effect increases when the diameter of the specimen increases during the experiment. At higher strain rates, the inertia effects are also expected to be higher as they increase with the square of the strain rate ($\dot{\varepsilon}$). Additionally, at the start and the end of the compression, when the strain rate is increasing or decreasing, the transient inertia effects can also be large. To reduce the inertia effects, the maximum strain reachable in the specimen is limited again.

Safety considerations are another reason why the strain in the specimen is limited. At large strains, the samples can disintegrate, rendering the test results useless, apart from being dangerous for the operators who can be hit by the flying fragments. Typical values of plastic strains are limited to less than 50%, as can be seen from the literature (Guo *et al.* (2005); Jaspers & Dautzenberg (2002); Seo *et al.* (2005); Treppmann (2001)).

The nominal strain rate in the specimen can be approximated by

$$\dot{\varepsilon} \;\;=\;\; \frac{V_{st}}{l_s}\,, \tag{3.10}$$

where V_{st} is the striker velocity. Thus to obtain higher strain rates, the velocity of the striker bar can be increased. There is a physical limit to this velocity as the incident bar must deform elastically at all times. On too high a velocity, the incident bar can be permanently damaged. As a consequence, to obtain higher strain rates, the size of the specimen is reduced. Since the starting $\frac{l_s}{d_s} \approx 1$ and $d_s \approx 0.8D$, some researchers have reduced the size of the whole SHPB setup to obtain high strain rates of the order of 10^4 s^{-1} (Jia & Ramesh (2004)). There is again a physical limit as to how small the specimen can be. If the specimen size is too small, only few grains of the material will be present in the specimen. Size effects will be important in such cases and the measured property will not be the same as the bulk material property. By convention, the specimen size should be sufficient to contain at least 10 grains in it.

Apart from the compression test, it is also possible to do tension or torsion tests using the Split Hopkinson bar apparatus. The torsion tests have the advantage that higher strains and strain rates can be obtained this way. The problem in tension tests is that the results are not usable after necking. In the case of torsion tests, shear localisation can take place in the specimen which renders the results useless.

Finally, during high temperature SHPB experiments, the specimen has to be placed in the furnace for a few minutes, so that a uniform temperature is attained in the specimen. For materials with bad heat conductivity, such as Titanium alloys, this time can be in the order of tens of minutes. This time is sufficient to cause significant diffusion within the specimen, changing its microstructure, leading to a change in the material properties.

The plastic work-generated heat is not able to diffuse to the surrounding environment in a high rate process due to the deformation of the workpiece: as a result, the sample temperature rises. The obtained results must be corrected for this deviation (Section 3.3).

3.3 Adiabatic and isothermal stress strain curves

The stress strain relation of a material is often dependent on physical parameters such as the temperature and the strain rate. To describe material behaviour using models such as the Johnson-Cook model, which considers the strain, strain rate and temperature effects to be uncoupled, the effect of each of these physical quantities has to be separated. For instance, at high strain rates, the material's self-heating is prominent and should be accounted for during data fitting.

Isothermal conditions exist when the temperature of the specimen does not change during the experimental test. Ideally, a truly isothermal deformation must take place infinitely slowly. Tests done at low strain rates can be approximated as an isothermal process. Using the isothermal assumptions, material parameters can be fitted for low strain rate tests at different temperatures with the Johnson-Cook equation

$$\sigma_{iso} = (A + B\varepsilon^n)\left[1 + C\ln\left(\frac{\dot{\varepsilon}}{\dot{\varepsilon}_0}\right)\right]$$
$$\left[1 - \left(\frac{T_{iso} - T_{room}}{T_{melt} - T_{room}}\right)^m\right], \tag{3.11}$$

using the specimen temperature (T_{iso}) directly during the fitting procedure.

Adiabatic conditions exist when a deformation process takes place infinitely fast, so that no heat enters or exits the control volume (the specimen in this case). High strain rate experiments are a good approximation of this. Adiabatic stress strain curves can be calculated from the isothermal curves by taking into account the continuous heating of the material with deformation. Thus the adiabatic stress strain curve can be expressed as

$$\sigma_{adia} = (A + B\varepsilon^n)\left[1 + C\ln\left(\frac{\dot{\varepsilon}}{\dot{\varepsilon}_0}\right)\right]$$
$$\left[1 - \left(\frac{T_{adia} - T_{room}}{T_{melt} - T_{room}}\right)^m\right], \tag{3.12}$$

where T_{adia} is given by

$$T_{adia} = T_{iso} + \frac{\beta_{TQ}}{\rho c}\int \sigma_{iso}d\varepsilon, \tag{3.13}$$

and ρ is the material density, c the specific heat capacity and β_{TQ}, the Taylor-Quinney coefficient, determines the percentage of plastic work

converted into heat. Often a value of 0.9 is used for β_{TQ} in the literature (Mabrouki & Rigal (2006); Trent & Wright (2000)).
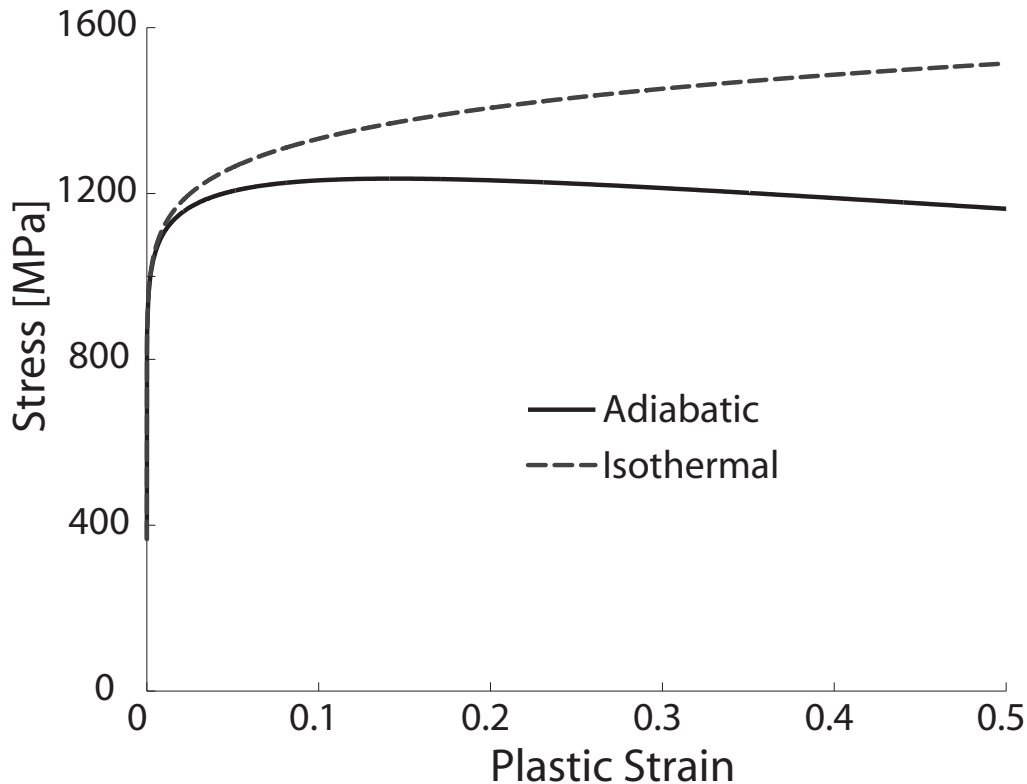
Figure 3.3: Isothermal and adiabatic stress strain curves for HY-100 steel

    The isothermal and adiabatic stress strain curves have been drawn in Figure 3.3 for HY-100 steel whose Johnson-Cook parameters have been given in Table 2.1 and Table 2.2. At very low strains, the temperature rise is not significant: therefore the adiabatic and isothermal stress strain curves have similar values initially. However, the difference between the curves is more significant at larger strains. Starting from similar stress values, the adiabatic curve deviates by about 7.5% at 10% of plastic strain and about 20% at a plastic strain of 30%.

    The deviation between the adiabatic and the isothermal curves are also dependent on the density and the specific heat capacity of the material, as can be seen from the equation 3.13. In identical conditions, a material with a greater density or specific heat will show a lower deviation from the isothermal curve. This has been illustrated in Figure 3.4. The adiabatic curves are drawn with increasing values of the specific heat capacity and the deviation between the isothermal and the adiabatic curve decreases.
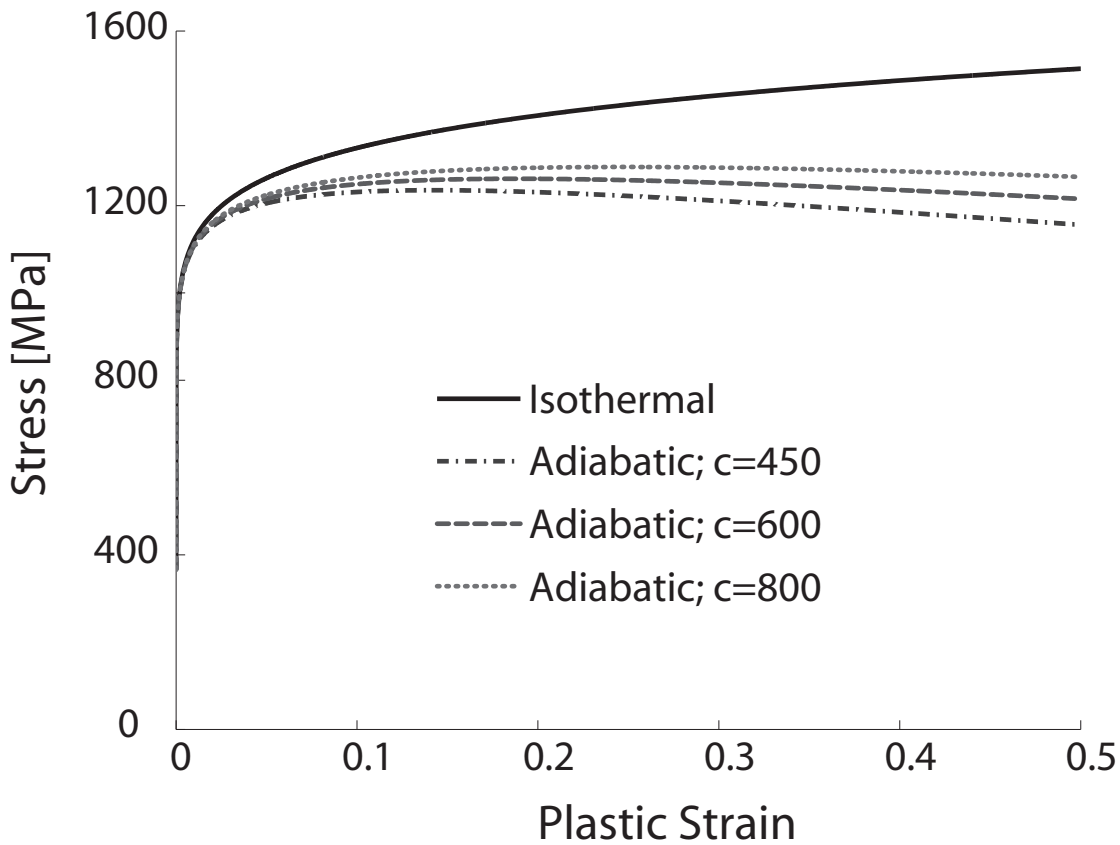
Figure 3.4: Isothermal and adiabatic stress strain curves for HY-100 steel with different specific heat capacities. The larger the specific heat capacity, the closer is the adiabatic curve to the isothermal curve

Correction for heating due to plastic work is important during the parameter identification procedure. Two strategies can be adopted in this case. The first strategy is to explicitly correct the experimentally determined high strain rate curves to isothermal curves. The adiabatic curve (σ_{adia}) can be converted to isothermal curve (σ_{iso}) at the temperature (T_{iso}) at the same strain rate of $\dot{\varepsilon}$ by using

$$\sigma_{iso}(\varepsilon) \quad = \quad \sigma_{adia}(\varepsilon) \frac{\left[1 - \left(\dfrac{T_{iso} - T_{room}}{T_{melt} - T_{room}}\right)^m\right]}{\left[1 - \left(\dfrac{T_{adia} - T_{room}}{T_{melt} - T_{room}}\right)^m\right]} . \tag{3.14}$$

This is useful for the manual fitting method in which different parts of the Johnson-Cook equation are fitted in a staggered manner (as in case of Ti-15-3-3-3 alloy as discussed in Section 3.5.1). Another strategy is to directly use the adiabatic stress-strain curve to find the parameters. This can be done by using a non-linear curve fitting algorithm, which

has been used for Alloy 625 and Ti-6246 as discussed in Sections 3.5.3 and 3.5.6.

3.4   Machinability of Titanium alloys and Nickel based superalloys

Alloys of Titanium, owing to their light weight and high strength properties along with high corrosion resistance and biocompatibility, are being used more and more in the fields of aerospace, oil refining, petrochemicals and medicine. Nickel-based superalloys, owing to their high hardness at high temperatures, are a natural choice for high temperature applications such as in gas turbines. Such alloys are, however, often found to be difficult to machine.

Titanium alloys are difficult to machine (Donachie (2000)) primarily because of their bad thermal conductivity, combined with a relatively high hardness at higher temperatures. The plastic heat which is generated during machining does not readily leave the process zone due to low thermal conductivity. As a result, a large rise in local temperatures near the tool-chip interface causes the tool to fail. The shear angle is usually of about 45° or more during the machining of Titanium and its alloys, while the thermal load is concentrated in a relatively small zone near the tool tip – another reason why the tool breakdown is rapid in this case. The high reactivity of Titanium with the tool coating material at high temperatures causes galling or welding of the chips on to the tool surface, further contributing to rapid tool failure. All these effects have a direct consequence upon the surface integrity, machining costs and productivity. Bad surface finish leads to bad fatigue life, rapid tool wear leads to frequent tool changes resulting in large machining costs and loss of productivity. The machining of Titanium alloys therefore has to be done at low cutting speeds, further reducing the productivity. Titanium alloys are also known to form long ribbon-like chips which are difficult to break automatically, preventing the manufacturing process from being automated. The cutting process has to be periodically stopped by the operator to manually remove the chips which wrap around the tool holder. These chips can also come in contact with the machined workpiece and damage the surface.

Nickel-based superalloys are designed for high temperature applications, and therefore retain high hardness even at high temperatures (Donachie & Donachie (2002)). The high temperatures generated during machining lead to the softening of some tool materials, relative to the

superalloy itself. This is an important reason for their being difficult to machine. Like Titanium alloys, Nickel-based superalloys also have poor thermal conductivity which leads to high local temperatures near the tool tip. The material in annealed state also shows high work hardening leading to high specific cutting forces. Similar to Titanium alloys, long ribbon-like chips are formed in this case, which causes similar problems.

For all the above mentioned reasons, Titanium alloys and Nickel-based superalloys are difficult to machine. To improve machinability, the chip formation process in these alloys has to be better understood. In order to do this quick-stop experiments and machining simulations can be conducted. For the machining simulations, Johnson-Cook material parameters are obtained from SHPB experiments in this work, which are used for machining simulations.

A brief background of the Titanium alloys and the Nickel based superalloy used in this work is given here (synthesized from Donachie (2000); Donachie & Donachie (2002); Leyens & Peters (2003); Reed (2006); Rodney *et al.* (1994)):

Titanium alloys: Pure Titanium is found in two different crystallographic forms (allotropes): the hexagonal close-packed (hcp) phase is also called the α phase, and the body-centered cubic (bcc) phase, also called the β phase. For pure Titanium, the α phase is stable at low temperatures and the β phase is stable at high temperatures. The α to β transition for pure Titanium takes place at 882 °C. This temperature is also called the beta transus temperature and is the minimum equilibrium temperature at which all the phase is β. This temperature plays an important role in deciding the processing and the heat treatment temperatures.

Al, Ga, Ge, O, C, N *etc.* are α stabilisers and raise the beta transus temperature. Mo, V, Nb and Ta belong to the β isomorphous class of elements which are miscible in the β phase. The second class of β stabilisers consist of Mn, Fe, Cr, Co, Ni, Cu and Si, which are eutectoid alloying elements and form intermetallic compounds. Sn and Zr are neutral elements as they do not strongly stabilise either of the phases, but have extensive solid solubility in both the phases. They are usually added to act as strengthening agents, primarily for the α phase.

Titanium alloys are divided into three classes according to the phase present at room temperature: α, $\alpha + \beta$ and β. Since the most important α stabilising element Al has a much lower density than β stabilising elements such as V or Mo, the density of α alloys is often lower than that of β alloys. As α alloys consist of

only a single phase, they are insensitive to heat treatments for strengthening them, although they may be annealed to relieve the residual stresses. Both $\alpha + \beta$ and β alloys can be hardened using heat treatments and β alloys in particular can be hardened to a very high degree. At high temperatures, diffusion is more difficult in the close packed structure of the α alloy. They therefore show better creep behaviour than β alloys.

At lower temperatures, a thin and dense film of TiO_2 on the material surface improves its corrosion behaviour. At higher temperatures though, Titanium shows bad oxidation behaviour – a reason why its alloys are not used above 600 °C (Leyens & Peters (2003)).

In this work, the Johnson-Cook parameters for Ti 6Al 2Sn 4Zr 6Mo (referred to as Ti-6246), an $\alpha + \beta$ alloy, and Ti 15V 3Cr 3Al 3Sn (referred to as Ti-15-3-3-3), a metastable β alloy, are found for the simulation of chip formation. The Ti-6246 alloy has been designed for use at high temperatures and has excellent creep resistance properties. It can withstand long term loads for up to 400 °C and short term loads for up to 540 °C (Rodney *et al.* (1994)). For this reason, Ti-6246 is used as forgings in the intermediate temperature regions of gas turbines. Due to its light weight and resistance to corrosion, this alloy is also being considered for use in sour oil wells (Hargrave *et al.* (2010)). Ti-15-3-3-3 is used primarily in the construction of airframes due to its high strength, light weight and ability to be cold-formed which allows it to be produced as cold rollable sheets (Blenkinsop (1993)). It has been used in aircraft fuselage frames due to its good formability. Its ability to be cast into high strength components makes it an attractive material for aircraft landing gears.

Nickel based superalloys: For high temperature applications, the chosen material should show good creep resistance and high resistance to oxidation. Ceramic materials (*e.g.* ZrO_2, Al_2O_3, SiC) and refractory metals (*e.g.* W, Mo) have high melting points but are not suitable for high temperature applications. Both of these materials are brittle. More importantly, Ceramics have low tensile strength due to low fracture toughness and limited creep strength due to the softening of glass phases. Refractory materials have low oxidation resistance.

Nickel is an attractive element for designing alloys for high temperature applications. It occurs in a stable close-packed face-centered

cubic (fcc) structure and retains its structure up to its melting point. Such a close-packed structure leads to low diffusion rates at high temperatures and low rates of thermally activated creep. A number of elements are soluble in Nickel, allowing it to be strengthened and improving its oxidation resistance at high temperatures.

The coherently precipitated γ' and γ'' phases significantly strengthen the fcc γ phase which forms a continuous matrix. Elements such as Co, Cr, Mo act as solid solution strengtheners of the γ matrix and can be found in significant concentrations in this phase. The γ' phase is formed primarily from Ti and Al, and generally forms cuboidal-shaped precipitates. The γ'' is a metastable phase consisting of body-centered tetragonal (bct) Ni_3Nb, which significantly strengthens the alloy. However, the metastable γ'' transforms at high temperatures to the orthorhombic δ phase, which is incoherent to the γ matrix and leads to severe reduction of strength and ductility. The formation of the orthorhombic δ phase must therefore be avoided. Fe is often added to the alloy for cost-cutting reasons and Co is added to decrease the stacking fault energy and increase the solution heat treatment window. Al and Cr improve the oxidation and corrosion resistance of the material, B and C act as grain boundary strengtheners and further improve the creep resistance.

The chemical composition of Alloy 625, whose chip formation simulations have been conducted as a part of this work, is given in Table 3.1. The relatively low percentage of Ti and Al in the alloy prevents the formation of γ' phase. The alloy derives its strength from the metastable γ'' phase, though long term exposures to temperatures above 600 °C leads to the formation of the δ phase which leads to degradation of properties. This alloy's excellent high temperature strength and very good oxidation resistance up to 850 °C makes it ideal for use in gas turbines and aerospace applications where short term thermal loads are present or application temperatures are below 600 °C. This alloy also shows excellent corrosion resistance over a broad range of corrosive environments due to the formation of Cr_2O_3. For this reason, it is used in marine and offshore applications, chemical plants and heat exchangers. Its high strength, resistance to stress cracking and pitting as well as high corrosion resistance, make it an attractive material for use in nuclear reactors and control rod components.

All these three materials are known to form segmented chips at high cutting speeds and continuous chips at low cutting speeds (Ostroushko

Ni	Cr	Mo	Nb	Fe	Ti	Al
bal.	22.10	9.10	3.43	4.73	0.33	0.21

Mn	Si	Co	C	Ta	S	P
0.11	0.1	0.08	0.03	0.01	0.001	0.006

Table 3.1: Chemical composition (wt.%) of Alloy 625 used in this work.

et al. (2012); Rokicki *et al.* (2010); Siemers *et al.* (2011)). The aim of the following sections is to determine if the Johnson-Cook parameters obtained from SHPB experiments can be used to simulate segmented chip formation at high cutting speeds in these materials and to determine how well the cutting force is predicted at given conditions. It is expected that the parameters thus determined will have limited applicability as the strains, strain rates and temperatures reached during machining are not attained during the SHPB tests, due to the limitations discussed in Section 3.2.2.

3.5 Material modelling and simulation

Using the flow stress data obtained from SHPB testing at different strain rates and temperatures, the Johnson-Cook parameters are obtained. For materials Alloy 625 and Ti-6246, parameters have been found using a non-linear data fitting algorithm of Matlab (Matlab (2010)). For Ti-15-3-3-3, the parameters have been obtained by manually fitting the different parts of the equation progressively. Using the Johnson-Cook parameters, chip formation simulations are performed and compared with experiments. All this is discussed in the subsequent sub-sections.

In order to compare the simulations and experiments, experimentally obtained chip shapes and cutting forces are required. The chip shape during high speed cutting can be obtained from orthogonal quick-stop experiments. In a quick-stop experiment, a workpiece is brought to a sudden stop during the cutting process and the chip root can be analysed to understand the chip formation process. The setup of the quick-stop mechanism has been described in literature (Hoffmeister & Ksiezyk (2010); Metsäjoki & Hoffmeister (2012)). Due to the impact of the workpiece on the tool holder, the cutting force signals can get corrupted due to the elastic waves developed during the impact event. Therefore the measurement of the cutting force has been performed on the Hopkinson split bar apparatus using the U-type specimens (Figure

3.5). A tool is placed between the arms of the U-type specimen and the assembly is placed in between the incident and the transmitted bars of the Hopkinson split bar setup. The uncut chip of required thickness is machined on to the specimen. On impact, the tool cuts the material forming the chip and the transmitted bar signal enables the measurement of the cutting force. However the chip is destroyed during or after the test as the reflected stress pulses impact the tool and the specimen several times after the first impact. This experiment has also been described in Hokka *et al.* (2012a).
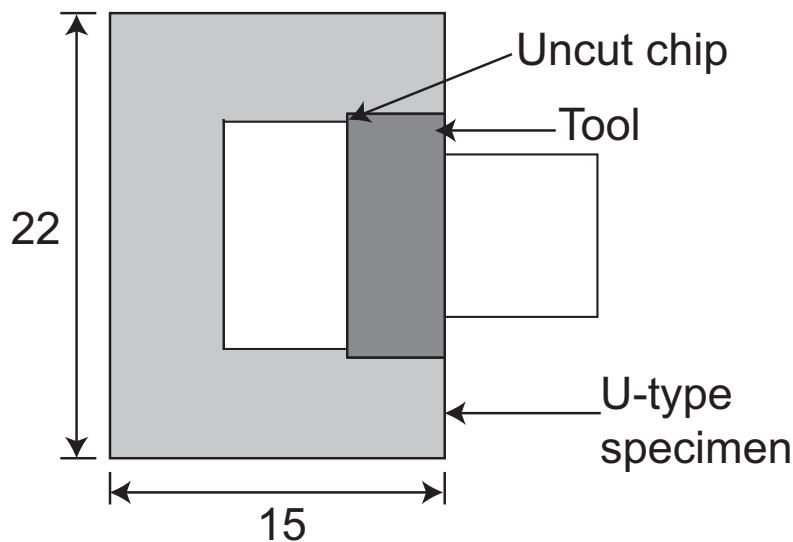
Figure 3.5: The schematic diagram of the U-type specimen along with the tool. The thickness of the specimen is 3 mm. All units in this figure are given in mm.

The simulations have been performed at the same cutting conditions as prevailing during the U-type cutting test. This enables a direct comparison of the specific cutting force. Comparing the chip shapes at exactly the same cutting conditions is impossible, as the chip shapes of the experiments are not available. However, a reasonable estimate of the chip shape can be made from the quick-stop results at slightly different conditions.

3.5.1 Parameter identification: Ti-15-3-3-3

For the Titanium alloy Ti-15-3-3-3, the Johnson-Cook parameters were found by sequentially identifying them from the experimental data (Hokka *et al.* (2012a)). The parameter m is first identified using the flow stress values at low plastic strains (less than 5% strain) $\sigma_{T_{\mathrm{ref}}}^{L}$ and $\sigma_{T_2}^{L}$

found at the reference temperature (T_{ref}) and at an elevated temperature (T_2) respectively and at a constant strain rate. The parameter m is determined using:

$$m \quad = \quad \frac{\ln\left(1 - \frac{\sigma^L_{T_2}}{\sigma^L_{T_{\text{ref}}}}\right)}{\ln\left(\frac{T_2 - T_{\text{ref}}}{T_{\text{melt}} - T_{\text{ref}}}\right)}. \tag{3.15}$$

At low strains, the temperature rise due to plastic heat is not significant, and obtaining the parameter m from the flow curve values at low strains is possible. For finding parameters A, B and n, the experimental curves at the reference temperature and strain rate are converted to isothermal curves. Parameter A is the yield strength at reference temperature and strain rate. The parameters A and m are further varied until the experimental stress is matched also at higher strains to the stresses predicted by the model. Parameters B and n are found by fitting a line to the $\log(\sigma - A)$ versus $\log(\varepsilon)$ plot. The line intercept on the $\log(\sigma - A)$ axis gives $\log(B)$ and the slope of the line gives n. Finally, the parameter C is obtained by comparing the stresses predicted by the model to the experimentally obtained stresses at the reference temperature but at different strain rates. A similar parameter determination method has also been reported in the literature (Samantaray *et al.* (2009)).

The Johnson-Cook parameters obtained from high strain rate tests have been shown in Tables 3.2 and 3.3.

Density [kg m^{-3}]	4760
Young's Modulus [GPa]	90
Poisson's Ratio	0.33
Specific Heat Capacity [$\text{J kg}^{-1}\,\text{K}^{-1}$]	500
Coefficient of thermal expansion [K^{-1}]	8.5×10^{-6}
Thermal Conductivity[$\text{W m}^{-1}\,\text{K}^{-1}$]	8.08
Element failure criterion:	
Equivalent plastic strain at failure ($\bar{\varepsilon}^{pl}_f$)	1.0

Table 3.2: Material properties for Ti-15-3-3-3 alloy.

3.5.2 Simulation of chip formation: Ti-15-3-3-3

An adiabatic finite element simulation was done using the Johnson-Cook parameters listed in Tables 3.2 and 3.3. A fine mesh with 44 elements

A [MPa]	B [MPa]	n	C	m	T_{melt} [K]	T_{room} [K]	$\dot{\varepsilon}_0$ [s^{-1}]
984	380	0.3	0.069	1.1	1942	300	1400

Table 3.3: Johnson-Cook parameters for Ti-15-3-3-3 alloy.

in the chip thickness direction is used. The simulation parameters are listed in the Table 3.4. A weakly segmented chip (Figure 3.6) is formed with an average specific cutting force of 1971 MPa and a standard deviation [1] of 78 MPa. The specific cutting force evolution from the U-type experiment and the simulation is plotted in Figure 3.7. The average specific cutting force from the U-type experiment is 2181 MPa and its standard deviation is 399 MPa. The difference in the frictional conditions and other simplifications such as a rigid sharp tool and adiabatic simulations can partially explain the 10% difference in the average specific cutting force. Moreover, there are significant differences in the chip shapes (Figure 3.8), as the segments are found to be prominent.

Cutting Speed [m s^{-1}]	15
Uncut chip thickness [µm]	44
Co-efficient of friction	0.1
Mesh element type for Workpiece	CPE4R
Mesh element type for Tool	R2D2
Workpiece mesh size	1µm × 1µm

Table 3.4: Cutting and simulation parameters used in the chip formation simulation of Ti-15-3-3-3 alloy.

The shear band formation is found to be extremely sensitive to the specific heat capacity of the material. The specific heat of the material rises at higher temperatures. Using a higher value of specific heat capacity of 650 J kg^{-1} K, the simulations did not produce any shear banding (Figure 3.9). The adiabatic stress-strain curve (Figure 3.10) with the higher specific heat capacity shows less adiabatic softening, which indicates that shear banding may be inhibited.

---

[1]The standard deviation values are quoted because the simulated chip formation is accompanied by a variation of the cutting force during segmentation. In the experimental case, it also gives an idea of the noise present in the experimental observation.
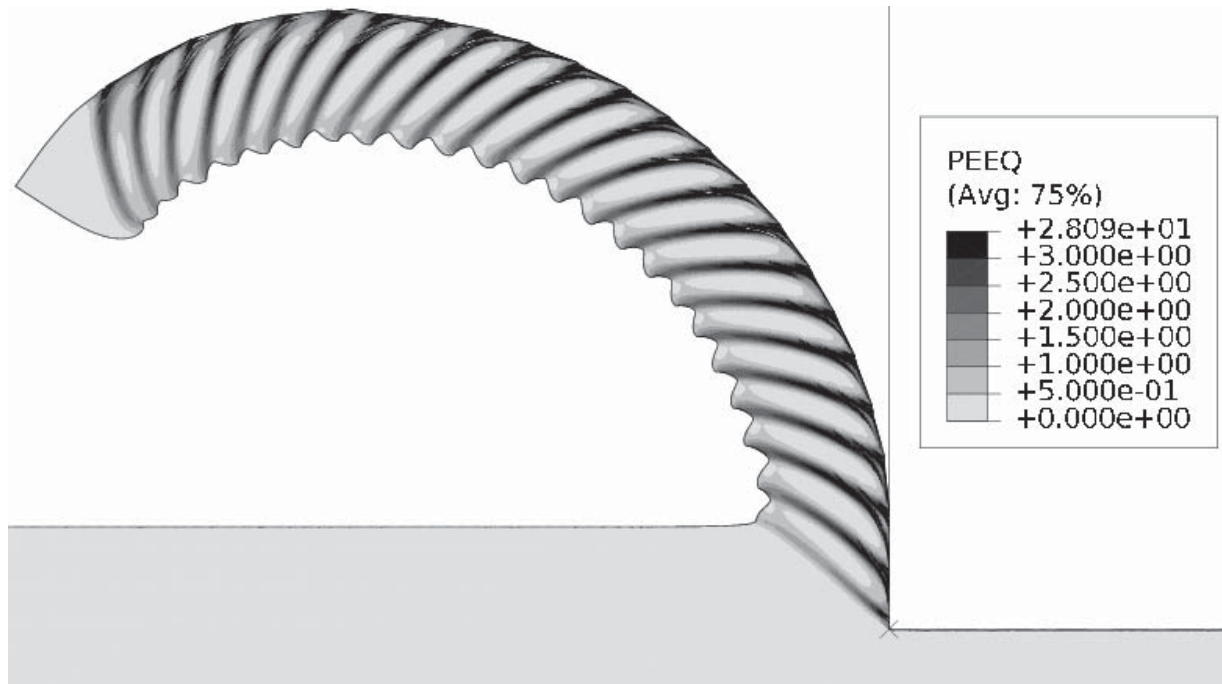
Figure 3.6: Plastic equivalent strain distribution in Ti-15-3-3-3 chip

This clearly shows the problem of identifying material parameters in a domain where strains, strain rates and temperatures are much lower in comparison to those obtained during machining. Extrapolations over several orders of magnitude of strains and strain rates make the prediction of flow stress in machining conditions inaccurate which in turn adversely affects the simulation results.

3.5.3 Parameter identification: Alloy 625

The identification of material parameters by using the method described for Ti-15-3-3-3 is both difficult and time consuming. Often, determining the correct parameter set this way requires a lot of adjusting of the parameters and the final choice is subjective. Therefore a more objective and automatic method of material parameter identification is used for the Alloy 625.

A nonlinear fitting routine of Matlab was used to identify the material parameters. The fitting procedure is an inverse identification algorithm where the material parameters are systematically changed until the values predicted by the material model are sufficiently close to the experimental results. In order to do this, a Matlab function, which is dependent on the Johnson-Cook parameters (A, B, n, C, m), is created which returns a vector of adiabatic stress values $(\bar{\sigma}_{calc}(\varepsilon_{exp}))$ for a given
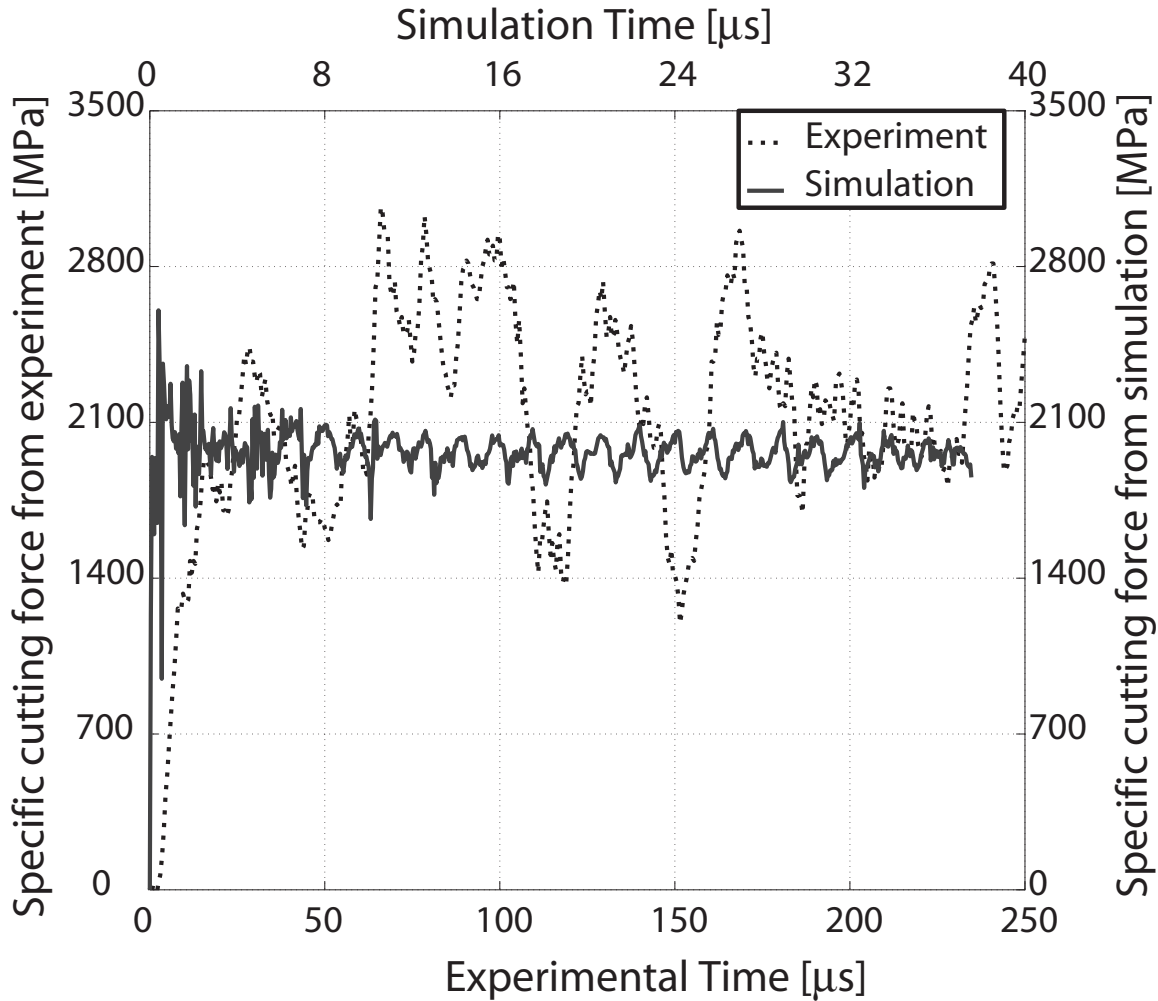
Figure 3.7: Specific cutting force evolution during experiment and simulation for Ti-15-3-3-3

set of strain values. The experimentally determined vector of stress values $(\bar{\sigma}_{exp}(\varepsilon_{exp}))$ can then be combined with the calculated stress values to give an error function:

$$e_{exp} = \sum_{i=1}^{N} \frac{\left|\left|\bar{\sigma}^i_{exp}(\varepsilon_{exp}) - \bar{\sigma}^i_{calc}(\varepsilon_{exp})\right|\right|^2}{M^i} \,, \qquad (3.16)$$

where $||\bullet||$ is the Euclidean norm. The superscript i refers to different curves obtained at different conditions and N is the total number of curves. M^i is the total number of entries in i^{th} curve. The material properties for Alloy 625 are listed in Table 3.5 and are needed for the calculation of the adiabatic curve. The error function is minimised using the Matlab non-linear curve fitting algorithm *lsqcurvefit*. A similar

Ti-15-3 (as received), QS 6 (v=20m/s ap=100μm)
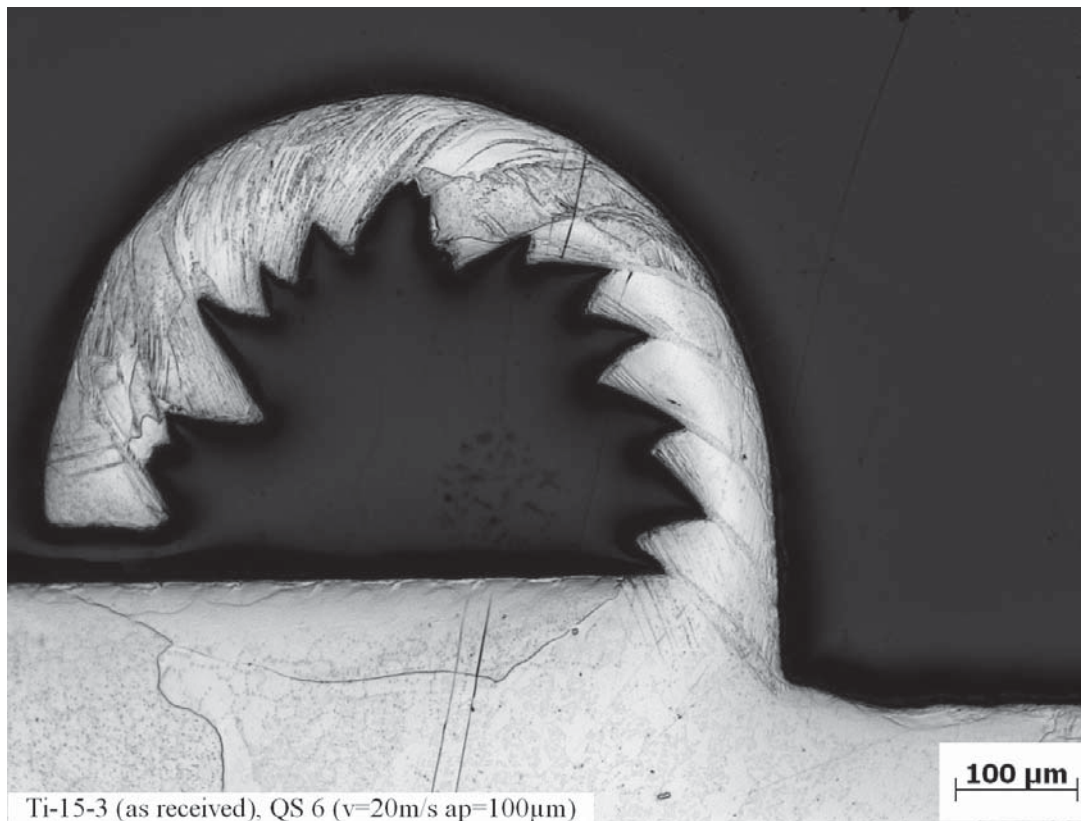
Figure 3.8: Chip shape obtained from quick-stop experiments for Ti-15-3-3-3 alloy in the as-received state. The uncut chip thickness is 100 μm and the cutting speed is 20 m s^{-1}. (Source: Dawid Ksiezyk, IWF, TU Braunschweig, 2012)

method of parameter identification has been used in literature before (Milani *et al.* (2009)).

Using this method, the Johnson-Cook parameters obtained from high strain rate tests are shown in Table 3.6. The experimental and the fitted curves are shown in in Figure 3.11.

It can be noticed from the flow curves and rather high value of parameter n that the material strain hardening is very high and is almost linearly increasing. The strain rate dependence is extremely low at high strain rates. On plotting the adiabatic stress-strain curve for Alloy 625 (Figure 3.12), the flow stress rises above 2000 MPa at strains over 0.80 up to a maximum of 2200 MPa at a strain of approximately 1.2. Since the maximum of the adiabatic stress-strain curve lies much higher than a strain of 1.0, the chances of shear band formation is reduced. This is indeed the case when the chip formation simulation is carried out. It can be seen from Figure 3.13 that no shear bands form using the Johnson-Cook parameters, even though a very good fit between
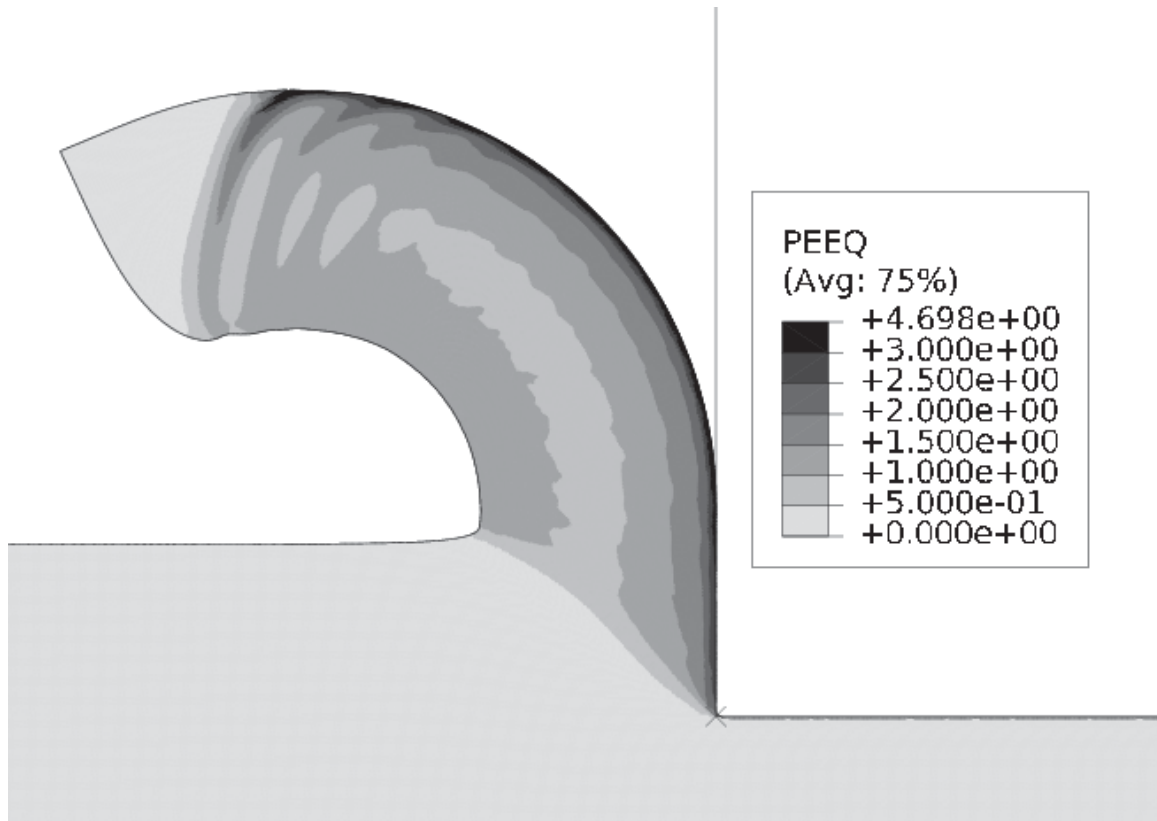
Figure 3.9: Plastic equivalent strain distribution in Ti-15-3-3-3 chip, simulated with a higher specific heat capacity of 650 J kg^{-1} K

Density [kg m^{-3}]	8440
Young's Modulus [GPa]	207
Poisson's Ratio	0.312
Specific Heat Capacity [J kg^{-1} K^{-1}]	410
Coefficient of thermal expansion [K^{-1}]	1.28×10^{-05}
Thermal Conductivity[W m^{-1} K^{-1}]	9.8
Element failure criterion:	
Equivalent plastic strain at failure ($\bar{\varepsilon}_f^{pl}$)	1.0

Table 3.5: Material properties for Alloy 625.

A [MPa]	B [MPa]	n	C	m	T_{melt} [K]	T_{room} [K]	$\dot{\varepsilon}_0$ [s^{-1}]
558.8	2201.3	0.80	0.000209	1.146	1623	298	1670

Table 3.6: Johnson-Cook parameters for Alloy 625 assuming adiabatic conditions.
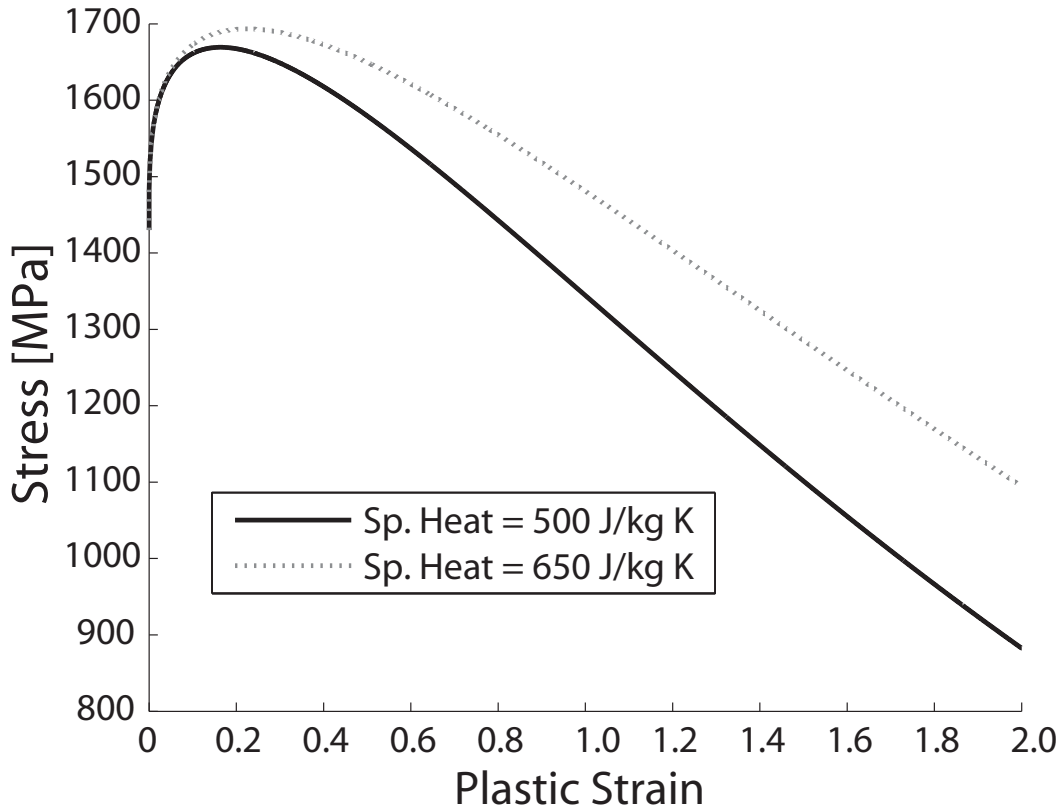
Figure 3.10: Comparing adiabatic stress-strain curves for Ti-15-3-3-3 drawn with the specific heat capacity of 650 $J\,kg^{-1}\,K$ and 500 $J\,kg^{-1}\,K$

the experimental data and the Johnson-Cook model is obtained. Some thermally softened striations are formed on the chip within which the stress level is much lower than the surrounding region. The tips of the striations are surrounded by high stress regions which prevent the striations from propagating across the chip surface to form segments.

The assumption that the SHPB testing is adiabatic is not critical to finding incorrect material parameters. Even if isothermal conditions are assumed, the identified parameter set (see Table 3.7) is very similar to the set obtained using the adiabatic assumptions.

A [MPa]	B [MPa]	n	C	m	T_{melt} [K]	T_{room} [K]	$\dot{\varepsilon}_0$ [s^{-1}]
551	2024	0.76	0.00053	1.14	1623	298	1668

Table 3.7: Johnson-Cook parameters for Alloy 625 assuming isothermal conditions.
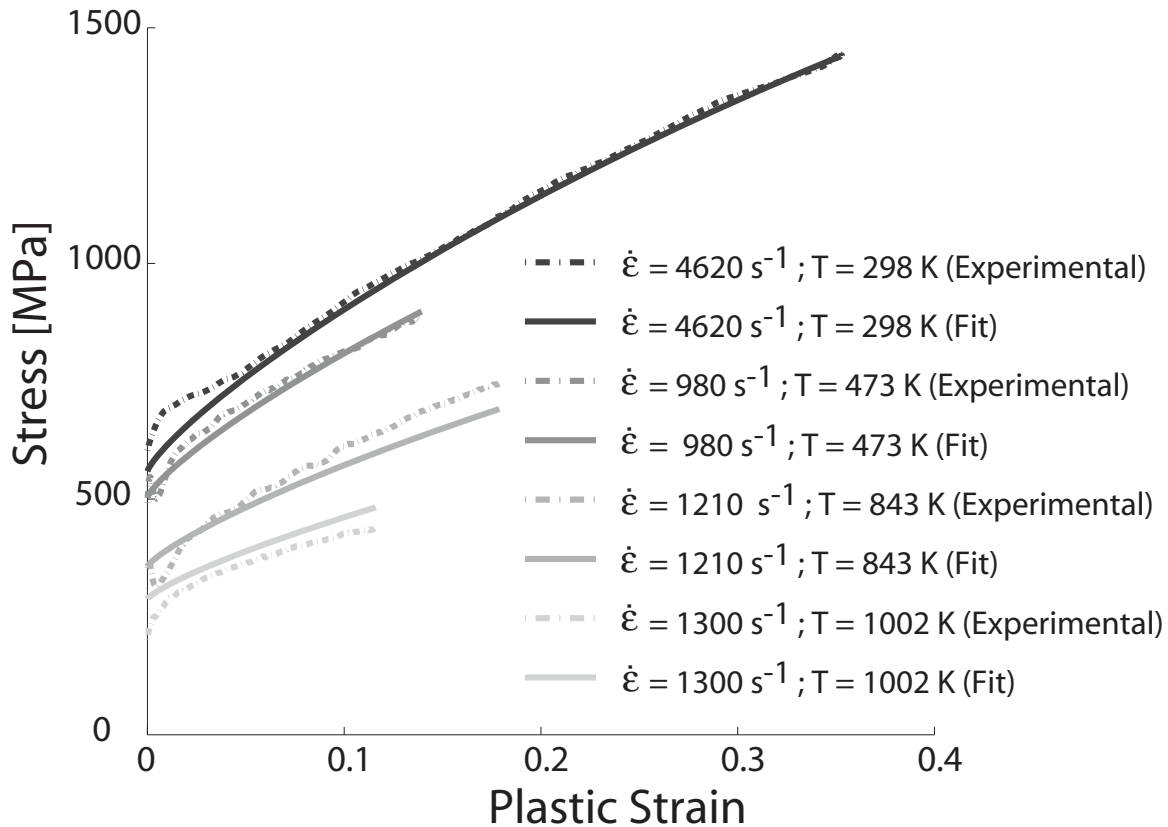
Figure 3.11: Experimentally obtained and fitted Johnson-Cook flow curves for Alloy 625

3.5.4 Modification of material model for Alloy 625

Using only the Johnson-Cook model, the material strength is overestimated at high strains. The high strain hardening factor n causes the material to harden far too much to allow the formation of the shear bands. Therefore the Johnson-Cook model was modified using an approach similar to that presented by Calamaz *et al.* (2008) and Sima & Özel (2010), in which a strain softening term is introduced so that the material strain-softens above a certain value of critical strain. The numerical equations of the models have already been shown in Equations 2.16, 2.17, 2.18, 2.19 and 2.20. The strain softening phenomenon is not well understood, though it has been attributed to different types of physical phenomena, mainly due to texture or microstructural softening at large deformations (Kassner *et al.* (2002); Pettersen & Nes (2003)). Dynamic recovery and/or recrystallisation leads to change in the grain size and a dramatic increase in the high-angle grain boundaries which are the sites where the dislocation annihilate.
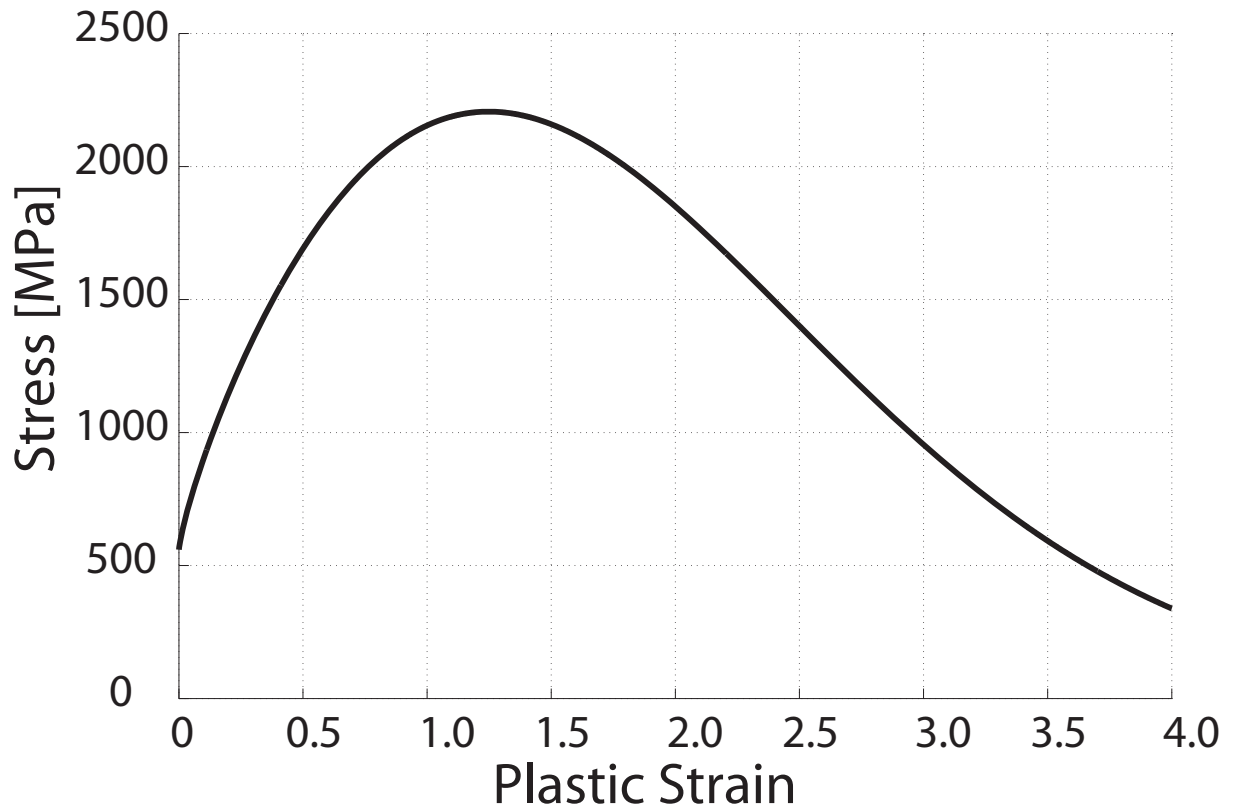
Figure 3.12: Adiabatic stress-strain curve for Alloy 625

In the modified material model for Alloy 625, a softening term is added to the Johnson-Cook model. The softening term introduces only a single extra parameter k. The modified model is given by:

$$\sigma_{mod} = \quad (A + B\varepsilon^n) \left[\tanh\left(\frac{1}{\varepsilon^k} \right) \right] \left[1 + C \ln\left(\frac{\dot{\varepsilon}}{\dot{\varepsilon}_0} \right) \right] \\ \left[1 - \left(\frac{T - T_{room}}{T_{melt} - T_{room}} \right)^m \right]. \tag{3.17}$$

On plotting the adiabatic stress-strain curves for the Johnson-Cook model (Figure 3.14), as well as the modified model with different k values, it can be seen that these curves match the experimental data very well at low strain values. However, at larger strains, there is a significant deviation of the modified model curves from the Johnson-Cook model curve. With progressively increasing values of k, the curves are seen to have significant and sharper softening, much before the strain of 1.0. This suggests that, with the increasing value of k, there is a greater tendency of shear band formation. In order to confirm this, finite element simulations were conducted.
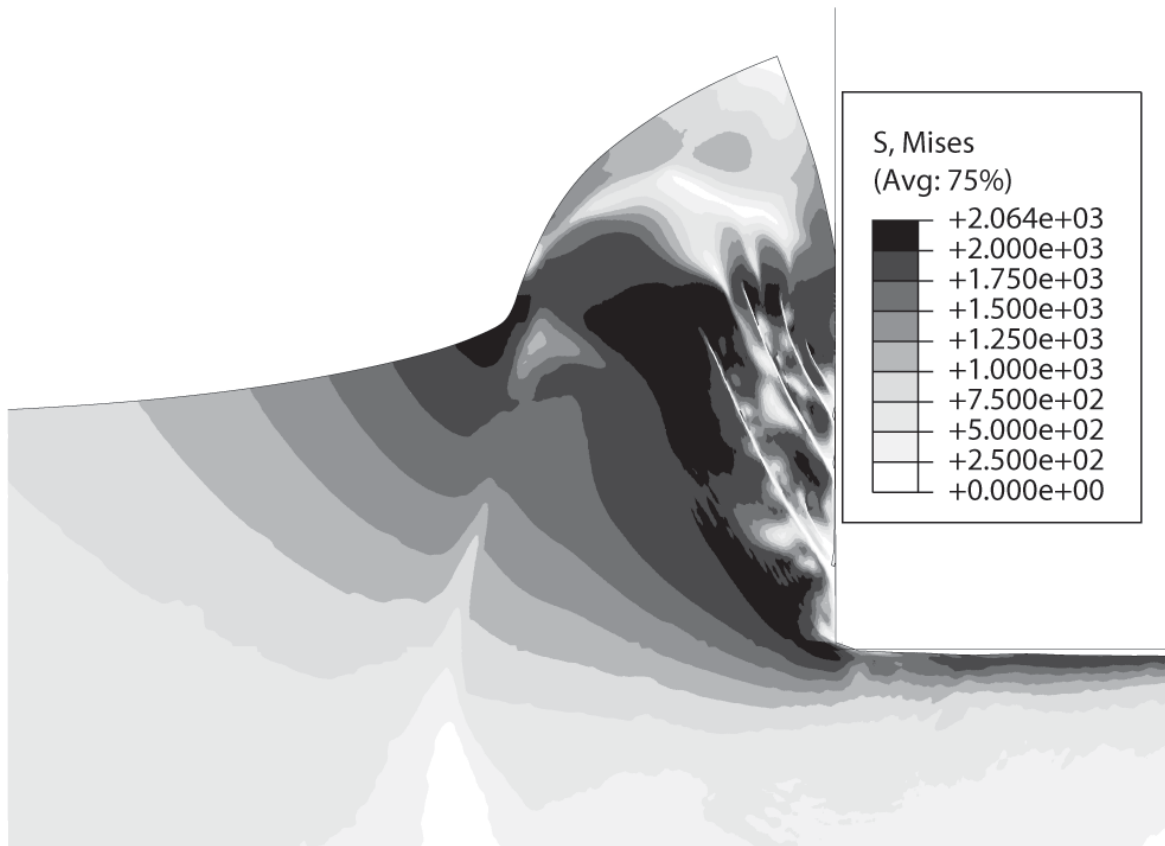
Figure 3.13: Von Mises stress distribution in Alloy 625 chip formed using the Johnson-Cook model

3.5.5 Chip formation simulation using the modified material model of Alloy 625

In order to simulate the chip formation of Alloy 625 using the modified material model, the isotropic hardening model has to be implemented using the VUHARD Fortran routine in Abaqus 6.9-1. The VUHARD routine is used to model the hardening behaviour *i.e.* the evolution of the yield surface of the material. The material states such as the equivalent plastic strain, the equivalent plastic strain rate and the temperature at an integration point are provided by the solver. As long as the material point is yielding, the stress values are given by the material model else the stress is equal to the elastic modulus times the elastic strain. The VUHARD routine returns the yield stress at a given material state.

In order to model the element deletion in the separation layer a damage model with linear damage evolution is implemented. The element damage starts at a damage initiation strain (ε_0^d) and when the critical
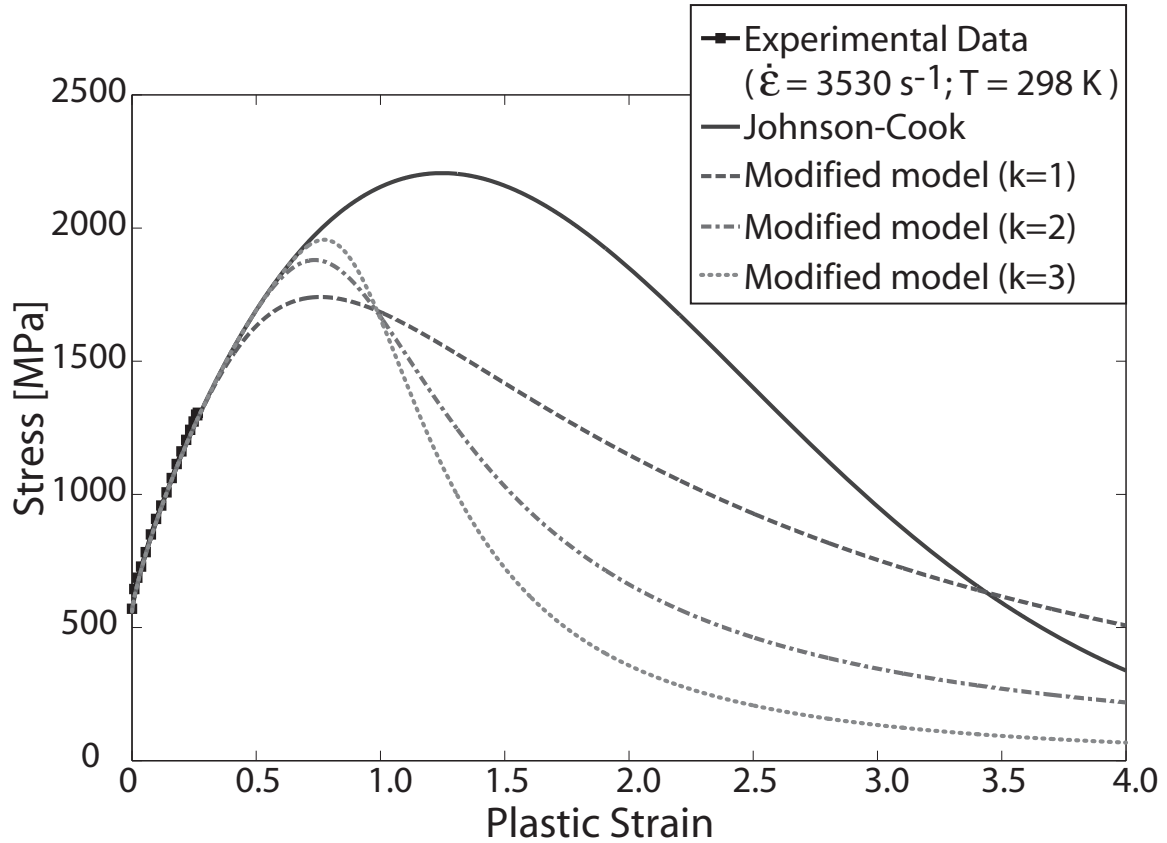
Figure 3.14: Comparison of the adiabatic stress-strain curves drawn using the Johnson Cook model and the modified model

failure strain (ε_{fail}) is reached the element is deleted. In between ε_0^d and ε_{fail}, a linear damage evolution model is used, which is expressed as:

$$d = \frac{\varepsilon - \varepsilon_0^d}{\varepsilon_{fail} - \varepsilon_0^d}, \tag{3.18}$$

where d is the damage variable. The stress during damage becomes $f_{yield} = (1 - d)\sigma_{mod}$. In Figure 3.15, the adiabatic stress-strain curve has been plotted comparing the curves with and without damage.

k	3.0
Element failure criterion:	
Equivalent plastic strain at failure ($\bar{\varepsilon}_f^{pl}$)	2.0
Damage initiation strain (ε_0^d)	1.5

Table 3.8: Additional material properties for Alloy 625 required for the modified model.
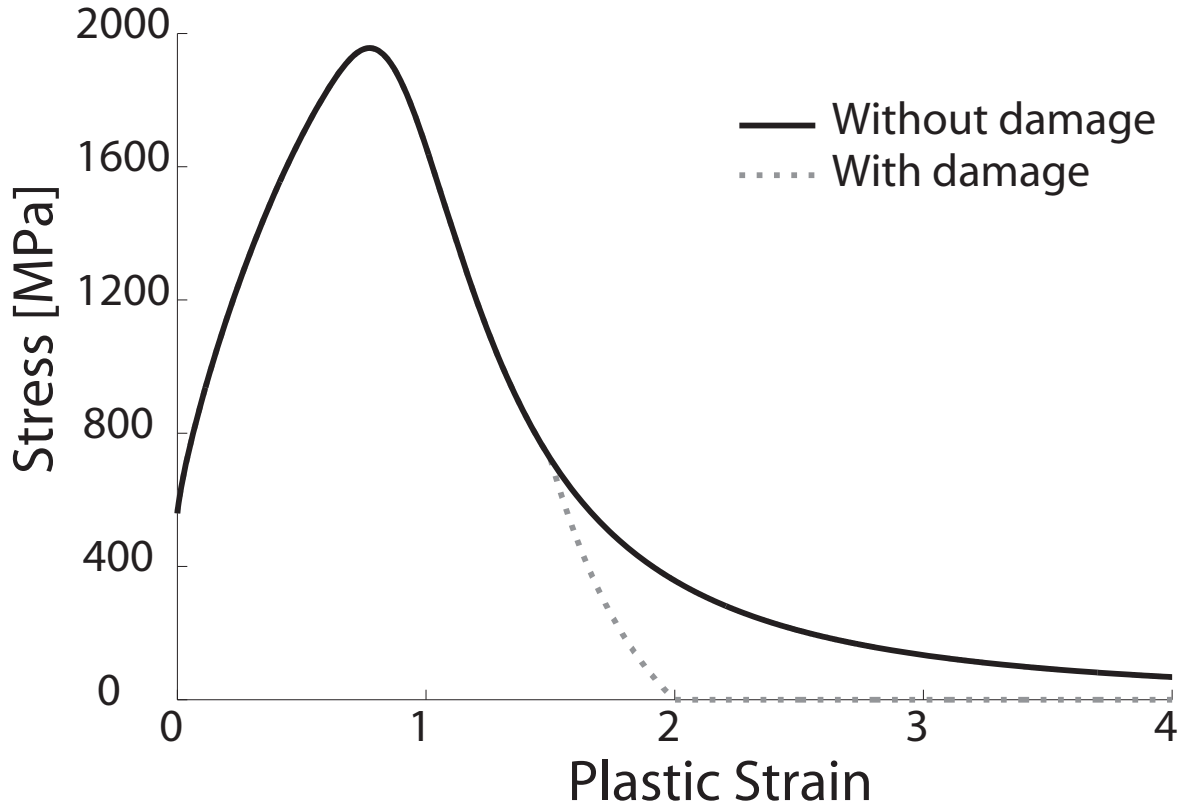
Figure 3.15: Comparison of the adiabatic stress-strain curves drawn using the modified model with and without damage

Using the modified material model, the chip formation simulation is conducted. The additional parameters used in the simulation have been listed in Table 3.8. However, due to high material hardening and very low strain rate dependence, the elements in the separation layer get deleted much before the tool moves forward. This leads to a crack propagating in front of the tool tip which affects the chip formation. Owing to the large material softening, having a large critical plastic strain (upto a value of 8.0) for element deletion does not prevent the crack from propagating. The elements in the separation layer show a strain rate of the order of 10^5 s^{-1} to 10^7 s^{-1} at the time of deletion. To strengthen the material at high strain rate, the strain rate sensitivity (C) is assumed to increase at very high strain rates and is given by

$$C(\dot{\varepsilon}) = C \left[1 + F_0 \left(1 - e^{-(\dot{\varepsilon} - \dot{\varepsilon}_0)/\dot{\varepsilon}_c} \right) \right], \tag{3.19}$$

where C is the strain rate sensitivity parameter from the Johnson-Cook Model, F_0 is the scaling factor equal to 200, $\dot{\varepsilon}_0$ is the reference strain rate and $\dot{\varepsilon}_c$ is a constant of value 10^5 s^{-1}. The scaling factor F_0 and the constant $\dot{\varepsilon}_c$ are obtained by trial and error. First the value of $\dot{\varepsilon}_c$ is fixed to 10^5 s^{-1}, so that around such high strain rates, the crack propagation

can be damped by hardening the material. Then F_0 is changed till a crack does not propagate in front of the tool tip. The value of $C(\dot{\varepsilon})$ varies from 0.000209 to a maximum of 0.042 (see Figure 3.16). Thus the viscosity term (Equation 3.17) ranges between 1.12 and 1.16 in the high strain rate range of 10^6 to 10^7 s^{-1}.
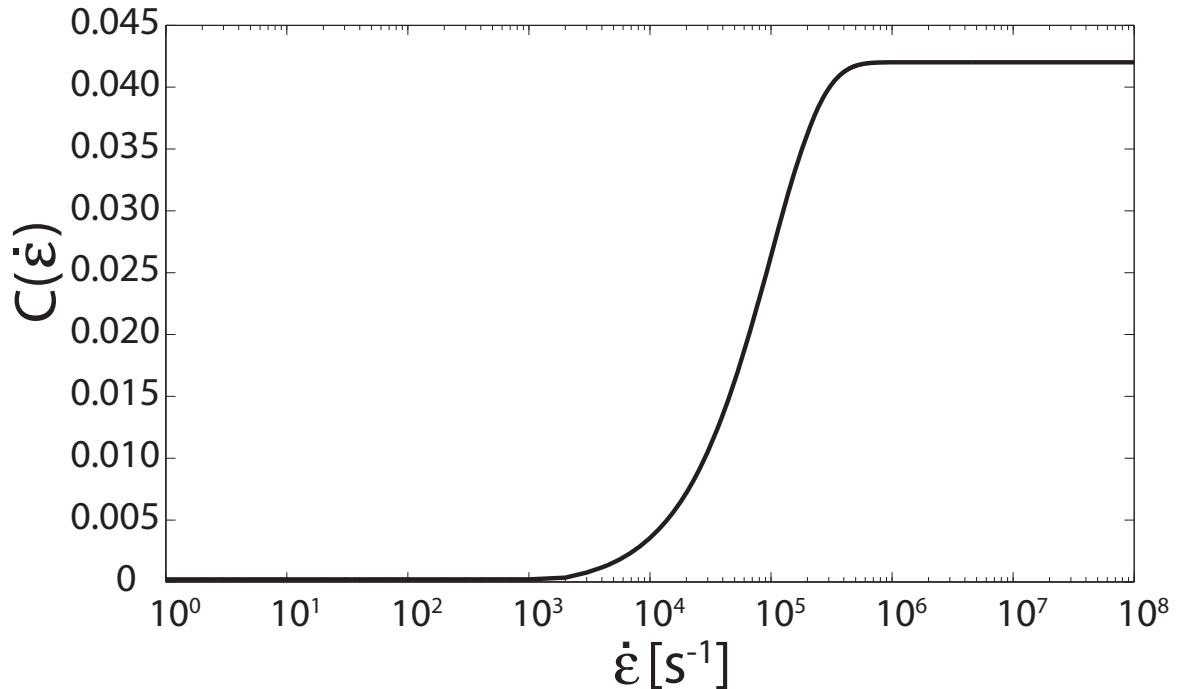
Figure 3.16: Evolution of strain rate sensitivity parameter with strain rate.

This measure is sufficient in preventing the crack propagation in the separation layer. However, this also prevents the shear localisation and chip segmentation. Therefore, Equation 3.19 is applied in the chip forming layer only when the equivalent plastic strain exceeds 1.5.

The finite element simulation was carried out using a very fine mesh with 47 elements along the chip thickness direction. The cutting and the simulation parameters have been listed in the Table 3.9. A strongly segmented chip (Figure 3.17) is formed using the modified material model. The average specific cutting force of 2013 MPa (standard deviation is 300 MPa) from simulation is more than the experimentally measured value of 1621 MPa (standard deviation is 40 MPa). This can be attributed to an overestimation of the material strength at high strains and strain rates. The chip obtained from the quick-stop experiment is shown in Figure 3.18 and is different from the chip obtained from simulations. A comparison of the geometrical parameters is shown in Table 3.10. The shear angles of the chips are quite similar. However, due to large strain

softening, the degree of segmentation of the simulated chip is about 40% higher than the experimentally obtained chip.

It is again seen that obtaining material parameters from standard experimental methods for machining simulations is very difficult. Despite a very good parameter fit of the experimentally obtained data, the flow stress in the domain of machining is not correctly predicted. The average cutting force predicted by the simulation is too high and therefore the average stress level at higher strains should be lower. The degree of segmentation of the simulated chip can be reduced by having a smaller strain softening term. Nevertheless, a better method of parameter identification is needed which can obtain material parameters directly from the machining process. An inverse material parameter identification process from machining is therefore shown in Chapter 5.

Cutting Speed [$\mathrm{m\,s^{-1}}$]	13
Uncut chip thickness [µm]	47
Co-efficient of friction	0.1
Mesh element type for Workpiece	CPE4R
Mesh element type for Tool	R2D2
Workpiece mesh size	1µm × 1µm

Table 3.9: Cutting and simulation parameters used in the chip formation simulation of Alloy 625.

	Simulation	Quick-stop
Degree of segmentation	0.44	0.31
Chip compression factor	1.28	1.15
Shear angle [°]	41	38
Normalised segment width	0.71	0.50
Normalised sheared distance	1.01	0.53

Table 3.10: A comparison of the geometrical parameters of the Alloy 625 chips obtained from finite element simulations and quick-stop experiments. The segment width and the sheared distance have been normalised w.r.t the uncut chip thickness.
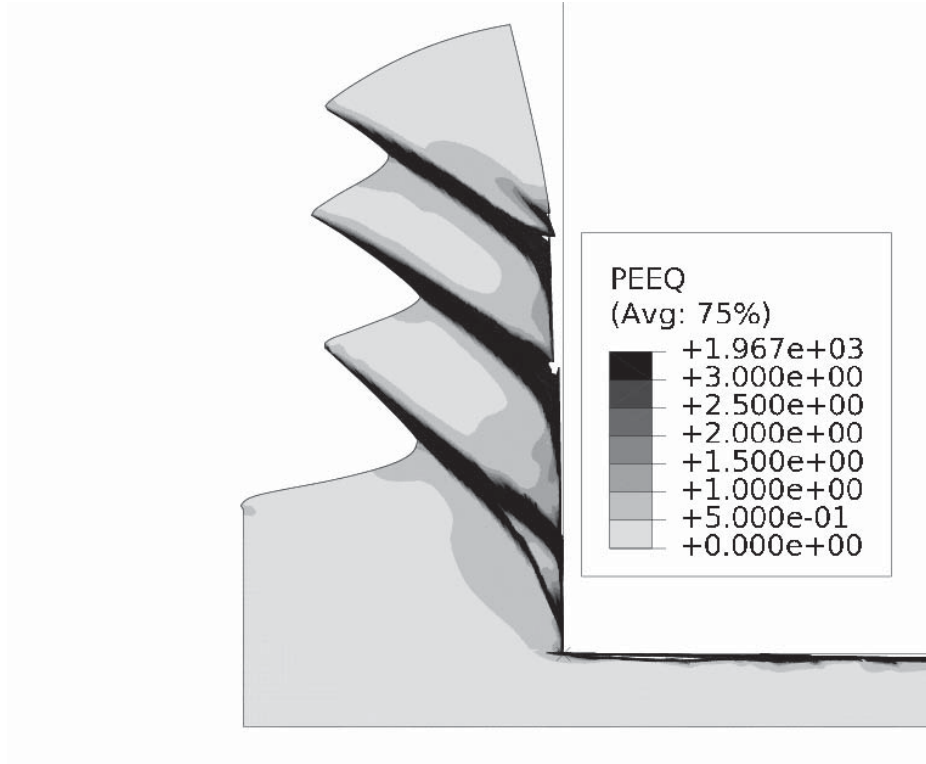
Figure 3.17: Plastic equivalent strain distribution in Alloy 625 chip formed using the modified model

3.5.6   Parameter identification: Ti-6246

For the Titanium alloy Ti-6246, the algorithm based inverse identification procedure used for Alloy 625 has been used to find the Johnson-Cook parameters. The material parameters are listed in Table 3.11. The Johnson-Cook parameters obtained from high strain rate tests are listed in Table 3.12.

Density [$\mathrm{kg\,m^{-3}}$]	4650
Young's Modulus [GPa]	114
Poisson's Ratio	0.342
Specific Heat Capacity [$\mathrm{J\,kg^{-1}\,K^{-1}}$]	508
Coefficient of thermal expansion [$\mathrm{K^{-1}}$]	9×10^{-6}
Thermal Conductivity[$\mathrm{W\,m^{-1}\,K^{-1}}$]	7.7
Element failure criterion:	
Equivalent plastic strain at failure ($\bar{\varepsilon}_f^{pl}$)	1.0

Table 3.11: Material properties for Ti-6246.
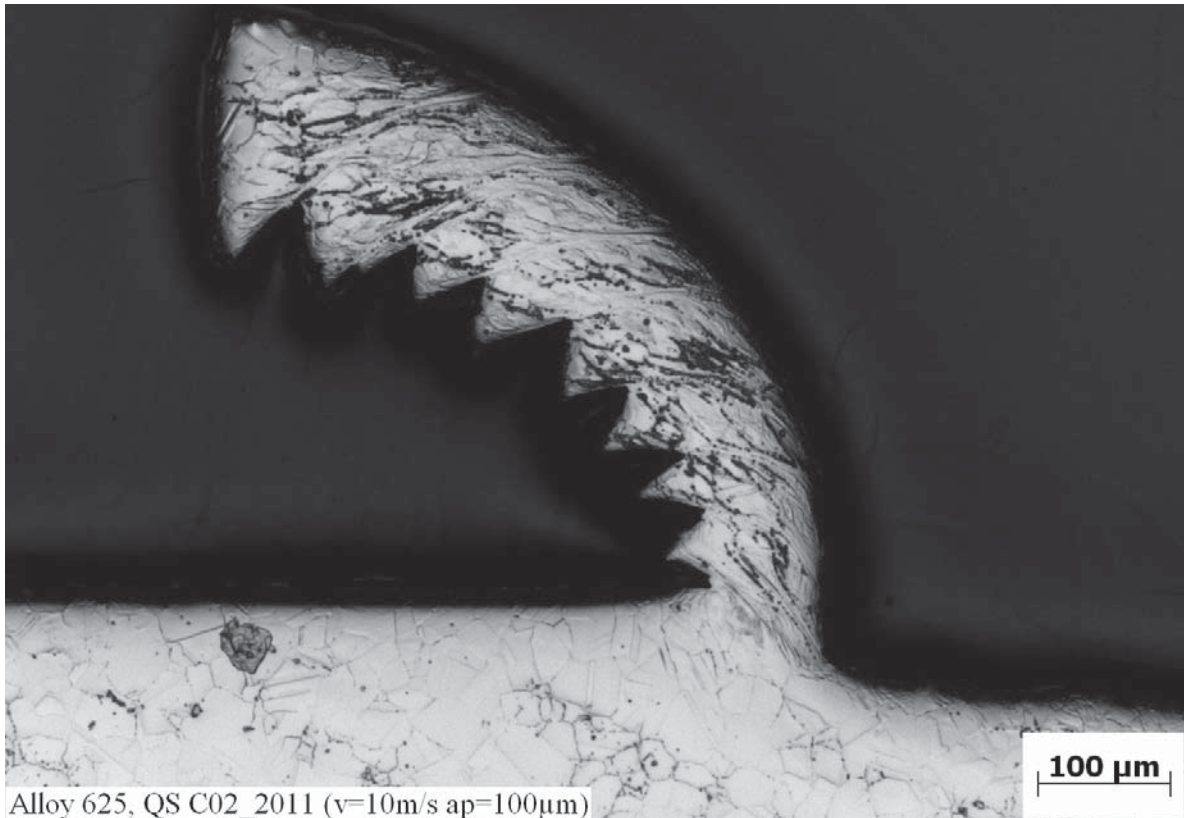
Figure 3.18: Chip shape obtained from quick-stop experiments for Alloy 625. The uncut chip thickness is 100 μm and the cutting speed is 10 m s^{-1}. (Source: Dawid Ksiezyk, IWF, TU Braunschweig, 2011)

A [MPa]	B [MPa]	n	C	m	T_{melt} [K]	T_{room} [K]	$\dot{\varepsilon}_0$ [s^{-1}]
1657	402	0.218	0.0054	0.8034	1898	298	1600

Table 3.12: Johnson-Cook parameters for Ti-6246.

3.5.7 Simulation of chip formation: Ti-6246

A finite element simulation was conducted using the material parameters listed in Tables 3.11 and 3.12 using a fine finite element mesh. There are 44 elements in the chip thickness direction. The cutting and the simulation parameters have been listed in the Table 3.13. A segmented chip (Figure 3.19) is formed at these conditions. On visual inspection, a number of similarities can be found between the simulated and the experimentally obtained chips (Figure 3.20). For an objective comparison, the geometric parameters from the two are listed in Table 3.14. It can be seen that the chip obtained from the simulations has around 40%

lower degree of segmentation than the experimentally obtained chip. Consequently, the sheared distance and the segment width in the chip from simulation are also smaller. This indicates that more thermal softening is required for a better match of these geometric parameters. There is about 10% difference in the shear angle which is possible due to difficulty in identifying the shear plane in the experimental chip.

The formation of split shear bands is observed in experimental tests (Figure 3.21) as well as simulations (Figure 3.19). The formation of a split shear band can be attributed to the fact that it is energetically more favourable for a newly forming band to bend slightly and join an already existing band than to deform the bulk of the chip material to form a new segment (Bäker (2004)).

The average specific cutting force from simulation is 1791 MPa (Standard deviation is 194 MPa) and from experiment is 1539 MPa (Standard deviation is 282 MPa). The specific cutting force evolution in the two cases is shown in Figure 3.22.

The parameter set obtained from the SHPB data can be further improved by using an inverse identification method as explained in Chapter 5. This way the flow stress in the machining domain can be better predicted, leading to a better match of chips and cutting forces.

Cutting Speed [$\mathrm{m\,s^{-1}}$]	15
Uncut chip thickness [µm]	200
Co-efficient of friction	0.1
Mesh element type for Workpiece	CPE4R
Mesh element type for Tool	R2D2
Workpiece mesh size	4µm × 4µm

Table 3.13: Cutting and simulation parameters used in the chip formation simulation of Ti-6246 alloy.

3.6   Discussion

Segmented chip formation can be simulated for the three materials viz. Ti-15-3-3-3, Alloy 625 and Ti-6246 using the respective material parameters obtained from the Hopkinson Split Bar experiments. The average specific cutting forces from simulations and experiments differed by up to 20% in these cases.
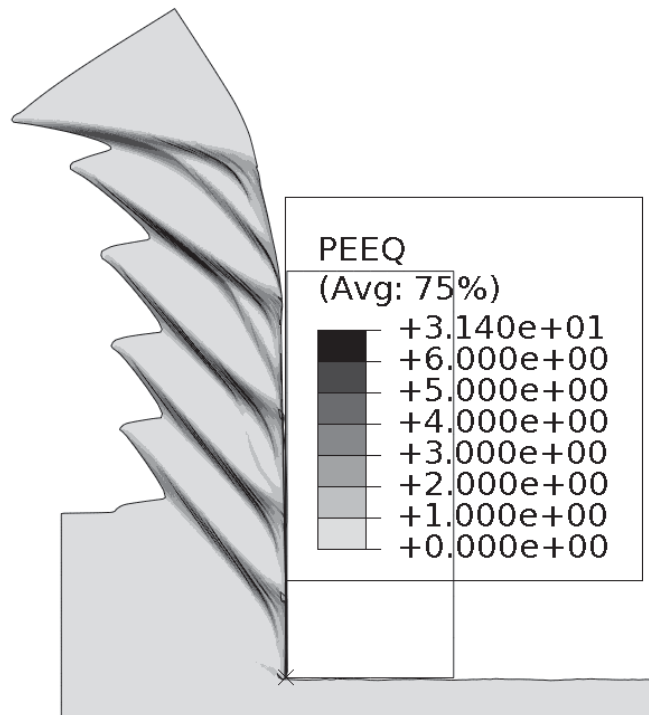
Figure 3.19: Plastic equivalent strain distribution in Ti-6246 chip formed using the Johnson-Cook model. A split shear band can also be seen.

	Simulation	Quick-stop
Degree of segmentation	0.30	0.53
Chip compression factor	0.88	0.75
Shear angle [°]	55	50
Segment width [µm]	76	100
Sheared distance [µm]	113	186

Table 3.14: A comparison of the geometrical parameters of the chips obtained from finite element simulations and quick-stop experiments. The geometrical parameters for the quick-stop chips are taken from Metsäjoki (2011).
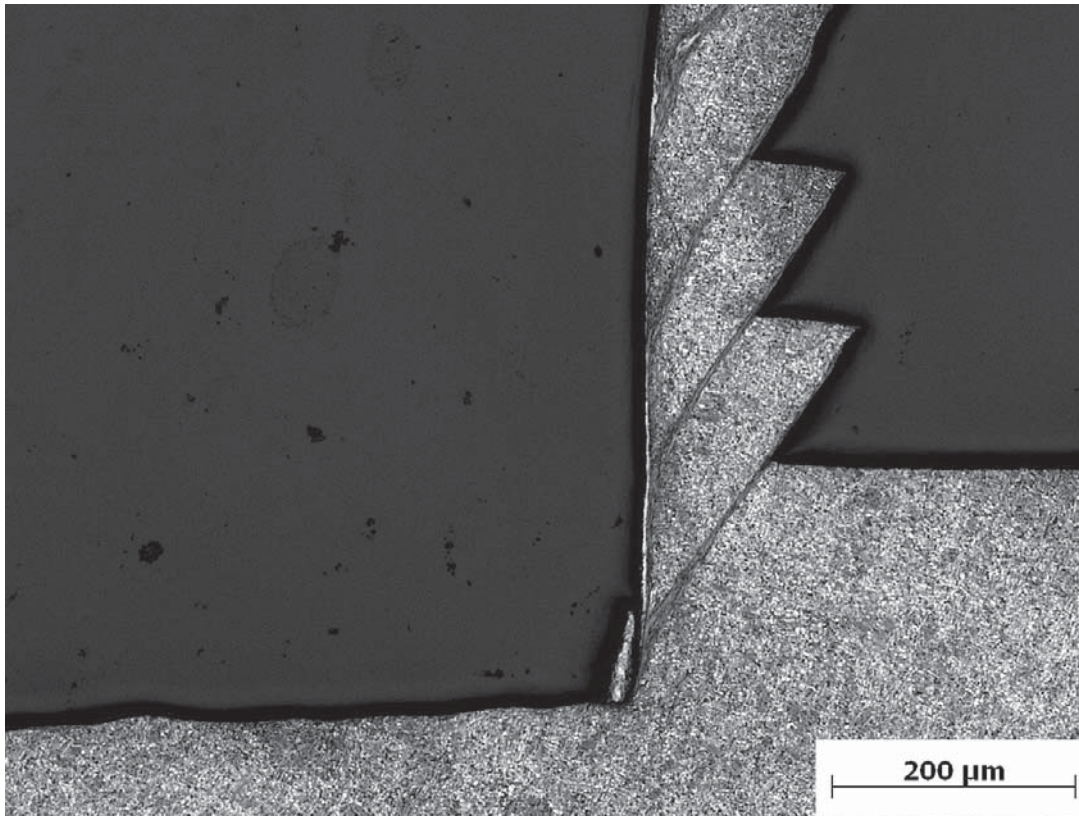
Figure 3.20: Chip shape obtained from quick-stop experiments for Ti-6246. The uncut chip thickness is 200 µm and the cutting speed is 20 m s^{-1}. (Source: Jarkko Metsäjoki, IWF, TU Braunschweig, 2011)

Such differences can be attributed to a number of reasons. The cutting force oscillates periodically and its frequency is the same as the chip segmentation frequency. However, a measurement of the segmentation frequency from the U-type experiments is very difficult due to the uncontrolled nature of the cutting process. This makes it difficult to ensure that the cut is symmetric on both the arms of the specimen. Moreover the friction conditions can be very different on the two arms, which can cause an unbalanced moment to rotate and misalign the tool. This in turn causes a non-symmetric cutting on the arms of the U-type specimen. The specimen is considered rigid, but in real life there is always some compliance in the arms of the U-type specimen, which can bend and cause a non-symmetric cut. This can change both the depth and the length of cut in the two arms. A relatively low friction coefficient is used for the simulations as at high cutting speeds the friction coefficient is small (Gente (2002); Hoffmeister *et al.* (1999)). With a higher coefficient, the cutting force can rise by up to 15%. Finally, sensitive measurements such as the segmentation frequency cannot be obtained from such a test.
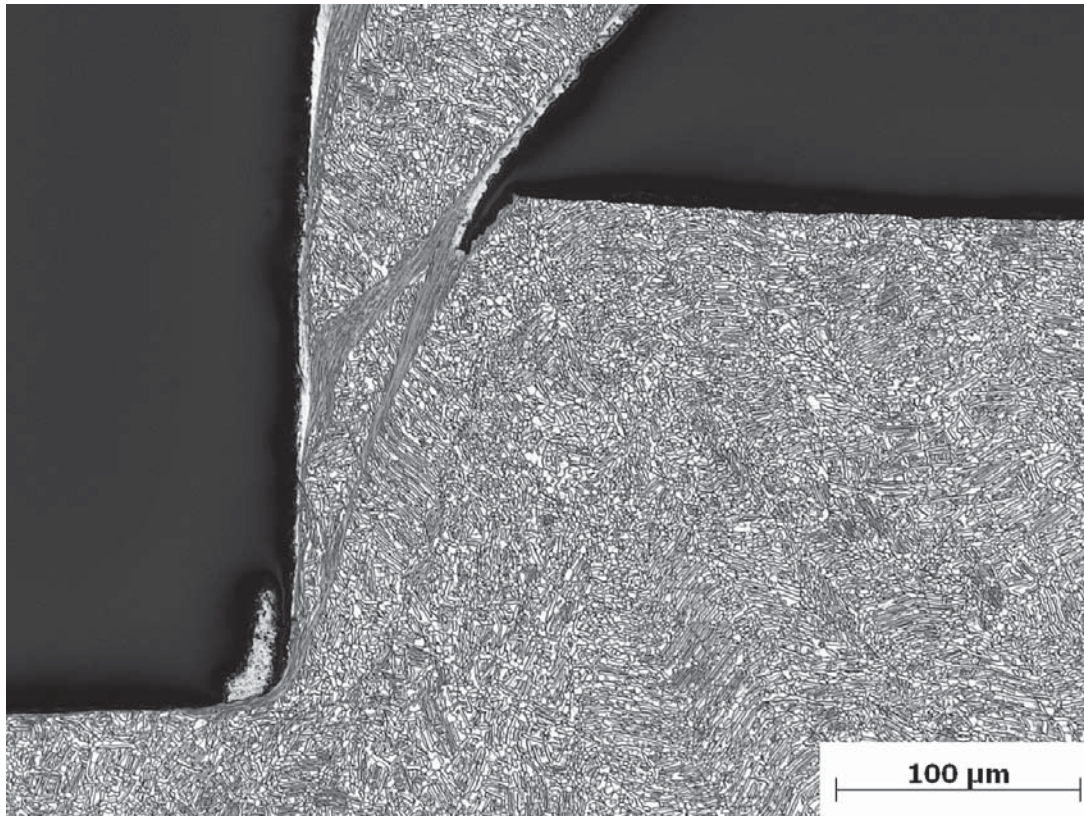
Figure 3.21: Split shear band in Ti-6246 can be seen in the chips obtained from quick-stop experiments. The cutting speed is $20\,\mathrm{m\,s^{-1}}$ and the cutting depth is $200\,\mathrm{\mu m}$. (Source: Jarkko Metsäjoki, IWF, TU Braunschweig, 2011)

It has been shown by Bäker that a match in the average cutting force is not sufficient to ensure that correct material parameters have been identified as they are not very sensitive (Bäker (2003a, 2004)) to inaccuracies in parameter values. He showed that materials having widely different hardening exponents (n) give rise to widely different looking chip shapes, however the average cutting force has roughly the same value. For a larger n value, the larger hardening is compensated by a higher thermal softening of the material. The time-resolved cutting force is a better measure for comparisons as the segmentation process causes the cutting force to oscillate, giving a distinct signature for comparison. Chip segmentation at high speeds being an extremely fast process, the experimental measurement of time-resolved cutting forces is extremely difficult. The chip shape is also very sensitive to small changes in the material parameters and is also a good way to compare the simulation and experimental results. It was observed that the chip shapes from simulations in Sections 3.5.2, 3.5.5 and 3.5.7 do not match well with
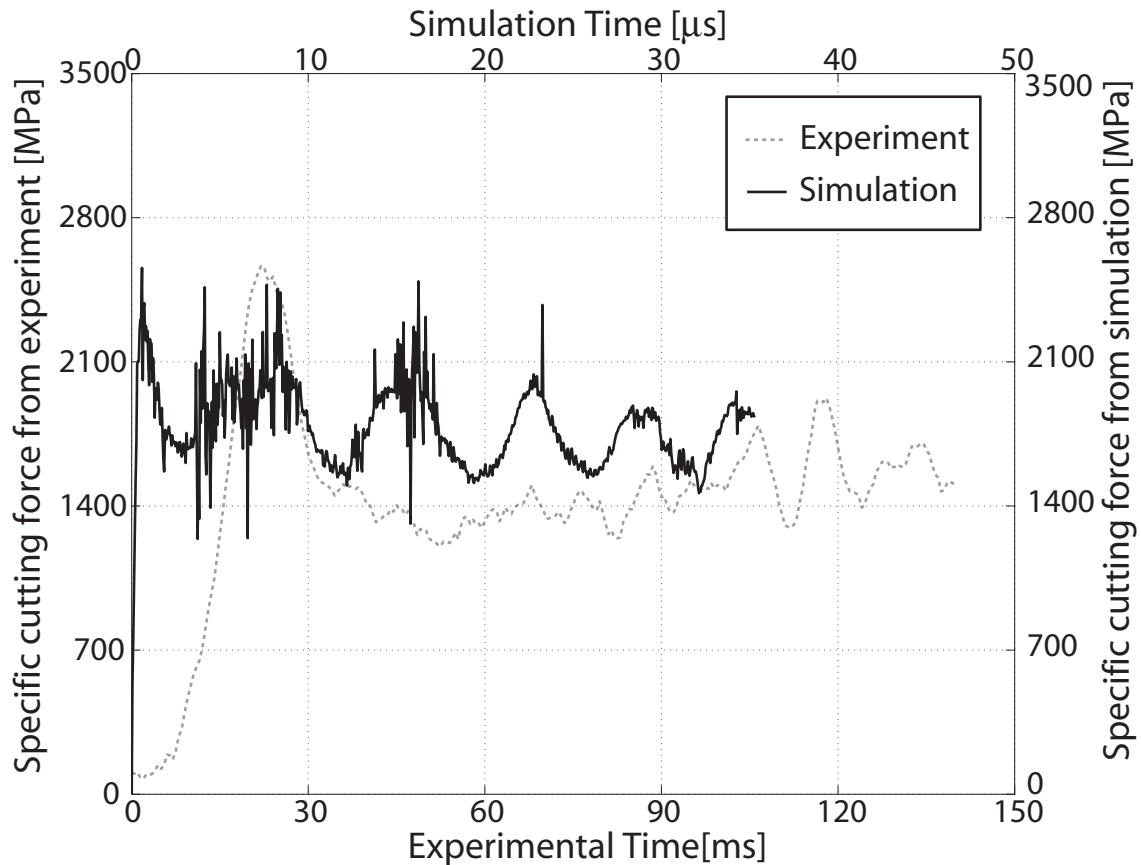
Figure 3.22: Specific cutting force evolution during experiment and simulation for Ti-6246

the experimental results. In this case, the match of the average specific cutting force does not prove that the material parameters have been correctly identified in the domain of machining.

Even after using the state-of-the-art experimental techniques, it is extremely difficult to obtain the strains and strain rates actually found during the machining process. Identifying material parameters to fit the data obtained from the Hopkinson Split Bar experiments is not sufficient to match the chip shapes and the cutting forces correctly. Better techniques are therefore needed to identify material parameters which are valid over a large range of strains, strain rates and temperatures. An inverse technique for identifying material parameters from the chip shapes and cutting forces is shown in Chapter 5. But before that the problem of non-uniqueness which is expected to occur due to the nature of the Johnson-Cook model is discussed in Chapter 4.

Chapter 4

Non-Uniqueness

In Chapter 3, it was observed that it is extremely difficult to reach the strains, strain rates and temperatures occurring during chip formation using experimental methods. As a result, the chip formation simulations conducted using the experimentally determined material parameters can only achieve partial success in predicting the cutting force and the chip shapes at high cutting speeds. To solve this problem, an inverse method of material parameter identification from machining experiments is proposed in Chapter 5. Before this, however, it is important to discuss the problem of non-uniqueness of parameters which occurs due to the parametric nature of the Johnson-Cook model.

The flow stress as a function of the state variables strain, strain rate and temperature, only in the domain of state variables reached during the machining process is relevant for machining simulations. It will be shown in this chapter, that there can be multiple sets of Johnson-Cook parameters which can predict the flow stress, within a given tolerance, in this domain equally well. Since all the parameter sets give rise to similar flow stress curves in the domain of machining, the chip shapes and the cutting forces are also similar. A robust parameter set should predict the correct chip shapes and cutting forces over a wide range of cutting conditions. Therefore, to distinguish parameter sets which are valid in a small domain, the cutting conditions should be strongly varied.

4.1 Analysis of the Johnson-Cook model

From the Johnson-Cook model (Equation 2.12) it can be seen that the stress increases with increasing strain and strain rate and decreases with

increasing temperature. The isothermal stress-strain curves for AISI 52100, 62 HRC steel have been plotted in Figures 4.1 and 4.2 to show this behaviour. The material parameters for the AISI 52100, 62 HRC steel are listed in Tables 2.3 and 2.4.
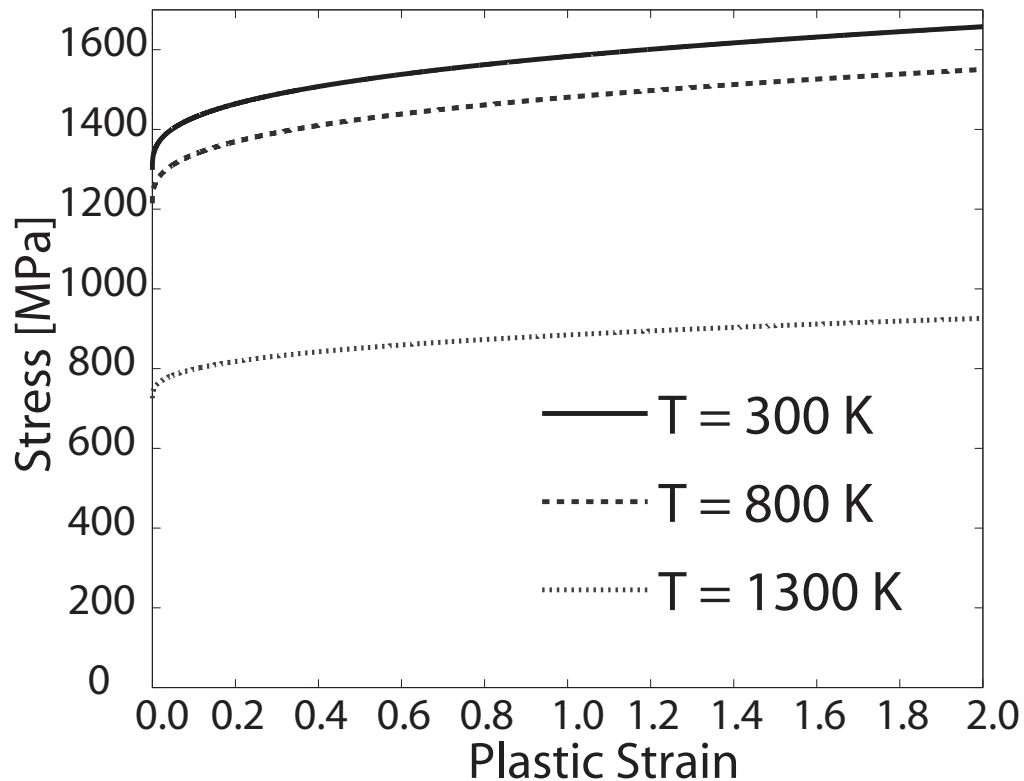
Figure 4.1: Isothermal stress strain curves for AISI 52100, 62 HRC steel drawn at a strain rate of 10^6 s^{-1} at different temperatures.

The adiabatic and isothermal stress-strain curves (described in Section 3.3) can be used to understand the material behaviour during the machining process. The adiabatic stress-strain curve describes the material behaviour at an infinitely high cutting speed and the isothermal stress-strain curve describes the material behaviour at an infinitely low cutting speed. At intermediate cutting speeds, the material behaviour is in between these two extremes, which are unachievable in realistic cases. However, the adiabatic stress-strain curve can be used to approximate the material behaviour at high cutting speeds, and at low cutting speeds, the isothermal stress-strain curve can be used to approximate the material behaviour.

The stress-strain curves can be used to understand the chip shape and the cutting force in a chip formation process. For a frictionless orthogonal cutting process with homogeneous deformation in the chip,
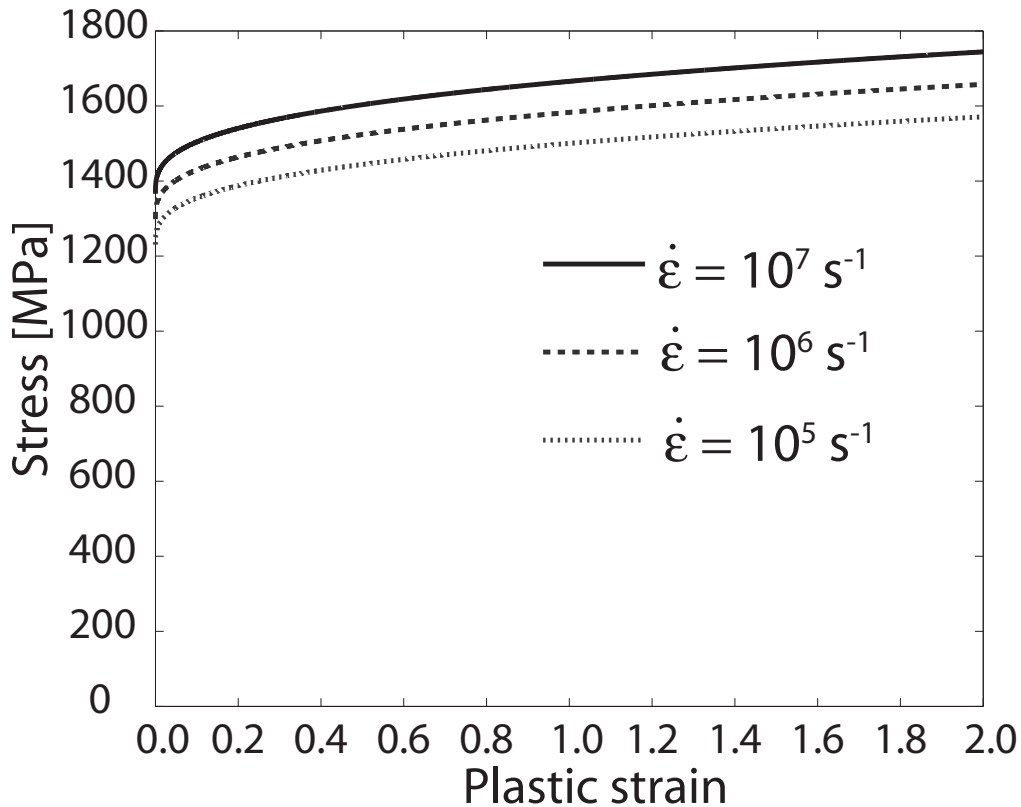
Figure 4.2: Isothermal stress strain curves for AISI 52100, 62 HRC steel drawn at a temperature of 300 K and at different strain rates.

the energy input from the cutting force results in the deformation in the material. If the length of cut is d_c, the width of cut is w_c and the depth of cut is t_c, then the energy balance is given by

$$d_c \cdot w_c \cdot t_c \int \sigma \, \mathrm{d}\varepsilon = F_c \cdot d_c \tag{4.1}$$

$$\Longrightarrow \int \sigma \, \mathrm{d}\varepsilon = \frac{F_c}{w_c \cdot t_c} \, . \tag{4.2}$$

Hence the cutting force is related to the area under the stress strain curve.

The shape of the stress-strain curve gives information about the chip shape as the shear angle is related to the material hardening. Oxley & Welsh (1963) showed from experiments that the shear angle is related to the ratio of the strain hardening to the flow stress ($\frac{d\sigma}{d\varepsilon}/\sigma$; to be referred as relative hardening). Out of two materials, the one with the larger relative hardening would form chips with a smaller shear angle, leading to the formation of thicker chips.

Since the shape of the stress-strain curve and the area under it are linked with the chip shape and the cutting force, if multiple parameter sets can give rise to similar stress-strain curves in the domain of machining, then the chip shapes and the cutting forces should also be similar. If such non-unique parameter sets exist, then the effect on the flow curve by changing one parameter should be counteracted by changing other parameters. Before conducting a search for non-unique parameter sets, by looking at the effect of variation of parameters on the isothermal and the adiabatic stress-strain curves, it can be checked if this would be feasible or not.

At a fixed strain rate and temperature, the effect of the variation of free parameters can be observed on isothermal curves (Figure 4.3). On varying the parameter A, the isothermal stress-strain curves can move up or down (*i.e.* the average stress level can be changed), without affecting the slope of the curves. The slope of the curve is independent of the parameter A as given by

$$
\begin{aligned}
\frac{\partial \sigma}{\partial \varepsilon} = &\ \left(nB\varepsilon^{(n-1)} \right) \left[1 + C \ln \left(\frac{\dot{\varepsilon}}{\dot{\varepsilon}_0} \right) \right] \\
&\ \left[1 - \left(\frac{T - T_{room}}{T_{melt} - T_{room}} \right)^m \right].
\end{aligned}
\tag{4.3}
$$

The variations of parameters C and m also cause the curves to move up or down, although there can be changes in the slope of the curves depending on the strain rate and the temperature. For certain combinations, the increase in strength due to strain rate increase can be compensated through thermal softening. Parameters B and n seem to affect the slope of the curve the most. It can be seen from Figure 4.4 that a lower value of parameter m causes a greater amount of thermal softening.

However, during high speed machining the material behaviour can be approximated by the adiabatic stress-strain curves. The temperature of the material continually increases during this process. The adiabatic stress-strain curves have been plotted after varying the free parameters (Figure 4.5). The curves show a roughly similar behaviour when compared with their isothermal counterparts, except the one for the parameter m. There is clearly a greater thermal softening in case of smaller m as the temperature increases during deformation.

From these illustrations, it is clear that the effect of change in one parameter on the stress strain curve can be compensated by a change in one or more parameters to recreate the original curve. For instance an increase in parameter A can be compensated by a decrease in B and correspondingly increasing n to get the original curve. Similarly, a

change in C or m can be compensated by changing A, B and n. Thus it can be anticipated that there exists a number of parameter sets which give rise to similar adiabatic or isothermal stress-strain curves, as the case may be. In Section 4.2, multiple parameter sets which give rise to similar adiabatic stress-strain curves are actually found out by an inverse identification process. It will also be shown that in the given domain of machining, all these parameter sets will give rise to similar chips and cutting forces.

4.2 Existence of non-uniqueness

At high cutting speeds, the material behaviour can be approximated using the adiabatic stress-strain curves. Since the chip shape and the cutting force are dependent on the adiabatic stress-strain curve, it is expected that similar adiabatic stress-strain curves should give rise to similar chips and cutting forces.

In order to test this hypothesis, the Levenberg-Marquardt algorithm (Press et $al.$ (1993)) is used to search for other sets of parameters that give rise to adiabatic stress-strain curves that are similar to that from the original parameter set given in Table 2.4. An error function defined using the norm error between a test curve and the standard curve is given by:

$$\chi^2 = ||\bar{\sigma}_{original} - \bar{\sigma}_{param}||^2 . \tag{4.4}$$

Here $\bar{\sigma}_{original}$ is a vector of points on the adiabatic stress-strain curve obtained using the standard Johnson-Cook parameters, $\bar{\sigma}_{param}$ is the vector of points on the adiabatic stress-strain curve obtained using the new Johnson-Cook parameters which are being searched and $|| \bullet ||$ is the Euclidean norm. The strain rate is kept at a constant value of 10^6 s^{-1} and consequently the parameter C is held constant: otherwise, an infinite number of combinations of A, B and C are possible which give rise to the same curve. The strains up to 2.0 were matched as this is a typical maximum strain value reached in a continuous chip when machining with a rake angle of 0°. Using this search method, seven distinct parameter sets (Table 4.1) are obtained which give rise to similar adiabatic stress-strain curves. The adiabatic stress-strain curves have been plotted in Figure 4.6.

Adiabatic finite element simulations are done using the different Johnson-Cook parameter sets. The cutting parameters are listed in Table 4.2. The chip shapes, von Mises stress and temperature distributions in the chip are found to be visually indistinguishable. An overlay of
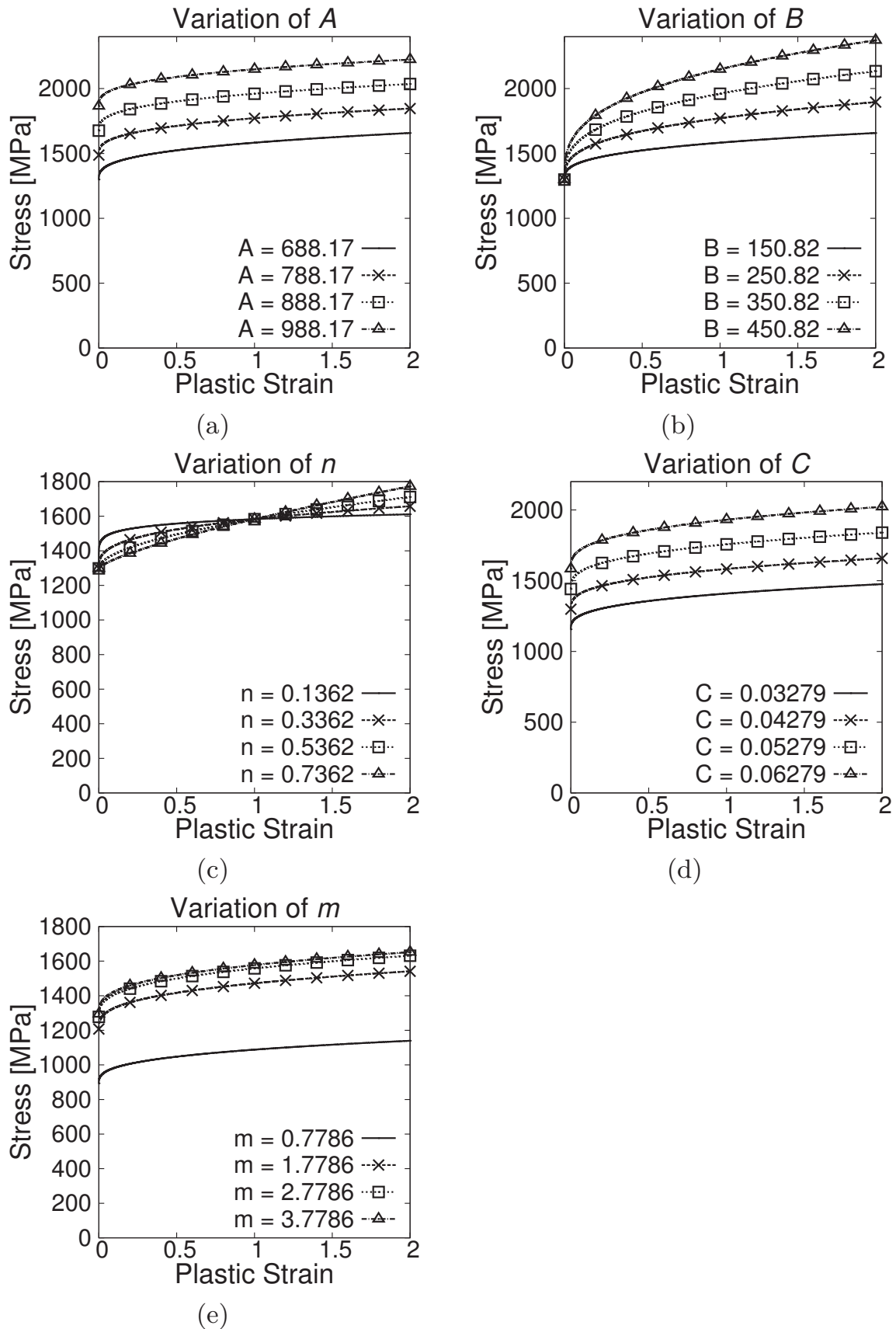
Figure 4.3: Effect of variation of free parameters on the isothermal curve. All the isothermal curves are drawn at a temperature of 300 K, except for Figure 4.3e, which is drawn at a temperature of 600 K.
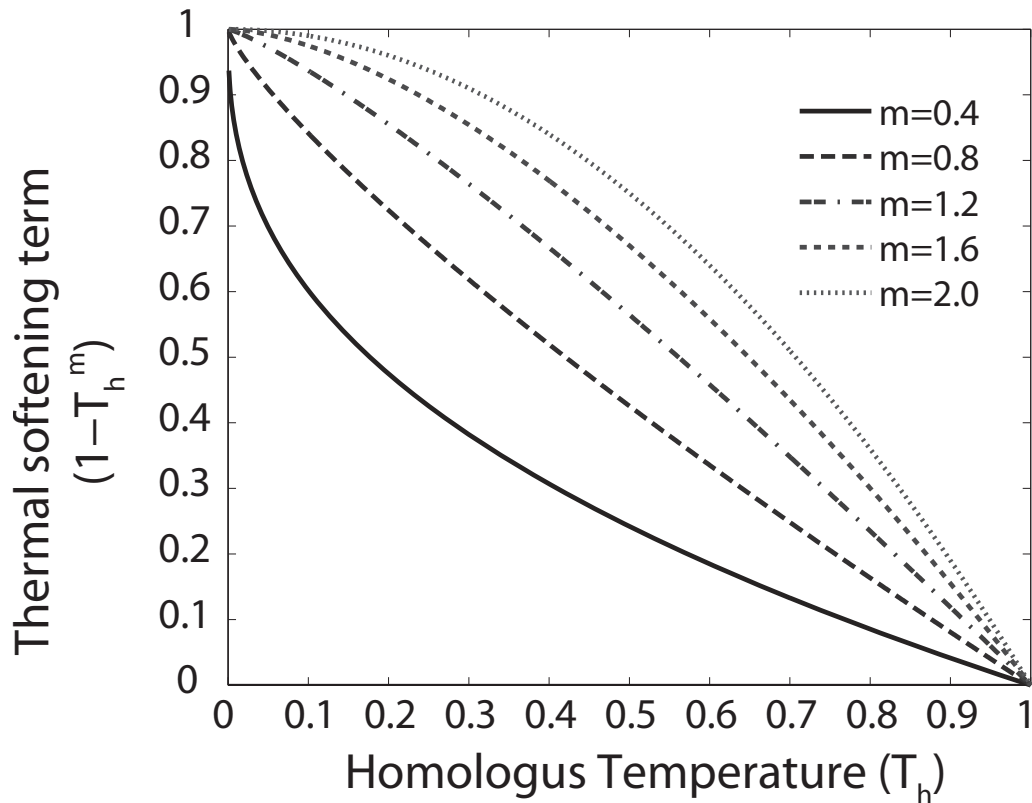
Figure 4.4: Thermal softening evolution for different m values

	A [MPa]	B [MPa]	n	C	m
AISI 52100, 62 HRC	688.170	150.820	0.3362	0.0428	2.7786
Set 1	400.000	431.848	0.0782	0.0428	3.3579
Set 2	739.277	100.000	0.5988	0.0428	2.6243
Set 3	716.538	128.716	0.5000	0.0428	2.4775
Set 4	487.095	344.833	0.1000	0.0428	3.3339
Set 5	667.168	168.196	0.2630	0.0428	3.0000
Set 6	726.486	130.220	0.6440	0.0428	2.1500
Set 7	553.150	273.579	0.1140	0.0428	4.0000

Table 4.1: Non-unique Johnson-Cook parameters used in simulation
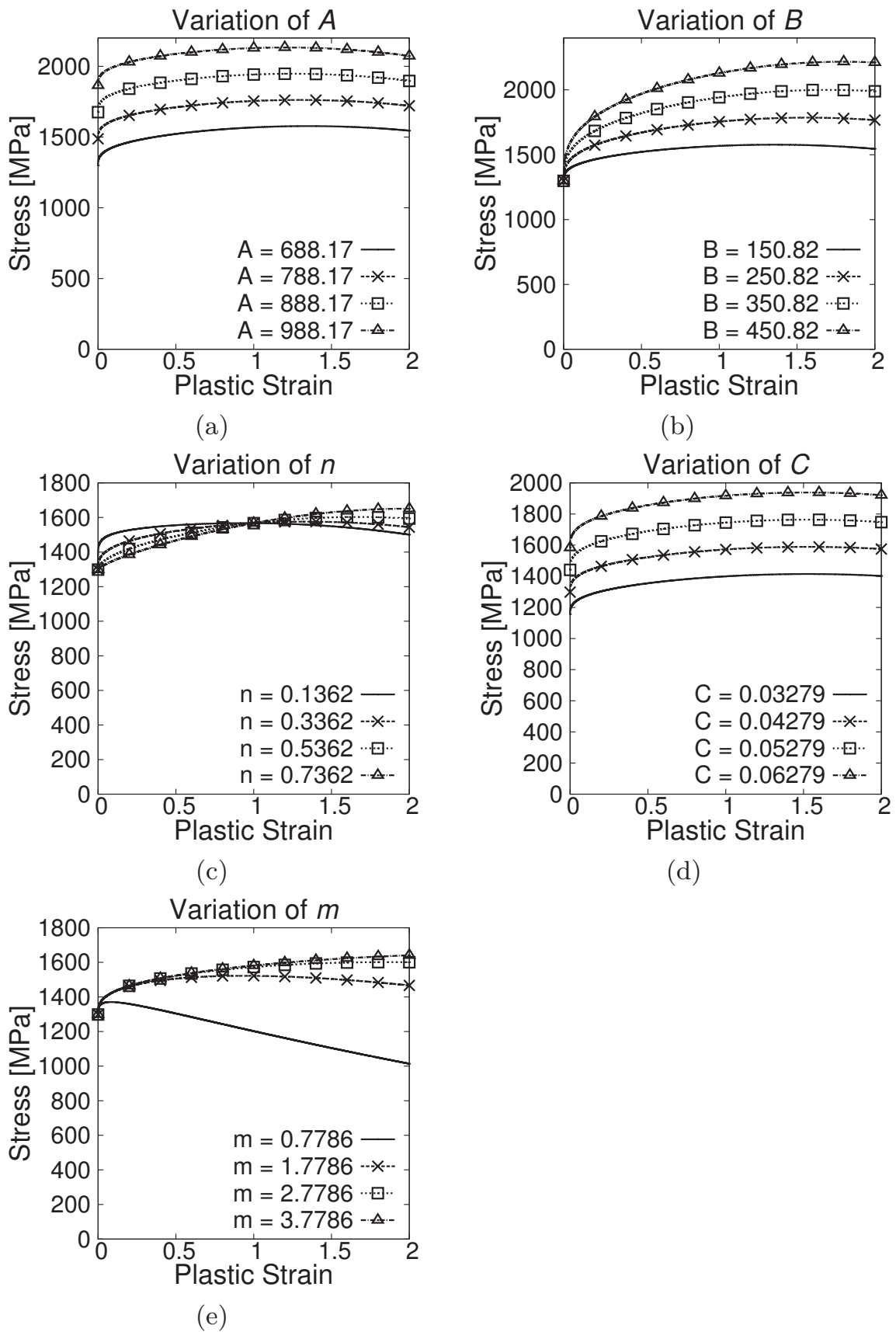
Figure 4.5: Effect of variation of free parameters on the adiabatic curve.
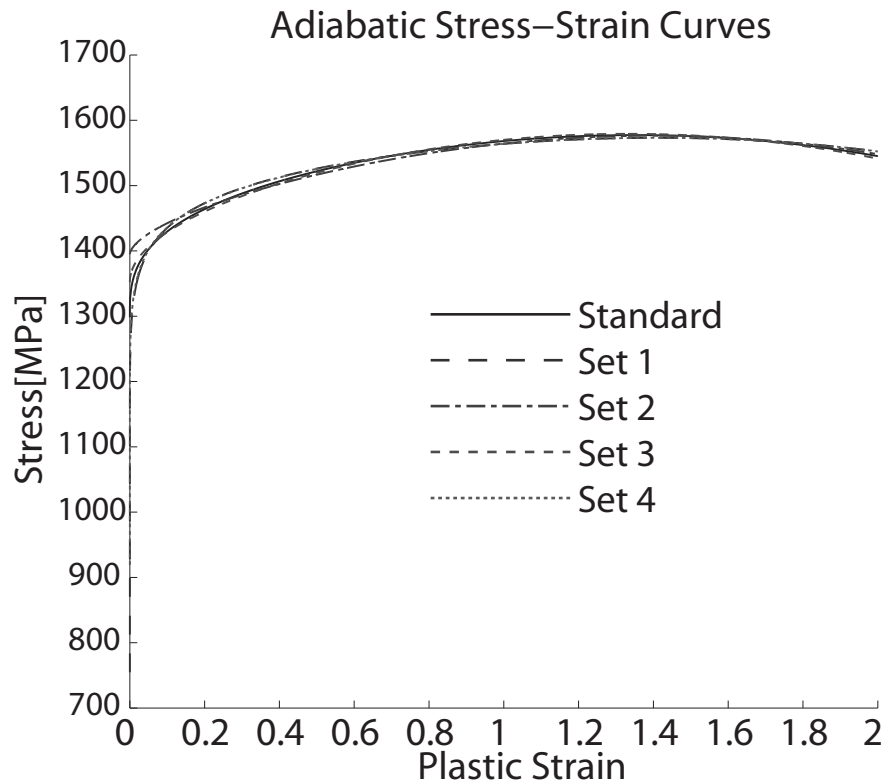
(a) An overlay of adiabatic stress-strain curves of the standard set and the material parameter sets 1 to 4.
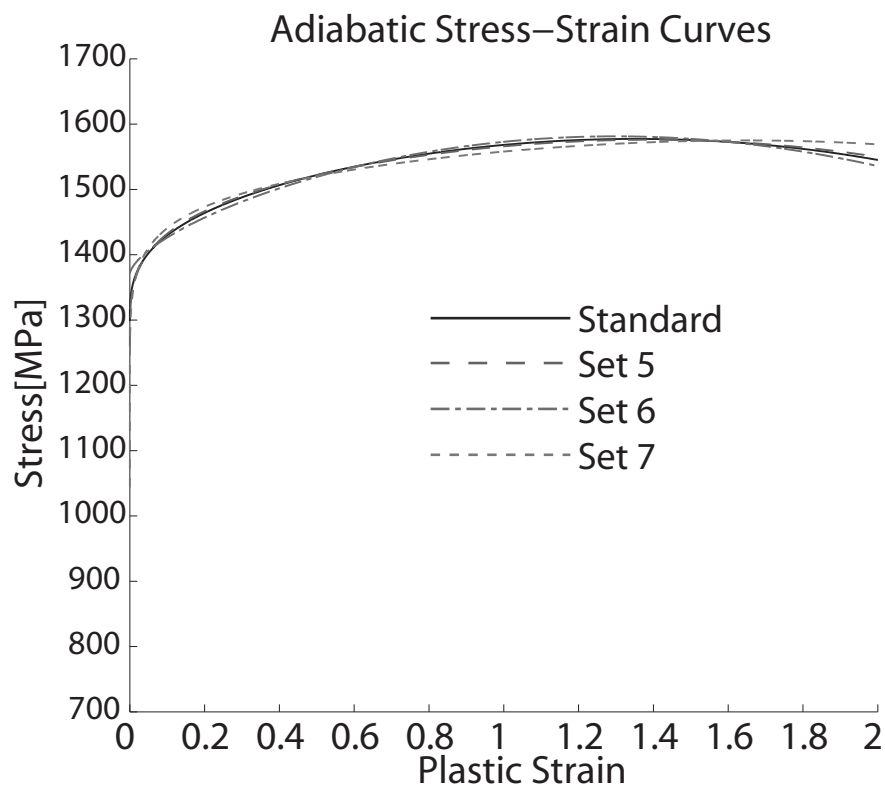
(b) An overlay of adiabatic stress-strain curves of the standard set and the material parameter sets 5 to 7.

Figure 4.6: Different parameter sets leading to similar adiabatic stress-strain curves.

Cutting Speed $[\mathrm{m\,s^{-1}}]$	33.3
Uncut chip thickness [µm]	200
Co-efficient of friction	0
Equivalent plastic strain at failure ($\bar{\varepsilon}_f^{pl}$)	1.0
Mesh element type for Workpiece	CPE4R
Mesh element type for Tool	R2D2
Workpiece mesh size	5µm × 5µm

Table 4.2: Cutting and simulation parameters used in the chip formation simulation of AISI 52100, 62 HRC.

the chip shapes has been shown in Figure 4.7 and the corresponding normalised non-overlap areas in Table 4.3. The normalised non-overlap area values are less than 3% and the match is considered very good.
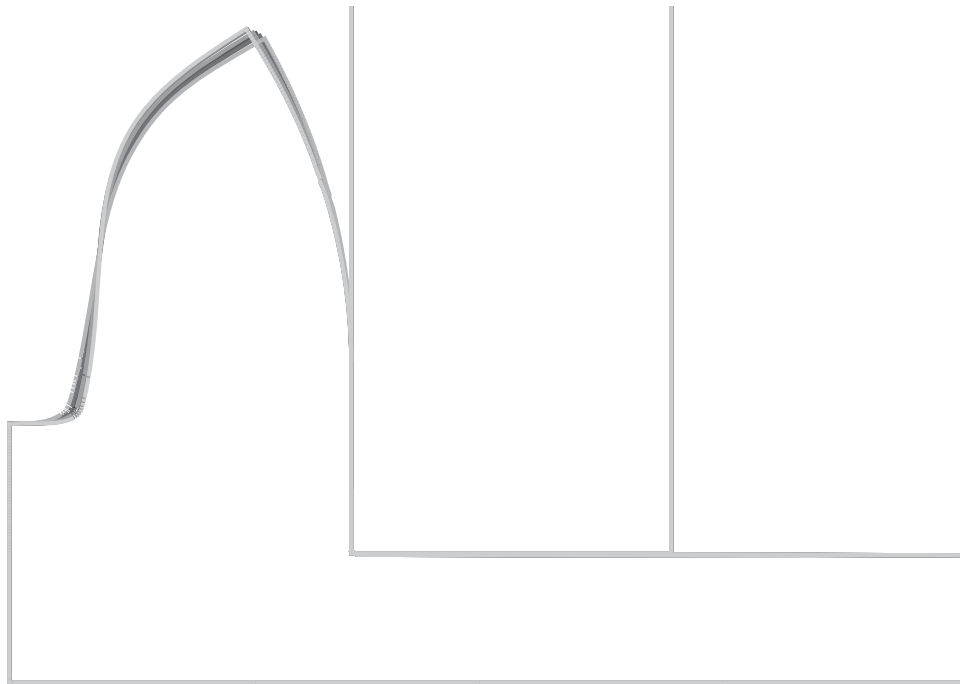
Figure 4.7: Overlay of chip shapes from adiabatic simulations using different Johnson-Cook parameter sets

The von Mises stress distribution for the standard chip and the chips from sets 1 and 4 have been shown in Figure 4.8 for comparison. Similarly the temperature distribution for the standard chip and the chips from sets 2 and 6 have been shown in Figure 4.9. An overlay of the cutting forces, which have been smoothed using the five-point

	$\Delta A_C\%$
Set 1	2.31
Set 2	0.28
Set 3	1.22
Set 4	2.31
Set 5	0.78
Set 6	2.54
Set 7	2.80

Table 4.3: Normalised non-overlap areas for chips shown in Figure 4.7, obtained from adiabatic simulations.

moving average method, has been shown in Figure 4.10. The cutting force evolution had to be smoothed since there is noise due to elastic waves propagating in the workpiece. The unsmoothed cutting force evolution for the standard parameter set is shown in Figure 4.11. The mean cutting force of simulations 1 to 7 is found to be within 5% of the mean cutting force of the standard simulation, which is within the numerical error caused due to the elastic waves in the model.

These results show that in a given domain, a number of completely different parameter sets can be used to represent the same adiabatic stress-strain curves which will give similar chip shapes and cutting forces. It is however possible that these material parameters were optimised over a small domain: the chip shapes and the cutting forces would be well predicted for a narrow range of cutting conditions, but the prediction would become poor when the cutting conditions are changed. In order to ensure that a parameter set is valid over a large domain, the material parameters should be optimised for strongly varying cutting conditions. In Section 4.4, ways to distinguish the parameter sets in Table 4.1 will be shown.

It can be seen from Figure 4.12 that at low strains there are significant differences in the adiabatic stress-strain curves drawn from the non-unique parameter sets. Similarly, the isothermal stress-strain curves at large strains have significant differences (Figure 4.13). If different parts of the domain can be explored by changing the cutting conditions, the non-unique parameter sets can be distinguished (see Section 4.4). The problem of non-uniqueness is studied systematically in the next section which will help in formulating strategies for distinguishing different parameter sets.
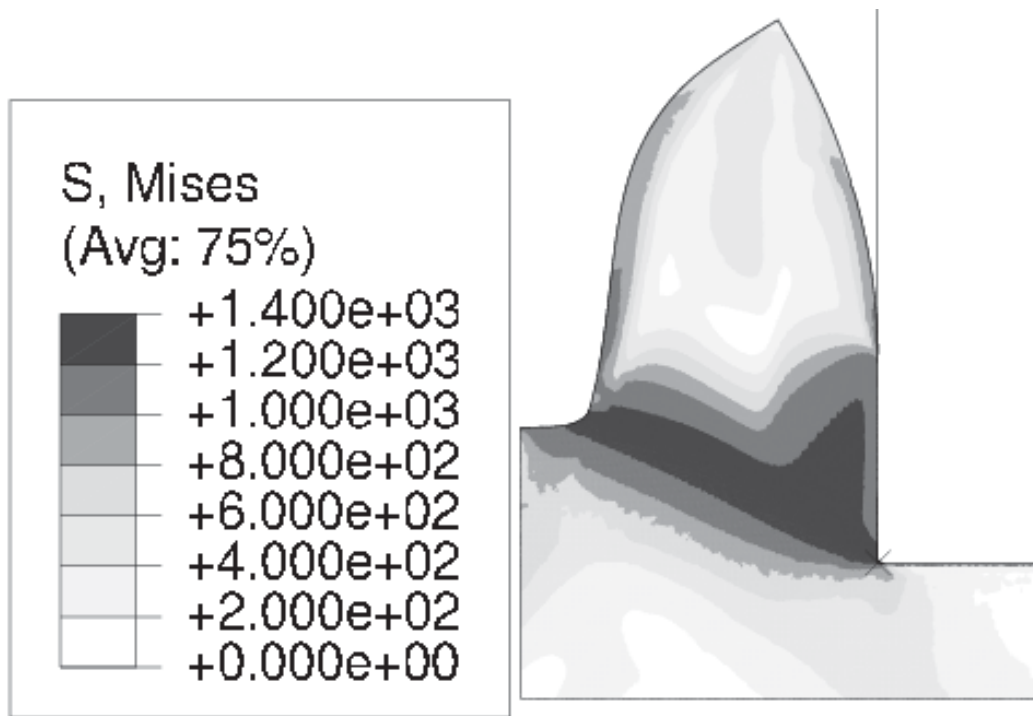
(a) Standard simulation
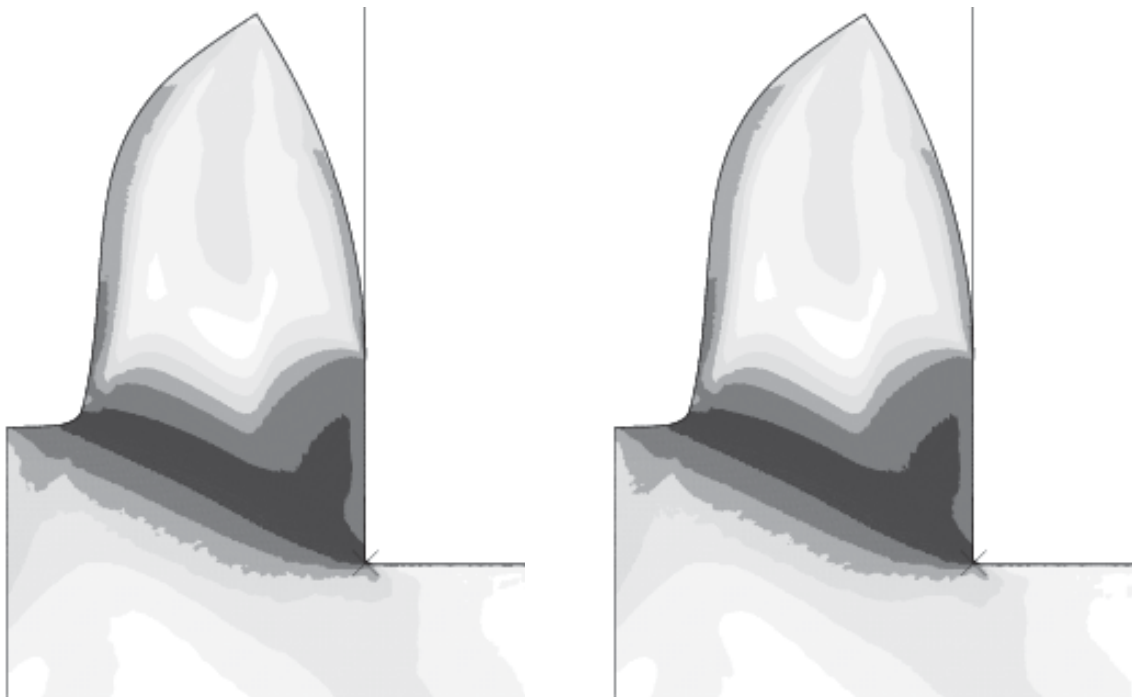
(b) Simulation with Set 1

(c) Simulation with Set 4

Figure 4.8: von Mises stress distributions in chips are indistinguishable
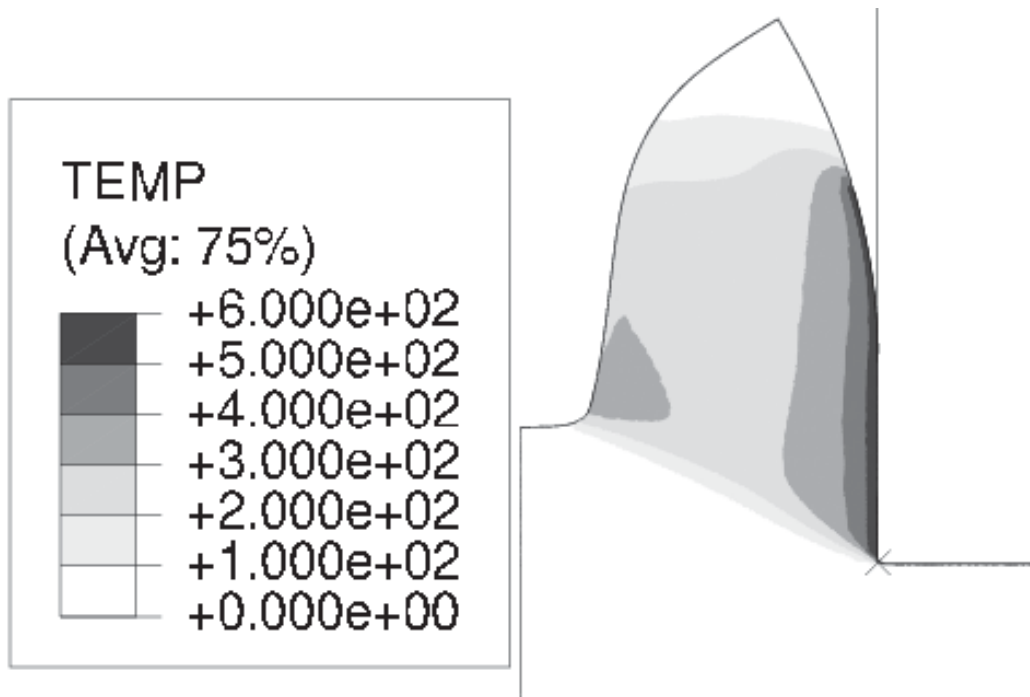
(a) Standard simulation
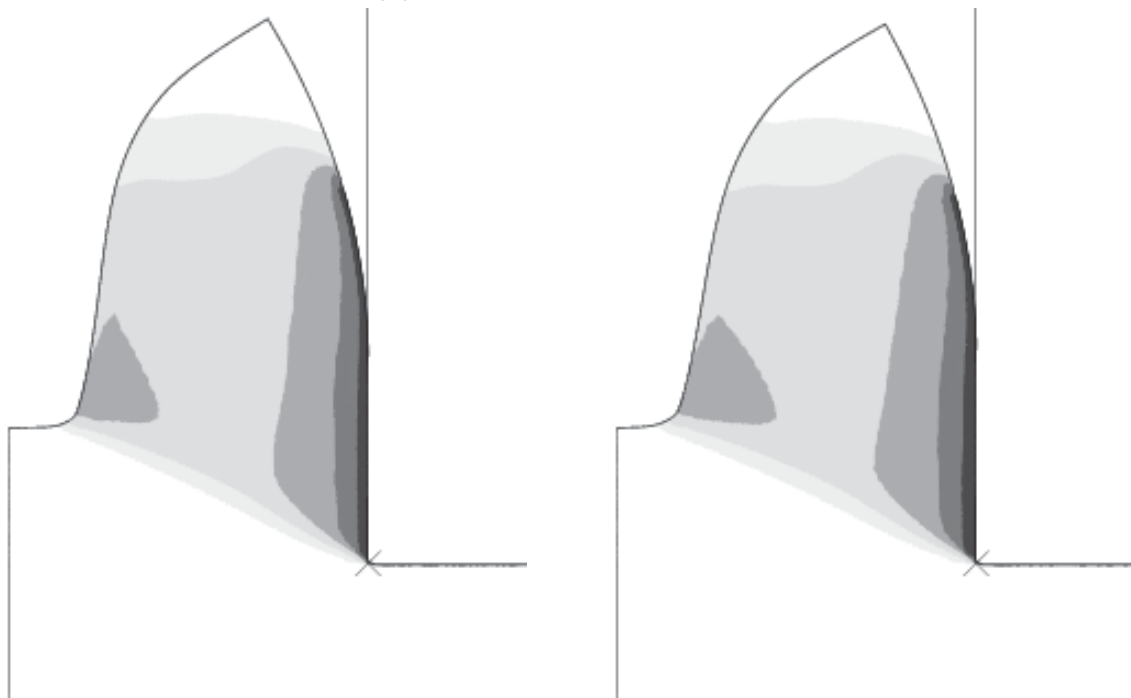
(b) Simulation with Set 2

(c) Simulation with Set 6

Figure 4.9: Temperature distributions (in degree Celsius) in chips are indistinguishable.
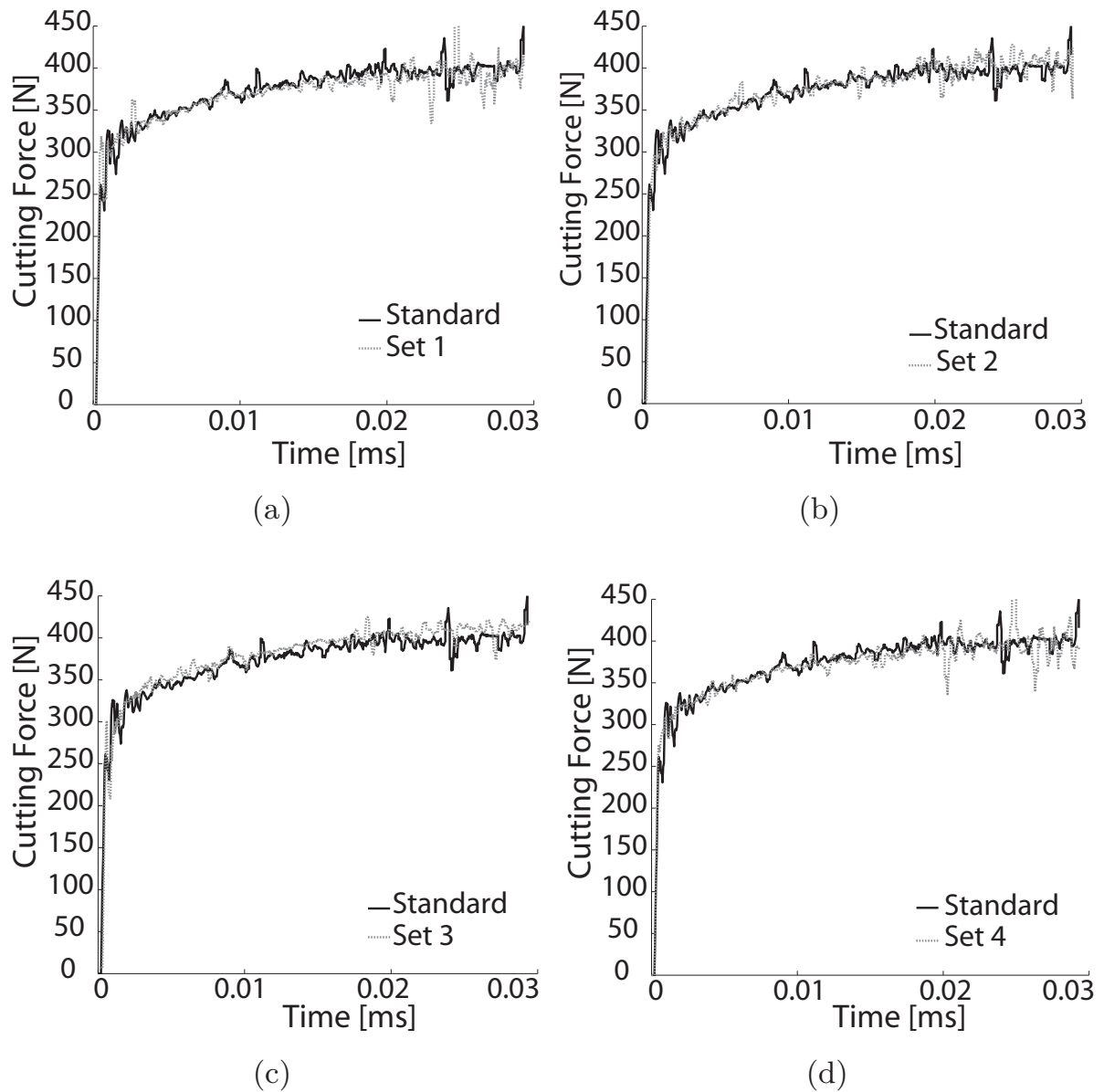
Figure 4.10: A comparison of cutting force evolution (smoothed using the five-point moving average) from adiabatic simulations using different Johnson-Cook parameter sets

(e)

(f)

(g)
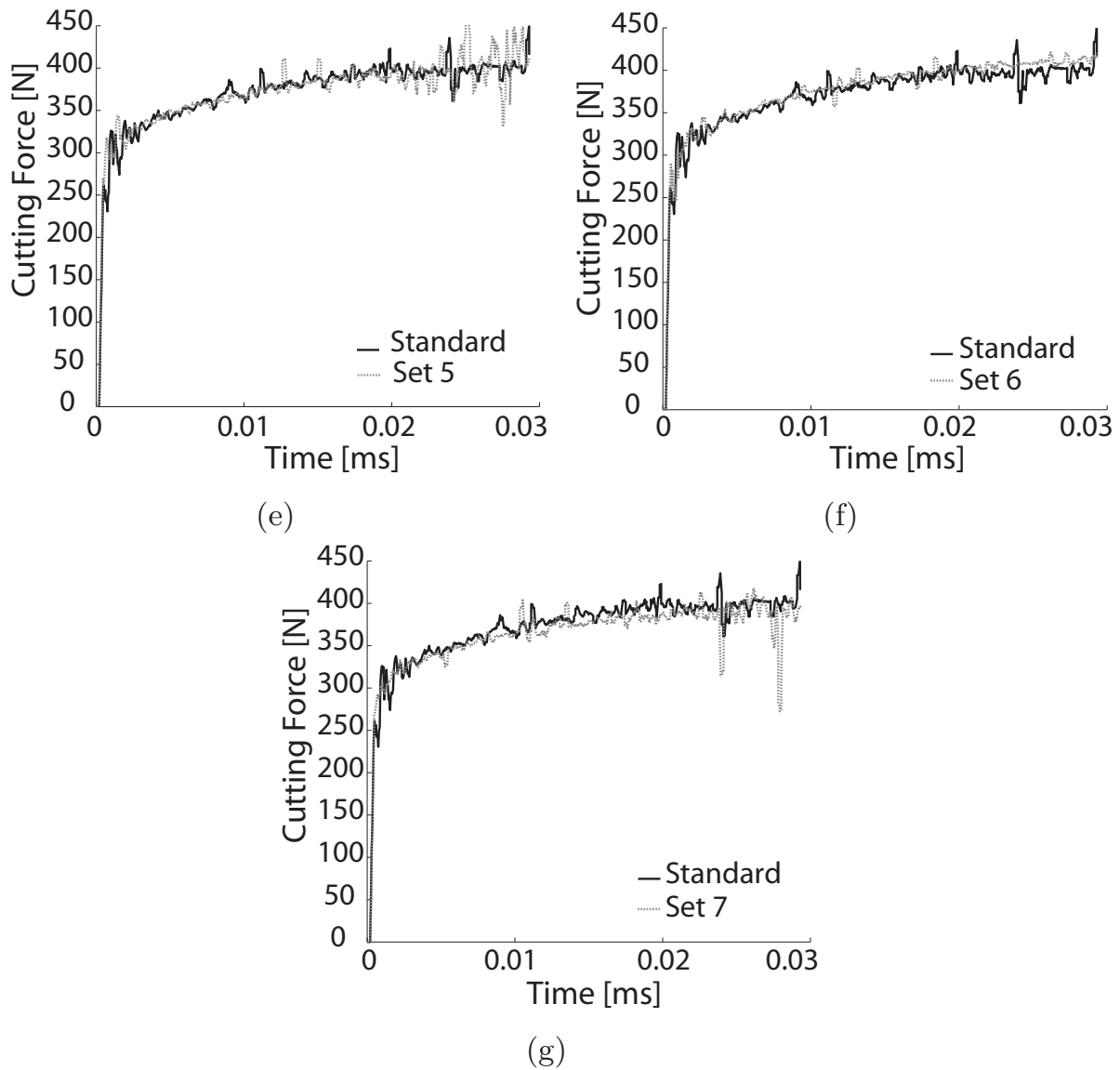
Figure 4.10: A comparison of cutting force evolution (smoothed using the five-point moving average) from adiabatic simulations using different Johnson-Cook parameter sets
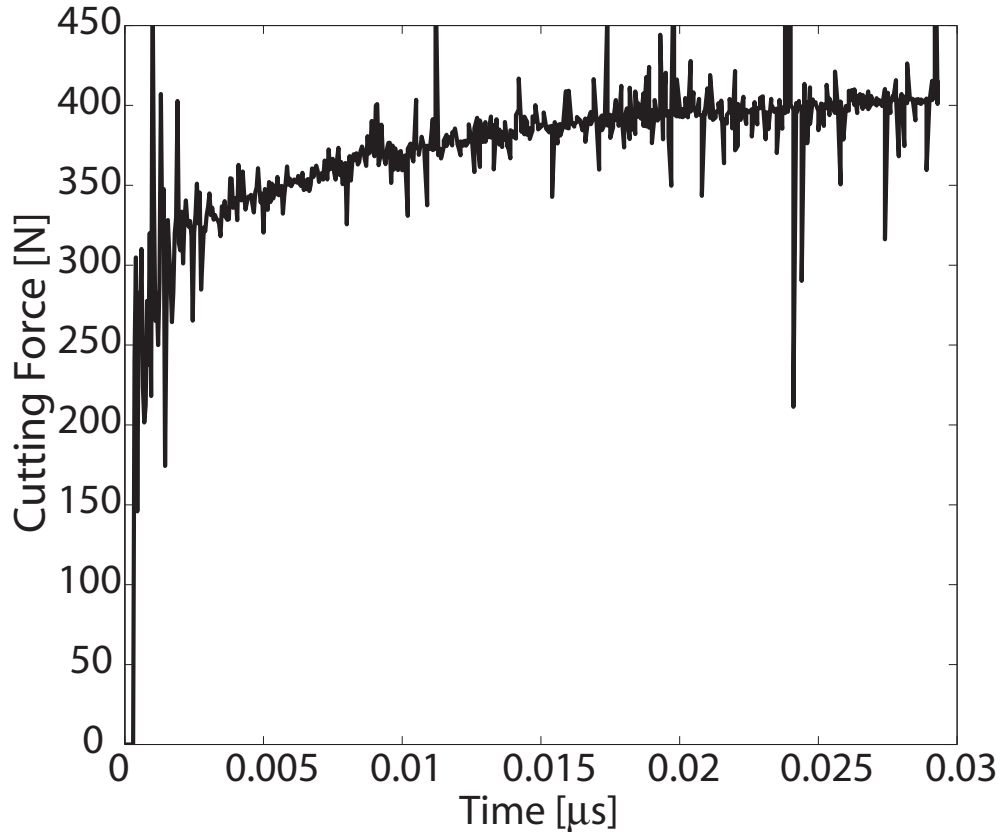
Figure 4.11: Unsmoothed cutting force evolution for adiabatic simulation using the standard Johnson-Cook parameter set given in Table 4.1.

4.3 Study of non-uniqueness

In this section, it is shown that if parameter sets can be found which give rise to stress-strain curves that are within a given tolerance to the standard curve, similar chips and cutting forces are formed. In order to do so, the Johnson-Cook parameter space (A, B, n) is systematically explored and parameter sets are found which can give rise to stress-strain curves within a given tolerance to the standard curve. This helps in estimating the amount of non-uniqueness and also for formulating the strategies to choose the cutting conditions for distinguishing parameter sets. This is a numerical study and the material parameters which have been used for this study are that of a steel (see Tables 4.4 and 4.5).

In order to compare if two curves are similar or not, the norm error per data point is calculated using the formula:

$$\mathcal{E} = \frac{||\bar{\sigma}(A_t, B_t, n_t) - \bar{\sigma}(A_s, B_s, n_s)||}{N} \ . \tag{4.5}$$

(a) An overlay of   standard
set and the mate

(b) An overlay of adiabatic stress-strain curves (at low strains) of the standard
set and the material parameter sets 5 to 7.

Figure 4.12: Differences at low strains in the adiabatic stress-strain
curves
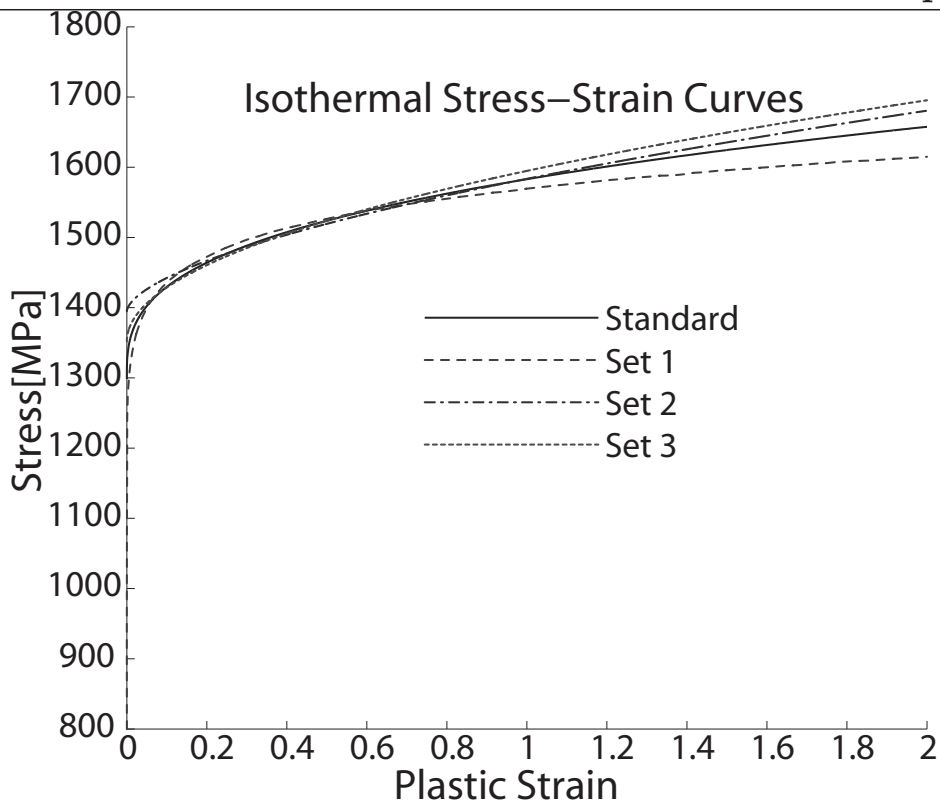
(a) An overlay of isothermal stress-strain curves of the standard set and the material parameter sets 1 to 3.
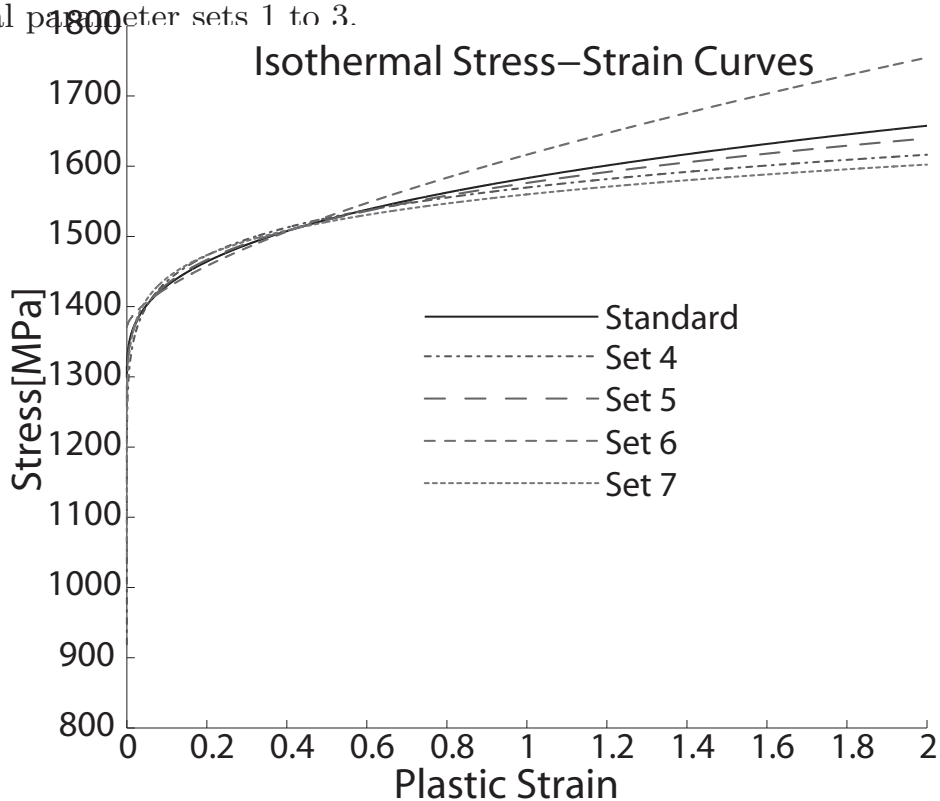
(b) An overlay of isothermal stress-strain curves of the standard set and the material parameter sets 4 to 7.

Figure 4.13: Even though the adiabatic stress-strain curves are similar, the isothermal stress-strain curves for the same parameter sets are different.

Density [$\mathrm{kg\,m^{-3}}$]	7860
Young's Modulus [GPa]	205
Poisson's Ratio	0.28
Specific Heat Capacity [$\mathrm{J\,kg^{-1}\,K^{-1}}$]	600
Coefficient of thermal expansion [$\mathrm{K^{-1}}$]	13.5×10^{-6}
Thermal Conductivity[$\mathrm{W\,m^{-1}\,K^{-1}}$]	46.6
Element failure criterion:	
Equivalent plastic strain at failure ($\bar{\varepsilon}_f^{pl}$)	2.0

Table 4.4: Material properties

A [MPa]	B [MPa]	n	C	m	T_{melt} [K]	T_{room} [K]
250	250	0.3	0	0.7	1500	300

Table 4.5: Johnson-Cook parameters

Here the subscript s is used for the standard parameters, the subscript t is used for the search parameters and $\bar{\sigma}$ is the vector of points on the stress-strain curve. N denotes the total number of data points in the curve and $||\bullet||$ denotes the Euclidean norm. Equation 4.4 is normalised by the total number of data points to give Equation 4.5. This way two curves which have been calculated for different maximum chip strains can also be compared. The set of points having the same $\mathcal{E}$ must result in stress-strain curves which are equally distant from the standard curve. For a sufficiently small $\mathcal{E}$, the chip shapes and cutting forces must be similar to those of the standard simulation.

The standard Johnson-Cook parameters (A_s, B_s, n_s) are taken from Table 4.5. The adiabatic and the isothermal curves are calculated up to a maximum strain of 2.0 and a Taylor-Quinney coefficient of 0.9 is used to calculate the adiabatic curve. The search parameters are varied (limits of variation are given in Table 4.6; each parameter is varied within the limits in 81 steps) and the norm error per data point ($\mathcal{E}$) is calculated for each set.

Error isosurfaces are drawn for adiabatic and isothermal curves for the $\mathcal{E}$ value of 0.1 MPa (Figure 4.14). The error isosurfaces are slightly bent (banana shaped) and the isothermal error isosurface is contained completely inside the adiabatic isosurface. Within the isosurface, an infinite number of parameter sets are there as the parameters are real numbers. Since the volume within the isosurface is discretised in this

Parameter	Minimum	Maximum
A_t [MPa]	150	350
B_t [MPa]	150	350
n_t	0.2	0.4

Table 4.6: Limits of variation of the Johnson-Cook parameters

analysis, it is possible to count the number of parameter sets[1]. Out of a total of 81^3 possible parameter sets 4316 parameter sets are within the adiabatic isosurface and 2610 are within the isothermal isosurface.

The size of the adiabatic isosurface can be changed by changing the Taylor-Quinney coefficient. If the Taylor-Quinney coefficient is 0 then the isothermal and the adiabatic surfaces are coincident. For a maximum possible value of 1.0, the size of the adiabatic error surface would be the largest. A surface with a smaller Taylor-Quinney coefficient is completely contained inside another surface with a greater Taylor-Quinney coefficient value. All this indicates that there is more non-uniqueness in the adiabatic case than in the isothermal case.

Five parameter sets each were chosen from the two isosurfaces. The parameters chosen from the isothermal isosurface are listed in Table 4.7 and are used for non-adiabatic simulations. The parameters from the adiabatic isosurface are listed in Table 4.8 and are used for adiabatic simulations.

	A [MPa]	B [MPa]	n	$\mathcal{E}_{adia}$ [MPa]
Standard Set	250	250	0.3	
Set 1 (adia)	150	350	0.2	0.0965
Set 2 (adia)	225	277	0.29	0.0898
Set 3 (adia)	292.5	202.5	0.3775	0.0868
Set 4 (adia)	307.5	192.5	0.4	0.0958
Set 5 (adia)	230	270	0.2775	0.0293

Table 4.7: Johnson-Cook parameter sets for adiabatic simulations

---

[1]The volume of the isosurface can calculated by multiplying the number of parameter sets to the volume of each discrete cell *i.e.* $V_P = N_P \frac{200}{81} \frac{200}{81} \frac{0.2}{81}$ MPa^2. Here V_P is the volume of the isosurface and N_P is the number of parameter sets inside the isosurface
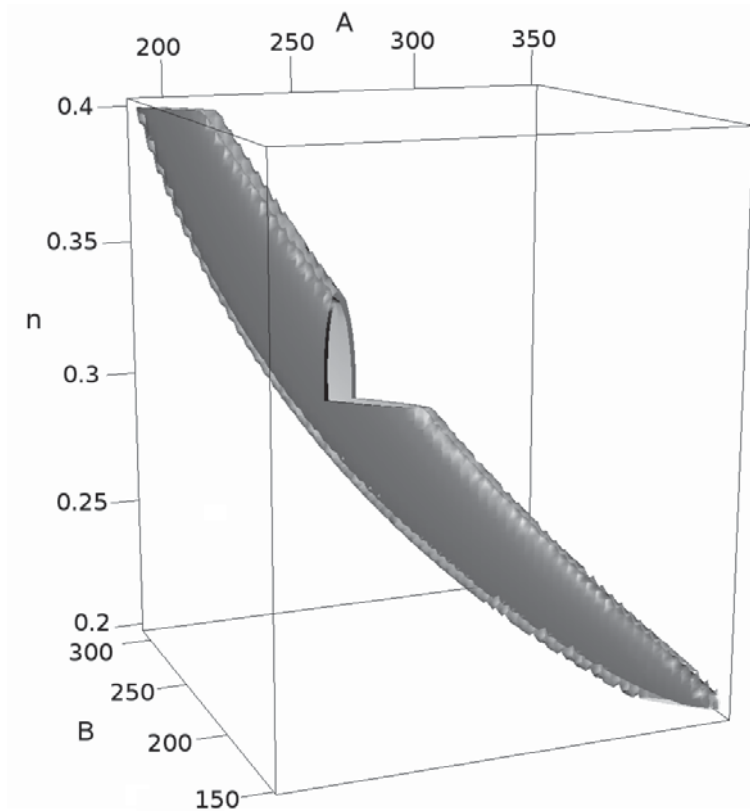
(a) The adiabatic and non-adiabatic error isosurfaces where norm error per data point is 0.1 MPa calculated using a strain value of 2. A section has been clipped to show the two isosurfaces. Parameters A and B are expressed in MPa.
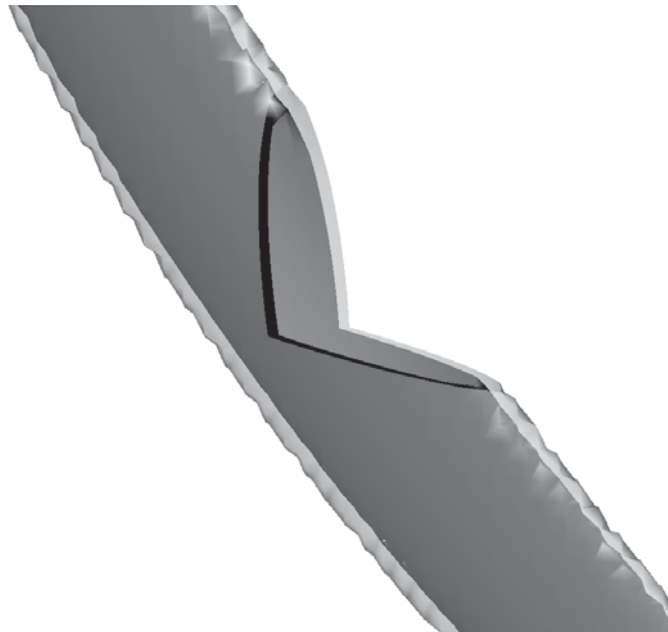
(b) Zoom near the clipped isosurfaces. The inner surface is the isothermal isosurface

Figure 4.14: Error Isosurfaces

	A [MPa]	B [MPa]	n	$\mathcal{E}_{iso}$ [MPa]
Standard Set	250	250	0.3	
Set 1 (iso)	152.5	350	0.2	0.0974
Set 2 (iso)	232.5	267.5	0.2775	0.0232
Set 3 (iso)	272.5	225	0.34	0.0509
Set 4 (iso)	307.5	190	0.4	0.0979
Set 5 (iso)	152.5	350	0.205	0.0997

Table 4.8: Johnson-Cook parameter sets for isothermal simulations

Adiabatic simulations conducted using the parameters listed in Table 4.7 lead to the formation of similar chips and cutting forces. An overlay of the chip shapes obtained from adiabatic simulations is shown in Figure 4.15. The normalised non-overlap areas are listed in Table 4.9 along with the cutting force difference percentages. For sets 3, 4 and 5, the chip shape match is extremely good ($\Delta A_C\%$ is within 3%) and the chips are visually indistinguishable. Sets 1 and 2 form chips which can be distinguished on a closer look ($\Delta A_C\%$ is above 3% but within 5%). However, when chip shapes are compared between simulations and real machining experiments, a chip shape match within 5% would be acceptable. The cutting force evolution for the adiabatic case using the standard parameter set has been shown in Figure 4.16. The cutting force stabilises after about 0.04 ms, therefore only the average cutting forces compared in Table 4.9.

Similar observations can be made also from non-adiabatic simulations using the parameters listed in Table 4.8. The cutting force evolution for the non-adiabatic case using the standard parameter set has been shown in Figure 4.18 and the cutting force stabilises after 3.5 ms. The normalised non-overlap areas for sets 2, 3 and 4 are within 3% and the chips are visually indistinguishable (Table 4.10). For sets 1 and 5, the chips can be distinguished only on a closer inspection ($\Delta A_C\%$ is above 3% but within 5%). In all the cases the cutting force differences are within 2% (Table 4.10). The overlay of chip shapes obtained from non-adiabatic simulations is shown in Figure 4.17.

From these results, it can be inferred that all parameter sets resulting in adiabatic or isothermal curves which are within a limited tolerance to the standard curves will give rise to similar chip shapes and cutting forces. Within the respective isosurfaces, there can be an infinite number of such parameter sets. If an inverse analysis is done to identify the material
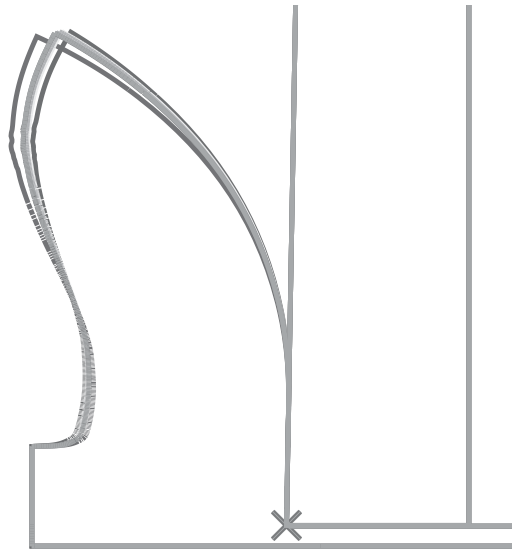
Figure 4.15: Overlay of chip shapes from adiabatic simulations (Johnson-Cook parameters are taken from Table 4.7).

	$\Delta A_C\%$	$\Delta F_C\%$
Set 1 (adia)	3.60	1.17
Set 2 (adia)	4.26	3.06
Set 3 (adia)	1.45	2.36
Set 4 (adia)	0.81	0.58
Set 5 (adia)	0.33	0.19

Table 4.9: Normalised non-overlap areas for chips shown in Figure 4.15 along with the cutting force difference percentage, obtained from adiabatic simulations.

	$\Delta A_C\%$	$\Delta F_C\%$
Set 1 (iso)	4.67	1.49
Set 2 (iso)	0.62	1.27
Set 3 (iso)	2.33	0.66
Set 4 (iso)	2.43	0.06
Set 5 (iso)	4.04	1.22

Table 4.10: Normalised non-overlap areas for chips shown in Figure 4.17 along with the cutting force difference percentage, obtained from non-adiabatic simulations.
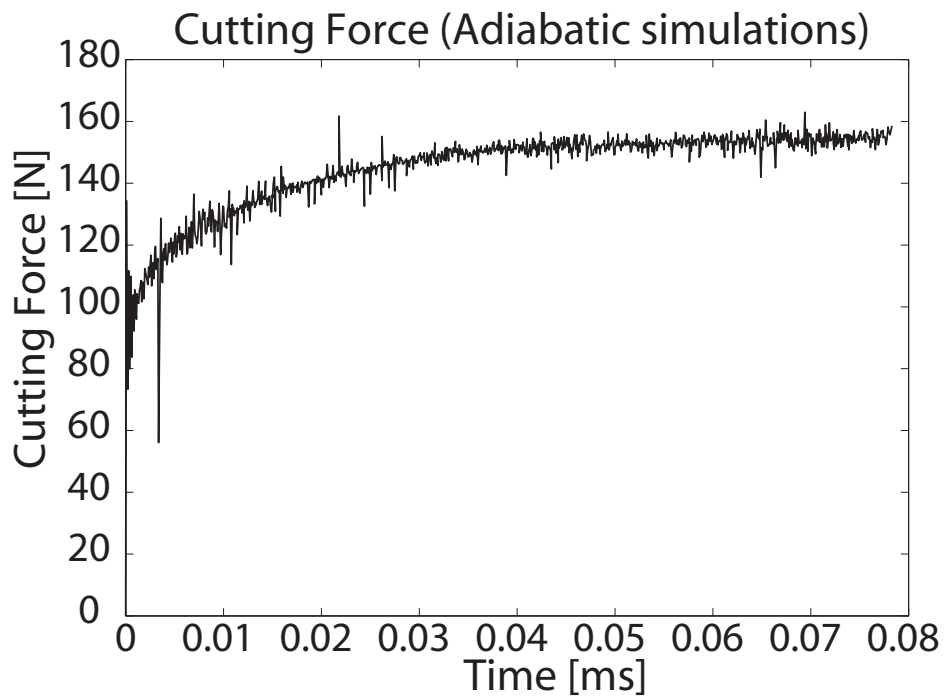
Figure 4.16: Cutting force evolution during adiabatic simulation using the standard Johnson-Cook parameter set given in Table 4.7.
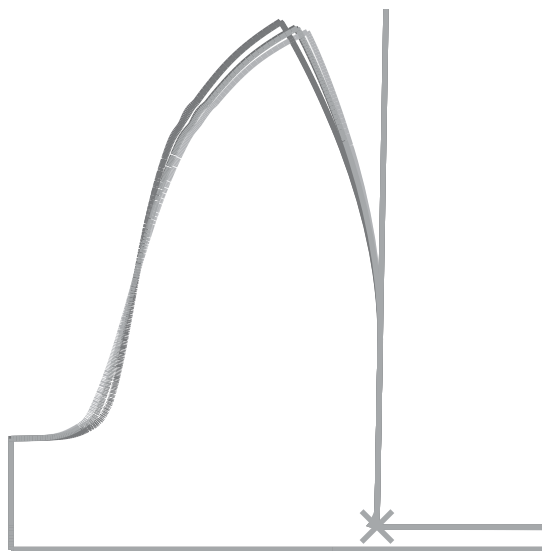
Figure 4.17: Overlay of chip shapes from non-adiabatic simulations (Johnson-Cook parameters are taken from Table 4.8).
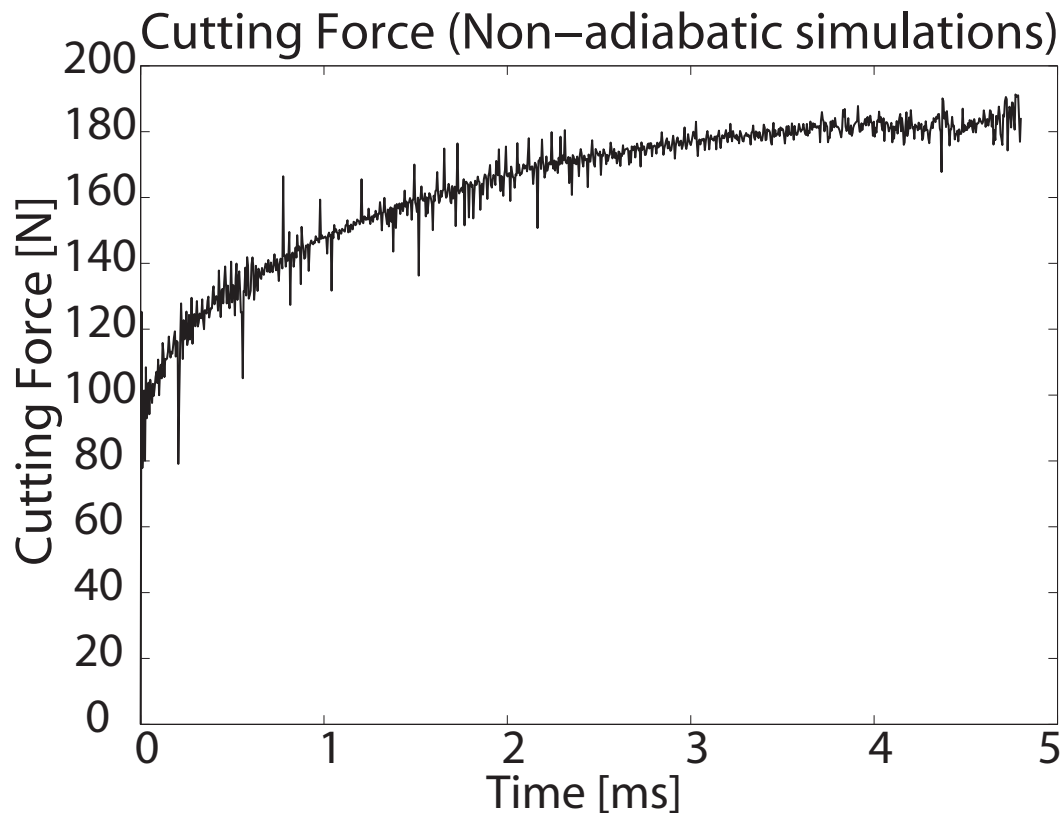
Figure 4.18: Cutting force evolution during non-adiabatic simulation using the standard Johnson-Cook parameter set given in Table 4.8.

parameters from real machining experiments, some variations are bound to occur in the measurement of experimental observables such as the chip shape and the cutting force. Multiple parameter sets will be found during an inverse identification process, so that the experimental result and the simulation results match within a given tolerance. However it must be ensured that the parameter sets which do not robustly describe the material behaviour over a large machining domain are eliminated. This can be done by conducting experiments over a wide range of cutting conditions. Since the isothermal error isosurface lies within the adiabatic isosurface, a smaller parameter set pool is expected in the non-adiabatic case. However, it is not always practical to conduct simulations only at non-adiabatic conditions: for instance, when the strain rate sensitivity parameter C of the Johnson-Cook model is to be identified, large variations of strain rate are needed, requiring higher cutting speeds and hence adiabatic simulations.

Another way of eliminating non-robust parameter sets is to explore the different parts of a stress-strain relation. This can be shown by drawing two different error isosurfaces with different strain values which

can be obtained by varying the rake angle. The parameter sets, which
are valid in both these domains, would then lie in the intersection of the
two isosurfaces. Isothermal isosurfaces have been drawn with maximum
chip strain values of 2 and 3 (Figure 4.19) and the intersecting region is
shown in Figure 4.20. The isothermal isosurface drawn with strain value
of 2 contains 2610 parameter sets and the isothermal isosurface drawn
with strain value of 3 contains 3785 parameter sets. The intersection of
the two isosurfaces contains 2111 parameter sets.
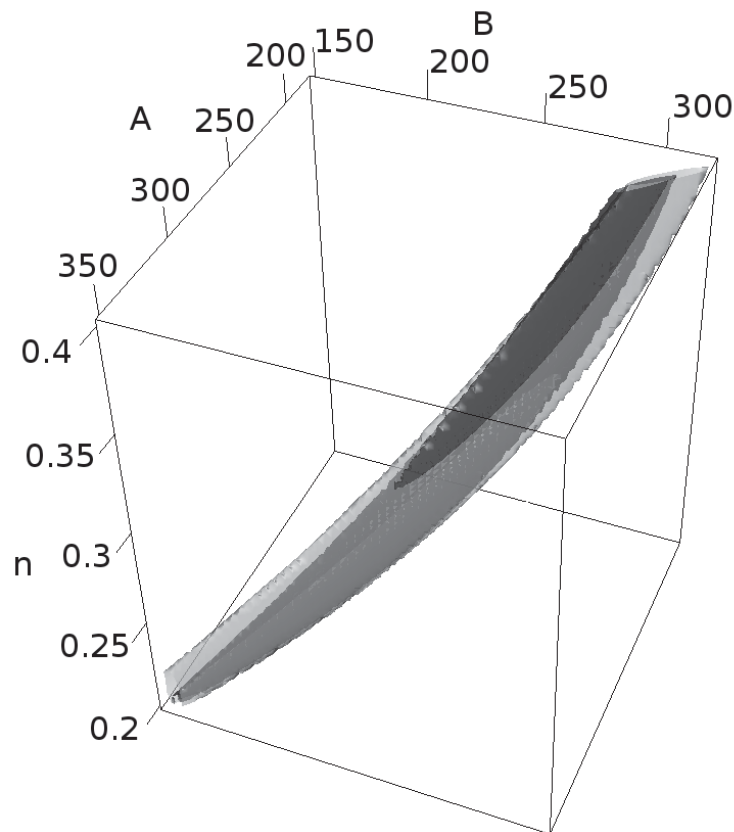
Figure 4.19: Error isosurfaces drawn with maximum chip strain values of
2 and 3. The isosurface with the darker shade corresponds to a maximum
chip strain of 2. Parameters A and B are expressed in MPa.

4.4   Differentiating similar parameter sets

In Section 4.2, it was observed that different parameter sets can be found
which are optimised for a given domain and give rise to similar chips and
cutting forces when machining simulations are carried out within this
domain. In Section 4.3, it is seen however that by changing the cutting
conditions, different domains can be explored and the non-uniqueness
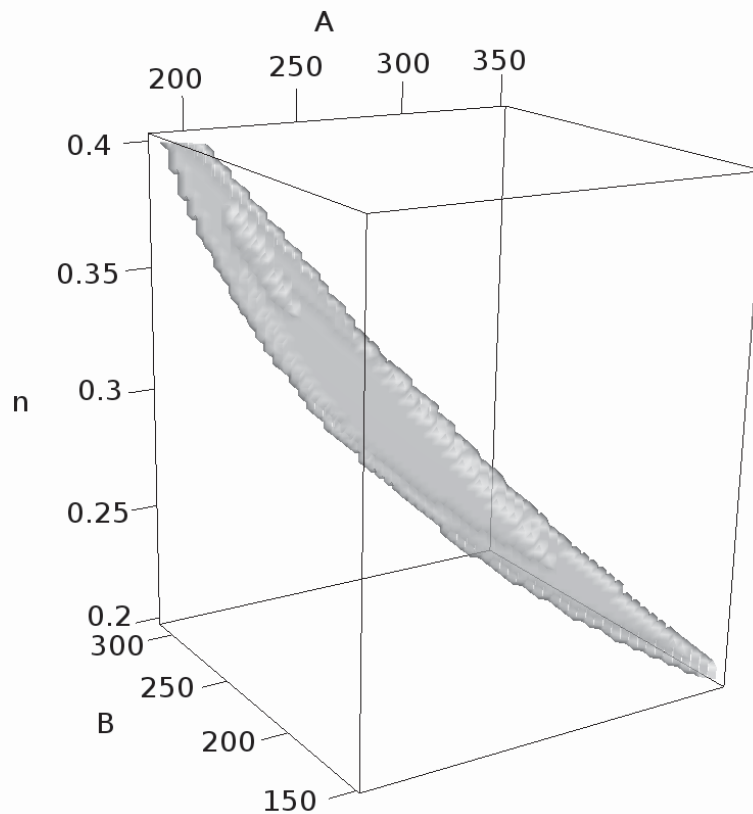
Figure 4.20: The intersection of the error isosurfaces leads to a smaller subset of suitable parameter sets. Parameters A and B are expressed in MPa.

can be reduced. Using this fact, the parameter sets shown in Table 4.1 will be distinguished in this section.

Two possible changes to the cutting conditions can be:

Changing the cutting speed: To understand the effect of the cutting speed on the strain, strain rate and temperature distributions, non-adiabatic simulations are conducted at three cutting speeds of 0.1 m s^{-1}, 1 m s^{-1} and 10 m s^{-1}. Strain, strain rate and temperature distributions from 31 elements from the middle of the workpiece (as shown in Figure 4.21) are plotted for each of the cutting conditions (Figure 4.22). At a low cutting speed of 0.1 m s^{-1}, the heat from the plastic work is conducted away to the near-by elements and hence the temperature distributions are well scattered (Figure 4.22a). At progressively higher cutting speeds, the process is more and more adiabatic and the temperature evolution converges to a single curve (Figures 4.22c and 4.22e). At lower cutting speeds, the strain in some elements can go as high as 2.5 and at higher

speeds the strains go up to 1.5. Finally, the strain rate at low cutting speed ranges in the order of 10^3 s^{-1} (Figure 4.22b) which rises up to 10^5 s^{-1} at a cutting speed of 10 m s^{-1} (Figure 4.22f).
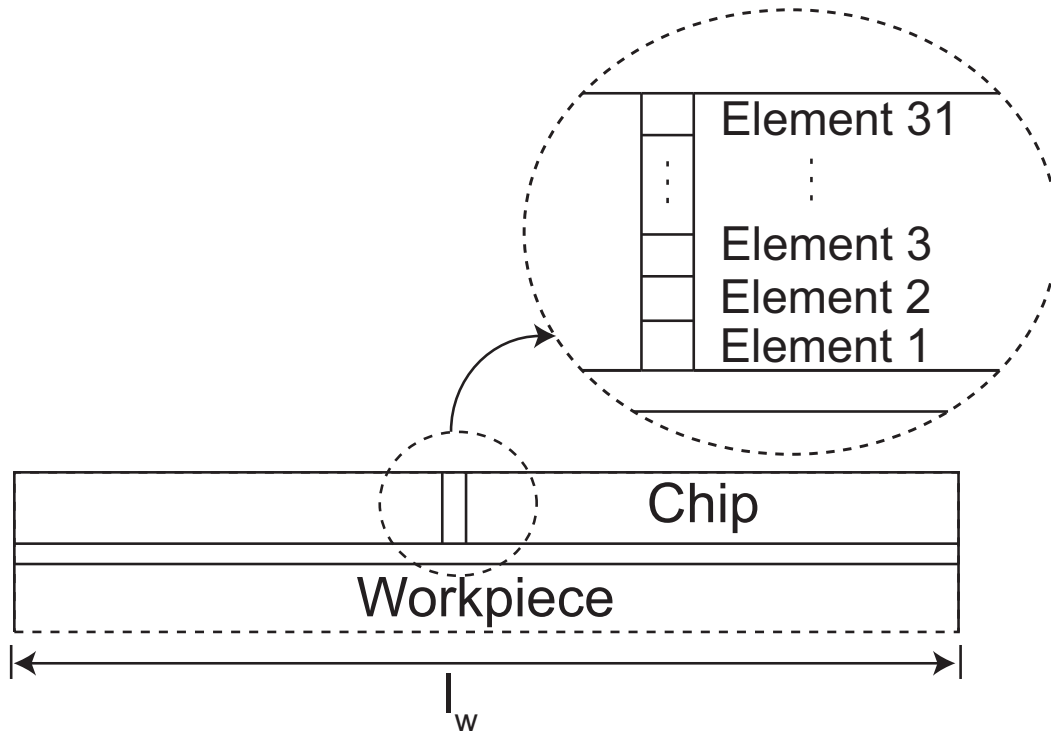
Figure 4.21: Element numbering along the chip thickness direction.

Changing the rake angle: On changing the rake angle, it is seen that more negative the rake angle, higher is the average strain in the chip. In Figure 4.23, it can be seen that as the rake angle is progressively changed from $+10°$ to $-10°$, the proportion of strains above 2.0 increases.

Using these two cutting condition variations, an attempt is made at distinguishing between the various parameter sets found in Section 4.2 which gave rise to similar chips and cutting forces. It was also noted in that Section that slight differences in the shape of the adiabatic stress-strain curves appear at lower strains while significant differences in the shape of the isothermal curves appear at higher strains.

To explore the lower strains of the adiabatic stress-strain curve, a positive rake angle of $+10°$ is used. The resulting adiabatic simulations give rise to chips which have different radii of curvature (Figure 4.24). The difference in the chip shapes can be used to distinguish some of the non-unique sets. The normalised chip non-overlap areas for the different sets are listed in Table 4.11. It can be seen that, except sets 2,
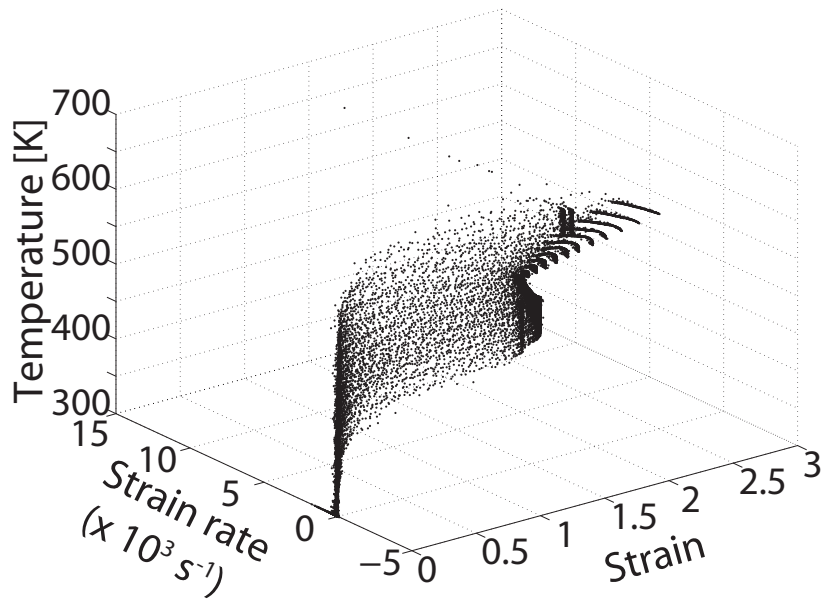
(a) Strain, strain rate and temperature temperature distribution for a cutting speed of 0.1 m s^{-1}.
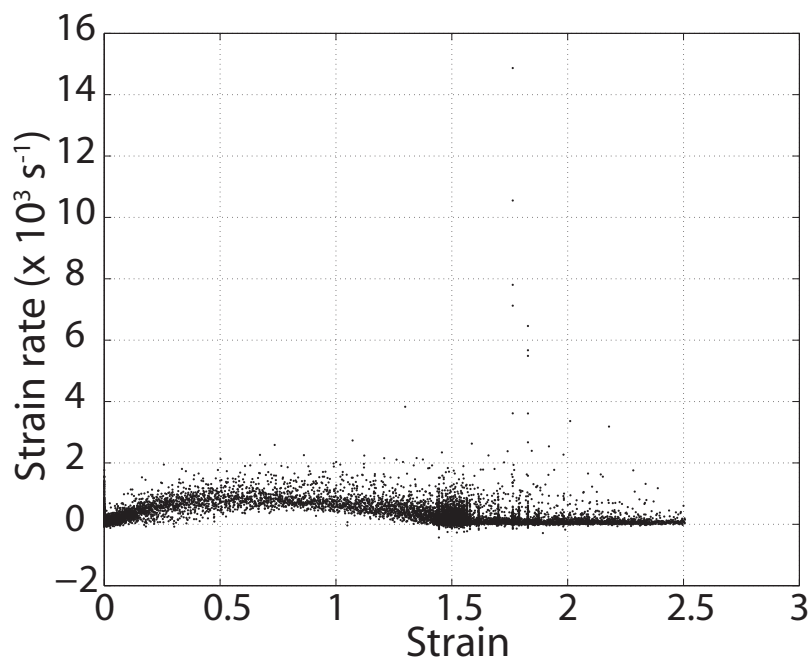
(b) Strain rate *vs.* strain distribution for a cutting speed of 0.1 m s^{-1}.

Figure 4.22: Strain, strain rate and temperatures during machining at different cutting speeds (rake angle = $+1°$; HY-100).
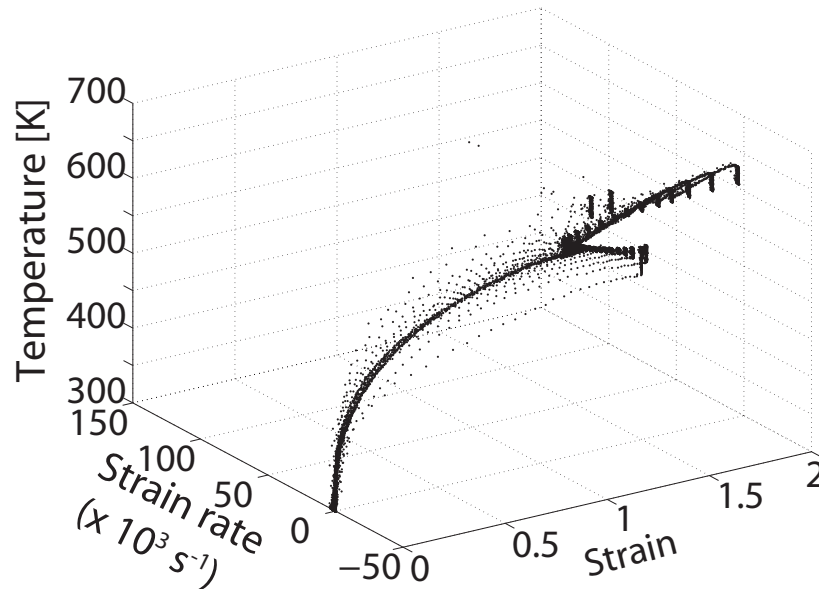
(c) Strain, strain rate and temperature temperature distribution for a cutting speed of $1\,\mathrm{m\,s^{-1}}$.
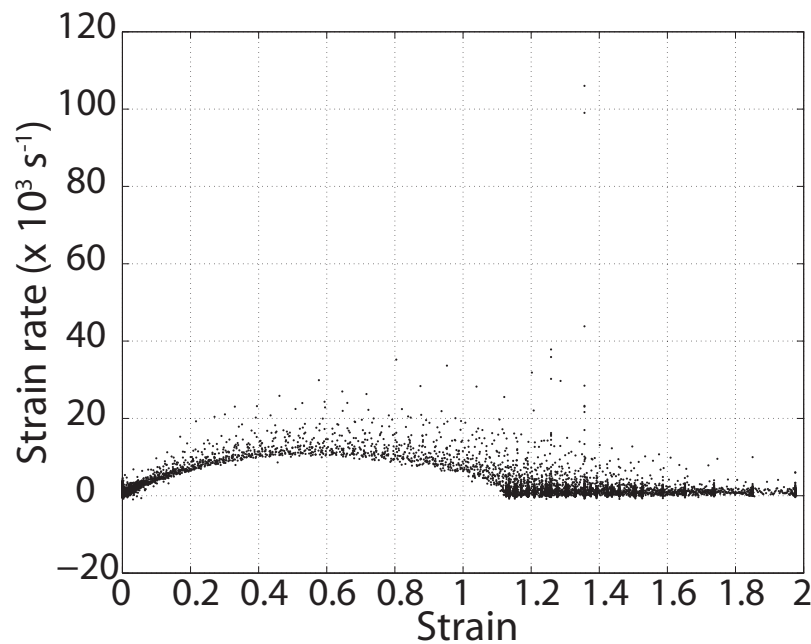
(d) Strain rate *vs.* strain distribution for a cutting speed of $1\,\mathrm{m\,s^{-1}}$.

Figure 4.22: Strain, strain rate and temperatures during machining at different cutting speeds (rake angle $= +1°$; HY-100).
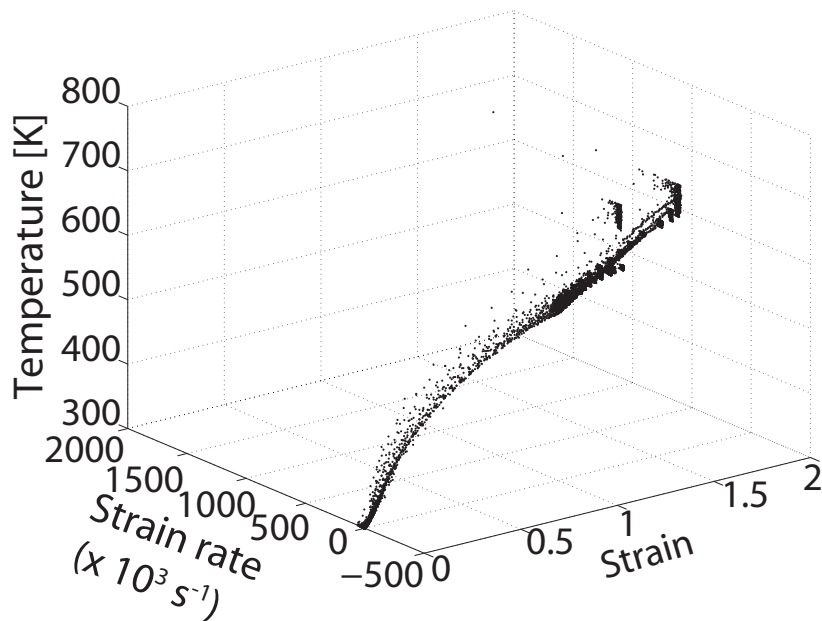
(e) Strain, strain rate and temperature temperature distribution for a cutting speed of 10 m s^{-1}.
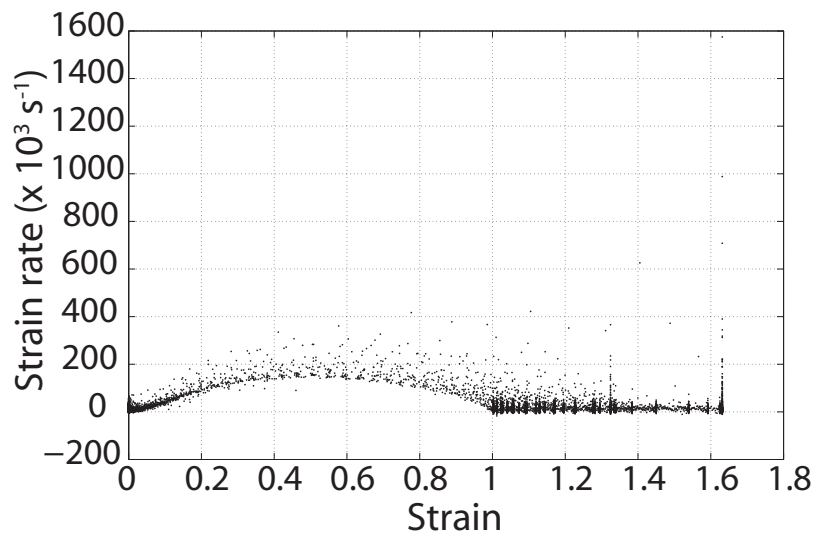
(f) Strain rate *vs.* strain distribution for a cutting speed of 10 m s^{-1}.

Figure 4.22: Strain, strain rate and temperatures during machining at different cutting speeds (rake angle = +1°; HY-100).

(a) Rake angle $= +10°$

(b) Rake angle $= 0°$
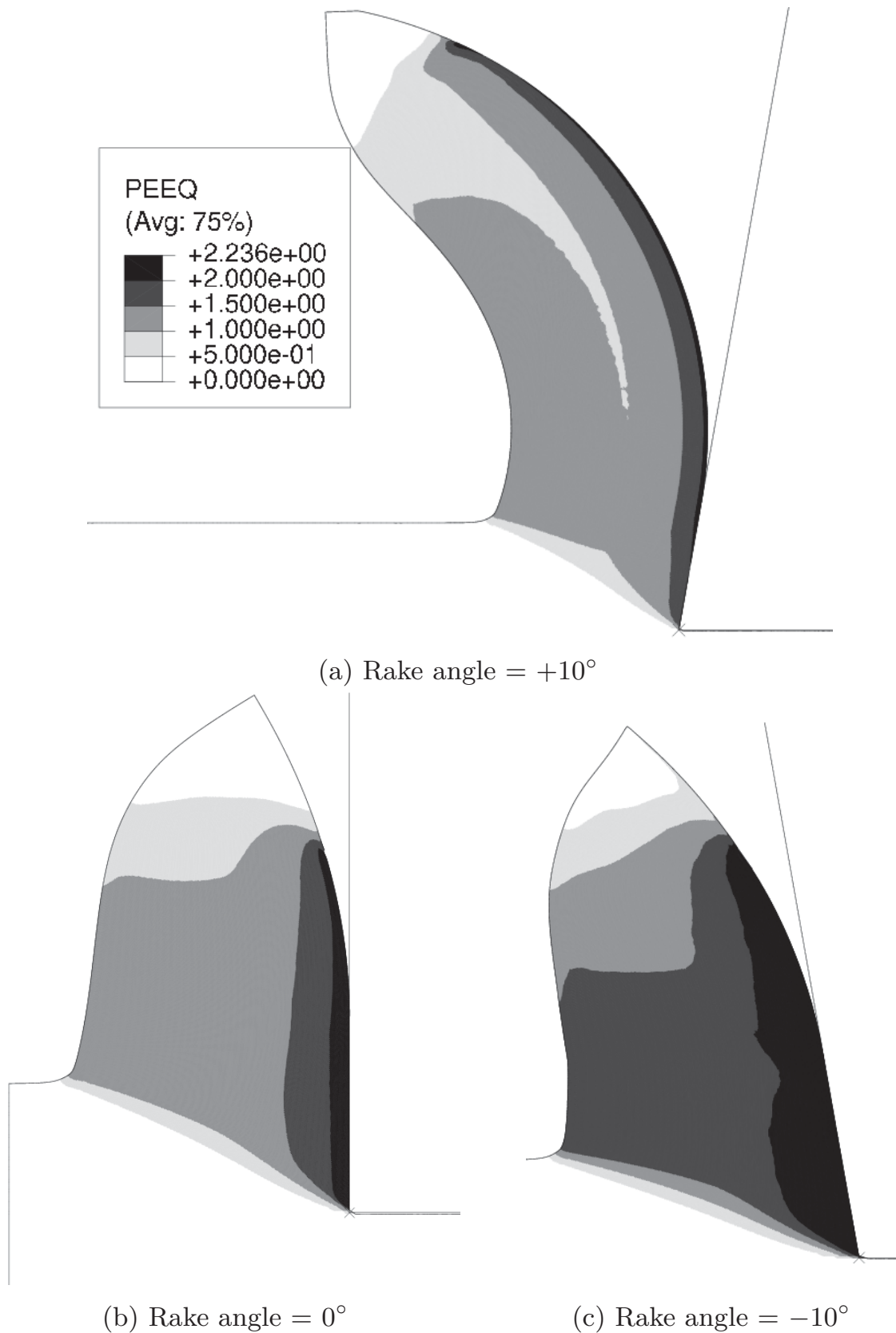
(c) Rake angle $= -10°$

Figure 4.23: Plastic equivalent strain distributions in chips at different rake angles (cutting speed $= 33.3$ m s^{-1}; AISI 52100, 62 HRC).

3 and 5, all sets have their areas of non-overlap above 3% and can be distinguished. It should also be expected that if the rake angle is made larger, the differences in the chip shapes should also become larger as the simulation would become more sensitive to the differences in the stress-strain curves at low strains.

Figure 4.24: Overlay of chip shapes from adiabatic simulations at rake angle of $+10°$ using different Johnson-Cook parameter sets

To explore the higher strains of the isothermal stress-strain curves, non-adiabatic simulations have been performed using the different Johnson-Cook parameter sets at a cutting speed of 3.33 m s^{-1} at a rake angle of $-10°$. Clear differences between the chip shapes can be seen in Figure 4.25. The normalised chip non-overlap areas listed in Table 4.12 also show that all the chips are distinguishable as the values are above 3% for all of them. A more negative rake angle is expected to further increase the chip shape difference.

	$\Delta A_C \%$
Set 1	4.89
Set 2	0.83
Set 3	2.97
Set 4	4.68
Set 5	1.78
Set 6	6.42
Set 7	6.54

Table 4.11: Normalised non-overlap areas for chips shown in Figure 4.24, obtained from adiabatic simulations at a rake angle of $+10°$.
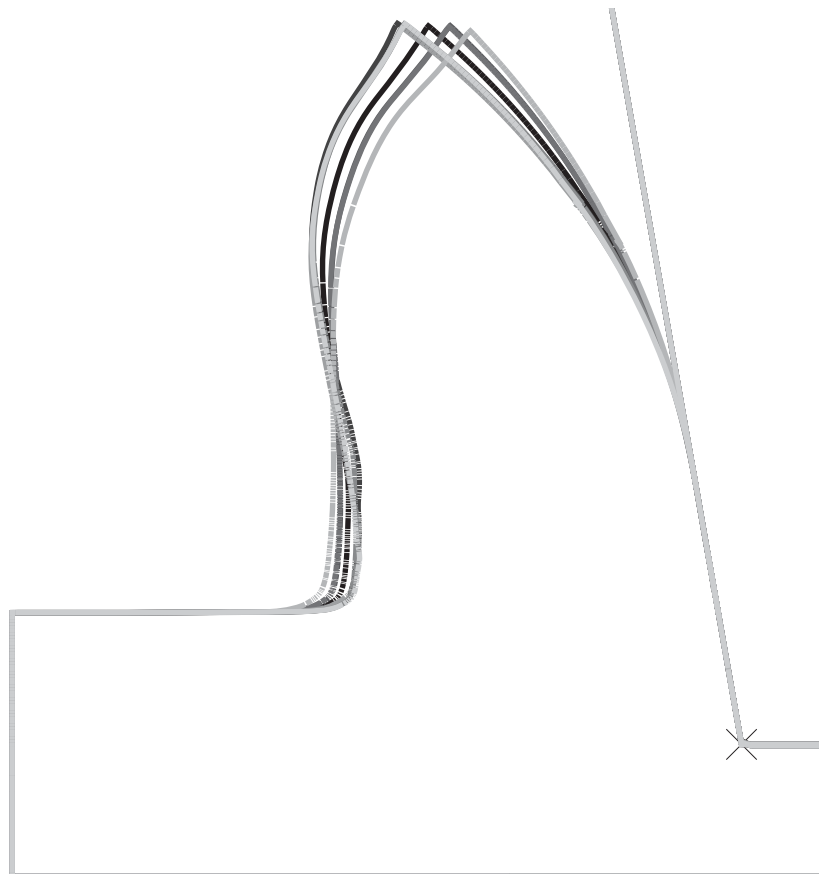
Figure 4.25: Overlay of chip shapes from non-adiabatic simulations at rake angle of $-10°$ using different Johnson-Cook parameter sets

	$\Delta A_C\%$
Set 1	5.79
Set 2	3.61
Set 3	3.88
Set 4	4.52
Set 5	4.09
Set 6	7.77
Set 7	4.38

Table 4.12: Normalised non-overlap areas for chips shown in Figure 4.25, obtained from non-adiabatic simulations at a rake angle of -10°.

As a conclusion, using a wide variation of cutting parameters, it was possible to differentiate between the different parameter sets. On further analysing the previous simulations, one can notice that under adiabatic conditions and at a rake angle of 0°, all the chip shapes were very similar (Figure 4.7). At a rake angle of +10° and also under adiabatic conditions, the chip shapes from most of the parameter sets differ (Figure 4.24). However, the chip shapes from Sets 2 and 5 are very similar to the original chip shape at this cutting condition. Finally at a rake angle of $-10°$ and non-adiabatic conditions, the chip shapes from Sets 2 and 5 can also be differentiated from the original chip shape. This has been separately shown in Figure 4.26.

Comparing the Tables 4.3, 4.11 and 4.12, it can be observed that when parameters sets are optimised to give similar flow stress curves in a particular machining domain and are used to conduct machining simulations in the same domain, the resulting chip shapes and the cutting forces are also similar. However, when the domain is changed by changing the cutting conditions, the parameter sets can be distinguished by looking at the chip shapes. For some parameter sets in Tables 4.11 and 4.12, the chips can be distinguished only after a closer inspection, usually when the normalised area of non-overlap is between 3% to 5%. To make the differences in the chip shapes larger, one can make the rake angle more positive or negative than the values used in this chapter.

4.5   Conclusion

It was seen in this chapter that non-unique parameter sets can be found which can give rise to similar chips and cutting forces in a given machining domain. Such parameter sets can be distinguished by widely varying the
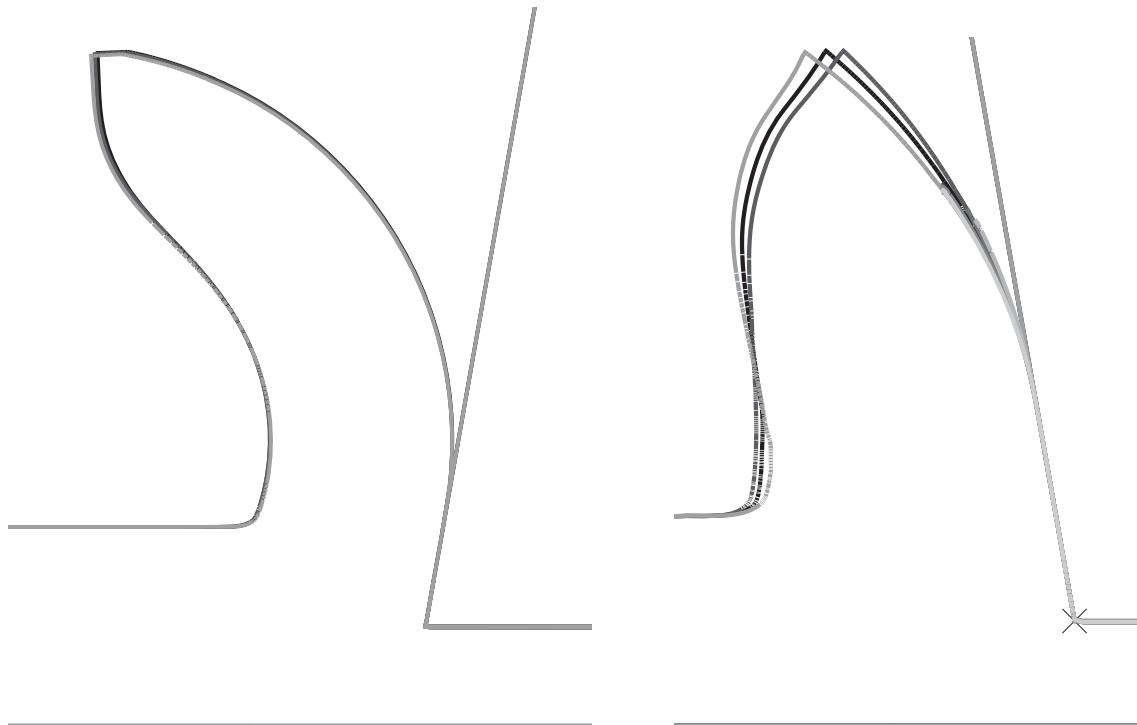
(a) Rake angle = $+10°$; Adiabatic simulation

(b) Rake angle = $-10°$; Non-adiabatic simulation

Figure 4.26: Overlay of chip shapes from simulations at different conditions. Chips shapes which are identical at a rake angle of $+10°$ during adiabatic simulations (cutting speed = 33.3 m s^{-1}) can be differentiated using non-adiabatic simulations (cutting speed = 3.33 m s^{-1}) at a rake angle of $-10°$.

cutting conditions. The problem of non-uniqueness can be anticipated during the inverse identification of the parameter sets due to the nature of the Johnson-Cook material model. Therefore, the cutting conditions for the identification process should be carefully chosen, to identify robust material parameters which describe the material behaviour over a wide range of cutting conditions.

While identifying the parameters A, B and n, smaller strains can be explored by using a positive rake angle test. At lower strains, the difference between the adiabatic and the isothermal stress-strain curves is small, therefore a positive rake angle test can be adiabatic or non-adiabatic. However, an adiabatic test may be more advantageous as the explicit simulation at high cutting speed is computationally less expensive (Section 2.5). Since non-adiabatic simulations lead to less non-uniqueness (Section 4.3) and large strains should also be explored, simulations at lower cutting speeds and more negative rake angles should be done.

When parameter m is to be identified, the temperature range must be explored. Both low speed and high speed cutting tests may be used as in both the cases a large temperature variation is found. However, when m is to be identified along with A, B and n, low speed cutting tests are required so that the strain and temperature space can be explored. When parameter C is to be identified, low cutting speeds are not useful as higher strain rates are not reached.

Chapter 5

Inverse Parameter Identification

5.1 Introduction

It was seen in Chapter 3 that obtaining material parameters from experiments can be difficult, as the strains and strain rates reached during machining cannot be replicated during Split Hopkinson Bar tests. When the material parameters obtained from such experimental procedures are used in machining simulations, large extrapolations of state variables are made outside the domain in which the parameters are experimentally determined. Therefore it is difficult to match the results from machining simulations and machining experiments.

A number of researchers (Kececioglu (1958); Lira & Thomsen (1967); Oxley & Stevenson (1967)) have proposed to use machining itself as a method of obtaining material flow stress at these extreme conditions. In these early works, the parallel sided shear zone theory (Oxley (1989)) is used to estimate the flow stress from the measured forces and the chip geometry obtained from quickstop micrographs. Material parameters for a power law (Equation 2.10) are then found using the flow stress values.

More recently Özel and Altan (Özel & Altan (2000)) identified the material and the friction parameters using an iterative procedure in which the cutting forces from the finite element simulations are matched to the experimental results for different cutting conditions. Only continuous chip formation was considered. For a given cutting condition, the flow stress was modified using the average strain rate and average temperature values obtained from the finite element simulation until the average

cutting force is matched. Furthermore, the friction parameters are modified till the tangential cutting force is matched. This is done for a number of cutting conditions and the flow stress and friction parameters are obtained for each of the cutting conditions. Finally, the material parameters are obtained using a least square minimisation method from the flow stress values at different average strain rate and temperature values. This work is one of the first times the finite element method was used to determine the material parameters. In the work of Maurel *et al.* (2008), a similar method is proposed, in which material parameters are varied till the cutting forces from simulations match the milling experiment results. However, the optimisation results are not actually shown in the paper.

Oxley's theory for machining calculations as described in Section 1.5.3 can also be used for estimating the flow stresses at machining conditions. In the original algorithm, the flow stress values are calculated using the power law, whose coefficients are obtained using the velocity modified temperature term (T_{mod}). With a slight modification, this algorithm can also be used to estimate the material parameters as shown by Shatla *et al.* (2001a). A computer program (OXCUT) based on the Oxley's algorithm was written so that the Johnson-Cook material parameters are systematically varied using a downhill simplex algorithm until the results from the program match the experimental results. A number of orthogonal slot milling experiments were conducted at different cutting speeds for this reason. For each cutting speed, the cutting depth changes during the rotation of the tool, leading to a large variation in cutting conditions in a single revolution. The results of these experiments were matched to the results from the OXCUT program. It was also shown (Shatla *et al.* (2001b)) that the cutting forces predicted by the finite element simulations also match well with the measured values. This method was also used to identify material parameters for other material models (Sartkulvanich *et al.* (2004)). Similarly, in another work (Özel & Karpat (2007)), evolutionary computer algorithms were used to fit the stresses obtained from Split Hopkinson Bar tests and the stresses from orthogonal cutting tests, as predicted by Oxley's method, to the Johnson-Cook model.

The major limitation of these methods is that a match in the average cutting force does not guarantee that material parameters have been correctly identified (as shown by Bäker (2003a)). Since Oxley's algorithm is only valid for continuous chip formation, these methods cannot be extended to materials which form segmented or separated chips. The chip shape is also not taken into consideration in these identification techniques.

Another method was proposed to identify the material parameters by Tounsi *et al.* (2002). A parallel-sided shear zone was assumed and the physical quantities such as the effective shear strain, the effective strain rate and the temperature are assumed to be constant on the planes parallel to the shear plane and to vary only in the direction perpendicular to it. A continuous chip is assumed to be formed. In order to obtain the Johnson-Cook parameters, the flow stress, strain, strain rate and temperature in the primary shear zone are estimated using a theoretical model in the following manner:

1. Quick-stop micrographs are used to obtain geometrical parameters such as the thickness of the primary shear zone and the fraction by which the shear plane divides the shear zone between the uncut chip and the formed chip. They are used in the estimation of state variables.

2. Relating the cutting velocity and the coordinates of a given material point, the velocity field in the primary shear zone is determined.

3. The velocity field from step 2 is used to estimate the strain rate field in the shear zone.

4. The strain rate from step 3 is integrated to predict the effective plastic strain in the shear plane.

5. The stress distribution is determined from the measured cutting forces and the shear angle.

6. The temperature distribution is obtained by assuming adiabatic conditions and that all the plastic work is converted into heat.

7. The Johnson-Cook parameters are obtained using parameter fitting methods, to relate the theoretically obtained flow stress values to the flow stress values predicted by the Johnson-Cook model by using the theoretically obtained strain, strain rate and temperature values.

The Johnson-Cook parameters obtained using this method are compared to those obtained from Split Hopkinson Bar tests, already published in the literature. A good agreement is found between the two. This method provides a useful way of obtaining material parameter from machining experiments. However, it is very difficult to experimentally verify the strain, strain rate and temperature values given by such a model. Moreover, machining simulations were not conducted to prove that the obtained material parameter set can be used to predict the

cutting forces and chip temperatures outside the range of the cutting conditions at which they have been found.

The above method was revised and improved by using FE simulations as virtual experiments to estimate the strain, strain rate and temperature distributions in the shear zone, in the work of Shi *et al.* (2010a). Based on the results obtained from the FE simulations, the distributions in the shear zone are further simplified using analytical models. The parameters (A, B, n) of the Johnson-Cook model are identified using quasi-static indentation tests (Shi *et al.* (2010b)). The parameters C and m are identified using cutting tests conducted at room temperature and at high temperature. The identified Johnson-Cook parameter set is reported to be unique. This is because the authors did not take into account the variation in the flow stresses due to measurement errors. Since the set (A, B, n) is not identified at high strain rates and temperatures, the flow stress is over estimated at machining conditions. The cutting force is found to be over estimated by 105% when the material parameters identified for Inconel 718 this way are used for FE simulation of the machining process.

In this chapter a method for inverse determination of material parameters is shown. The cutting force and chip shape are the observables in a machining process. These observables are a function of the material behaviour and the cutting conditions. Ideally, by conducting finite element simulations at cutting conditions identical to those of the machining experiment and using the correct material parameters, the simulation and the experimental results should match. If the material parameters are not known initially (or incorrectly known), inverse techniques can be used to find the material parameters. In this method, the chip shapes and the cutting forces are matched to a standard experiment by systematically varying the material parameters. The distinct advantages of the inverse identification method over the previously discussed methods are:

1. Both chip shape and cutting forces are matched, avoiding the problem of having incorrect parameter sets which give rise to correct mean cutting force but not the correct chip shape.

2. Idealising assumptions related to the stress, strain, strain rate and temperature distributions are not made as they can be directly predicted by the finite element model.

3. Finite element simulation results are compared directly to the results of the standard experiment[1], avoiding the use of an interme-

---

[1]In this work, all standard experiments are numerical

diate theoretical model, which may lead to errors due to limiting assumptions related to the model.

4. This method does not assume continuous chip shape for it to work. Therefore it can also be extended to predict material parameters for segmented or separated chip formation.

5. Even though this method is demonstrated for obtaining Johnson-Cook parameters in this work, material parameters for other material models can also be obtained using the same method.

In Section 5.2, the inverse identification problem is discussed along with the optimisation methods used to determine the parameters. The error function, the choice of the optimisation parameters and the computational expense for the optimisation process are also discussed. In Section 5.3, the inverse method is validated by reidentifying first 1, then 2 and 3 material parameters by matching the chip shapes and the cutting forces. During the validations, a coarse mesh is used to save computational time. In the error function, the effect of the cutting force and the chip shape mismatch is balanced using a weight parameter, whose choice can affect the convergence. Moreover, the choice of the method by which the Jacobian (explained in Section 5.2.1) is determined can also affect the convergence, adding to the computational costs. Therefore the effect of the choice of the Jacobian calculation method and the weight parameter on the optimisation are studied. In Section 5.5, a finer mesh is used for identification of 3 parameters (A, B, n) and the effect of the mesh size on the identification process is studied. By a judicious choice of the optimisation parameter there can be significant savings in the computational time as shown in Section 5.6.

In all the cases until now, the Levenberg-Marquardt algorithm is used for optimisation until the cutting force and chip shapes from test simulations match well with the ones from the standard simulation. If either of the two would not match within a given tolerance, it would imply that the algorithm has converged to a local minimum. To resolve this problem, the weighting parameter in the error function or the step size while numerically calculating the Jacobian is changed. This can be a time taking process, requiring trial and error. To avoid this, multi-stage optimisation is carried out in Section 5.7. Staggered optimisation and a dual method are two types which were studied. In staggered optimisation, different parameter combinations are optimised in each stage to preferentially reduce different components of the error function. In dual method optimisation, the Levenberg-Marquardt algorithm is used in conjunction with the simplex algorithm to minimise the error.

This method is very robust in determining the parameters as it does not require constant human guidance to match both the chip shape and the cutting force. In Section 5.8, the effect of the choice of the error function on parameter identification is studied. In Section 5.9, material parameters are identified from non-adiabatic simulations as lower non-uniqueness is expected in such cases (see Chapter 4). In Section 5.10, other parameter combinations such as (m, C), (A, n, C) and (A, B, C) are identified.

Parameter identification using the dual stage method can be computationally intensive. In Section 5.11, a better way of improving the solution using the knowledge of the stress-strain curves is proposed, which can reduce the optimisation time. Using this method, 4 parameters (A, B, n, m) are identified using the adiabatic simulations and 3 parameters (A, B, n) are identified using the non-adiabatic simulations.

In this chapter, each identification problem is given a unique identifier. For example, $\mathcal{S}_{An}^k$ represents the kth identification problem where A and n are being identified.

5.2   The inverse identification problem

In this work, a standard Johnson-Cook material parameter set is inversely reidentified using machining simulations. A *standard simulation* is conducted at given cutting conditions, using a known material parameter set (*standard set*) found from the literature. At the same cutting conditions, a *test simulation* using a *test set* of material parameters is carried out. If the observables from the standard and the test simulations match for a large range of cutting conditions, the test set which gave rise to the match is the *identified set*.

During the identification process, the difference in the chip shapes and the cutting forces from standard and test simulations is quantified using an error function (Section 5.2.2). For inverse identification, the error function is minimised using optimisation algorithms which are described in Section 5.2.1.

5.2.1   Minimisation algorithms used

The inverse identification process requires the minimisation of the error function $\chi^2(\mathbf{a})$. The error function can be represented as the sum

of squares of N residual functions $\Phi_i^2(\mathbf{a})$ which are a function of the parameter set $\mathbf{a}$ as

$$\chi^2(\mathbf{a}) = \frac{1}{2} \sum_{i=1}^{N} \Phi_i^2(\mathbf{a}) = \frac{1}{2} ||\Phi(\mathbf{a})||^2 \tag{5.1}$$

$$= \frac{1}{2} \mathbf{\Phi}^T \cdot \mathbf{\Phi}, \tag{5.2}$$

where $\mathbf{\Phi}$ is a vector of dimension N with $\Phi_i(\mathbf{a})$ being its component and $|| \bullet ||$ is the Euclidean norm. The residual function $\Phi_i(\mathbf{a})$ can be further defined in terms of the differences in chip shapes and cutting forces, as shown in Section 5.2.2. In this section, methods to minimise a function having the form of the Equation 5.1 are discussed.

In this work, both the Levenberg-Marquardt algorithm and the downhill simplex algorithm are used for optimisation. The Levenberg-Marquardt algorithm is used as it is a gradient based method which shows fast convergence. However, as will be shown in Section 5.3.2, the error landscape is very noisy close to the minimum, leading the Levenberg-Marquardt algorithm to be stuck in a local minimum. Therefore, in later attempts, a second stage of optimisation using the downhill simplex algorithm is used to further improve the first stage solutions. Due to its heuristic nature, the downhill simplex algorithm is seen to be more robust as compared to the Levenberg-Marquardt algorithm in a noisy error landscape. In the two-stage optimisation process, the converged set from the Levenberg-Marquardt stage is used as the starting set for the downhill simplex stage.

The Levenberg-Marquardt algorithm

A brief introduction to the Levenberg-Marquardt algorithm is given in this section, along with the choice of the damping factor which can affect convergence. Parts of this sub-section are synthesised from Fletcher (1971); Galassi *et al.* (2002); Hebden (1973); Levenberg (1944); Marquardt (1963); Moré (1978); Press *et al.* (1993).

The error function $\chi^2(\mathbf{a})$ can be approximated near the current trial parameter set $\mathbf{a}_{\text{cur}}$ using the Taylor series as

$$\chi^2(\mathbf{a}) = \chi^2(\mathbf{a}_{\text{cur}}) + \sum_i \frac{\partial \chi^2}{\partial a_i} a_i + \frac{1}{2} \sum_{i,j} \frac{\partial^2 \chi^2}{\partial a_i \partial a_j} a_i a_j + \dots$$

$$\approx \gamma - \mathbf{d}^T \cdot \mathbf{a} + \frac{1}{2} \mathbf{a}^T \cdot \mathbf{H} \cdot \mathbf{a}, \tag{5.3}$$

where

$$\gamma \equiv \chi^2(\mathbf{a}_{\mathrm{cur}}) \qquad [d]_i \equiv -\frac{\partial \chi^2}{\partial a_i}\bigg|_{\mathbf{a}_{\mathrm{cur}}} \qquad [H]_{ij} \equiv \frac{\partial^2 \chi^2}{\partial a_i \partial a_j}\bigg|_{\mathbf{a}_{\mathrm{cur}}} . \quad (5.4)$$

If M is the number of parameters in the parameter set to be identified, then $\mathbf{d}$ is a vector with M components and $\mathbf{H}$ is an $M \times M$ matrix.

If the approximation by Equation 5.3 is perfect, then the minimising parameter set ($\mathbf{a}_{\mathrm{min}}$) can be obtained from the current trial parameter set ($\mathbf{a}_{\mathrm{cur}}$) in a single step using the formula

$$\mathbf{a}_{\mathrm{min}} = \mathbf{a}_{\mathrm{cur}} + \mathbf{H}^{-1} \cdot \mathbf{d} . \quad (5.5)$$

Equation 5.5 is the same as the formula used in the Newton's method (Press *et al.* (1993)). However, if the approximation given by Equation 5.3 is poor, it is better to take a step in the direction of the steepest descent *i.e.*

$$\mathbf{a}_{\mathrm{next}} = \mathbf{a}_{\mathrm{cur}} + \mathrm{constant} \cdot \mathbf{d} . \quad (5.6)$$

Here the constant chosen in such a way that $\chi^2(\mathbf{a}_{\mathrm{next}}) < \chi^2(\mathbf{a}_{\mathrm{cur}})$. If the downhill direction is overstepped and the condition is not satisfied, the value of the constant must be reduced.

To use Equation 5.5, the second derivative matrix, also known as the Hessian matrix ($\mathbf{H}$), is required. Furthermore, to use the Equation 5.6, the first derivative matrix is required. The components of the gradient of $\chi^2(\mathbf{a})$ with respect to parameter set $\mathbf{a}$ are given by

$$\frac{\partial \chi^2}{\partial a_k} = \sum_{i=1}^{N} \Phi_i(\mathbf{a}) \frac{\partial \Phi_i(\mathbf{a})}{\partial a_k} . \quad (5.7)$$

In matrix notation the derivative matrix can be written as

$$\nabla \chi^2(\mathbf{a}_{\mathrm{cur}}) = \mathbf{J}^T \cdot \mathbf{\Phi} , \quad (5.8)$$

where $\mathbf{J}$ is the Jacobian matrix whose components are given by

$$J_{ik} = \frac{\partial \Phi_i(\mathbf{a})}{\partial a_k} \qquad i = 1, 2, \ldots, N; k = 1, 2, \ldots, M . \quad (5.9)$$

The components of the Hessian matrix can be found by taking a derivative of Equation 5.7 and are given by

$$\frac{\partial^2 \chi^2}{\partial a_k \partial a_l} = \sum_{i=1}^{N} \frac{\partial \Phi_i(\mathbf{a})}{\partial a_k} \frac{\partial \Phi_i(\mathbf{a})}{\partial a_l} + \Phi_i(\mathbf{a}) \frac{\partial^2 \Phi_i(\mathbf{a})}{\partial a_l \partial a_k} . \quad (5.10)$$

The second term in the Equation 5.10 can be neglected because in a successful model, the term $\Phi_i(\mathbf{a})$ should be a random measurement error of each point which can have either sign and in general is not correlated with the model (Press *et al.* (1993)). Thus the second term in Equation 5.10 tends to cancel out, when summed over i. It has also been reported (Press *et al.* (1993)) that if the second term is included in the Hessian calculation, it can destabilise the optimisation if the model fits badly or there are outlier points in the data set. Thus the Hessian matrix ($\mathbf{H}$) can be approximated in terms of the Jacobian matrix as

$$\mathbf{H} = \mathbf{J}^T \cdot \mathbf{J} . \tag{5.11}$$

Levenberg (Levenberg (1944)) combined the Equations 5.5 and 5.6 and rewrote them in the form

$$\delta\mathbf{a} = -[\mathbf{J}^T \cdot \mathbf{J} + \lambda_{LM}\mathbf{I}]^{-1} \cdot \mathbf{J}^T \cdot \mathbf{\Phi} , \tag{5.12}$$

where $\delta\mathbf{a}$ is the correction to be added to the current parameter set $\mathbf{a}_{\text{cur}}$ to give the new parameter set $\mathbf{a}_{\text{next}}$ and λ_{LM} is a damping parameter which is used to control the step size. A disadvantage of this formulation is that when the value of the damping factor λ_{LM} is large, then

$$[\mathbf{J}^T \cdot \mathbf{J} + \lambda_{LM}\mathbf{I}]^{-1} \approx \frac{1}{\lambda_{LM}}\mathbf{I} , \tag{5.13}$$

which leads to very slow convergence at small gradients. Marquardt (1963) modified Equation 5.12 in order to scale the gradient components according to the curvature. In order to do so, the identity matrix was replaced in Equation 5.12 with the diagonal of the Hessian matrix giving

$$\delta\mathbf{a} = -[\mathbf{J}^T \cdot \mathbf{J} + \lambda_{LM}\text{diag}(\mathbf{J}^T \cdot \mathbf{J})]^{-1} \cdot \mathbf{J}^T \cdot \mathbf{\Phi} . \tag{5.14}$$

The Levenberg-Marquardt algorithm, as proposed by Marquardt, is listed in Algorithm 1 in Appendix A. The main iteration in the algorithm takes place after the evaluation of the Jacobian and a step is taken towards the direction of the steepest descent. If χ^2 reduces on taking the step, the damping parameter (λ_{LM}) is reduced to increase the next step size. If the step size is too large and the minimum is overstepped, then the damping parameter (λ_{LM}) is increased to reduce the step size in subsequent sub-iterations till χ^2 is smaller than the previous step. How λ_{LM} is chosen is therefore important and is discussed in detail further in this section.

In this work, the implementation of the Levenberg-Marquardt algorithm available in the GNU Scientific Library (Galassi *et al.* (2002))

is used. For optimisation, the algorithm requires the starting parameter set $\mathbf{a}_0$, the residual function matrix $\mathbf{\Phi}$ and the Jacobian matrix $\mathbf{J}$. This implementation differs notably from Algorithm 1 in Appendix A and its details have been discussed in Moré (1978). The important differences in the GNU Scientific Library (GSL) implementation and the original algorithm pertain to the choice of the scaling matrix and the Levenberg-Marquardt parameter λ_{LM}.

Choice of the scaling matrix: Marquardt replaced the identity matrix $\mathbf{I}$ with the diagonal of the Hessian matrix $(\mathrm{diag}(\mathbf{J}^T \cdot \mathbf{J}))$ which takes into account the scaling of the problem. However, this implementation is found to be computationally inefficient. A better solution proposed in Moré (1978) is to have a diagonal matrix $\mathbf{D}_k$ at k^{th} iteration, whose entries are given by

$$d_i^{(k)} \quad = \quad \begin{cases} \dfrac{\partial \Phi_i(\mathbf{a}_k)}{\partial a_i}, & k = 0 \\ \max\left\{ d_i^{(k-1)}, \dfrac{\partial \Phi_i(\mathbf{a}_k)}{\partial a_i} \right\}, & k \geq 1 \end{cases} \tag{5.15}$$

where

$$\mathbf{D}_k = \mathrm{diag}\left(d_1^{(k)}, d_2^{(k)}, \ldots, d_M^{(k)} \right). \tag{5.16}$$

Thus the Equation 5.14 is replaced by

$$\delta\mathbf{a} = -[\mathbf{J}^T \cdot \mathbf{J} + \lambda_{LM}\mathrm{diag}(\mathbf{D}_k^T \cdot \mathbf{D}_k)]^{-1} \cdot \mathbf{J}^T \cdot \mathbf{\Phi}, \tag{5.17}$$

to give the parameter correction $\delta\mathbf{a}$.

Choice of the damping parameter λ_{LM}: Levenberg orginally suggested that the optimisation should be repeated for different values of the parameter λ_{LM} to arrive at the optimal solution. However, it is extremely inefficient to look for the solutions of λ_{LM} for optimisation as there is a non-linear relationship between the choice of λ_{LM} and the converged solution. Marquardt suggested the use of a moderate λ_{LM} of 0.01 initially, which would be later increased or decreased in factors of $(\nu_{LM} =)$ 10. The problem with such a choice is that, if this initial choice is poor, a number of function evaluations have to be done before a realistic λ_{LM} is found. This can be even more problematic if the multiplying factor ν_{LM} is small, leading to a number of wasteful function evaluations. On the other hand, if the factor ν_{LM} is too big, the reduction of λ_{LM}

to λ_{LM}/ν_{LM} can be excessive, leading to destabilisation of the optimisation.

Different authors have presented mostly heuristic arguments for an efficient choice of the damping parameter (*e.g.*Fletcher (1971)). The GSL implementation uses the algorithm proposed by Moré (1978) which takes into account the algorithms by Fletcher (1971) and Hebden (1973). The basic strategy when choosing λ_{LM} is based on Fletcher's algorithm. If the ratio (R_{LM}) of the actual reduction to the predicted reduction is close to 1, then Equation 5.3 is a good approximation of the the error function, and therefore λ_{LM} must be reduced. If R_{LM} is close to 0 or negative, λ_{LM} must be increased to take a downhill step. However, for some intermediate values of R_{LM}, it is better to leave λ_{LM} unchanged. The ratio R_{LM} is evaluated by

$$R_{LM} = \frac{||\Phi(\mathbf{a})||^2 - ||\Phi(\mathbf{a} + \delta\mathbf{a})||^2}{||\Phi(\mathbf{a})||^2 - ||\Phi(\mathbf{a}) + \mathbf{J} \cdot \delta\mathbf{a}||^2} \, . \tag{5.18}$$

Fletcher proposed that if $0 < R_{LM} < 0.25$ then λ_{LM} should be increased, if $0.75 < R_{LM} < 1$ then λ_{LM} should be decreased and if $0.25 < R_{LM} < 0.75$ then λ_{LM} should not be changed. In the GSL algorithm, this strategy has been adopted, although with a slight modification. Instead of directly changing λ_{LM}, the step bound (Δ) is modified at each step, which indirectly changes λ_{LM}. The step bound Δ is a positive number which applies an upper bound to $||\mathbf{D} \cdot \delta\mathbf{a}||$ *i.e.* $||\mathbf{D} \cdot \delta\mathbf{a}|| \leq \Delta$. The strategy for updating Δ is given in Algorithm 2 in Appendix A.

The damping parameter λ_{LM0} obtained from the step bound update algorithm is further optimised using a modified form of Hebden's algorithm (Hebden (1973)). This update strategy is listed in Algorithm 3 in Appendix A. The functions $\psi(\lambda_{LM})$ and $\psi'(\lambda_{LM})$ used in this algorithm are given by

$$\psi(\lambda_{LM}) = ||\mathbf{D} \cdot (\mathbf{J}^T \cdot \mathbf{J} + \lambda_{LM}\mathbf{D}^T \cdot \mathbf{D})^{-1} \cdot \mathbf{J}^T \cdot \mathbf{\Phi}|| - \Delta, \tag{5.19}$$

and

$$\psi'(\lambda_{LM}) = -\frac{(\mathbf{D}^T \cdot \mathbf{D} \cdot \delta\mathbf{a}(\lambda_{LM}))^T(\mathbf{J}^T \cdot \mathbf{J} + \lambda_{LM}\mathbf{D}^T \cdot \mathbf{D})^{-1}(\mathbf{D}^T \cdot \mathbf{D} \cdot \delta\mathbf{a}(\lambda_{LM}))}{||\mathbf{D} \cdot \delta\mathbf{a}(\lambda_{LM})||} \, .$$
$$\tag{5.20}$$

To calculate $\delta\mathbf{a}(\lambda_{LM})$, Equation 5.17 is used.

Jacobian calculation: The Jacobian matrix ($\mathbf{J}$) which is required in the Levenberg-Marquardt algorithm is estimated numerically using the finite difference method. Using the forward difference formula, the Jacobian entries are given by

$$\frac{\partial \Phi_i(\mathbf{a})}{\partial a_j} = \frac{\Phi_i\left(\mathbf{a} + \delta_j \mathbf{e_j}\right) - \Phi_i\left(\mathbf{a}\right)}{\delta_j} \,, \tag{5.21}$$

where $\mathbf{e_j}$ is the unit vector in the jth coordinate direction and δ_j is an appropriate increment in that direction. The value of δ_j is dependent on the noise level present in the error function (Ramm & Smirnova (2001)). δ_j should ideally be as small as possible. However, if δ_j is too small, the change in the error function value will be too small as compared to the noise and the direction of the steepest descent will be incorrect. If δ_j is too large, the algorithm will have difficulty converging to the minimum accurately. As the noise level in the error function is also dependent on the material parameters, it is impossible to know it accurately before conducting the simulations. Obtaining the δ_j beforehand is a non-trivial problem (Ramm & Smirnova (2001)). From numerical experiments it appears that a good choice for the δ_j value for parameter A is between 5 MPa and 10 MPa, for parameter B between 4 MPa and 10 MPa and for parameter n between 0.05 and 0.1. The seemingly large value of δ_n is necessary to overcome the noise and correctly estimate the Jacobian in the direction of n. The δ_j value is chosen conservatively so that the convergence still occurs even after a large variation of the material parameters.

The Jacobian calculation using the central difference formula is given by

$$\frac{\partial \Phi_i}{\partial a_j}(\mathbf{a}) = \frac{\Phi_i\left(\mathbf{a} + \delta_j \mathbf{e_j}\right) - \Phi_i\left(\mathbf{a} - \delta_j \mathbf{e_j}\right)}{2\delta_j} \,. \tag{5.22}$$

The Jacobian is evaluated using two nearby points and the slope is the average of the value found using the forward and the backward difference methods. This method of evaluation gives a more accurate slope estimate, with the truncation error expected to be of $\mathcal{O}(\delta_j^2)$ (Yang *et al.* (2005)).

Computational expense: Optimisation using the Levenberg-Marquardt algorithm is known to show super-linear convergence (Yamashita & Fukushima (2001)). For the parameter identification problem, this is an attractive property because fast convergence is expected even

if the starting parameter set is far from the standard parameter set. Compared to the optimisation process itself, the machining simulations take a much longer time. A typical machining simulation in Section 5.5 with 20 elements in the chip thickness direction takes approximately 45 minutes whereas the optimisation routine takes a few minutes to read an odb file and determine the next parameter set for machining simulation.

If τ_s is the simulation time, S_n the number of cutting conditions, N_I the total number of main iterations and N_s the total number of sub-iterations, then the total computational time for the optimisation using the forward difference formula will be

$$
\tau_{comp} = \underbrace{S_n \cdot \tau_s}_{\text{initial calculation}} + \underbrace{N_I \cdot S_n \cdot \tau_s}_{\text{main iteration}} + \underbrace{N_s \cdot S_n \cdot \tau_s}_{\text{sub-iteration}}
$$
$$
+ \underbrace{M \cdot N_I \cdot S_n \cdot \tau_s}_{\text{Jacobian calculation}} + \underbrace{\tau_O}_{\text{overheads}} \qquad (5.23)
$$
$$
= S_n \cdot \tau_s \cdot (1 + N_I + N_s + M \cdot N_I) + \tau_O .
$$

Here M is the number of parameters to be identified. When using the central difference formula, one extra simulation has to be carried out in each parameter direction. For this the total computational time will be

$$
\tau_{comp} = S_n \cdot \tau_s \cdot (1 + N_I + N_s + 2 \cdot M \cdot N_I) + \tau_O . \quad (5.24)
$$

There is a significant increase in the computational expense due to the extra simulations. However, the increase in the computational cost of using the central difference formula can be justified if this increase is in turn compensated by an improvement in estimating the slope and reducing the number of main iterations. A comparison of the two Jacobian estimating formulas is shown in Section 5.3.2.

The downhill simplex algorithm

The downhill simplex algorithm, also known as the Nelder-Mead algorithm, is a heuristic algorithm used for function minimisation (Nelder & Mead (1965)). A simplex is an M-dimensional geometric entity consisting of $M + 1$ vertices, each connected to all others by line segments, and encloses an M-dimensional volume. A triangle is a simplex in two dimensions and a tetrahedron is a simplex in three dimensions.

Using four basic transformations, *viz.* reflection, expansion, contraction and reduction, the simplex explores the parameter space and finds the minimum. The implementation of the simplex algorithm in the GNU Scientific Library is used for optimisation in this work. The starting parameter set ($\mathbf{a}_0$) and the edge sizes of the initial simplex (l_i) are the input to the program. The algorithm has been listed in Algorithm 4 in Appendix A.

The initial edge sizes have an important bearing on the results of the optimisation. If the initial simplex size is very small, then only local search near the starting point will take place and it is probable that the simplex will not be able to crawl out of a local minimum. If the simplex is too large, a number of expensive function evaluations will take place till the simplex size reduces enough to allow for a sensible search of the parameter space. The starting edge lengths used in this work are therefore dependent on the problem and have been specified in each of the sections.

The simplex algorithm was tested as a method of optimisation when the starting parameter set was far from the standard set. However, even after taking a large number of evaluation steps, the algorithm was not able to converge to a resonable minimum. Therefore this algorithm has been used only in conjuction with the Levenberg-Marquardt algorithm (see Section 5.7).

The computational expense in this method is dependent on the number of finite element evaluations. If the starting parameter set is far from the standard set, a large number of evaluations are needed. Unless a limiting simplex size is defined, the optimisation can take place until the size of the simplex becomes very small taking a very large number of expensive evaluations. Therefore, the optimisation was stopped when the size of the simplex became so small that the parameter values change by less than 10%. The simplex size is given by

$$S^{(k)}_{simplex} = \frac{\sum_0^M ||\mathbf{a}_i^{(k)} - \tilde{\mathbf{a}}^{(k)}||}{M+1} , \tag{5.25}$$

where $\tilde{\mathbf{a}}^{(k)}$ is the centroid of the simplex $\{\mathbf{a}_0^{(k)}, \mathbf{a}_1^{(k)}, \ldots, \mathbf{a}_M^{(k)}\}$.

5.2.2 Error Function

The non-overlap area (described in Section 2.6) between the standard and the test chip is taken as a measure of the difference in the chip shapes. This error (also referred to as the *chip overlap error*) is denoted by e_i^A where the subscript i refers to i^{th} observation. Similarly the

difference of cutting forces is the error in cutting forces (*cutting force error*) and is denoted by e_i^F. The magnitudes of the chip overlap error and the cutting force error are combined using a weighting factor w, which is used to balance the contribution of the two factors in the overall optimisation, to give an aggregate error function ($\Phi_i(\mathbf{a})$) as

$$\Phi_i(\mathbf{a}) = \left|e_i^A(\mathbf{a})\right| + w.\left|e_i^F(\mathbf{a})\right| . \tag{5.26}$$

The error function $\chi^2(\mathbf{a})$ is obtained by summing the square of the aggregate error functions over all the observations and is given as

$$\chi^2(\mathbf{a}) = \frac{1}{2}\sum_{i=1}^{N}\Phi_i^2(\mathbf{a}) = \frac{1}{2}\sum_{i=1}^{N}\left(\left|e_i^A(\mathbf{a})\right| + w.\left|e_i^F(\mathbf{a})\right|\right)^2 . \tag{5.27}$$

In total 30 frames of observation are recorded from standard or test simulations. When only one set of cutting condition is used, all the 30 frames come from a single test and standard simulation during the creation of the error function. However, when two different cutting conditions are used, 15 frames come from each of the simulations.

The error function shown in Equation 5.27 is used for all the inverse identification problems except in Section 5.8, where the effect of the error function choice on the identification process is studied.

To calculate the error function, a C++ code is written to read the deformed chip shape coordinates and the cutting force values from the Abaqus odb files (Abaqus Analysis User's Manual, V. 6.9).

5.3 Validation

The initial validation runs of the inverse identification algorithm were done using an extremely coarse mesh, with 8 elements in the chip thickness direction, to validate the program in a short amount of time. Each machining simulation took approximately 3 minutes, which allowed the whole optimisation to be finished in a few hours. It is acknowledged that such a coarse mesh cannot be used for actual optimisation processes due to the occurrence of large approximation errors. However, the coarse mesh does not influence the solution during validation as both the standard and the test simulations are conducted using the same mesh. For the validation runs, a single standard simulation was conducted and 100 simulation frames were recorded. In these simulations, raw cutting force values are recorded for 40 observations and the last 30 moving averaged cutting force values are used to calculate the error function during the optimisation. The machining conditions are listed in Table

5.1. The material parameters used for the standard simulations are that of AISI 52100, 62 HRC which are taken from literature and are listed in Tables 2.3 and 2.4. As seen in Section 4.3, there is non-uniqueness even in a small subset (A, B, n) of the Johnson-Cook parameter set. The inverse identification is therefore first done for the set (A, B, n).

Material	AISI 52100, 62 HRC
Cutting Speed $[\mathrm{m\,s^{-1}}]$	33.3
Uncut chip thickness $[\mathrm{\mu m}]$	200
Coefficient of friction	0
Rake angle	0°
Equivalent plastic strain at failure $(\bar{\varepsilon}_f^{pl})$	2.0
Mesh element type for Workpiece	CPE4R
Mesh element type for Tool	R2D2
Weighting factor w $[\mathrm{mm^2\,N^{-1}}]$	10^{-3}

Table 5.1: Details for the simulation and the optimisation during the validation runs.

5.3.1   Single parameter identification

As a first step to validation, single parameters are identified. The Jacobian, which is required to give the direction of the steepest descent for the Levenberg-Marquardt algorithm, is calculated numerically by using the forward difference finite difference formula (Equation 5.21).

Parameter A

The re-identification of parameter A $(\mathcal{S}_A^1)$ is shown in Table 5.2. The starting value (A_0) is taken as 600 MPa and the standard value (A_s) is 688.17 MPa. The value of δ_A used for calculating the Jacobian is 5 MPa. The optimisation converges in 5 main iterations. Sub-iterations are done within the main iteration of the Levenberg-Marquardt algorithm: the damping factor is increased to take smaller steps near the minimum. The converged value of A is 689.868 MPa, less than 0.15% different from the target value.

Parameter B

For the re-identification of parameter B $(\mathcal{S}_B^2)$, the starting value (B_0) is 100 MPa and the standard value (B_s) is 150.82 MPa. The value of δ_B

Sl. No.	$\#_M$	$\#_S$	A [MPa]	χ^2
1	0	0	600	0.094091
2	1	0	646.507	0.022969
3	2	0	675.799	0.006453
4	3	0	687.523	0.000941
5	4	0	690.811	0.002214
6		1	689.868	0.000713
7	5	0	692.195	0.001871
8		1	690.337	0.0012945
9		2	689.915	0.0014776
10		3	689.873	0.001050
11		4	689.868	0.000713

Table 5.2: $\mathcal{S}_A^1$: Parameter A at the end of each iteration and the corresponding χ^2. The standard value (A_s) is 688.17 MPa. $\#_M$ represents the main iteration number and $\#_S$ represents the sub-iteration number.

used for calculating the Jacobian is 4 MPa. The optimisation converges in 4 main iterations (Table 5.3). While the converged value of 149.502 MPa is found in 3 iterations, the algorithm tests in the next step that this is indeed the minimum value. The optimisation in the last iteration could have been stopped at the 4th sub-iteration, as the changes in the value of B takes place only after the 2nd decimal place. The optimisation is allowed to be run up to the 6th sub-iteration to see its effect on the χ^2 value. The χ^2 values in different sub-iterations of the 4th iteration indicate that there is a lot of noise close to the minimum. The closeness of the value of the test parameter B to the standard value does not mean that the χ^2 value is also small (Figure 5.1).

Parameter n

The starting value (n_0) for the identification process ($\mathcal{S}_n^3$) is 0.2 and the standard value (n_s) is 0.3362. The value of δ_n used for calculating the Jacobian is 0.08. After 3 main iterations, the optimisation converges to a value of 0.3449 (Table 5.4). The effect of noise in χ^2 values can also seen in this case: the test parameter value of 0.3397 in the 2nd sub-iteration of the 3rd iteration is much closer to the standard value than the finally converged value, but the χ^2 value for the converged value is smaller than that of the test parameter.

Sl. No.	$\#_M$	$\#_S$	B [MPa]	χ^2
1	0	0	100	0.018888
2	1	0	124.511	0.006515
3	2	0	142.677	0.001427
4	3	0	149.502	0.000140
5	4	0	152.226	0.000405
6		1	151.147	0.000244
7		2	149.773	0.000402
8		3	149.529	0.000156
9		4	149.505	0.000672
10		5	149.503	0.001083
11		6	149.502	0.000140

Table 5.3: $\mathcal{S}_B^2$: Parameter B at the end of each iteration and the corresponding χ^2. The standard value (B_s) is 150.82 MPa.

Sl. No.	$\#_M$	$\#_S$	n	χ^2
1	0	0	0.2000	0.010672
2	1	0	0.3798	0.002003
3	2	0	0.3462	0.001797
4	3	0	0.2840	0.003107
5		1	0.3253	0.002437
6		2	0.3397	0.002318
7		3	0.3449	0.000771

Table 5.4: $\mathcal{S}_n^3$: Parameter n at the end of each iteration and the corresponding χ^2. The standard value (n_s) is 0.3362.

5.3.2   Identification of 2 parameters

Having ensured that the single parameter identification was working correctly, 2 parameter identifications are carried out. The δ_j values chosen for single parameter identifications are first used for 2 parameter identifications also. If the optimisation does not converge or gets stuck in a local minimum, the values of δ_j and w are subsequently changed so that the convergence improves.
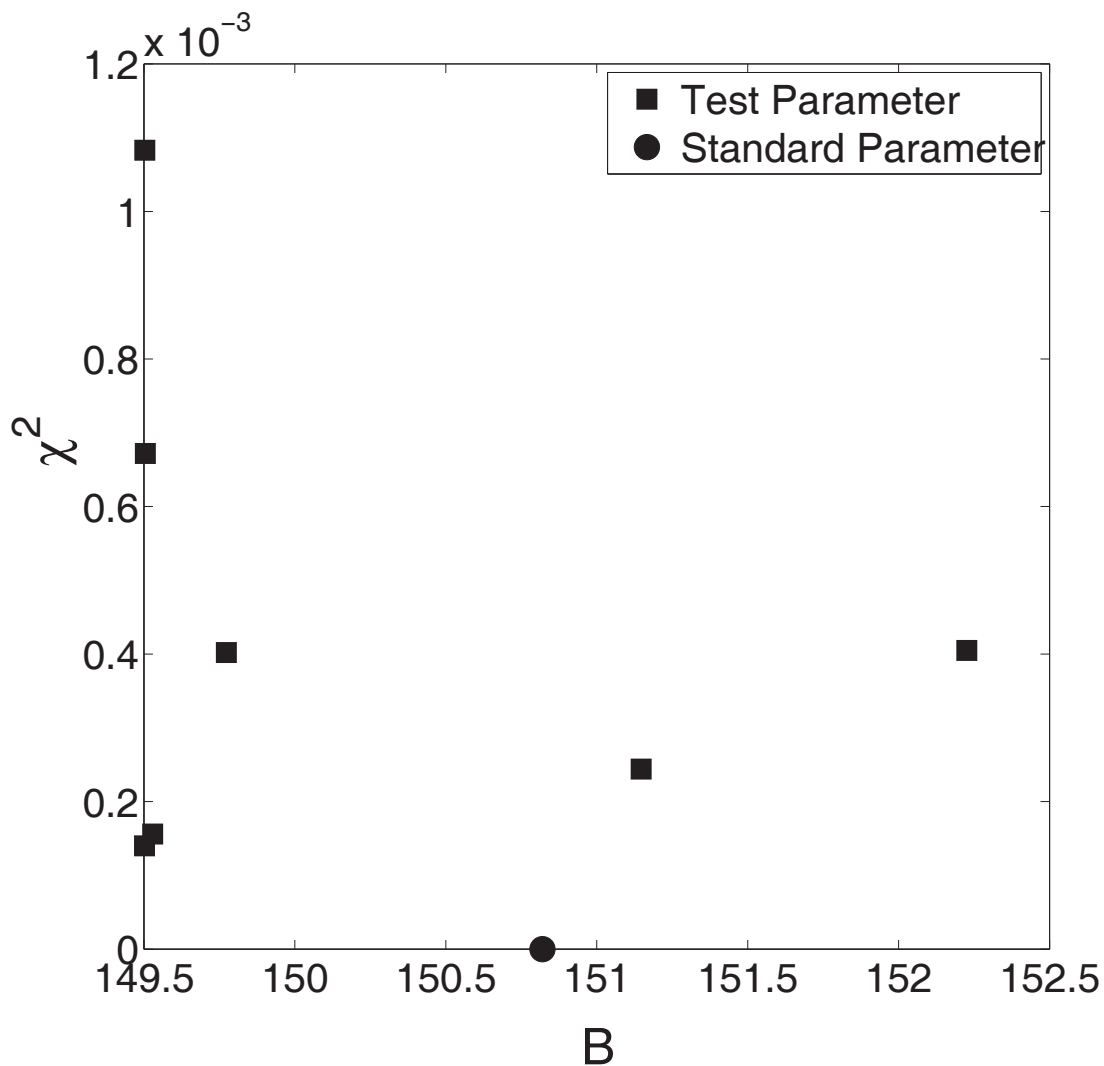
Figure 5.1: Plotting the test parameter values of B *vs.* the χ^2 value obtained during the sub-iterations of the 4th iteration

Parameters A and B

The starting parameter set (A_0, B_0) for the identification process $(\mathcal{S}^4_{AB})$ is (600 MPa, 100 MPa). The optimisation (Table 5.5) takes 3 main iterations to converge to the value of (690.862 MPa, 148.239 MPa). The converged parameters are identified at the end of 2 iterations and are confirmed in the third iteration. After the 3rd sub-iteration of the 3rd iteration the changes in the parameter values only occur in the third decimal place. Even though the standard set (A_s, B_s) is not matched exactly, the match in the chip shapes and cutting forces is excellent - this shows that the non-unique parameter sets can also equally well represent the flow stress curve in the given domain. The normalised non-overlap area is less than 1% and the cutting forces differ by less than 2%.

Sl. No.	$\#_M$	$\#_S$	A [MPa]	B [MPa]	χ^2
1	0	0	600	100	0.123050
2	1	0	703.920	129.904	0.007774
3	2	0	690.862	148.239	0.000866
4	3	0	696.530	146.401	0.001172
5		1	693.745	146.326	0.002724
6		2	691.255	147.830	0.001212
7		3	690.923	148.172	0.001013
8		4	690.868	148.232	0.000906
9		5	690.863	148.239	0.001838
10		6	690.862	148.239	0.000866

Table 5.5: $\mathcal{S}^4_{AB}$: Inverse identification of parameters A and B and corresponding χ^2. The standard set (A_s, B_s) is (688.17 MPa, 150.82 MPa).

Parameters A and n

The starting parameter set (A_0, n_0) for the identification process $(\mathcal{S}^5_{An})$ is (600 MPa, 0.2). The optimisation, when carried out with the usual values of w, δ_A and δ_n, gets stuck in a local minimum where the cutting force still differs by 10% from the standard cutting force. Since the cutting force does not converge well, factors likely to influence its convergence the most are identified. Increasing the weighting factor w gives more influence to the cutting force in the error function and is the obvious first choice for adjusting. However, it was seen in Chapter 4 that by changing parameter A, the stress-strain curve can be translated up or down, strongly influencing the cutting force. Therefore changing δ_A is also expected to influence the cutting force optimisation more than changing δ_n. The values for w and δ_A were obtained through trial and error. The contribution of the cutting force to the aggregate error function is first increased to $w = 10^{-2}\,\mathrm{mm^2\,N^{-1}}$. However, the convergence is still not satisfactory. δ_A is also increased to 10 MPa to improve the Jacobian estimation and this combination shows a better convergence for both the cutting force and the chip shape. The value of δ_n is maintained at 0.08.

When the two-stage optimisation is used later, the problem of adjusting the parameters for the Levenberg-Marquardt stage does not arise: the results from the first stage are used as the starting point in the

second stage, and the parameter space is searched around this point by using the downhill simplex method (Section 5.7). If the optimisation is stuck in a local minimum, the second stage provides a chance for the simplex to crawl out of it.

Using the new values of w and δ_A, the optimisation converges in 10 iterations (Table 5.6). The converged set (693.867 MPa, 0.3264) still differs from the standard set of (688.17 MPa, 0.3362). In the converged set, a slightly larger value of A is compensated by a slightly smaller value of n.

Sl. No.	$\#_M$	$\#_S$	A [MPa]	n	χ^2
1	0	0	600	0.2	4.081588
2	1	0	612.750	0.2608	3.160770
3	2	0	638.941	0.3656	0.979088
4	3	0	678.966	0.0510	0.620019
5	4	0	688.580	0.0812	0.407615
6	5	0	701.877	0.1292	0.144369
7	6	0	705.936	0.2570	0.068019
8	7	0	697.652	0.3645	0.028137
9	8	0	694.494	0.3293	0.047263
10		1	695.525	0.3367	0.009460
11	9	0	693.300	0.3280	0.021189
12		1	693.867	0.3264	0.008645
13	10	0	693.713	0.3169	0.026163
14		1	693.840	0.3255	0.014924
15		2	693.864	0.3263	0.021455
16		3	693.866	0.3264	0.035600
17		4	693.867	0.3264	0.008645

Table 5.6: $\mathcal{S}^5_{An}$: Inverse identification of parameters A and n and corresponding χ^2. The standard set (A_s, n_s) is (688.17 MPa, 0.3362).

Parameters B and n

The starting parameter set (B_0, n_0) for the identification process $(\mathcal{S}^6_{Bn})$ is (100 MPa, 0.2). In this optimisation the value of simulation parameters are: $w = 10^{-2} \ \mathrm{mm}^2 \, \mathrm{N}^{-1}$, $\delta_B = 8$ MPa and $\delta_n = 0.08$. These values are again obtained from trial and error, so that the converged solution is close to the standard set. The simulation converges in 5 main iterations and the converged set is (157.659 MPa, 0.3158). Even with a seemingly

large value of δ_n, the converged n is close to the standard value. This can be attributed to chance. The shape of the error landscape is roughly that of a parabolic cylinder (see Section 5.3.2), and the slope at a given point far from the minimum can be well estimated even with a large δ_n. Once the solution is close to the minimum, however, the solution cannot be further improved due to the noisy error landscape.

In Table 5.7 the values of n have been shown up to the 6th decimal place as even a small variation in n significantly changes the value of χ^2 due to noise. The converged value of B is slightly higher than the standard value, which is compensated by an n value slightly lower than the standard.

Sl. No.	$\#_M$	$\#_S$	B [MPa]	n	χ^2
1	0	0	100	0.2	2.39682
2	1	0	143.956	0.455315	0.23055
3	2	0	175.59	0.238017	0.21055
4	3	0	154.609	0.319006	0.15248
5	4	0	173.02	0.0382305	0.64496
6		1	162.886	0.303709	0.17790
7		2	157.659	0.315837	0.08085
8	5	0	153.72	0.287095	0.12744
9		1	156.682	0.308795	0.12547
10		2	157.561	0.315132	0.11453
11		3	157.649	0.315766	0.10886
12		4	157.658	0.31583	0.15877
13		5	157.659	0.315836	0.12490
14		6	157.659	0.315837	0.08085

Table 5.7: $\mathcal{S}^6_{Bn}$: Inverse identification of parameters B and n and corresponding χ^2. The standard set (B_s, n_s) is (150.82 MPa, 0.3362).

Noisy error landscape

It is evident from the results of optimisation that the error landscape is noisy. The noise in the error function comes mainly from the elastic waves in the workpiece which leads to a noise in the cutting force and, to a smaller extent, from chip vibration. To visualise the error landscape, the aggregate error function is evaluated using the mean cutting force error and the mean non-overlap error over the last 30 frames of observation. Parameter B is varied from 0 MPa to 250 MPa and parameter n from 0.1

to 0.5, and the aggregate error function is plotted (Figure 5.2). Clearly, when far from the global minimum, which lies at (150.82 MPa, 0.3362), the error landscape seems quite smooth. However, when zooming near the global minimum (Figure 5.3), a number of peaks and valleys can be seen. The Levenberg-Marquardt algorithm, when starting from a far-off point, takes larger steps towards the minimum and is not affected much due to the presence of noise in the landscape. Yet close to the minimum, the derivative estimate is incorrect due to the noisy error landscape and the algorithm gets stuck in a local minimum.

Figure 5.2: Error Landscape w.r.t parameters B and n. The global minimum lies in the region near $B = 150$ MPa and $n = 0.3$. ($A = 688.17$ MPa and $w = 10^{-3}$ mm^2 N^{-1})

To resolve this problem different strategies are evaluated:

Jacobian calculation using the central difference formula: In this strategy, the Jacobian is evaluated using the central difference formula, so that a better slope estimate is obtained at a point. The disadvantage of this method is that an extra machining simulation has to be done for each parameter direction, which adds to the computational expense (see Equation 5.24). For a finer mesh and

Figure 5.3: Zoom of error landscape near the region of $B = 150$ MPa and $n = 0.3$. A number of peaks and valleys can be seen due to the presence of noise.

for the identification of more than a few parameters, this method can become very expensive computationally.

Changing the weight parameter: The weight parameter w can be changed to give different weights to the non-overlap and the cutting force errors. This can also improve the convergence but needs a few trials to obtain the best value for w.

Changing the optimisation method (dual stage optimisation): After the first stage of optimisation, the converged set is used in a downhill simplex method. In this algorithm, if the size of the simplex is large enough, the local minimum can be overcome. Even in a noisy landscape, the parameter space is heuristically explored which makes the simplex algorithm more robust than the derivative-based optimisation mehtods. Using a dual stage optimisation process is attractive as no human intervention is required to adjust the parameters. However, the optimisation process can be time taking.

Central difference formula and weight parameter

Parameter identification has been carried out using the Levenberg-Marquardt algorithm in which the central difference method is used

to calculate the Jacobian (Equation 5.22). Parameters B and n are identified using this method for different values of parameter w (with $\delta_B = 5$ MPa and $\delta_n = 0.05$). For a comparison, identification runs were also carried out using the forward difference method for estimating the Jacobian. The δ_j values used in the central difference case are doubled in the forward difference case (with $\delta_B = 10$ MPa and $\delta_n = 0.1$) so that the distance between the two points remains the same for the Jacobian calculation. The starting set in all the cases was (100 MPa, 0.2).

	Id. No.	w $[\mathrm{mm}^2\,\mathrm{N}^{-1}]$	B [MPa]	n	$\Delta A_C\%$	$\Delta F_C\%$
Central difference formula	$\mathcal{S}_{Bn}^7$	10×10^{-3}	166.206	0.2610	1.52	1.49
	$\mathcal{S}_{Bn}^8$	2×10^{-3}	127.649	0.4354	1.47	2.52
	$\mathcal{S}_{Bn}^9$	1×10^{-3}	133.667	0.3612	0.90	2.74
Forward difference formula	$\mathcal{S}_{Bn}^{10}$	10×10^{-3}	173.509	0.2842	0.46	1.98
	$\mathcal{S}_{Bn}^{11}$	2×10^{-3}	156.785	0.3112	0.86	1.65
	$\mathcal{S}_{Bn}^{12}$	1×10^{-3}	157.41	0.2891	1.08	1.84

(a) Chip shape and cutting force agreement.

	Id. No.	w $[\mathrm{mm}^2\,\mathrm{N}^{-1}]$	N_I	N_s	# FE evals.
Central difference formula	$\mathcal{S}_{Bn}^7$	10×10^{-3}	4	3	23
	$\mathcal{S}_{Bn}^8$	2×10^{-3}	2	1	11
	$\mathcal{S}_{Bn}^9$	1×10^{-3}	3	4	19
Forward difference formula	$\mathcal{S}_{Bn}^{10}$	10×10^{-3}	5	6	21
	$\mathcal{S}_{Bn}^{11}$	2×10^{-3}	3	2	11
	$\mathcal{S}_{Bn}^{12}$	1×10^{-3}	3	6	18

(b) Number of iterations, sub-iterations and finite element evaluations.

Table 5.8: Comparison of the Jacobian estimation methods with different w values. The standard set $(B_s,\, n_s)$ is (150.82 MPa, 0.3362).

The parameter identification results are shown in Table 5.8. It can be observed that, in all the cases, the chip shapes and the cutting forces match, even though the converged parameters are not the same as the standard parameters (refer Table 5.8a). The chip shapes are indistinguishable and the cutting forces are also within 3% of the standard cutting force in all the cases. The choice of the Jacobian calculation method does not affect the optimisation result.

In Table 5.8b the number of iterations required for convergence are listed. In general, the central difference method needs marginally

fewer main and sub-iterations for convergence. However, when the total number of finite element evaluations is calculated for each of the cases, the forward difference formula requires a slightly smaller number of evaluations. The number of evaluations is counted only up to the penultimate main iteration (along with the Jacobian calculation for the final main iteration): in the last iteration, a number of sub-iterations take place while the damping parameter is increased and the parameter set converges to the parameter set from the penultimate main iteration. The number of these sub-iterations depends on the value of the damping parameter at the start of the iteration and is not affected by the method of Jacobian estimation.

It can be concluded from these results that using the central difference method is not more beneficial in terms of optimisation result than the forward difference method. However, this way the slope estimate is better than the forward difference method and fewer main iterations are needed for convergence. Therefore, when the starting parameter sets are far off from the standard set, using the central difference method might be advantageous to come as close as possible to the minimum in fewer iterations. Close to the minimum, however, the problem of noisy error landscape would still remain. A possible solution to this problem is to use the simplex algorithm in the next stage of optimisation.

5.4 Identification of 3 parameters

The identification algorithm is extended for the identification of 3 parameters: the parameter set (A, B, n) is to be identified. The central difference formula is used for Jacobian estimation. Two different starting points are used (identifications S_{ABn}^{13} and S_{ABn}^{14}): the first starting point (for S_{ABn}^{13}) is close to the standard set and the second one (for S_{ABn}^{14}) is further away. The parameters used during optimisation are : $w = 10^{-3}$ mm^2 N^{-1}, $\delta_A = 5$ MPa, $\delta_B = 5$ MPa, $\delta_n = 0.05$.

S_{ABn}^{13}: $A_0 = 650$ MPa, $B_0 = 120$ MPa, $n_0 = 0.25$

The optimisation converges in 8 iterations. The values for material parameters at each iteration are shown in Table 5.9.

S_{ABn}^{14}: $A_0 = 600$ MPa, $B_0 = 100$ MPa, $n_0 = 0.20$

The simulation converges in 8 iterations. The values for material parameters at each iteration are shown in Table 5.10.

In both the cases (identifications S_{ABn}^{13} and S_{ABn}^{14}), slightly different parameter sets are obtained which also differ from the standard parameter set. However, as can be seen in Table 5.11, the chip shapes and the cutting forces match extremely well. In the optimisation, two independent

Sl. No.	$\#_M$	$\#_S$	A [MPa]	B [MPa]	n	χ^2
1	0	0	650.000	120.000	0.250000	0.067171
2	1	0	647.738	152.973	0.434729	0.045822
3	2	0	653.236	152.629	0.268969	0.012355
4		0	668.871	143.700	0.434600	0.026138
5	3	1	664.304	156.053	0.371009	0.016724
6		2	662.817	156.311	0.298875	0.006529
7	4	0	677.874	168.313	0.355723	0.011007
8		1	671.314	160.625	0.307824	0.005656
9	5	0	666.391	159.417	0.300975	0.003755
10	6	0	674.911	163.086	0.310449	0.003114
11	7	0	680.358	164.165	0.314146	0.003295
12		1	677.137	163.512	0.311871	0.001606
13		0	680.453	164.912	0.307573	0.002870
14		1	677.731	163.755	0.311112	0.002104
15	8	2	677.199	163.537	0.311793	0.003897
16		3	677.144	163.515	0.311863	0.002649
17		4	677.138	163.512	0.311871	0.001898
18		5	677.137	163.512	0.311871	0.001606

Table 5.9: $\mathcal{S}_{ABn}^{13}$: Johnson-Cook parameters at the end of each iteration and the corresponding error function value. The standard set (A_s, B_s, n_s) is (688.17 MPa, 150.82 MPa, 0.3362).

observations, *viz.* the chip shape and the cutting force, have been used to identify three parameters, which is possible due to non-uniqueness (see Chapter 4). In Section 4.3, it was shown that a number of parameter sets can be found which give rise to adiabatic stress-strain curves similar to the standard adiabatic stress-strain curve, leading to similar chips and cutting forces at high cutting speeds. Within certain limits, if one of the parameters is fixed, the other two parameters can be found such that the chips and the cutting forces match. This can also be explained geometrically. The intersection of the isosurface (Figure 4.14a) with a plane whose value is that of the fixed parameter will give rise to a curve. The parameter set which leads to a chip shape and cutting force matching those of the standard set should lie inside this curve. In the current case, in which three parameters are being identified, the choice of the converged parameter set from the infinite number of possible combinations is arbitrary as none of the parameters are explicitly fixed by the user. To optimise the parameters over a large machining domain,

Sl. No.	$\#_M$	$\#_S$	A [MPa]	B [MPa]	n	χ^2
1	0	0	600.000	100.000	0.20000	0.13958
2	1	0	686.151	103.498	0.66921	0.05075
3	2	0	611.290	158.234	0.06359	0.11955
4		1	689.291	182.402	0.36449	0.01932
5	3	0	683.764	177.091	0.23906	0.00803
6	4	0	680.850	182.886	0.38879	0.03299
7		1	679.345	156.377	0.28141	0.00552
8	5	0	677.289	178.919	0.32260	0.01125
9		1	680.424	169.993	0.28407	0.00395
10	6	0	676.826	163.583	0.29082	0.00196
11	7	0	676.629	155.483	0.31947	0.00373
12		1	676.696	161.107	0.29591	0.00193
13	8	0	676.678	162.982	0.29628	0.00463
14		1	676.694	161.295	0.29595	0.00220
15		2	676.695	161.126	0.29591	0.00318
16		3	676.696	161.109	0.29591	0.00251
17		4	676.696	161.107	0.29591	0.00193
18		5	676.696	161.107	0.29591	0.00193

Table 5.10: $\mathcal{S}^{14}_{ABn}$: Johnson-Cook parameters at the end of each iteration and the corresponding error function value. The standard set (A_s, B_s, n_s) is (688.17 MPa, 150.82 MPa, 0.3362).

two standard simulations will be later used in fitting three parameters which give rise to four independent observations (Section 5.7.1).

Id. No.	Converged Set			$\Delta A_C\%$	$\Delta F_C\%$
	A [MPa]	B [MPa]	n		
$\mathcal{S}^{13}_{ABn}$	677.137	163.512	0.31187	0.32	1.61
$\mathcal{S}^{14}_{ABn}$	676.696	161.107	0.29591	0.61	1.76

Table 5.11: The converged sets showing the normalised non-overlap area and the cutting force difference at the end of the optimisation. The simulations were performed using a coarse mesh.

5.5   Effect of the mesh size

After a validation with an extremely coarse mesh, parameter identification is now carried out using a finer mesh with 20 elements in the

chip thickness direction. The standard parameter set is the same as that used during the validation runs *i.e.* AISI 52100, 62 HRC, and so are the cutting conditions (Table 5.1). The parameters used during the optimisation are: $w = 10^{-3}$ mm^2 N^{-1}, $\delta_A = 5$ MPa, $\delta_B = 5$ MPa, $\delta_n = 0.05$. The central difference formula is used for Jacobian estimation. Two different starting parameter sets are used so that one is close and the other far off from the standard set.

$\mathcal{S}_{ABn}^{15}$: $A_0 = 650$ MPa, $B_0 = 120$ MPa, $n_0 = 0.25$

In this case the starting set (650 MPa, 120 MPa, 0.25) is relatively close to the standard set (688.17 MPa, 150.82 MPa, 0.3362). The simulation converges in 6 iterations. The minimum value for χ^2 is reached at the end of the 5th iteration. During the 6th iteration the values of A, B and n change very slightly: the simulation is therefore stopped after the 3rd sub-iteration. The values for material parameters at each iteration and sub-iteration step are shown in Table 5.12.

Sl. No.	$\#_M$	$\#_S$	A [MPa]	B [MPa]	n	χ^2
1	0	0	650.000	120.000	0.250	0.237459
2	1	0	629.997	142.186	0.381	0.073710
3	2	0	646.212	145.045	0.390	0.062985
4	3	0	656.062	157.296	0.398	0.014958
5	4	0	655.854	135.097	0.437	0.019137
6		1	652.794	144.926	0.412	0.011674
7	5	0	658.781	141.315	0.405	0.049008
8		1	653.295	143.956	0.410	0.003965
9	6	0	652.478	141.996	0.407	0.062732
10		1	653.173	143.731	0.410	0.004123
11		2	653.241	143.857	0.410	0.050301
12		3	653.290	143.947	0.410	0.048858

Table 5.12: $\mathcal{S}_{ABn}^{15}$: JC parameters at the end of each iteration and the corresponding error function value. The standard set (A_s, B_s, n_s) is (688.17 MPa, 150.82 MPa, 0.3362).

$\mathcal{S}_{ABn}^{16}$: $A_0 = 200$ MPa, $B_0 = 50$ MPa, $n_0 = 0.050$

The starting set (200 MPa, 50 MPa, 0.050) is very different from the standard set (688.17 MPa, 150.82 MPa, 0.3362). The simulation converged in 4 iterations. The values for material parameters at each iteration are shown in Table 5.13.

In identification $\mathcal{S}_{ABn}^{15}$, the normalised non-overlap area of the starting chip is about 12% and the cutting force differs by around 10% from the standard cutting force (Table 5.14). At the end of the optimisation, the

Sl. No.	$\#_M$	$\#_S$	A [MPa]	B [MPa]	n	χ^2
1	0	0	200.000	50.000	0.050	2.10055
2	1	0	117.411	315.600	0.179	3.41683
3		1	483.766	113.322	0.131	0.71496
4	2	0	441.276	166.665	0.277	0.97535
5		1	649.217	175.218	0.216	0.07132
6	3	0	633.172	191.615	0.298	0.00242
7		0	635.283	195.298	0.267	0.00477
8		1	633.055	193.594	0.279	0.01407
9		2	630.937	190.456	0.297	0.02646
10	4	3	632.958	191.481	0.298	0.02872
11		4	633.149	191.600	0.298	0.02866
12		5	633.170	191.613	0.298	0.02731
13		6	633.172	191.614	0.298	0.02956
14		7	633.172	191.615	0.298	0.00242

Table 5.13: $\mathcal{S}^{16}_{ABn}$: JC parameters at the end of each iteration and the corresponding error function value. The standard set (A_s, B_s, n_s) is (688.17 MPa, 150.82 MPa, 0.3362).

chip shape is very similar to the standard chip shape as the normalised non-overlap area is less than 3% and the cutting force difference is around 3%. In identification $\mathcal{S}^{16}_{ABn}$, a similar result is observed: the chip shapes and the cutting force values of the converged chip are quite close to those of the standard. The cutting force which initially differs by about 70%, differs by less than 1% at the end of the optimisation. The normalised non-overlap area is around 6% at the end of the optimisation though (Table 5.14). Often when simulated chips are matched to experimentally obtained chips, such a difference can be acceptable (Calamaz *et al.* (2008)). However, in this theoretical study, the first stage results can be further optimised for an even better match, which will be described in detail in Section 5.7. An overlay of chip shapes for the two cases is shown in Figure 5.4.

Adiabatic stress-strain curves can be used to describe the deformation behaviour during a high speed machining process (Bäker (2004)). These curves are drawn for the starting, converged and standard sets for identification $\mathcal{S}^{16}_{ABn}$ to demonstrate the large changes in the curve shapes before and after optimisation as well as their comparison with the standard curve. At the start of the optimisation, the starting adiabatic stress-strain curve was far off from the standard curve while at the end

	A [MPa]	B [MPa]	n	$\Delta A_C\%$	$\Delta F_C\%$
Starting set	650	120	0.25	12.20	9.91
Converged set	653.295	143.956	0.410	2.62	3.09
Standard set	688.17	150.82	0.3362	-	-

(a) $\mathcal{S}^{15}_{ABn}$

	A [MPa]	B [MPa]	n	$\Delta A_C\%$	$\Delta F_C\%$
Starting set	200	50	0.05	9.38	70.22
Converged set	633.172	191.615	0.298	5.68	0.77
Standard set	688.17	150.82	0.3362	-	-

(b) $\mathcal{S}^{16}_{ABn}$

Table 5.14: The starting and the converged sets showing the normalised non-overlap area and the cutting force difference percentages. The simulations were performed using a fine mesh.

(a) $\mathcal{S}^{15}_{ABn}$ (b) $\mathcal{S}^{16}_{ABn}$
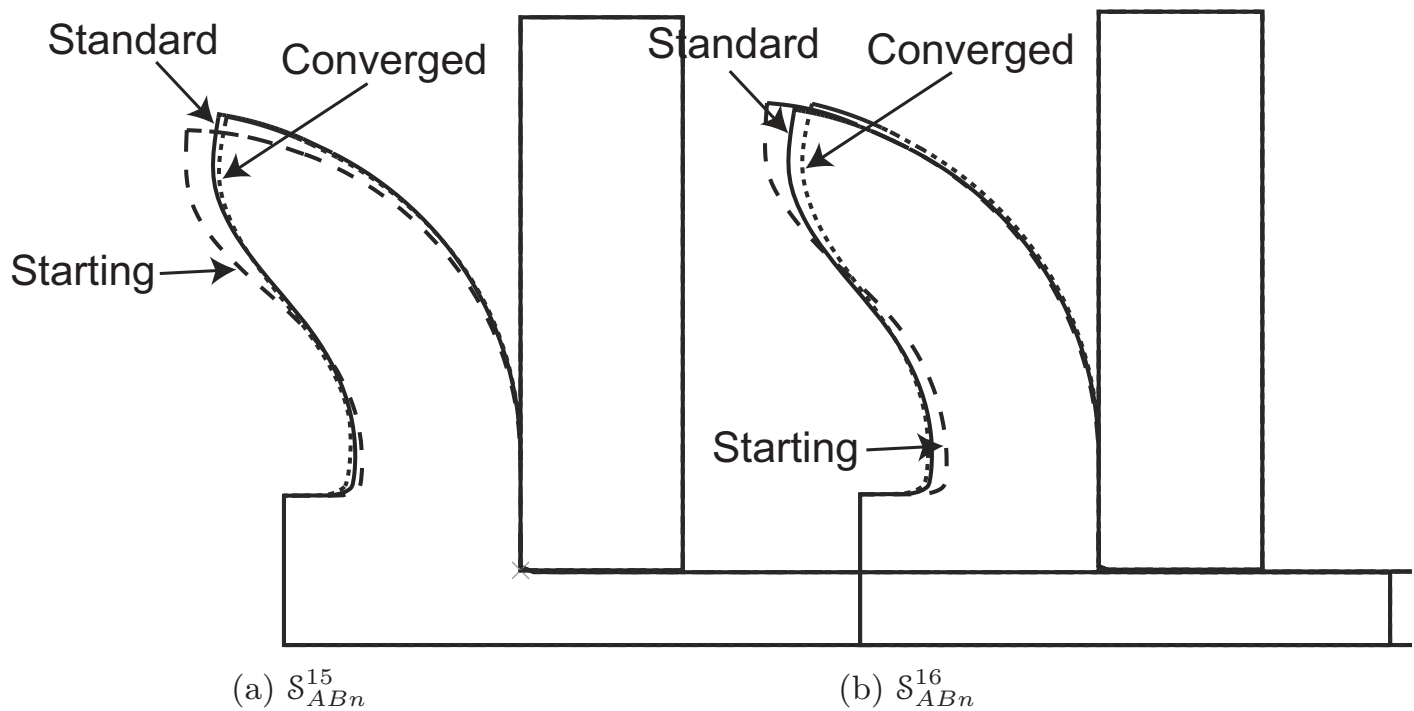
Figure 5.4: An overlay of standard, starting and converged chip shapes for the two cases

of the optimisation the converged curve is very close to the standard curve (Figure 5.5).
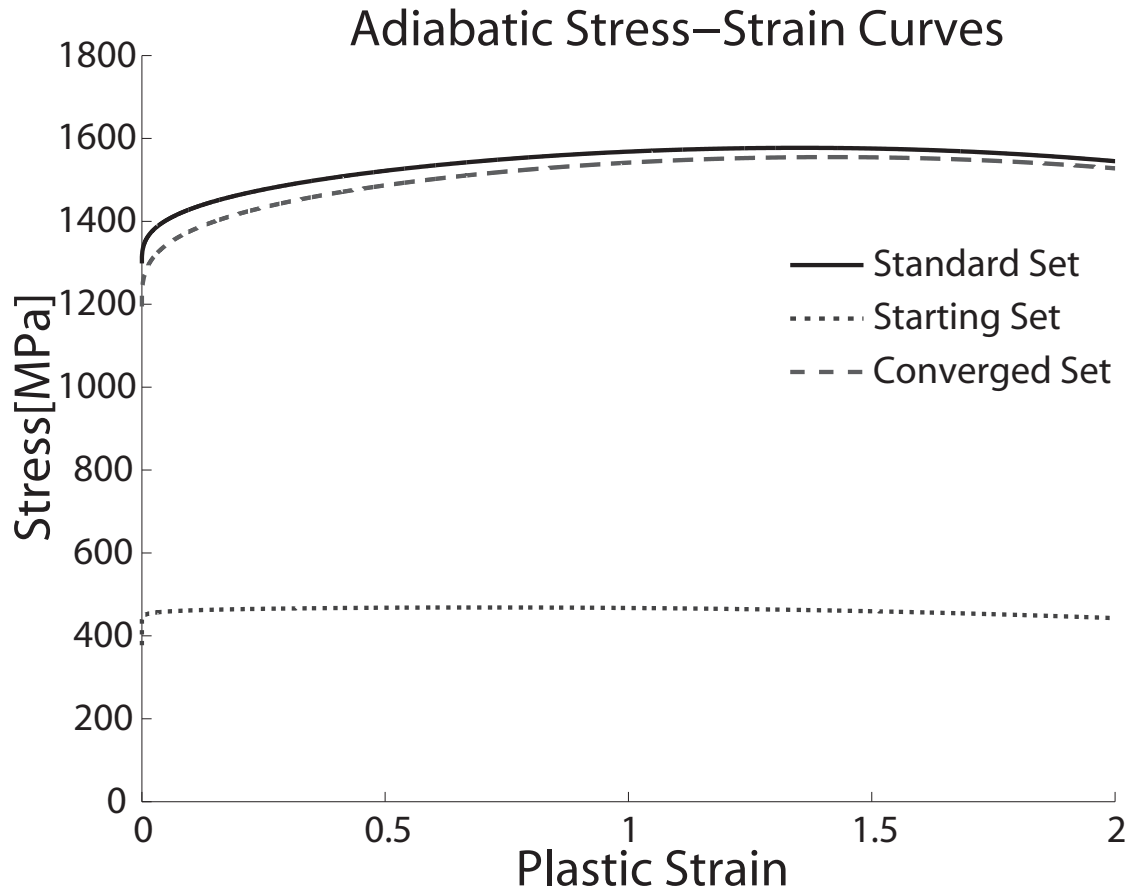
Figure 5.5: Comparison of adiabatic stress-strain curves for identification S_{ABn}^{16}.

In this case, the parameter identification is not sensitive to changes in the mesh density, even though with a finer mesh the noise in the error landscape is expected to be smaller. It was seen in Section 5.3.2 that even with a coarse mesh, the shape of the error landscape can be well approximated and therefore the identification with a coarse mesh is also good. Since in this theoretical study the mesh density can be kept constant for the standard and the test simulations, it does not influence the identification. However, when doing inverse identification for real life problems, a fine mesh will be required. This is in accordance with the basic fact of the finite element method, in which the finer the mesh, the smaller the approximation error and therefore the closer the simulation to reality.

5.6   Transformed optimisation variables

The choice of the optimisation variables can affect the convergence. Until now, parameters A, B and n have been used as the optimisation variables. A different choice of optimisation variables can however lead to better convergence rates, as shown in this section. The adiabatic stress-strain curves, which have been used before to approximate the material behaviour during high speed chip formation process, are used to determine the optimisation variables for inverse determination. The standard parameter set used is that of HY-100 steel (Tables 2.1 and 2.2). The standard set is changed from AISI 52100, 62 HRC to HY-100 in the following sections to check if the identification process is robust enough to work for a different parameter set. The parameter n in HY-100 is small and therefore should be more difficult to identify. The parameter m for HY-100 is small as compared to AISI 52100, 62 HRC, implying more thermal softening in case of HY-100.

The Johnson-Cook parameters A and B are varied from the standard values A_s and B_s in order to estimate the deviations between the corresponding adiabatic stress-strain curves. The root mean squared error (Equation 5.28) between the curves, expressed as

$$E_{rms}(A, B) = \frac{||\bar{\sigma}_{adia}(A, B) - \bar{\sigma}_{adia}(A_s, B_s)||}{\sqrt{M_{adia}}}, \tag{5.28}$$

is a measure of such deviations. Here $\bar{\sigma}_{adia}(A, B)$ is a vector consisting of points lying on the adiabatic stress-strain curve from parameters A and B, A_s and B_s are the target Johnson-Cook parameters and M_{adia} is the total number of points on the curve. $|| \bullet ||$ is the Euclidean norm.

On plotting E_{rms} w.r.t parameters A and B, a valley containing the minimum is seen to run in the direction of $(A - B)$ (Figure 5.6). Consequently the direction $(A + B)$ is the direction of steepest ascent. In case of HY-100, the value of n is small. Therefore, as long as $A + B$ is constant, E_{rms} is also almost constant.

New parameters K and L are defined so that

$$K = A + B \tag{5.29a}$$
$$L = A - B\,. \tag{5.29b}$$

Using the transformed variables (Equations 5.29a and 5.29b), the Johnson-Cook equation can be rewritten as

$$\sigma = \left(\frac{K + L}{2} + \frac{K - L}{2}\varepsilon^n\right) f(\dot{\varepsilon}, T), \tag{5.30}$$
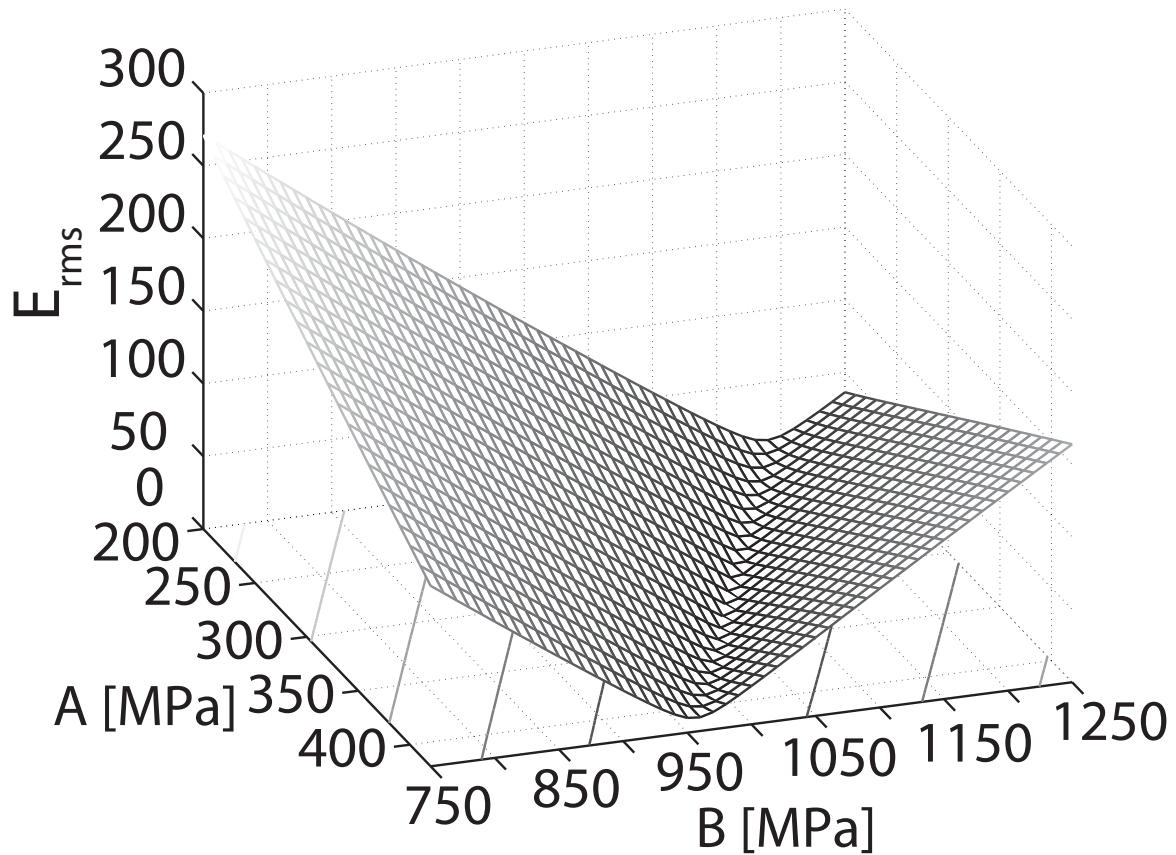
Figure 5.6: Three dimensional plot for E_{rms} along with the contour lines in the AB plane.

where

$$f(\dot{\varepsilon}, T) = \left[1 + C \ln\left(\frac{\dot{\varepsilon}}{\dot{\varepsilon}_0}\right)\right] \left[1 - \left(\frac{T - T_{room}}{T_{melt} - T_{room}}\right)^m\right] . \qquad (5.31)$$

Using the transformed variables, the identification of parameters is carried out for different values of weighting factor w. The starting parameter set (A_0, B_0) for optimisation using untransformed variables is (250 MPa, 900 MPa). In case of transformed variables the corresponding starting set (K_0, L_0) is (1150 MPa, -650 MPa). The cutting conditions for the simulations are listed in Table 5.15. A non-uniform mesh is used (as described in Section 2.5).

In both the cases, the weighting parameter w plays an important role in the optimisation. When a larger weight is given to the cutting force difference error, the cutting forces are well matched but the non-overlap area error is large (Tables 5.16 and 5.17). However, for smaller w values, the chip shapes are also well matched. For $w = 1/500$, the chip shape and cutting forces both are well optimised, especially when transformed variables are used for optimisation (Table 5.17).

Material	HY-100
Cutting Speed $[\mathrm{m\,s^{-1}}]$	33.3
Uncut chip thickness $[\mathrm{\mu m}]$	200
Coefficient of friction	0
Rake angle	0°
Mesh element type for Workpiece	CPE4R
Mesh element type for Tool	R2D2

Table 5.15: Cutting conditions for standard and test simulations for transformed and untransformed variables.

Clearly, using the transformed variables has a profound effect on the rate of convergence: on using the transformed variables, the convergence is achieved in fewer main iterations than in the case of untransformed variables. At each main iteration step, a Jacobian evaluation step is involved in which extra simulations have to be carried out for each parameter (one when the forward difference formula is used; two in the case of the central difference formula). Thus using the transformed variables leads to savings in the computational cost, which can be seen by comparing the total number of finite element evaluations until convergence is achieved for the two cases.

Id. No.	w	A [MPa]	B [MPa]	N_I	# FE evals.	$\Delta A_C\%$	$\Delta F_C\%$
$\mathbb{S}_{AB}^{17}$	1	455.567	925.945	8	32	8.34	0.74
$\mathbb{S}_{AB}^{18}$	1/100	502.960	878.904	4	22	10.67	0.92
$\mathbb{S}_{AB}^{19}$	1/500	392.528	918.596	7	31	0.75	3.80
$\mathbb{S}_{AB}^{20}$	1/1000	383.703	920.506	8	32	0.11	4.23

Table 5.16: Converged parameter sets for which optimisation is carried out with untransformed variables, A and B, for different values of w. The standard set (A_s, B_s) is (316 MPa, 1067 MPa).

5.7 Multistage optimisation

The steepest descent algorithms such as the Levenberg-Marquardt algorithm often converge to the local minimum closest to the starting point. In the previous sections, it was observed that the converged sets were

Id. No.	w	A [MPa]	B [MPa]	N_I	# FE eval.	$\Delta A_C\%$	$\Delta F_C\%$
$\mathcal{S}_{KL}^{21}$	1	395.530	988.869	5	23	5.06	0.69
$\mathcal{S}_{KL}^{22}$	1/100	384.363	1001.159	4	23	4.59	0.70
$\mathcal{S}_{KL}^{23}$	1/500	328.790	1035.145	5	22	0.09	1.06
$\mathcal{S}_{KL}^{24}$	1/1000	388.063	912.474	5	26	0.06	4.46

Table 5.17: Converged parameter sets for which optimisation is carried out with transformed variables, K and L, for different values of w. The standard set (A_s, B_s) is (316 MPa, 1067 MPa).

close to the minimum, but the cutting force and the chip shape match could be further improved in some cases (*e.g.* $\mathcal{S}_{ABn}^{16}$, $\mathcal{S}_{AB}^{17}$, $\mathcal{S}_{AB}^{18}$ *etc.*). Therefore two different possibilities are evaluated for further optimisation of the results obtained from the first stage.

1. Staggered optimisation

2. Dual method

The cutting conditions for the test and the standard simulations used in this section are listed in Table 5.18. A non-uniform mesh as described in Section 2.5 is used in all of these cases to reduce the computational expense. It was argued in Section 4.5 that a wide variation of the cutting conditions is required so that the identified parameter sets are valid over a large machining domain. It was also recommended that a positive and a negative rake angle simulation should be used to explore both the low and the high strains. In the following sections and sub-sections, two different rake angle are used for simulations. The positive rake angle used is $+10°$ and the other rake angle is either $0°$ or $+1°$. A negative rake angle is not used because during identification a large variation of parameter sets takes place during which it is possible that segmented chip formation might take place. Similarly, due to large variation, for some parameter combinations, the machined workpiece is soft and deforms so that the nodes from the separated chip come underneath the tool causing the simulation to crash. A slightly positive rake angle of $+1°$ is sufficient to promote the separated chip to move up the tool and prevent this problem.

Material	HY-100
Cutting Speed $[\mathrm{m\,s^{-1}}]$	33.3
Uncut chip thickness $[\mathrm{\mu m}]$	200
Coefficient of friction	0
Mesh element type for Workpiece	CPE4R
Mesh element type for Tool	R2D2

Table 5.18: Cutting conditions for standard and test simulations for multistage optimisations.

5.7.1 Staggered optimisation

In this method, different combinations of parameters are optimised at a given stage so that individual components of the error function are reduced preferentially. For example, parameters A and B play a greater role in setting the overall stress level (Section 4.1), which affects the cutting force value. Therefore, a good optimisation strategy to reduce the cutting force error is to optimise only these two parameters. In the case of transformed parameters, only K and L can influence parameters A and B. They are therefore used to improve the cutting force match.

Parameters A, B and n are identified using the staggered optimisation method. Two standard simulations are conducted at rake angles of 0° and 10° so as to optimise the parameter sets for low as well as high strain domains in machining. The weighting factor w is 1/500 during the optimisation. The last 15 frames of observations are used from each simulation to calculate the aggregate error function. Transformed variables K and L are used for the optimisation process using the Levenberg-Marquardt algorithm. The following steps are used for staggered optimisation:

Stage 1: Optimise parameters K, L and n to match the cutting force and the chip shape.

Stage 2: If the cutting force is not well matched, optimise parameters K and L to improve the cutting force match. The error function is not changed as the aim is not to match solely the cutting force irrespective of its effect on the chip shape.

Stage 3: Optimise parameters K, L and n together. After stage 2, the optimisation is out of the local minimum of stage 1 as the cutting force match is improved. It is possible that the cutting force and the chip shape can be further improved in this stage.

At the start of the identification ($\mathcal{S}^{25}_{KLn}$), the chip shapes differ significantly from the standard chips and the cutting force difference is higher than 10%. After the first stage of optimisation, the chip shapes and the cutting forces do not match well (Table 5.19b). While the difference in the chip shapes is around 4-5%, the cutting forces differ by approximately 9%, *i.e.* the cutting force difference improved only slightly in the first stage. In the second stage, only K and L are used for the optimisation, so that the cutting force difference improves. At the end of the second stage, the cutting force difference reduces to approximately 6% and the chip shape error worsens marginally. In the final stage of optimisation, parameters K, L and n are optimised together, as in the first stage. At the end of the third stage, the chip shape matches almost perfectly (normalised non-overlap area is around 1% or lower) and the cutting force difference remains around 6%. The starting and the converged parameter sets at each stage are shown in Table 5.19a. A chip shape overlay for each stage of optimisation is shown in Figures 5.7 and 5.8.

	A [MPa]	B [MPa]	n	N_I	N_T
Starting Set	250	900	0.020	-	-
Stage 1	287.11	935.36	0.080	3	10
Stage 2	255.52	1013.20	0.080	5	8
Stage 3	250.07	1020.18	0.088	2	9
Standard Set	316	1067	0.107	-	-

(a) $\mathcal{S}^{25}_{KLn}$: Starting and converged parameter sets along with the number of iterations for convergence. Transformed variables (K and L) are used during the optimisation. Here N_I represents the number of main iterations and N_T represents the total number of iterations.

	$\Delta A_C\%$		$\Delta F_C\%$	
	Rake 0°	Rake 10°	Rake 0°	Rake 10°
Starting Set	27.33	30.61	11.38	10.43
Stage 1	4.15	5.77	9.12	8.52
Stage 2	5.33	6.55	6.24	6.06
Stage 3	0.30	1.03	6.02	6.33

(b) $\mathcal{S}^{25}_{KLn}$: Chip shape and cutting force agreement at the end of each optimisation stage.

Table 5.19: $\mathcal{S}^{25}_{KLn}$: Parameter sets, chip shape and cutting force agreements at each stage of staggered optimisation.

(a) Start

(b) Stage 1

(c) Stage 2
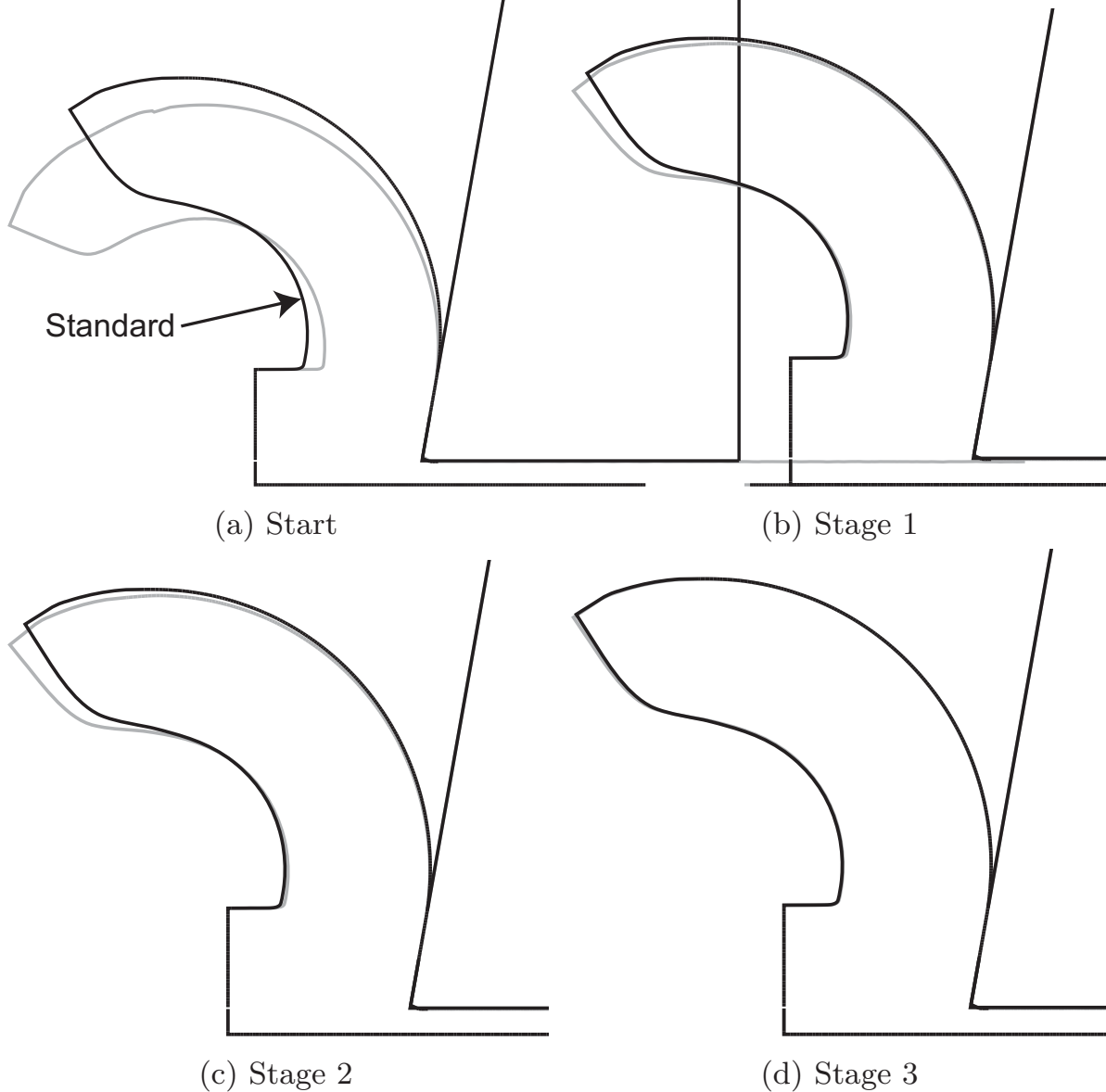
(d) Stage 3

Figure 5.7: $\mathbb{S}^{25}_{KLn}$: Chip shape overlay at various stages of optimisation for a rake angle of $+10°$.

The second stage, in which two parameters are optimised, allows the algorithm to come out of a local minimum and a new starting parameter set is found for the final stage. The disadvantage of this method is that constant human intervention is required to check the results of the converged sets. Furthermore, human assistance is also required for deciding if another stage of optimisation is still required.

5.7.2 Dual method

In a dual stage optimisation method, the Levenberg-Marquardt algorithm is used for the first stage and the downhill simplex algorithm is used for further optimisation. After the first stage, the converged

(a) Start   (b) Stage 1

(c) Stage 2   (d) Stage 3
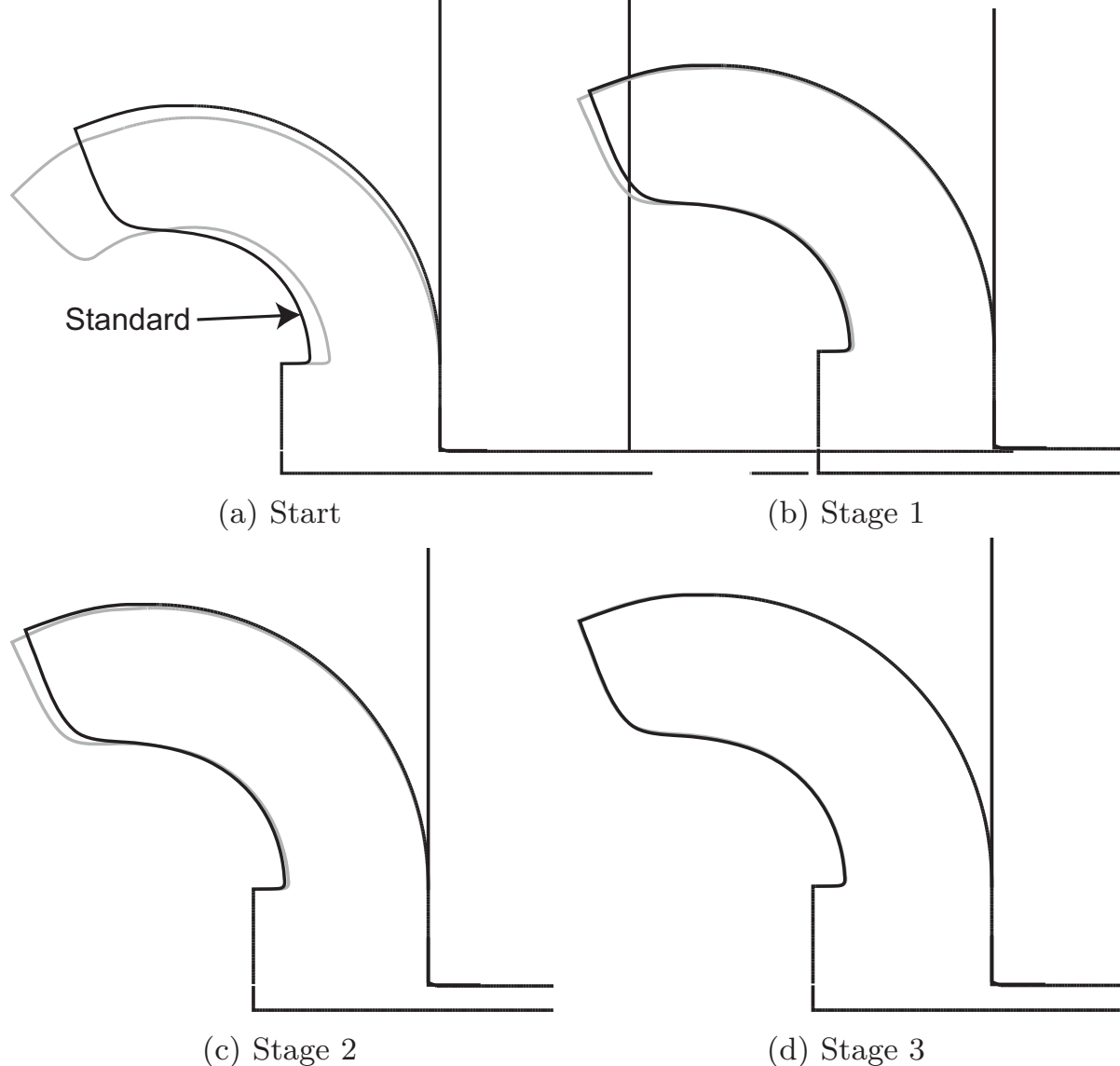
Figure 5.8: $\mathcal{S}^{25}_{KLn}$: Chip shape overlay at various stages of optimisation for a rake angle of $0°$.

chip shapes and cutting forces are usually close to the standard chip shapes and cutting forces. In the second stage, the simplex searches the parameter space around the first stage parameters and can overcome a local minimum to find a better solution. The size of the starting simplex determines the size of region which will be searched initially. The starting lengths of each of the sides of the simplex, used in this section, are shown in Table 5.20. In this sub-section, the first stage optimisation uses transformed optimisation parameters and the second stage uses untransformed parameters.

Case 1 ($\mathcal{S}^{26}_{KLn}$): The parameter set obtained from the Stage 1 of optimisation $\mathcal{S}^{25}_{KLn}$ in the previous Section 5.7.1 is used as an input for the simplex stage. The optimisation ran for 16 iterations and the cutting

Δ_A [MPa]	Δ_B [MPa]	Δ_n
30	30	0.05

Table 5.20: Side lengths of the starting simplex

force and chip shapes are perfectly matched. The iterations have been shown in Table 5.21. The first evaluation of the second stage is the same as the evaluation of the converged set from the first stage. The next 3 evaluations are the neighbouring nodes in each of the parameter directions.

The sub-iterations take place when the expansion, contraction or reduction steps occur after the mandatory reflection step. In Figure 5.9, the change in the size of the simplex with the progress of the optimisation is shown. Initially the size of the simplex marginally reduces. Once it crawls out of a local minimum, its size increases so that it takes long steps towards the minimum. Finally, its size reduces gradually till the solution converges to the final set. The crawl of the simplex through the parameter space (A, B, n) can be visualised by drawing a tetrahedron for each step of the iteration (Figure 5.10). At the end of the optimisation, the chip shapes and the cutting forces match extremely well (Table 5.22b). The starting set and the converged sets from each stage have been shown in Table 5.22a.

Case 2 ($\mathcal{S}_{KLn}^{27}$) and 3 ($\mathcal{S}_{KLn}^{28}$): To test the robustness of the method, parameter identification was carried out for two different starting points which differed significantly from the standard set (Tables 5.23a and 5.24a). Two standard simulations are carried out at rake angles of $+1°$ and $+10°$. Using the dual optimisation method, the chip shapes and the cutting forces are optimised. In case 2 ($\mathcal{S}_{KLn}^{27}$), while the match is already extremely good after the Levenberg-Marquardt step, the second step of the simplex is done to see if the standard set parameters can be re-identified. However, the result does not improve much after this step. The comparison of the chip shapes and the cutting forces for case 2 ($\mathcal{S}_{KLn}^{27}$) at each stage of optimisation is listed in Table 5.23b. The results are more interesting in case 3 ($\mathcal{S}_{KLn}^{28}$). The starting set is extremely far from the standard set and therefore the cutting force and the chip shapes are initially completely different. After the first optimisation step, the chip shapes match almost perfectly but the cutting forces still differ by around 10%. After the simplex step, the chip shapes and the cutting forces are almost perfectly matched (Table 5.24b).

Sl No.	$\#_M$	$\#_S$	A [MPa]	B [MPa]	n	χ^2
1	0	0	287.11	935.36	0.080	0.0665
2			317.11	935.36	0.080	0.0689
3			287.11	965.36	0.080	0.0635
4			287.11	935.36	0.130	0.2874
5	1	0	307.11	955.36	0.030	0.3592
6		1	292.11	940.36	0.105	0.0969
7	2	0	302.11	950.36	0.055	0.1918
8		1	294.61	942.86	0.092	0.0335
9	3	0	262.11	960.36	0.088	0.0444
10	4	0	275.44	977.03	0.094	0.0352
11	5	0	267.67	954.80	0.103	0.1222
12		1	282.25	962.72	0.086	0.0367
13	6	0	306.09	961.38	0.093	0.0201
14		1	328.08	961.89	0.096	0.0199
15	7	0	316.51	958.46	0.102	0.0313
16	8	0	350.69	931.78	0.100	0.0178
17		1	388.31	909.16	0.102	0.0218
18	9	0	368.91	958.56	0.106	0.0078
19		1	406.06	966.41	0.112	0.0056
20	10	0	406.71	948.26	0.103	0.0214
21		1	384.16	950.81	0.103	0.0176
22	11	0	432.53	937.44	0.114	0.0074
23	12	0	464.48	971.33	0.120	0.0280
24		1	379.14	941.67	0.105	0.0115
25	13	0	427.65	946.21	0.118	0.0019
26		1	449.40	943.90	0.126	0.0010
27	14	0	479.52	956.84	0.130	0.0084
28		1	454.43	953.05	0.124	0.0035
29	15	0	440.73	971.46	0.127	0.0032
30	16	0	490.31	945.87	0.139	0.0078
31		1	427.12	961.27	0.119	0.0020

Table 5.21: $\mathcal{S}^{26}_{KLn}$: Parameter sets during the simplex stage (Case 1). The minimum χ^2 is obtained in the 1st sub-iteration of the 13th main iteration. The standard set (A_s, B_s, n_s) is (316 MPa, 1067 MPa, 0.107).
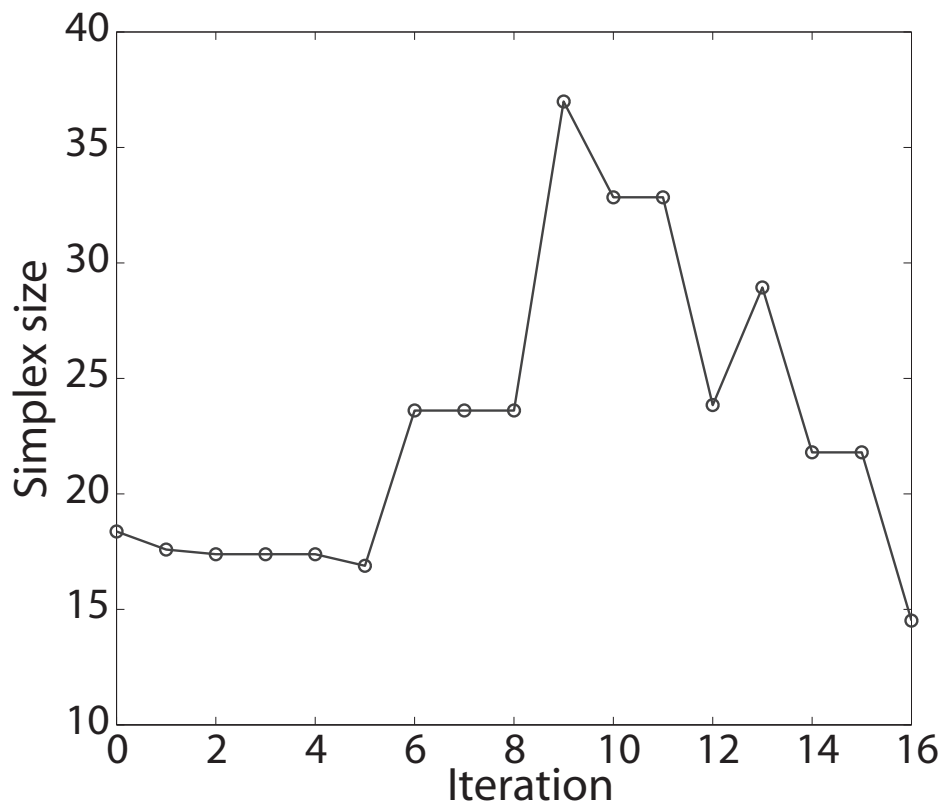
Figure 5.9: Change in the size of the simplex during the identification $\mathcal{S}^{26}_{KLn}$.

	A [MPa]	B [MPa]	n
Starting Set	250	900	0.020
LM Stage	287.11	935.36	0.080
Simplex Stage	449.4	943.9	0.126
Standard Set	316	1067	0.107

(a) Starting and converged parameter sets at each stage of optimisation.

	$\Delta A_C\%$		$\Delta F_C\%$	
	Rake 0°	Rake 10°	Rake 0°	Rake 10°
Starting Set	27.33	30.61	11.38	10.43
LM Stage	4.15	5.77	9.12	8.52
Simplex Stage	0.38	0.13	1.11	1.24

(b) Chip shape and cutting force agreement at the end of each optimisation stage.

Table 5.22: Case 1 ($\mathcal{S}^{26}_{KLn}$): Identification of parameters (A, B, n) using the dual stage optimisation method.

(a) iteration = 0

(b) iteration = 1

(c) iteration = 2

(d) iteration = 3

(e) iteration = 4

(f) iteration = 5

Figure 5.10: $\mathcal{S}^{26}_{KLn}$: Crawl of the simplex through the parameter space (A, B, n).

(g) iteration = 6

(h) iteration = 7

(i) iteration = 8

(j) iteration = 9

(k) iteration = 10

(l) iteration = 11

Figure 5.10: $\mathcal{S}_{KLn}^{26}$: Crawl of the simplex through the parameter space (A, B, n).

(m) iteration = 12

(n) iteration = 13

(o) iteration = 14

(p) iteration = 15

(q) iteration = 16
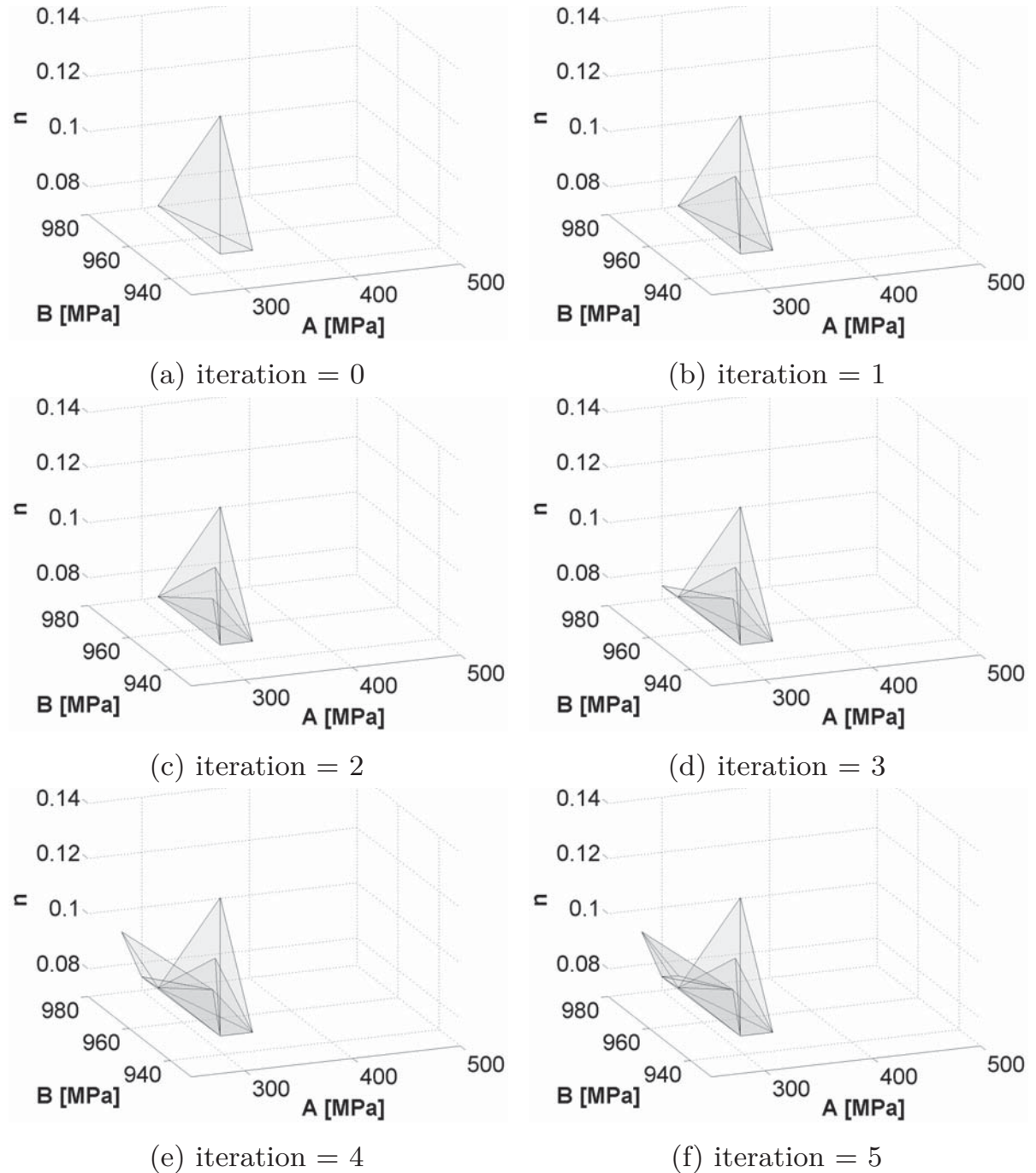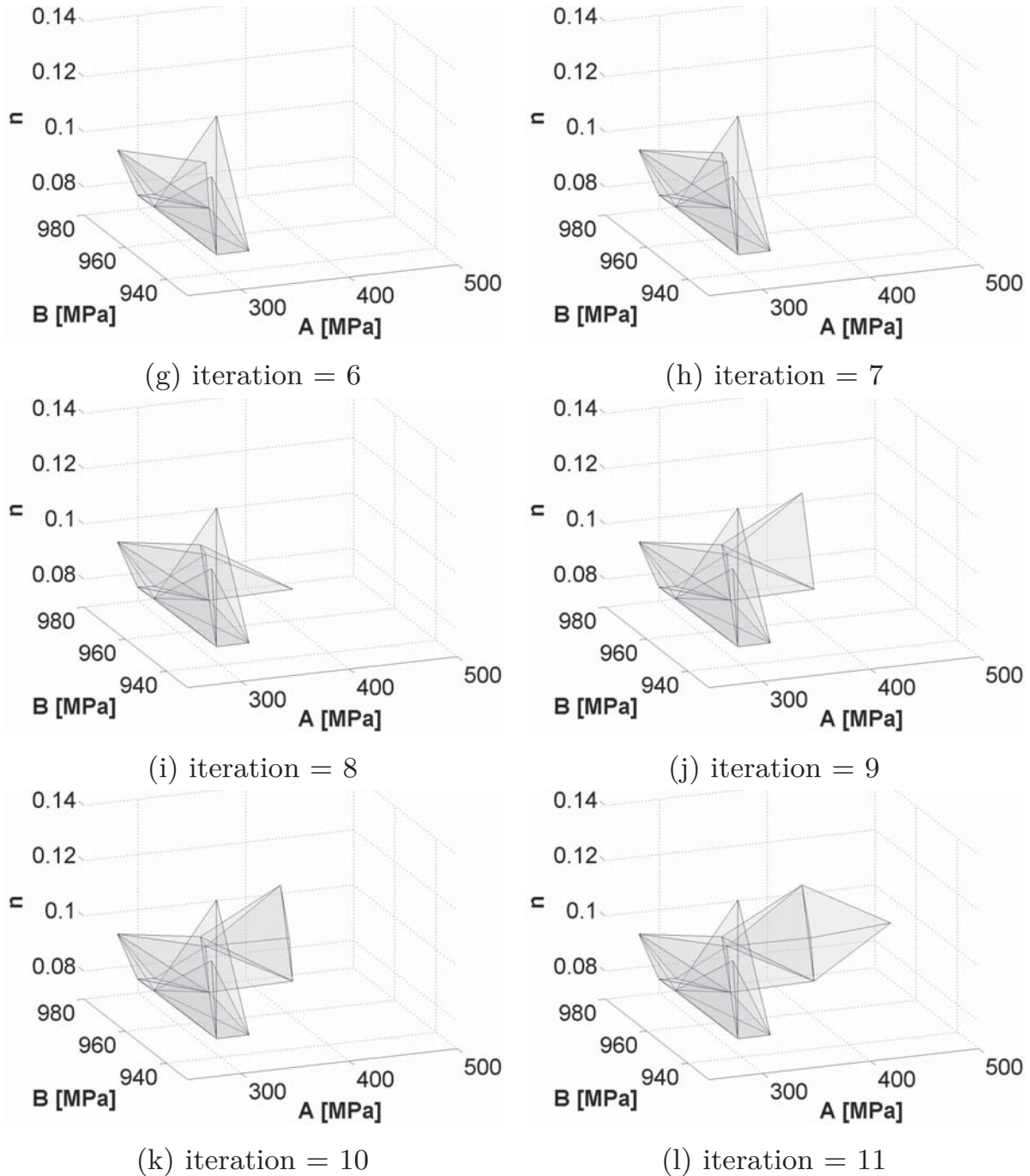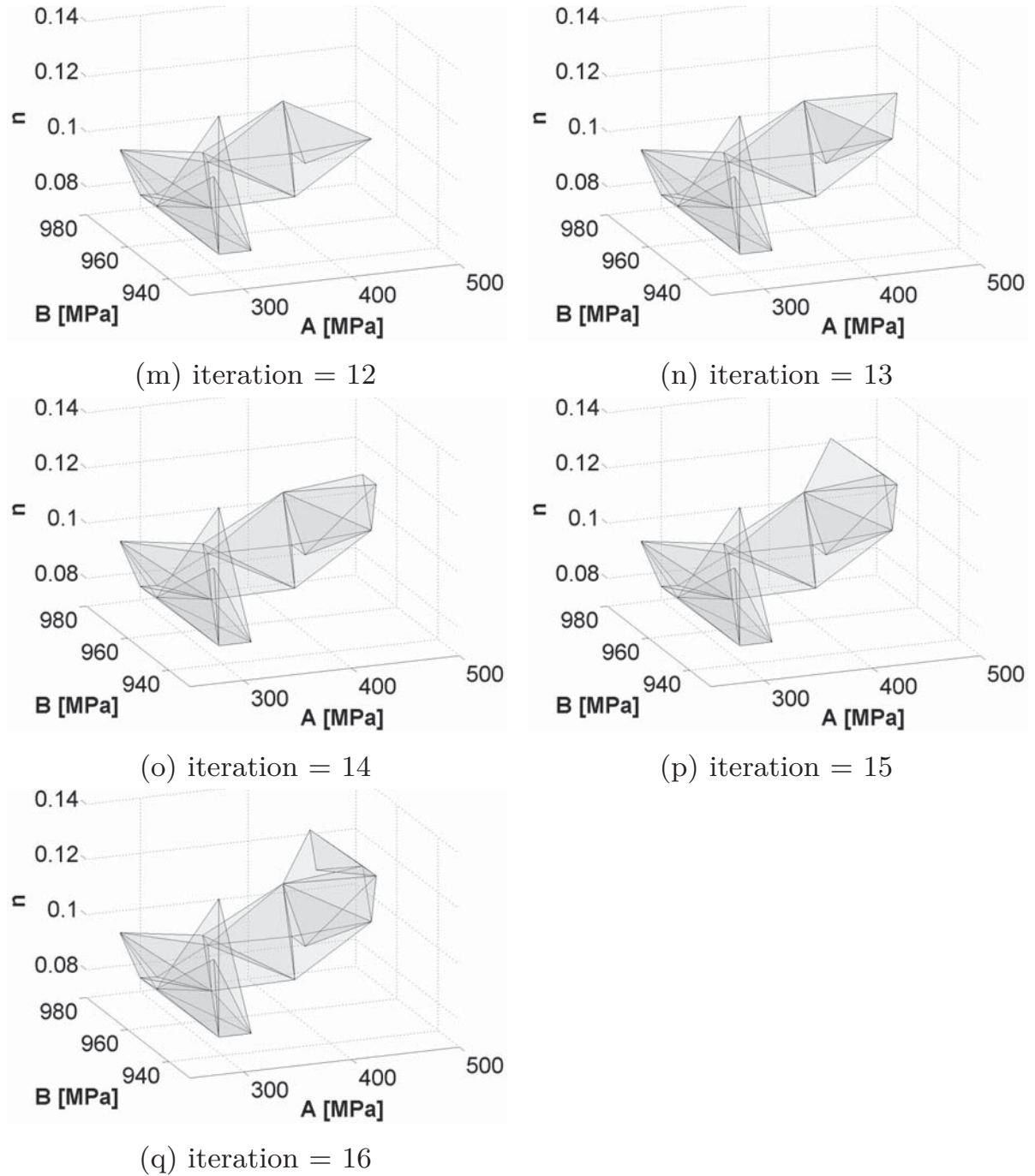
Figure 5.10: $\mathcal{S}_{KLn}^{26}$: Crawl of the simplex through the parameter space (A, B, n).

The non-uniqueness of the parameter sets is evident in all these cases (S_{KLn}^{26}, S_{KLn}^{27} and S_{KLn}^{28}) as the converged parameter sets are different from the standard set (Tables 5.22a, 5.23a and 5.24a). The adiabatic stress-strain curves at every stage of optimisation have been plotted for each of the cases. It can be observed that the adiabatic stress-strain curve comes as close as possible to the standard curve as the optimisation progresses, so that at the end of the optimisation the standard and the optimised curves are indistinguishable (Figure 5.11).

For cases 1 (S_{KLn}^{26}) and 3 (S_{KLn}^{28}), it was observed that the chip shapes were well optimised after the first step of optimisation but the cutting forces differed by approximately 10% (Tables 5.22b and 5.24b). This can be observed in the adiabatic stress-strain curves: the shapes of the curves are very close to the standard curve after the first optimisation stage. However, the average stress levels differ by around 10%.

For case 2 (S_{KLn}^{27}), the cutting forces and chip shapes already match extremely well after the first optimisation step. Correspondingly the stage 1 and standard adiabatic stress-strain curves also match very well for this case. Finally the chip shape and the cutting force match almost perfectly to the standard after the simplex step and so do the adiabatic stress-strain curves to the standard curve. The insights gained from these results will be used for a faster optimisation method, which will be described in Section 5.11.

	A [MPa]	B [MPa]	n
Starting Set	800	50	0.4
LM Stage	943.6	435.6	0.306
Simplex Stage	942.4	445.3	0.309
Standard Set	316	1067	0.107

(a) Starting and converged parameter sets at each stage of optimisation.

	$\Delta A_C\%$		$\Delta F_C\%$	
	Rake 1°	Rake 10°	Rake 1°	Rake 10°
Starting Set	7.81	9.09	30.95	30.91
LM Stage	0.21	2.60	1.01	0.89
Simplex Stage	1.05	1.34	0.86	1.01

(b) Chip shape and cutting force agreement at the end of each optimisation stage.

Table 5.23: Case 2 (S_{KLn}^{27}): Identification of parameters (A, B, n) using the dual stage optimisation method.

(a) Case 1 $(\mathcal{S}_{KLn}^{26})$

(b) Case 2 $(\mathcal{S}_{KLn}^{27})$

(c) Case 3 $(\mathcal{S}_{KLn}^{28})$
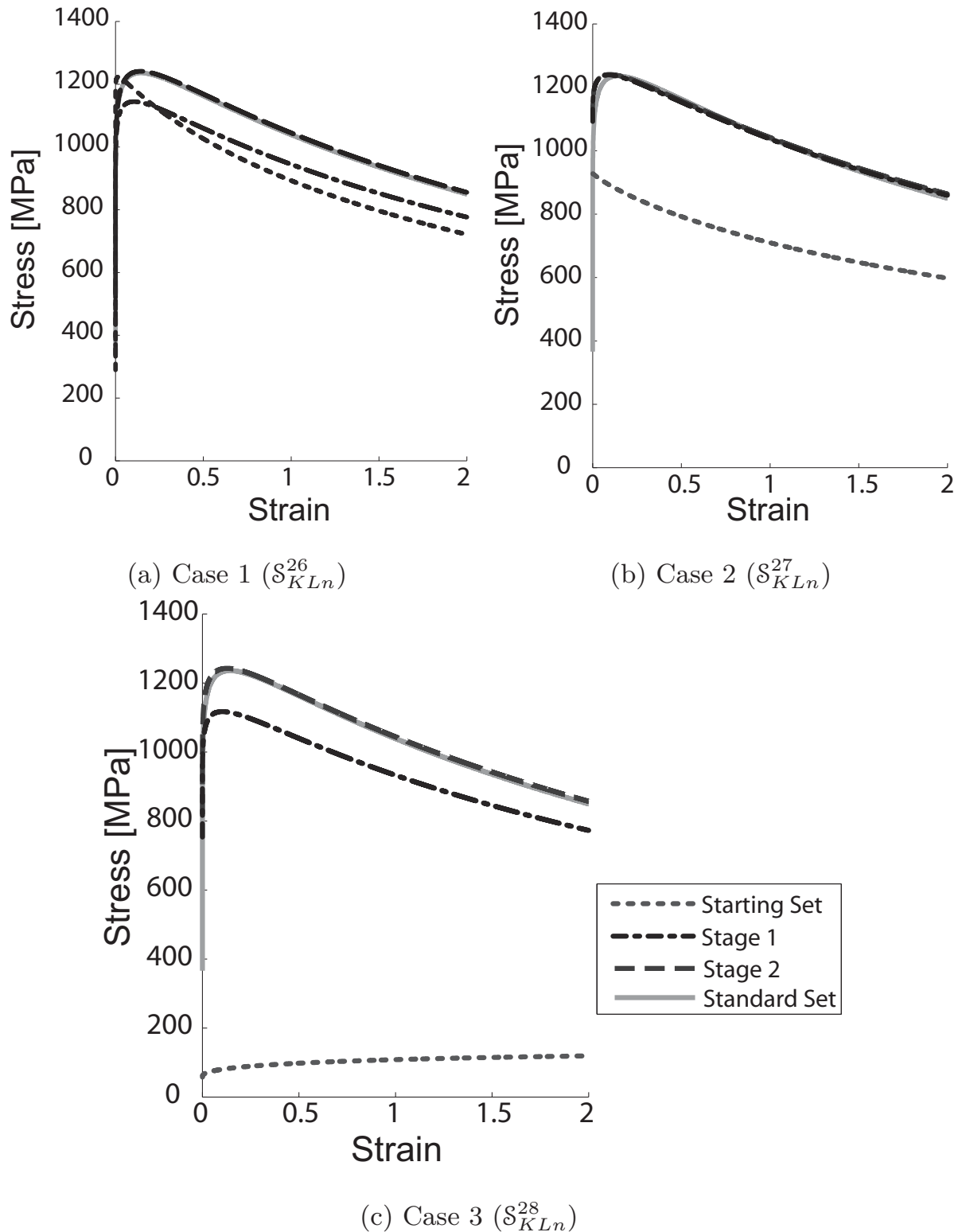
Figure 5.11: Adiabatic stress-strain curves at different stages of optimisation

	A [MPa]	B [MPa]	n
Starting Set	50	50	0.4
LM Stage	650.6	549.3	0.151
Simplex Stage	707.7	684.4	0.180
Standard Set	316	1067	0.107

(a) Starting and converged parameter sets at each stage of optimisation.

	$\Delta A_C\%$		$\Delta F_C\%$	
	Rake 1°	Rake 10°	Rake 1°	Rake 10°
Starting Set	72.85	80.74	82.62	85.32
LM Stage	0.68	1.16	9.82	10.37
Simplex Stage	0.03	1.23	0.93	1.06

(b) Chip shape and cutting force agreement at the end of each optimisation stage.

Table 5.24: Case 3 ($\mathcal{S}^{28}_{KLn}$): Identification of parameters (A, B, n) using the dual stage optimisation method.

5.8   Effect of the error function

Until now, Equation 5.27 has been used in the inverse identification method. Multiple frames of observation are used in calculating the error function. In a real life identification process, however, only the final chip shape and the average cutting force will be available as the recording of chip shape evolution and cutting force evolution at high cutting speeds is difficult. It is possible that the extra information obtained from the intermediary frames can influence the identification process. It is assumed that the effect is negligible on the identification process, but this assumption must still be verified.

In order to do this, an error function is created which uses the chip shape overlap errors at the last frame of the simulation and the difference of the average cutting force. Two different rake angles are used for the standard simulation ($+1°$ and $+10°$) and the average cutting force is calculated over the last 15 frames of simulation. The error function is given by

$$\chi^2(\mathbf{a}) = \frac{1}{2}\left(e^A_{\alpha 1}(\mathbf{a})^2 + w^2.e^F_{\alpha 1}(\mathbf{a})^2 + e^A_{\alpha 2}(\mathbf{a})^2 + w^2.e^F_{\alpha 2}(\mathbf{a})^2\right) . \quad (5.32)$$

Here $\alpha 1$ and $\alpha 2$ represent the two rake angles used during identification.
    The optimisation ($\mathcal{S}^{29}_{KLn}$) was conducted using the Levenberg-Marquardt algorithm in which parameters (A, B, n) are re-identified. Transformed

parameters are used during the optimisation. The standard parameter set is that of HY-100 and the cutting parameters are given in Table 5.18. A non-uniform mesh is used to reduce the computational expense. A weighting factor of $w = 1/500$ mm^2 N^{-1} is used during the optimisation. The starting parameter set is (50 MPa, 50 MPa, 0.4) and in the Levenberg-Marquardt step the transformed parameters (K, L) are used for optimisation. In 12 main iterations, the optimisation converges to (774.74 MPa, 610.33 MPa, 0.204) (Table 5.25a) and the chip shapes and the cutting forces match extremely well (Table 5.25b).

	A [MPa]	B [MPa]	n	χ^2
Starting set	50	50	0.4	0.293
Converged set	774.74	610.33	0.204	8.12×10^{-06}
Standard Set	316	1067	0.107	-

(a) Parameter sets at each stage of optimisation.

	$\Delta A_C \%$		$\Delta F_C \%$	
	Rake 1°	Rake 10°	Rake 1°	Rake 10°
Starting Set	72.85	80.74	82.62	85.32
LM Stage	0.21	0.91	0.05	0.08

(b) Chip shape and cutting force agreement at the end of each optimisation stage.

Table 5.25: $\mathcal{S}^{29}_{KLn}$: Parameter identification using Equation 5.32 as the error function.

Both the error functions given by Equation 5.27 and Equation 5.32 are effective in re-identifying the material parameters, as evidenced by Tables 5.24 and 5.25. When using Equation 5.27 as the error function, the magnitude of the cutting force difference is used. Thus during the estimation of the Jacobian it is not known if the test cutting force is higher or lower than the standard cutting force. This problem is however not there when using Equation 5.32, making it better when using the Levenberg-Marquardt algorithm. Due to the non-uniqueness of the parameter sets, as discussed in Chapter 4, the converged parameter set is not the same as the standard set, which is not affected by the choice of the error function.

5.9   Non-adiabatic optimisation

As discussed in Section 4.4, simulations should be carried out with widely varying cutting conditions to identify robust parameter sets which predict the correct flow stress in the domain of machining. Non-adiabatic simulations along with varying rake angles were found to eliminate the parameter sets which do not represent the flow the curve in a large machining domain. Therefore, in this section, parameter identification ($\mathcal{S}_{KLn}^{30}$) is carried out using two different standard simulations with a cutting speed of 0.5 m s^{-1} and rake angles of $+1°$ and $+10°$. Non-adiabatic simulations are conducted with a mass scaling factor of 3000. The cutting conditions used in this section are listed in Table 5.26. Parameters (A, B, n) are to be re-identified.

Material	HY-100
Cutting Speed [m s^{-1}]	0.5
Uncut chip thickness [µm]	200
Coefficient of friction	0
Rake angle	$+1°$ and $+10°$
Mesh element type for Workpiece	CPE4RT
Mesh element type for Tool	R2D2
Mass scaling factor	3000

Table 5.26: Cutting conditions for standard and test simulations for non-adiabatic optimisations.

Similar to Section 5.6, on plotting E_{rms} for parameters A and B using the isothermal stress-strain curves, a valley containing the minimum is seen to run in the $(A - B)$ direction. Consequently, transformed variables (K, L) are used during the optimisation. The dual optimisation method is used for parameter identification. For the Levenberg-Marquardt step, the optimisation parameter is $w = 10^{-3}$ mm^2 N^{-1}.

The parameter sets at the end of each stage of optimisation are listed in Table 5.27a. At the start of the optimisation, the chip shapes and the cutting forces differ widely from the standards. In Table 5.27b, notably, the normalised chip shapes percentages are greater than 100%: this happens when the chip shapes differ so much that the area of non-overlap is greater than the area of the standard chip itself. After the first stage of optimisation, the chip shapes agree extremely well ($\Delta A_C\%$ around 1%); however the cutting force differs by approximately 50%. Since a large improvement is expected in the cutting force in the simplex

	A [MPa]	B [MPa]	n
Starting Set	50	50	0.4
LM Stage	308.4	258.1	0.111
Simplex Stage	610.2	769.1	0.148
Standard Set	316	1067	0.107

(a) Starting and converged parameter sets. Transformed variables (K and L) are used during the optimisation using non-adiabatic simulations.

	$\Delta A_C\%$		$\Delta F_C\%$	
	Rake 1°	Rake 10°	Rake 1°	Rake 10°
Starting Set	113.35	118.40	84.39	86.78
LM Stage	1.26	1.67	50.83	51.64
Simplex Stage	1.01	2.61	1.12	1.13

(b) Chip shape and cutting force agreement at the end of each optimisation stage.

Table 5.27: $\mathbb{S}^{30}_{KLn}$: Identification of parameters (A, B, n) using the dual stage optimisation process from non-adiabatic simulations.

stage, the starting size of A and B sides (Δ_A and Δ_B) are increased to 100MPa as these parameters should influence the cutting force the most. The starting size of the n side is kept unchanged at 0.05. After the simplex stage, the chip shapes and cutting forces match almost perfectly, with $\Delta A_C\%$ around 1-2% and $\Delta F_C\%$ around 1%.

The chip shapes for different rake angles and the isothermal stress strain curves at each optimisation stage are plotted in Figures 5.12, 5.13 and 5.14. The corresponding parameter sets at each stage of optimisation are shown in Table 5.27a. It can also be noticed that the isothermal stress-strain curves come closer to the standard curve at each stage and are finally indistinguishable.

5.10 Identification of other parameter combinations

It was demonstrated in previous sections that parameters (A, B, n) can be re-identified robustly, although the converged sets are non-unique. In this section, the re-identification of other parameter set combinations will be shown.

(a) Starting stage

(b) Levenberg-Marquardt stage
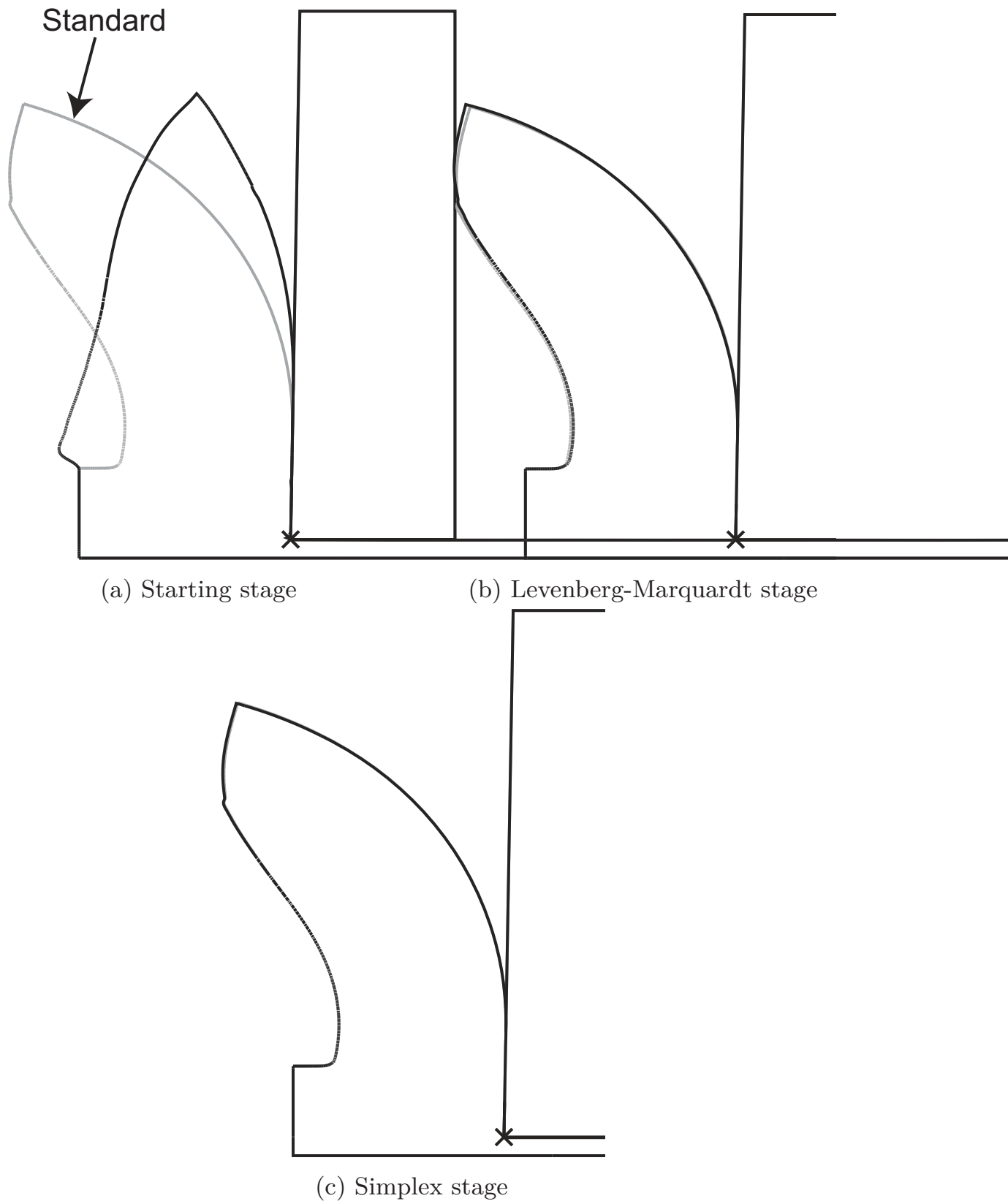
(c) Simplex stage

Figure 5.12: $\mathcal{S}^{30}_{KLn}$: Comparison of the chip shapes (Rake angle $= +1°$) at different stages of optimisation
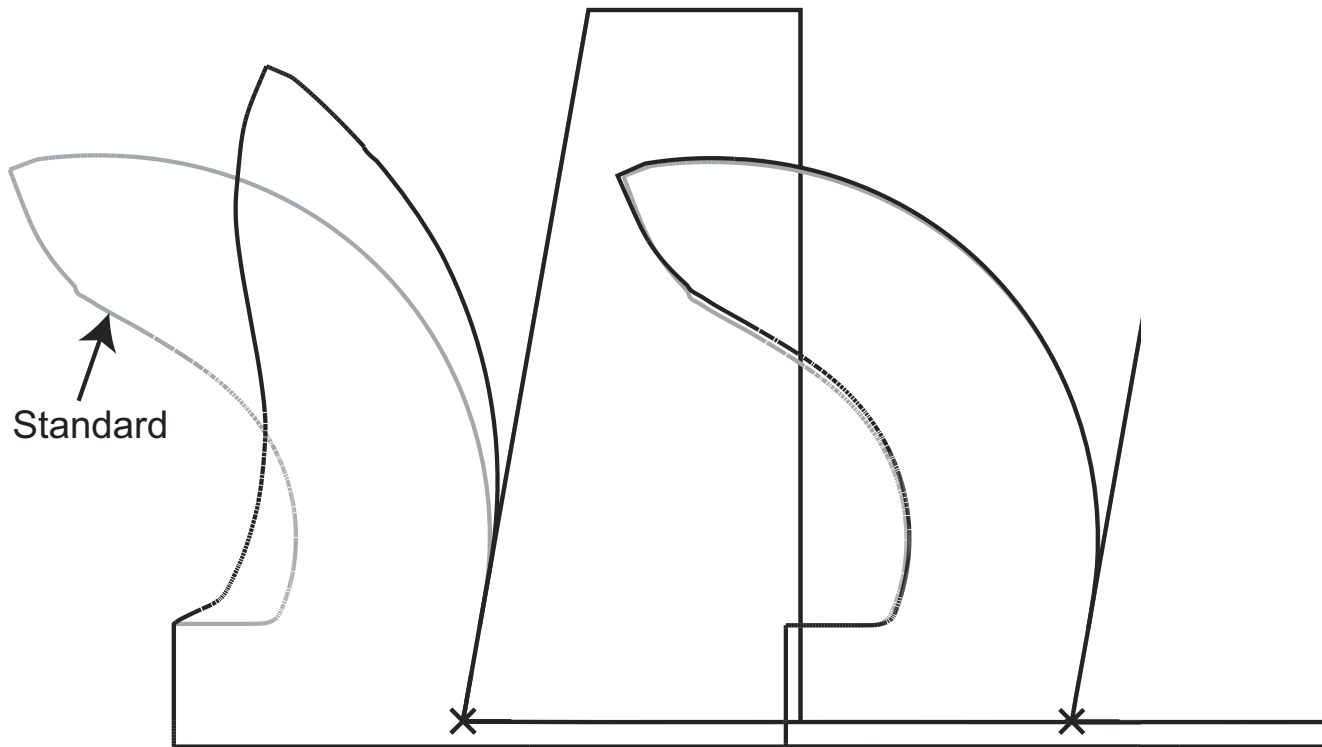
(a) Starting stage

(b) Levenberg-Marquardt stage
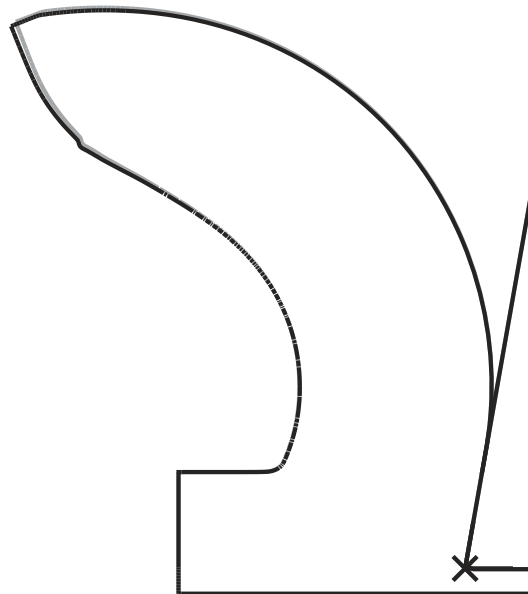
(c) Simplex stage

Figure 5.13: $\mathcal{S}^{30}_{KLn}$: Comparison of the chip shapes (Rake angle $= +10°$) at different stages of optimisation

(a) Starting stage

(b) Levenberg-Marquardt stage

(c) Simplex stage
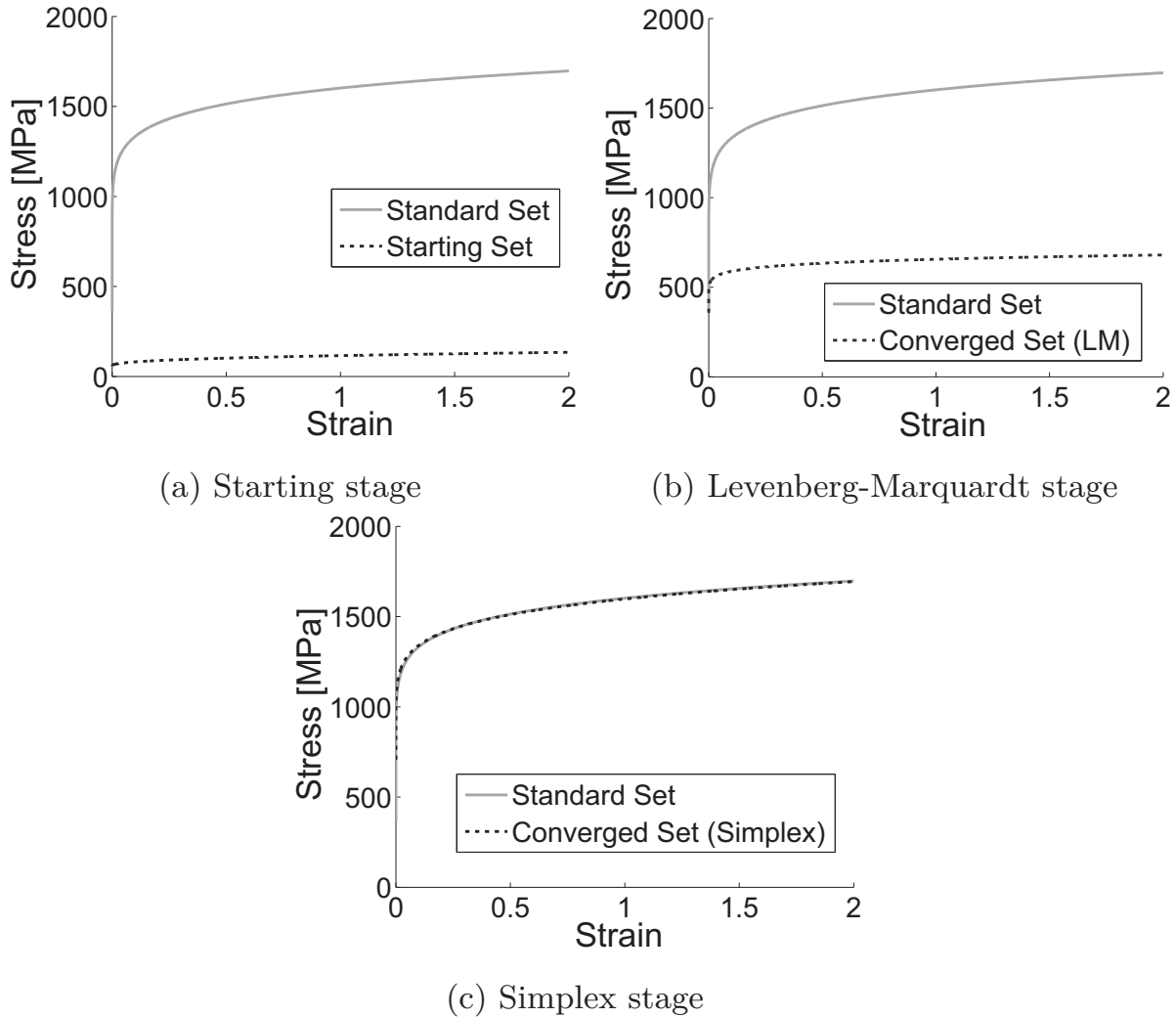
Figure 5.14: S^{30}_{KLn}: Isothermal stress-strain curves at different stages of optimisation

5.10.1 Parameters m and C

In order to identify the parameters m and C, the cutting conditions must be chosen so that there is a wide variation of the strain rate and temperature during the machining. A high cutting speed of 33.3 m s^{-1} is chosen, so that the strain rate goes up to the order of 10^5 s^{-1} and the temperature rises up to 850 K. The rake angle during the simulations is $+1°$. The cutting conditions used for the simulations are listed in Table 5.28

A dual stage optimisation (S^{31}_{mC}) is carried out in which the first stage Levenberg-Marquardt starts from $(0.5, 0.1)$ with a standard set $(0.7, 0.0277)$. The cutting force at the start is about 7% more than the standard value and the chip shape is also very different from the standard chip shape. The first stage of optimisation converges in 3

Material	HY-100
Cutting Speed [m s^{-1}]	33.3
Uncut chip thickness [µm]	200
Coefficient of friction	0
Rake angle	$+1°$
Mesh element type for Workpiece	CPE4R
Mesh element type for Tool	R2D2

Table 5.28: $\mathcal{S}_{mC}^{31}$ and $\mathcal{S}_{mC}^{32}$: Cutting conditions for standard and test simulations for identification of parameters m and C.

main optimisation steps, to a value of (0.431, 0.1002). The cutting force matches well ($\Delta F_C\%$ is around 1%) after the first stage. However, the chip shapes do not agree at all ($\Delta A_C\%$ is around 23%).

In the second stage, the simplex algorithm is used for optimisation and the starting size of m and C sides of simplex (Δ_m and Δ_C) is taken as 0.1. The optimisation converges in 23 iterations to (0.708, 0.0279), which is approximately within 1% of the standard set (0.7, 0.0277). The parameter sets at the end of different stages along with the normalised chip shape error and the cutting force error values can be seen in Table 5.29.

	m	C	$\Delta A_C\%$	$\Delta F_C\%$
Starting Set	0.50	0.10	20.65	7.10
Stage 1 (LM)	0.431	0.1002	23.18	1.14
Stage 2 (Simplex)	0.708	0.0279	0.33	0.57
Standard Set	0.7	0.0277	-	-

Table 5.29: $\mathcal{S}_{mC}^{31}$: Parameter sets at each stage of optimisation along with the normalised chip shape error and cutting force difference

No non-uniqueness is observed in this case. A similar result has also been reported by Yang *et al.* (2011). During the identification the reference strain rate ($\dot{\varepsilon}_0$) is held constant at the standard value of 3300 s^{-1}. In a real life problem, both C and $\dot{\varepsilon}_0$ would be unknown and both would need to be varied during the optimisation. It might be possible to find another combination of m, C and $\dot{\varepsilon}_0$ so that the chip shapes and cutting forces are well matched. To check this, a two dual stage parameter identification ($\mathcal{S}_{mC}^{32}$) for m and C was carried out by fixing

the $\dot{\varepsilon}_0$ to 100 s^{-1} instead of 3300 s^{-1}. It is possible to obtain a different parameter set again in this case. The converged parameter set is (0.669, 0.0173), which is different from the standard set and still the chip shapes and the cutting forces are well matched ($\Delta A_C\%$ and $\Delta F_C\%$ are less than 1%). The parameter sets along with the agreement of cutting force and chip shapes at each stage of optimisation are shown in Table 5.30. This means that there is non-uniqueness also in the parameter set $(m, C, \dot{\varepsilon}_0)$. A reasonable variation in $\dot{\varepsilon}_0$ can be compensated by a corresponding change in parameters m and C in a given domain of state variables. As mentioned before, the numerical value of the parameters is however not important as long as the stress-strain curves are predicted correctly in the domain of machining.

	m	C	$\Delta A_C\%$	$\Delta F_C\%$
Starting Set	0.50	0.10	29.15	29.82
Stage 1 (LM)	0.275	0.1007	37.37	1.21
Stage 2 (Simplex)	0.669	0.0173	0.18	0.94
Standard Set	0.7	0.0277	-	-

Table 5.30: $\mathcal{S}^{32}_{mC}$: Parameter sets at each stage of optimisation along with the normalised chip shape error and cutting force difference, when the reference strain rate ($\dot{\varepsilon}_0$) is fixed to 100 s^{-1} instead of 3300 s^{-1}

5.10.2 Parameters A, n, C

To identify parameters (A, n, C), one high speed (33.3 m s^{-1}) and one low speed (0.5 m s^{-1}) cutting simulation are done (identification $\mathcal{S}^{33}_{AnC}$). The rake angle for the high speed simulation is $+1°$ and for the low speed simulation is $+10°$. The cutting conditions for the simulations are listed in Table 5.31.

The starting parameter set is (600 MPa, 0.3, 0.1), and at the end of the first Levenberg-Marquardt stage, the chip shape and the cutting force show only a slight improvement and do not match well ($\Delta A_C\%$ is greater than 5% and cutting force differs by more than 20%). The first stage of optimisation converges in 3 main optimisation steps to (605 MPa, 0.268, 0.1015). However, the chip shapes and the cutting forces match extremely well after the simplex stage ($\Delta A_C\%$ is less than 5% and cutting force differs by less than 3%). The starting edge sides for the simplex are: $\Delta_A = 100$ MPa, $\Delta_n = 0.05$, $\Delta_C = 0.1$. The converged set at the end of the simplex stage is (367 MPa, 0.107, 0.0161) which

Material	HY-100	HY-100
Cutting Speed $[\mathrm{m\,s^{-1}}]$	0.5	33.3
Uncut chip thickness [µm]	200	200
Coefficient of friction	0	0
Rake angle	$+10°$	$+1°$
Mesh element type for Workpiece	CPE4RT	CPE4R
Mesh element type for Tool	R2D2	R2D2
Mass scaling factor	12000	1

Table 5.31: S^{33}_{AnC}: Cutting conditions for standard and test simulations for identification of parameters A, n and C.

differs from the standard set (316 MPa, 0.107, 0.0277). The increase in parameter A is compensated by a smaller parameter C. The parameter sets at each stage of optimisation are shown in Table 5.32a and the corresponding chip shape and cutting force agreement are shown in Table 5.32b.

	A [MPa]	n	C
Starting Set	600	0.300	0.1000
Stage 1 (LM)	605	0.268	0.1015
Stage 2 (Simplex)	367	0.11	0.0161
Standard Set	316	0.107	0.0277

(a) Starting and converged parameter sets when identifying (A, n, C).

	$\Delta A_C\%$		$\Delta F_C\%$	
	Rake 1°	Rake 10°	Rake 1°	Rake 10°
Starting Set	7.91	34.94	38.94	29.20
Stage 1 (LM)	6.58	25.66	36.34	23.67
Stage 2 (Simplex)	4.22	0.84	1.20	2.68

(b) Chip shape and cutting force agreement at the end of each optimisation stage when identifying (A, n, C).

Table 5.32: S^{33}_{AnC}: Identification of parameters (A, n, C) using the dual stage optimisation process.

5.10.3   Parameters A, B, C

The cutting conditions used for identification of parameters (A, n, C) are also used for the identification $(\mathcal{S}^{34}_{ABC})$ of parameters (A, B, C) (Table 5.31). The starting parameter set (50 MPa, 50 MPa, 0.3) is used in the Levenberg-Marquardt stage in which it converges in 5 main iterations to (96 MPa, 734.4 MPa, 0.247). At the start of the optimisation, the chip shapes and the cutting forces do not match. They both improve by the end of the first stage, but do not match well with the standard values. For the rake angle of 1°, $\Delta A_C\%$ is more than 20% and for the rake angle of 1° $\Delta F_C\%$ is around 30%. After the second stage of simplex optimisation, the converged set is (354.4 MPa, 1039.3 MPa, 0.0226). At the end of the optimisation, both the chip shapes and the cutting forces match well ($\Delta A_C\%$ and $\Delta F_C\%$ are less than 2%). The starting edge sides for the simplex are: $\Delta_A = 100$ MPa, $\Delta_B = 100$ MPa, $\Delta_C = 0.1$.

	A [MPa]	B [MPa]	C
Starting Set	50	50	0.3
Stage 1 (LM)	96	734.4	0.247
Stage 2 (Simplex)	354.4	1039.3	0.0226
Standard Set	316	1067	0.0277

(a) Starting and converged parameter sets when identifying (A, B, C).

	$\Delta A_C\%$		$\Delta F_C\%$	
	Rake 1°	Rake 10°	Rake 1°	Rake 10°
Starting Set	51.10	6.40	78.09	88.62
Stage 1 (LM)	21.31	1.15	8.69	29.88
Stage 2 (Simplex)	1.49	0.47	1.55	1.76

(b) Chip shape and cutting force agreement at the end of each optimisation stage when identifying (A, B, C).

Table 5.33: $\mathcal{S}^{34}_{ABC}$: Identification of parameters (A, B, C) using the dual stage optimisation process.

5.11   Solution improvement using the knowledge of stress-strain curves

During the dual stage optimisation process, it can be noted in some cases that, after the first stage, one of the components of the error function is well matched to the standard and the other component does not agree

well. For instance in identification $\mathcal{S}_{KLn}^{28}$ (Section 5.7.2), the chip shapes are well matched but the cutting forces differ by approximately 10% after the first stage of optimisation. The solution from the first stage is directly used in the simplex stage, in which the solution converges in a large number of optimisation stages. If the adiabatic stress-strain curve of the first stage solution can be offset in such a way that the average stress level rises by approximately 10%, then the cutting forces of the two simulations can be matched. An inverse identification can then be carried out using the points on the offset adiabatic stress-strain curve to obtain the corresponding Johnson-Cook parameter set. This inverse identification is computationally cheap as no finite element evaluation has to be conducted to obtain the parameter set value. The offset curve is expected to be closer to the standard curve, from where further optimisation can be carried out if needed.

There are two possible ways to offset a curve:

1. By adding a fixed value of stress to the standard curve, translating the curve higher (Translation)

2. By multiplying the standard curve with a scale factor (Stress scaling)

The two possibilities are investigated to study their effect on the chip shape and the cutting force.

5.11.1   Translation

The standard curve can be translated by a known stress value by adding or subtracting a translation stress (t_c). The proportion by which the cutting force changes is given by the ratio of areas under the stress-strain curve, after and before scaling.

Three different cases are studied in which the standard adiabatic stress-strain curve is translated by -100 MPa, +200 MPa and +400 MPa. The parameter set for HY-100 is used to calculate the standard adiabatic stress-strain curve. The Levenberg-Marquardt algorithm is used to identify the Johnson-Cook parameters from the translated stress curves. The parameter C is held constant to the standard value during the identification process due to non-uniqueness (described in Section 4.2). The parameters have been listed in Table 5.35. The cutting conditions have been listed in Table 5.34.

On comparing the cutting forces and chip shapes obtained using the translated curves to the standard curves (Table 5.36), the following observations are made:

Cutting Speed [$\mathrm{m\,s^{-1}}$]	33.3
Uncut chip thickness [µm]	200
Coefficient of friction	0
Rake angle	$+1°$
Mesh element type for Workpiece	CPE4R
Mesh element type for Tool	R2D2

Table 5.34: Cutting conditions for simulations with curve offset.

1. The cutting force is proportional to the area under the stress strain curve.

2. The chip shape changes on offsetting the stress-strain curves by translation. This is due to the change in the relative hardening $(\frac{d\sigma}{d\varepsilon}/\sigma)$ on translating the curves (Section 4.1).

	A [MPa]	B [MPa]	n	C	m
Standard Set	316	1067	0.107	0.0277	0.7
$t_c = -100$ MPa	10	1517	0.112	0.0277	0.476
$t_c = +200$ MPa	1046	1909	0.422	0.0277	0.334
$t_c = +400$ MPa	1330	945	0.609	0.0277	0.648

Table 5.35: Johnson-Cook parameters corresponding to translated standard curve.

	$\Delta A_C\%$	Ar_T/Ar_S	F_T^{av}/F_S^{av}
$t_c = -100$	7.74	0.90	0.91
$t_c = +200$	8.78	1.19	1.21
$t_c = +400$	26.16	1.38	1.39

Table 5.36: Effect of the translation of adiabatic stress-strain curves on the chip shape and cutting force. Here Ar_T/Ar_S is the ratio of area under the test and standard adiabatic stress-strain curves; F_T^{av}/F_S^{av} is the ratio of test and standard average cutting force.

5.11.2 Stress scaling

To offset the standard curve by scaling, the set of points in the standard curve is multiplied by a factor (s_c). This changes the area under the adiabatic stress-strain curve by a factor (s_c) and the cutting force is consequently expected to change by the same factor.

Four different cases are studied where the standard adiabatic stress-strain curve is scaled by factors of 0.7, 0.8, 1.2 and 1.5. Corresponding Johnson-Cook parameters are identified for the scaled curves, in the same way as in Section 5.11.1.

Simulations are conducted with the different Johnson-Cook parameters corresponding to the scaled adiabatic stress-strain curves and the chip shapes and the cutting force are compared. The material parameters have been listed in Table 5.37. The cutting conditions are listed in Table 5.34. The average cutting force scales proportional to the scale factor s_c (Table 5.38). More importantly, the chip shape does not change even when there is a large offset of the stress-strain curve (Table 5.38). In this case the relative hardening of the material stays the same (Section 4.1). This property can be utilised to obtain the final parameter set after the first optimisation stage, once the chip shape is well matched by scaling the flow curve by the required factor. This will lead to tremendous savings in the computational expense. It is also possible to extend this idea into an optimisation method.

	A [MPa]	B [MPa]	n	C	m
Standard Set	316	1067	0.107	0.0277	0.7
$s_c = 0.7$	0.01	1319	0.124	0.0277	0.353
$s_c = 0.8$	109	1190	0.117	0.0277	0.47
$s_c = 1.2$	884	2385	0.346	0.0277	0.3
$s_c = 1.5$	1336	2850	0.452	0.0277	0.341

Table 5.37: Johnson-Cook parameters corresponding to scaled standard curve.

5.11.3 Identification of 4 parameters

Using the dual stage optimisation, parameters (A, B, n, m) are identified (identification S^{35}_{ABnm}). The cutting conditions used for the simulations are the same as those used in Section 5.5. A fine mesh with 20 elements in the chip thickness direction and a rake angle of 0° is used for the

	$\Delta A_C\%$	F_T^{av}/F_S^{av}
$s_c = 0.7$	1.37	0.70
$s_c = 0.8$	1.66	0.81
$s_c = 1.2$	3.60	1.21
$s_c = 1.5$	0.41	1.54

Table 5.38: The agreement of chip shapes and the ratio of the average cutting force from test simulation to the average cutting force from the standard simulation. The standard curve is scaled by a factor s_c. F_T^{av}/F_S^{av} is the ratio of test and standard average cutting force.

simulations. The standard material parameters are that of AISI 52100, 62 HRC. For the Levenberg-Marquardt step, the optimisation parameter $w = 10^{-3}$ mm^2 N^{-1}. The starting parameter set is (200 MPa, 50 MPa, 0.050, 1.5) and is different from the standard set (688.17 MPa, 150.82 MPa, 0.3362, 2.7786). The first step converged in 8 iterations to (635.926 MPa, 101.703 MPa, 0.649, 2.259). The chip shapes match extremely well ($\Delta A_C\%$ is around 2%) but the average cutting force from the standard set is 13% more than the average cutting force from the converged set. Therefore the adiabatic stress-strain curve of the converged set is scaled by a factor of 1.13 and the corresponding Johnson-Cook parameter set is obtained. The resulting parameter set (716 MPa, 112 MPa, 0.592, 2.726) is used as a starting set for a second stage simplex optimisation. At the start of the second stage, the chip shapes and the cutting forces match extremely well ($\Delta A_C\%$ is around 4% and $\Delta F_C\%$ is less than 1%) already and in 4 main iterations, the final converged set (713.8 MPa, 108 MPa, 0.606, 2.740) is obtained in which the parameter set is finely tuned. The chip shapes and the cutting forces are indistinguishable in the end ($\Delta A_C\%$ is around 2% and $\Delta F_C\%$ is less than 1%), even though the parameter set is non-unique.

5.11.4   Non-adiabatic optimisation

In Section 5.9, at the end of the first stage of the optimisation S_{KLn}^{30}, the chip shapes match well but the cutting forces differ by around 50% from the standard simulation. In this section, the material parameters for identification S_{KLn}^{30} will be improved after the first stage using the knowledge of the stress-strain curves. This identification process is named S_{KLn}^{36} as transformed parameters are used for the identification (during second stage). At low cutting speeds the material behaviour

	A [MPa]	B [MPa]	n	m
Starting Set	200	50	0.050	1.5
Stage 1 (LM)	635.926	101.703	0.649	2.259
Stage 2 (Start)	716	112	0.592	2.726
Stage 2 (End)	713.8	108	0.606	2.740
Standard Set	688.17	150.82	0.3362	2.7786

(a) Johnson-Cook parameters corresponding to each stage of optimisation along with the standard set for comparison.

	$\Delta A_C\%$	F_S^{av}/F_T^{av}
Starting Set	17.16	3.43
Stage 1 (LM)	1.27	1.13
Stage 2 (Start)	4.07	1.00
Stage 2 (End)	1.71	1.00

(b) The agreement of chip shapes and the ratio of the average cutting force from test simulation to the average cutting force from the standard simulation for each stage of optimisation.

Table 5.39: $\mathcal{S}_{ABnm}^{35}$: Identification of parameters (A, B, n, m) using the knowledge of stress-strain curves to improve the solution.

can be approximated by the isothermal stress-strain curve. To improve the solution, the isothermal stress-strain curve from the first stage must be scaled. In order to determine the scale factor, the areas under the isothermal stress-strain curve from the standard parameter set (Ar_s) and the converged parameter set (Ar_{C1}) are calculated. The scale factor is given by $s_c = Ar_s/Ar_{C1}$. In this case the scale factor is $s_c = 2.42$.

The new Johnson-Cook parameter set is identified corresponding to the scaled curve, which is used for a second stage of optimisation. On plotting the isothermal stress-strain curves for the standard and the scaled parameter set, it is observed that the curve shapes are very different, even though the area under the curves are approximately the same (Figure 5.15). This is because, for non-adiabatic simulations, isothermal stress-strain curves are only an approximation of the material behaviour and when scaled by such a large factor, the difference in the curve shapes are magnified. Thus chip shapes formed from the scaled parameter set are expected to be different from those obtained from the standard set. The Levenberg-Marquardt algorithm is used for optimisation in the second stage. At the end of the optimisation, the chip shapes and the cutting forces match well ($\Delta A_C\%$ is less than 4% and $\Delta F_C\%$ is less than 1%). The parameter sets at each stage of

optimisation are given in Table 5.40a and the agreement of the chip shapes and the ratio of the cutting forces are given in Table 5.40b.
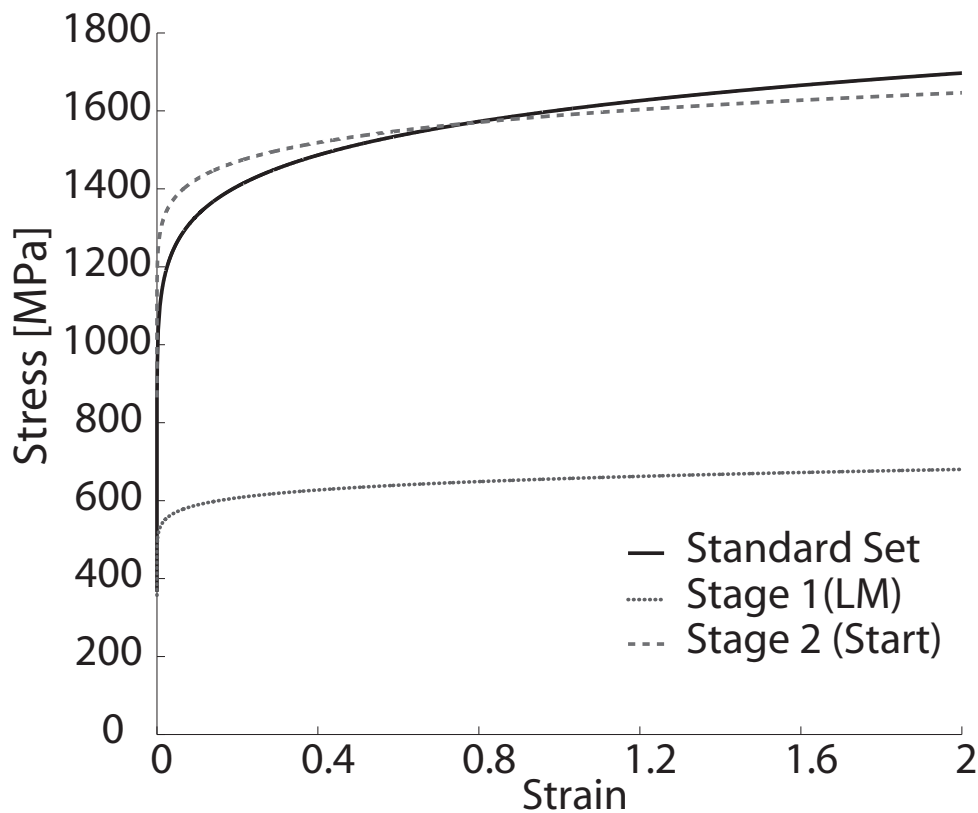
Figure 5.15: Isothermal stress-strain curves corresponding to the stage 1 converged set (of identification $\mathcal{S}^{30}_{KLn}$), scaled set (of identification $\mathcal{S}^{36}_{KLn}$) and the standard set.

5.12   Conclusion

This chapter shows the method of inverse identification of material parameters from machining simulations. The material parameters are varied until the chip shapes and cutting forces from simulations and experiments match. Since the identification process is studied numerically, a standard simulation conducted using a known parameter set is considered as a virtual experiment and the standard set is sought to be reidentified. For the identification process, an error function is created using the difference in the chip shapes and the cutting forces. It is then minimised using optimisation algorithms such as the Levenberg-Marquardt and the downhill simplex algorithm.

Validation of the inverse identification method is carried out by using a coarse mesh and reidentifying first 1, then 2 and 3 parameters.

	A [MPa]	B [MPa]	n
Starting Set	50	50	0.4
Stage 1 (LM)	308.4	258.1	0.111
Stage 2 (Start)	746.6	624.9	0.111
Stage 2 (End)	728.4	665.3	0.175
Standard Set	316	1067	0.107

(a) Johnson-Cook parameters corresponding to each stage of optimisation.

	$\Delta A_C\%$		F_S^{av}/F_T^{av}	
	Rake 1°	Rake 10°	Rake 1°	Rake 10°
Starting Set	113.35	118.40	6.41	7.56
Stage 1 (LM)	1.26	1.67	2.03	2.07
Stage 2 (Start)	52.63	44.74	1.07	1.05
Stage 2 (End)	0.59	3.98	0.99	0.99

(b) Chip shape and cutting force agreement at the end of each optimisation stage.

Table 5.40: $\mathcal{S}_{KLn}^{36}$: Parameter identification from non-adiabatic simulations using the knowledge of stress-strain curves to improve solution.

Identifying a single parameter is easy as no non-uniqueness is expected in this simple case. However, it was observed that the standard parameter could not be exactly reidentified using the Levenberg-Marquardt method. The reasons for this are the following:

1. The error landscape is noisy (Figure 5.1 in a 1 parameter case and 5.3 in a 2 parameter case) and, when close to the minimum, it prevents the Jacobian to be correctly estimated. The behaviour of the Levenberg-Marquardt algorithm in the vicinity of the minimum should be akin to Newton's method, and therefore be more sensitive to the inaccuracies in the Jacobian estimation.

2. The Jacobian is estimated by numerical differentiation. The δ_j values are chosen to be large enough so that the change in the error function is greater than the noise during the complete optimisation. Thus the choice of δ_j is conservative, which prevents the optimisation to converge to the standard parameter.

In the case of the identification of 2 and 3 parameters, apart from the above mentioned reasons, the non-uniqueness of the parameter sets also prevents the exact reidentification of the standard set. It is however not important that the identified parameter sets are the same as the

standard set. It is because in the given domain of machining, non-unique parameter sets can also predict the flow curves correctly. Consequently the identified chip shapes and the cutting forces are also similar to those from standard simulations.

It was shown in Section 5.3.2 that the error landscape is very noisy close to the minimum. Therefore, when close to the minimum, the optimisation can get stuck in one of the numerous local minima. Despite this, the overall shape of the error landscape is well approximated even by simulations conducted with a coarse mesh. As a consequence, parameter reidentification using a coarse mesh is also possible (See Section 5.5).

Different strategies are investigated to improve the identification process. To improve the Jacobian estimation, the central difference method is used. It requires marginally fewer main and sub iterations than when the forward difference method is used for Jacobian estimation. However, the total number of finite element evaluations until convergence are almost similar in the two cases. There is added computational expense when the central difference method is used, as an extra simulation has to be conducted for each parameter - as compared to the forward difference method (Section 5.3.2). This strategy does not provide a significant advantage in terms of improved convergence or lower computational expense.

The weighting factor w is used to balance the chip shape error to the cutting force error in the error function. Its variation influences the convergence of the optimisation. As expected, when the influence of one of the components of the error function is increased, this component tends to be better optimised. However, to arrive at a reasonable value of w, identifications have to be done at different w values. A reasonable value of w should optimise both the cutting force and the chip shape, so that $\Delta A_C\%$ and $\Delta F_C\%$ are ideally less than 3% and 5% respectively. To arrive at such a value for w is time taking as full optimisations have to carried at different w.

In Section 5.6 it is shown that the convergence can be significantly improved by using judiciously chosen optimisation variables, which can be found by using the stress-strain curves. This strategy is effective in both adiabatic and non-adiabatic optimisations (Sections 5.6 and 5.9).

The Levenberg-Marquardt algorithm is a gradient based algorithm which shows fast convergence. Irrespective of the starting parameter set choice, the optimisation converges within 10 main iterations in most of the cases. As compared to this, the downhill simplex algorithm takes at least 15 main iterations to converge, even if the starting parameter set is close to the minimum. However, the downhill simplex method explores the parameter space around the minimum and the chip shape and the

cutting force difference at the end of the optimisation is often less than 3%. Therefore a combination of the two optimisation methods provides a robust method of parameter identification. When the starting parameter set is far from the standard set, the Levenberg-Marquardt algorithm is used for first stage of optimisation. The converged set from the first stage is then used for optimisation using the downhill simplex algorithm which further improves the solution. Using the dual optimisation method, the parameter identification is robust. Chip shapes and cutting forces were successfully matched for the following different cases:

1. For different standard parameter sets

2. For different starting parameter sets

3. For different parameter combinations

4. For different cutting conditions (*e.g.* adiabatic, non-adiabatic, different rake angles)

The effect of the choice of the error function is studied in Section 5.8. In most of the identification problems, a number of frames of observations are used to determine the error function. However, in the case of a real life identification problem, the chip shape evolution or the cutting force evolution will not be available for parameter identification. Consequently, a different error function is created which uses only the final chip shape and the average cutting force to identify the material parameters. It is shown that both the error functions are effective in identifying the material parameters. However, the error function given by Equation 5.32 is found to be better for the Levenberg-Marquardt algorithm, as the Jacobian estimation is better when it is known whether the test cutting force is higher or lower as compared to the standard cutting force (Section 5.8).

The optimisation of different parameters in a staggered manner can be used to improve the convergence of the optimisation. Parameters A and B were shown to strongly influence the average stress level of the stress-strain curve in Chapter 4. If the optimisation gets stuck in a local minimum so that the cutting forces are not well matched, parameters A and B can be optimised to reduce the cutting force mismatch. After this stage, all the parameters can be optimised together to match both the cutting force and the chip shape.

To identify robust parameter sets which predict the correct flow stress in a wide machining domain, the parameter identification is carried out at different cutting conditions:

   1. Different cutting speeds

   2. Different rake angles

By reducing the cutting speed, the thermal conditions can be changed from adiabatic to non-adiabatic. It was shown in Chapter 4 that there is less non-uniqueness for non-adiabatic cutting conditions than for adiabatic cutting conditions. As a result, in Section 5.9, non-adiabatic identification is carried at a low cutting speed. In order to explore both low and high strains, two different rake angles are used during the optimisations. A negative rake angle is not used as there is a possibility of segmented chip formation when the parameters are varied widely during the optimisation.

Apart from the parameter set (A, B, n), other parameter sets were also identified using this method. The parameter set (m, C) does not show non-uniqueness as long as the parameter $\dot{\varepsilon}_0$ is fixed. However, it is shown that the set $(m, C, \dot{\varepsilon}_0)$ is non-unique. This is because a reasonable variation in $\dot{\varepsilon}_0$ can be compensated by changing the parameters m and C. Similarly, some non-uniqueness is also observed in parameter sets (A, n, C) and (A, B, C). It is observed that a smaller C can be compensated by a larger A and a correspondingly changed B or n.

In all the identifications, it is observed that the match in the chip shapes and the cutting forces are also reflected in a match in the shape of the stress-strain curve and the area under the stress-strain curve. When an identification is done using the adiabatic conditions, the adiabatic stress-strain curves of the converged and the standard parameter set match. When an identification is done at low cutting speeds, the isothermal stress-strain curves of the converged and the standard parameter set match. Even when the parameter sets are non-unique, the stress-strain behaviour for the converged and the standard sets are similar. Therefore, an important conclusion is that it does not matter what parameters are used to describe a stress-strain curve: as long as the stress-strain curves are matched within the machining domain, the chip shapes and the cutting forces are also going to be similar in this domain.

Using the knowledge of the stress-strain curves, a method of improving the solution is proposed in Section 5.11. The knowledge that the area under the stress-strain curve is related to the cutting force and the relative hardening of the curve is related to the chip shape (Section 4.1) can be used to reduce the cutting force and chip shape mismatch. In some simulations (*e.g.* $\mathcal{S}^{28}_{KLn}$, $\mathcal{S}^{30}_{KLn}$, $\mathcal{S}^{35}_{ABnm}$), the chip shape agrees well with the standard chip but the cutting force does not after the first stage of Levenberg-Marquardt optimisation. In this case, the solution can be improved by scaling the converged curve by the ratio of the average

standard cutting force to average converged cutting force. Corresponding to the scaled curve, material parameters are found using an inverse identification method. However, as no finite element evaluations need to be done during this identification, it is computationally less expensive than using a second stage simplex method which requires finite element evaluations. On scaling the curve using a constant factor, the chip shape does not change as the relative hardening remains the same as the unscaled curve. This however is not the case when a curve is offset by translation – it results in a change in both the cutting force and the chip shape.

Chapter 6

Conclusion and outlook

The main thesis of this work is that material parameters which are valid in the domain of machining can be directly identified from machining processes using an inverse parameter identification method. The chip shape and the cutting force are the observables of machining. By systematically changing material parameters in a finite element simulation of machining, the resulting observables can be matched to those obtained from standard numerical experiments. The inversely identified material parameter set is valid in the domain of machining. Robust material parameters can be found by optimising the material parameters for widely varying cutting conditions. The numerical value of the identified material parameters is not the same as the standard set. Nevertheless both the parameter sets represent the same flow curve in the given machining domain. An important conclusion from this is that the main objective of the inverse identification process is to identify the correct flow stress curve in the domain of machining. Different parameter sets mathematically represent the same flow curve in this domain and therefore they give rise to similar observables.

In Chapter 1, the basics of the machining process and some important analytical models for understanding the cutting mechanics are discussed. The shear plane model assumes that all the deformation occurs in the shear plane and that the shear plane is oriented so that the work is minimised. A predictive analytical theory of machining by Oxley and his coworkers is useful in calculating physical quantities such as the cutting force, chip temperature, strain rate, strain *etc*. This theory has also been used later to determine material parameters for machining simulations (see Section 5.1). Due to the fact that complex machining processes cannot be studied using analytical models, the finite element method has been extensively used to simulate the chip formation process.

In Chapter 2, the finite element modelling for machining is discussed. In particular, the models used in the simulations in this work, along with the associated issues, are also discussed in detail. The Johnson-Cook material model is used in the simulations in this work as it is a relatively simple phenomenological material model with 5 free parameters which can predict material behaviour over large ranges of strains, strain rates and temperatures. Other material models which have a greater number of free parameters are expected to have the following problems:

1. Material parameters for different materials are not readily available in literature.

2. A new material model has to be implemented using a subroutine in the finite element software, which in general takes a larger computational time.

3. The material models with a larger number of free parameters are expected to show more non-uniqueness as there is a greater degree of freedom to change the parameters and to compensate each other's effects.

A more complex material model is introduced when the Johnson-Cook model is not sufficient for capturing effects such as dynamic material softening at large deformations, which occurs due to microstructural changes. Such a material model is used for simulating chip formation in Alloy 625 in Section 3.5.5. Deciding beforehand if a material model is appropriate for a machining simulation or not is not a trivial problem. The flow stress can only be obtained from experimental methods for limited strains, strain rates and temperatures. Using material parameters obtained from such a data set for machining simulations is inappropriate as the flow stress is extrapolated over several orders of magnitude of strains and strain rate. Inevitably, the simulation results do not robustly match the machining results, even though the material parameters fit the experimentally obtained flow stress well. In such a case, it is unreasonable to write off the model itself, as the data set which was used for parameter identification was not sufficient. Since phenomenological models do not consider the physics of deformations, they are highly dependent on the quality of the data set. This makes a strong case for using inverse identification methods which can obtain material data at machining conditions.

During the simulation of segmented chip formation, severe distortions of the mesh can take place due to hourglassing (see Section 2.4). As a

result some form of numerical hourglass control is necessary. The choice of the stiffness type hourglass control parameter is difficult as setting its value too high can cause the segmentation to not take place at all and too small a value will not be effective in stopping hourglassing. As a result, a compromise has to be found by trial and error. The simulations of Ti-15-3-3-3, Ti-6246 and Alloy 625 use the same hourglass control values and the degree of segmentation in these cases might be lower due to a conservative value of the hourglass stiffness parameter. An important issue in detecting hourglassing is that in the finite element software, only a local criterion is used: the software is thus not able to differentiate between a pure bending mode and an hourglassing mode of deformation. Developing better element types which do not hourglass is another solution to this problem.

Machining simulations are computationally expensive and three strategies have been very useful in reducing the computational time (Section 2.5):

1. Using non-uniform meshing is advised for continuous chip formation simulations.

2. Using high cutting speeds for adiabatic simulations.

3. Using mass scaling technique for low cutting speed simulations. The mass scaling factor must be determined by trial and error, so that the chip shapes and the cutting forces are not adversely influenced.

Chip formation simulations in this work have been done using the Lagrangian mesh whose limitations are discussed in detail in Sections 2.2.2 and 2.2.2. For comparison, the chip formation in AISI 52100, 62 HRC was studied using the Eulerian method in Hembuch (2012). It is observed that the chip shapes and the cutting forces using the two methods were similar for a comparable mesh size. The critical plastic strain for element deletion used in the parameter identification studies in Chapter 5 is 2.0. Using the Eulerian method, a plastic strain of 2.8 is found in front of the tool tip, before the chip separates. However, the residual stresses in the workpiece surface are found to be different in the two methods. Eulerian simulations of chip formation process holds promise for future, as the limitations due to the mesh distortion and mesh separation occurring in Lagrangian simulations are not present in this method and it can also be used to estimate the residual stresses in the machined workpiece.

In Chapter 3, the chip formation simulations using the experimentally determined Johnson-Cook material parameters show segmented chip

formation. However the degree of segmentation is low as compared to the experimentally obtained chips and there are differences in the chip morphology. Damage models may be used to enhance the segmentation and the friction conditions between the chip and the tool are not known. Determining damage and friction parameters experimentally can be challenging. An inverse identification process similar to the one described in Chapter 5 can also be used to identify these parameters. The comparison of chip shapes as described in Section 2.6 might have to be modified for segmented chips. Two chips must be first aligned to match their segments, otherwise two similar but unaligned can chips can give a large area of non-overlap (Figure 6.1).
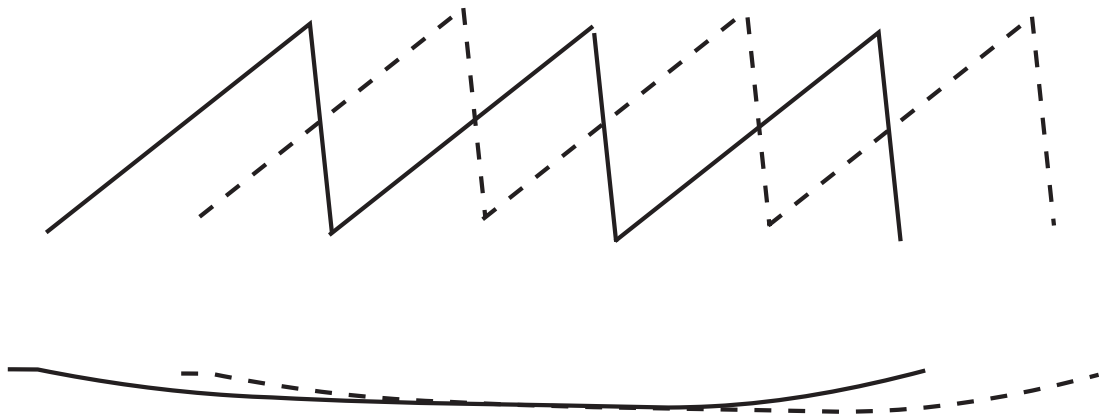
Figure 6.1: Two similar but unaligned segmented chips can give a large area of non-overlap.

The cutting force prediction from simulations using the experimentally determined Johnson-Cook material parameters in Chapter 3 show reasonable success. The average cutting force from simulations were within 20% of the average cutting force determined from U-type specimen tests. Large extrapolations between the domain in which the parameters are experimentally identified and the domain in which the machining simulations are carried out is the reason for this mismatch. To improve the cutting force prediction, the adiabatic stress-strain curve can be scaled by a factor equal to the ratio of the average experimental cutting force to the average cutting force predicted by the simulation (see Section 5.11.2) and corresponding to the scaled curve, Johnson-Cook parameters can be obtained. This way, without changing the chip shape, the cutting force can be corrected.

The actual stress-strain behaviour of the material during the machining simulation can be obtained only after the simulation is done, by looking at the effective stress-strain curves. Analytically calculating the

effective stress-strain curve for low speed cutting simulations is difficult due to the conduction of heat to the surrounding material. However, at sufficiently low cutting speeds, the material behaviour can be approximated by isothermal stress-strain curves. At high cutting speeds, the material behaviour can be approximated by the adiabatic stress-strain curve. The actual material behaviour is expected to be in between these two extremes.

In Chapter 4, it is shown that adiabatic stress-strain curves are central to understanding high speed cutting processes. Even if the material parameter sets are different, as long as the adiabatic stress-strain curves are similar, chip shapes and cutting forces will also be similar. An infinite number of parameter sets are possible which can give such results. Even in a small parameter combination such as (A, B, n), there is non-uniqueness (Section 4.3). If more than 3 parameters are to be identified, then the identification is expected to be easier as there would be greater non-uniqueness. Using a large variation of the cutting conditions, some non-uniqueness can be reduced and the different parameter sets can be distinguished (Section 4.4). For instance, by changing the cutting speed, the thermal conditions during the chip formation can be changed and by changing the rake angle, different strain ranges can be explored. This idea is used for a number of identifications in Chapter 5, in which optimisations are done with more than one cutting condition to reduce non-uniqueness. This means that the optimised parameter set should produce chips and cutting forces which match those produced from the standard parameter set at all the cutting conditions for which the optimisation is done. This optimised parameter should predict the correct cutting force and the chip shape when simulation is conducted at an intermediate cutting condition as the strain, strain rate and temperature conditions only are interpolated in such as case.

The adiabatic and isothermal stress-strain curves can also be used to determine optimisation parameters (Section 5.6). Significant reduction in the optimisation time occurs when the optimisation parameters are chosen judiciously.

In Chapter 5, a number of inverse identifications are done to match the chip shapes and the cutting forces for different cutting conditions. In almost all the cases, it was found that inverse identification is indeed possible, but reidentification of the standard set exactly is difficult due to non-uniqueness. At the end of the optimisations, it was observed that the adiabatic stress-strain curves, in the case of high speed cutting, and isothermal stress-strain curves, in the case of low speed cutting, of the converged sets matched well with those of the standard set. Thus it is

evident that it does not matter what parameters are used to represent the stress-strain curve as long as the correct stress-strain curve is identified. In other words, it is not the parameter which is being identified but the stress-strain curve. An important consequence of this is that the knowledge of the stress-strain curves (see Section 5.11) can be directly used to match chip shapes and cutting forces. Ultimately, for a robust optimisation, the flow stress field over a large range of strain, strain rate and temperature has to be optimised and not just single curves.

The inverse identification method can be used to identify material parameters from machining simulations which are valid for large ranges of strain, strain rates and temperatures. Although this method has been used here for the Johnson-Cook material model, it can be applied for more complicated models.

It has many advantages, the first being that it is a robust method, which can be used to identify parameters for different materials, the identification process being independent of the starting parameter set. Another advantage is that the material parameters can be directly obtained from comparing the machining simulations to experiments and does not rely on intermediate theoretical models. Simplifying assumptions are not necessary, which means that this method can also be used for complicated machining processes or chip morphologies. The knowledge of the stress-strain curves can be used as well to improve the cutting force or the chip shape match.

The difficulty with this method is that the identification process is computationally expensive. However this will become less of a problem as computational costs reduce. Other difficulties are inherent to the finite element software as it may not be able to simulate complex processes which involve large mesh distortion, complex interactions or complicated material separation *etc.* With the development of better algorithms, these problems can also be reduced.

In this work, inverse parameter identification is shown for continuous chip formation. With this basis, the identification process should be extended to materials which form segmented or discontinuous chips. Damage and friction parameters can also affect the segmented chip formation. Therefore, a systematic study of damage parameters can be conducted, following which the friction, damage and the Johnson-Cook parameters can be optimised together to yield the chip shapes and cutting forces.

To validate the inverse identification method, this method must be used for parameter identification from real chip formation experiments. The practical issues arising from it must be studied. Obtaining time resolved cutting forces or measuring the segmentation frequency experi-

mentally is still a challenge. Therefore, ways must be found to determine the material parameters from the available experimental data.

A new optimisation method using the knowledge of the stress-strain curves can be developed, so as to reduce the computational expense. If a physical understanding of the effect of the stress-strain curves on the observables can be found, the flow curves can be directly modified. Thus the number of computationally expensive finite element calculations can be reduced.

Another course of research should be the development of better numerical algorithms for adaptive mesh refinement and remeshing in Abaqus/Explicit as well as for resolving the problem of hourglassing. The use of Eulerian methods for chip formation simulation must also be investigated further. Since chip separation in Eulerian method does not involve element deletion, the residual stresses in the workpiece can be better studied. The effect of material and the cutting parameters on the residual stresses can help in improving the machined workpiece integrity. Including effects such as the tool wear, heat conduction into the tool, effect of coolant *etc.* can help not only in developing a better understanding of their effects on the machined workpiece, but also help in optimising the process parameters as well as designing better cutting tools.

Identification of material parameters from machining experiments is an important method of obtaining material parameters in the domain of machining. Using material parameters obtained this way, it is expected that the prediction of chip shapes and cutting forces would become more reliable and a better understanding of the machining process can be obtained. Machining simulations can therefore be used for determining the process parameters and reducing the wastage of valuable resources.

Appendix A

Algorithms

Algorithm 1 Levenberg-Marquardt algorithm

1: Set $\mathbf{a}_{cur} \leftarrow \mathbf{a}_0$
2: Set $\lambda_{LM} \leftarrow 0.01$ ▷ Take a moderate value of λ_{LM}
3: Evaluate $\chi^2(\mathbf{a}_{cur})$
4: Evaluate $\mathbf{J}$ at $\mathbf{a}_{cur}$
5: Evaluate $\delta\mathbf{a}$ using Equation 5.14
6: $\mathbf{a}_{next} \leftarrow \mathbf{a}_{cur} + \delta\mathbf{a}$
7: Evaluate $\chi^2(\mathbf{a}_{next})$
8: **if** $\chi^2(\mathbf{a}_{next}) \geq \chi^2(\mathbf{a}_{cur})$ **then**
9:      Set $\lambda_{LM} \leftarrow 10 \times \lambda_{LM}$ ▷ Multiply λ_{LM} by a substantial factor
10:      **if** $C_{STOP} ==$ TRUE **then** ▷ C_{STOP} is the stopping condition
11:          End program
12:      **else**
13:          **go to** line 5
14:      **end if**
15: **else**
16:      Set $\lambda_{LM} \leftarrow 0.1 \times \lambda_{LM}$ ▷ Reduce λ_{LM} by a substantial factor
17: **end if**
18: $\mathbf{a}_{cur} \leftarrow \mathbf{a}_{next}$
19: **if** $C_{STOP} ==$ TRUE **then**
20:      End program
21: **else**
22:      **go to** line 4
23: **end if**

Algorithm 2 Algorithm for updating the step bound Δ as used in the GNU Scientific Library

---

1: Set $\Delta^{(0)} \leftarrow 100||\mathbf{D}_0 \cdot \delta\mathbf{a}_0||$

2: Set $\Delta^{(1)} \leftarrow \min(\Delta, ||\mathbf{D}_1 \cdot \delta\mathbf{a}_1||)$ $\quad\quad\quad\quad\quad$ ▷ For the first iteration

3: Evaluate $r_a^{(k)} \leftarrow 1 - \left(\dfrac{||\Phi(\mathbf{a}_k + \delta\mathbf{a}_k)||}{||\Phi(\mathbf{a}_k)||} \right)^2$ $\quad\quad\quad\quad$ ▷ For $k \geq 1$

4: Evaluate $\gamma \leftarrow - \left[\left(\dfrac{||\mathbf{J}_k \cdot \delta\mathbf{a}_k||}{||\Phi(\mathbf{a}_k)||} \right)^2 + \left(\sqrt{\lambda_{LM}^{(k)}} \dfrac{||\mathbf{D}_k \cdot \delta\mathbf{a}_k||}{||\Phi(\mathbf{a}_k)||} \right)^2 \right]$

5: **if** $R^{(k)} < 0.25$ **then**

6: $\quad$ **if** $r_a^{(k)} \geq 0$ **then**

7: $\quad\quad$ $\mu \leftarrow 0.5$

8: $\quad$ **else**

9: $\quad\quad$ $\mu \leftarrow \dfrac{0.5\gamma}{\gamma + 0.5 r_a^{(k)}}$

10: $\quad$ **end if**

11: $\quad$ **if** $(||\Phi(\mathbf{a}_k + \delta\mathbf{a}_k)|| \geq 10||\Phi(\mathbf{a}_k)||)$ OR $(\mu < 0.1)$ **then**

12: $\quad\quad$ $\mu \leftarrow 0.1$

13: $\quad$ **end if**

14: $\quad$ $\Delta^{(k+1)} \leftarrow \mu \cdot \min\left\{ \Delta^{(k)}, 10||\mathbf{D}_k \cdot \delta\mathbf{a}_k|| \right\}$

15: $\quad$ $\lambda_{LM0}^{(k+1)} \leftarrow \dfrac{\lambda_{LM}^{(k)}}{\mu}$ $\quad$ ▷ $\lambda_{LM0}^{(k+1)}$ is further refined to yield $\lambda_{LM}^{(k+1)}$ (refer Algorithm 3)

16: **else**

17: $\quad$ **if** $r_a^{(k)} \geq 0.75$ **then**

18: $\quad\quad$ $\Delta^{(k+1)} \leftarrow 2||\mathbf{D}_k \cdot \delta\mathbf{a}_k||$

19: $\quad\quad$ $\lambda_{LM0}^{(k+1)} \leftarrow \dfrac{\lambda_{LM}^{(k)}}{2}$

20: $\quad$ **else**

21: $\quad\quad$ $\Delta^{(k+1)} \leftarrow \Delta^{(k)}$

22: $\quad\quad$ $\lambda_{LM0}^{(k+1)} \leftarrow \lambda_{LM}^{(k)}$

23: $\quad$ **end if**

24: **end if**

Algorithm 3 Algorithm for determining the Levenberg-Marquardt parameter λ_{LM} as used in the GNU Scientific Library

---

1: **procedure** LMPAR($\mathbf{J}$, $\mathbf{D}$, f, λ_{LM0}, Δ)
2:      $k = 0$
3:      $\lambda_{LM} \leftarrow \lambda_{LM0}$
4:      Evaluate $\psi(0)$ ▷ Using Equation 5.19
5:      **if** $\psi(0) \leq 0.1\Delta$ **then** $\lambda_{LM} \leftarrow 0$
6:          **return** (λ_{LM})
7:      **end if**
8:      **if** Rank($\mathbf{J}$) $< M$ **then**
9:          $\lambda_l^{(0)} \leftarrow 0$ ▷ If the Jacobian is rank deficient then set the lower bound (λ_l) to 0
10:      **else**
11:          $\lambda_l^{(0)} \leftarrow -\dfrac{\psi(0)}{\psi'(0)}$ ▷ Using Equations 5.19 and 5.20
12:      **end if**
13:      $\lambda_u^{(0)} \leftarrow \dfrac{||(\mathbf{J} \cdot \mathbf{D}^{-1})^T \cdot \mathbf{\Phi}||}{\Delta}$ ▷ λ_u is the upper bound to λ_{LM}
14:      **if** $\lambda_u^{(0)} == 0$ **then**
15:          $\lambda_u^{(0)} \leftarrow \dfrac{\text{eps}}{\min\{\Delta, 0.1\}}$ ▷ eps is a very small value equal to the machine precision
16:      **end if**
17:      **if** $\lambda_{LM} > \lambda_u^{(0)}$ **then**
18:          $\lambda_{LM} \leftarrow \lambda_u^{(0)}$
19:      **else**
20:          **if** $\lambda_{LM} < \lambda_l^{(0)}$ **then**
21:              $\lambda_{LM} \leftarrow \lambda_l^{(0)}$
22:          **end if**
23:      **end if**
24:      **if** $\lambda_{LM} == 0$ **then**
25:          $\lambda_{LM} \leftarrow \dfrac{||(\mathbf{J} \cdot \mathbf{D}^{-1})^T \cdot \mathbf{\Phi}||}{||\mathbf{D} \cdot \delta a(0)||}$
26:      **end if**

Algorithm 3 Algorithm for determining the Levenberg-Marquardt parameter λ_{LM} as used in the GNU Scientific Library (Continued)

27:     **for** $k = 1 \rightarrow 10$ **do**

28:        **if** $(\lambda_{LM} < \lambda_l^{(k-1)})$ OR $(\lambda_{LM} > \lambda_u^{(k-1)})$ **then**

29:           $\lambda_{LM} \leftarrow \max\{0.001\lambda_u^{(k-1)}, \sqrt{\lambda_l^{(k-1)}\lambda_u^{(k-1)}}\}$

30:        **end if**

31:        **if** $\lambda_{LM} == 0$ **then**

32:           $\lambda_{LM} \leftarrow \max\{0.001\lambda_u^{(k-1)}, \text{eps}\}$

33:        **end if**

34:        Evaluate $\psi(\lambda_{LM})^{(k)}$ $\triangleright$ Using Equation 5.19

35:        **if** $|\psi(\lambda_{LM})^{(k)}| \leq 0.1\Delta$ **then**

36:           **return** (λ_{LM})

37:        **end if**

38:        **if** $(\lambda_l^{(k-1)} == 0)\text{AND}(\psi(\lambda_{LM})^{(k)} \leq \psi(\lambda_{LM})^{(k-1)})\text{AND}(\psi(\lambda_{LM})^{(k-1)} < 0)$ **then**

39:           **return** (λ_{LM})

40:        **end if**

41:        **if** $k == 10$ **then**

42:           **return** (λ_{LM})

43:        **else**

44:           $\lambda_c \leftarrow -\dfrac{\psi(\lambda_{LM})^{(k)}}{\psi'(\lambda_{LM})^{(k)}}$

45:           **if** $\psi(\lambda_{LM})^{(k)} > 0$ **then**

46:              $\lambda_l^{(k)} \leftarrow \max\{\lambda_l^{(k-1)}, \lambda_{LM}\}$

47:           **end if**

48:           **if** $\psi(\lambda_{LM})^{(k)} < 0$ **then**

49:              $\lambda_u^{(k)} \leftarrow \min\{\lambda_u^{(k-1)}, \lambda_{LM}\}$

50:           **end if**

51:           $\lambda_{LM} \leftarrow \max\{\lambda_l^{(k)}, \lambda_{LM} + \lambda_c\}$

52:        **end if**

53:     **end for**

54: **end procedure**

Algorithm 4 Downhill simplex algorithm

1: Given $\mathbf{a}_0^{(0)} = \{a_0^1, a_0^2, a_0^3, \ldots, a_0^M\}$ ▷ Starting parameter set

2: Given $\mathbf{l} = \{l^1, l^2, l^3, \ldots, l^M\}$ ▷ Starting edge lengths

3: $\mathbf{a}_i^{(0)} = \mathbf{a}_0 + l^i \mathbf{e}_i$ ▷ Generate the vertices of the Simplex. $\mathbf{e}_i$ is the unit vector in i^{th} dimension. The simplex at k^{th} iteration has vertices $\{\mathbf{a}_0^{(k)}, \mathbf{a}_1^{(k)}, \mathbf{a}_2^{(k)}, \ldots, \mathbf{a}_M^{(k)}\}$

4: Evaluate $\Phi(\mathbf{a}_i^{(0)})$; i = 0 to M

5: **for** $k = 0 \rightarrow k_{max}$ **do**

6:      Rearrange $\mathbf{a}_i^{(k)}$ so that $\Phi(\mathbf{a}_0^{(k)}) < \Phi(\mathbf{a}_1^{(k)}) < \Phi(\mathbf{a}_2^{(k)}) < \ldots < \Phi(\mathbf{a}_M^{(k)})$

7:      Evaluate $\bar{\mathbf{a}}^{(k)} \leftarrow \dfrac{\sum_{i=0}^{M-1} \mathbf{a}_i^{(k)}}{M}$ ▷ $\bar{\mathbf{a}}^{(k)}$ is the centroid of the simplex $\{\mathbf{a}_0^{(k)}, \mathbf{a}_1^{(k)}, \ldots, \mathbf{a}_{M-1}^{(k)}\}$

8:      Evaluate $\Phi(\mathbf{a}_r^{(k)}) \leftarrow \Phi(2 \cdot \bar{\mathbf{a}}^{(k)} - \mathbf{a}_M^{(k)})$ ▷ Reflection operation

9:      **if** $\Phi(\mathbf{a}_0^{(k)}) \leq \Phi(\mathbf{a}_r^{(k)}) < \Phi(\mathbf{a}_{M-1}^{(k)})$ **then**

10:        $\mathbf{a}_M^{(k)} \leftarrow \mathbf{a}_r^{(k)}$

11:        **continue**

12:      **end if**

13:      **if** $\Phi(\mathbf{a}_r^{(k)}) < \Phi(\mathbf{a}_0^{(k)})$ **then**

14:        Evaluate $\Phi(\mathbf{a}_e^{(k)}) \leftarrow \Phi(3 \cdot \mathbf{a}_r^{(k)} - 2 \cdot \bar{\mathbf{a}}^{(k)})$ ▷ Expansion operation

15:        **if** $\Phi(\mathbf{a}_e^{(k)}) < \Phi(\mathbf{a}_r^{(k)})$ **then**

16:          $\mathbf{a}_M^{(k)} \leftarrow \mathbf{a}_e^{(k)}$

17:        **else**

18:          $\mathbf{a}_M^{(k)} \leftarrow \mathbf{a}_r^{(k)}$

19:        **end if**

20:        **continue**

21:      **else**

22:        Evaluate $\Phi(\mathbf{a}_c^{(k)}) \leftarrow \Phi(0.5 \cdot (\mathbf{a}_0^{(k)} + \mathbf{a}_M^{(k)}))$ ▷ Contraction operation

23:        **if** $\Phi(\mathbf{a}_c^{(k)}) < \Phi(\mathbf{a}_M^{(k)})$ **then**

24:          $\mathbf{a}_M^{(k)} \leftarrow \mathbf{a}_c^{(k)}$

25:        **else**

26:          $\mathbf{a}_i^{(k)} \leftarrow 0.5 \cdot (\mathbf{a}_i^{(k)} + \mathbf{a}_0^{(k)})$; with i = 1 to M   ▷ Reduction step Evaluate $\Phi(\mathbf{a}_i^{(k)})$; i = 1 to M

27:        **end if**

28:        **continue**

29:      **end if**

30: **end for**

References

Abaqus Analysis User's Manual, V. 6.9 (2009). *ABAQUS 6.9 Analysis User's Manual*. Dassault Systèmes, USA. 21, 24, 25, 26, 28, 36, 37, 41, 44, 47, 52, 149

ADVANTEDGE (2007). User's manual version 5.1 Third-wave Systems. 21

ALAUDDIN, M., CHOUDHURY, I.A., EL BARADIE, M.A. & HASHMI, M.S.J. (1995). Plastics and their machining: a review. *Journal of materials processing technology*, **54**, 40–46. 1

ARRAZOLA, P.J., UGARTE, D., MONTOYA, J., VILLAR, A. & MARYA, S. (2005). Finite element modeling of chip formation process with Abaqus/Explicit 6.3. *COMPLAS-2005*. 21

BÄKER, M. (2003a). The influence of plastic properties on chip formation. *Computational materials science*, **28**, 556–562. 17, 95, 136

BÄKER, M. (2003b). An investigation of the chip segmentation process using finite elements. *Technische Mechanik*, **23**, 1–9. 58, 59

BÄKER, M. (2004). *Finite element simulation of chip formation*. Shaker. 21, 25, 58, 59, 92, 95, 164

BÄKER, M. (2005). Does chip formation minimize the energy? *Computational materials science*, **33**, 407–418. 15, 17

BATRA, R.C. & KIM, C.H. (1990). Effect of viscoplastic flow rules on the initiation and growth of shear bands at high strain rates. *Journal of the Mechanics and Physics of Solids*, **38**, 859–874. xix, 34

BAUCCIO, M. & AMERICAN SOCIETY FOR METALS (1993). *ASM metals reference book*. ASM International, Materials Park, Ohio, 3rd edn. 43

BENSON, D.J. & OKAZAWA, S. (2004). Contact in a multi-material eulerian finite element formulation. *Computer methods in applied mechanics and engineering*, **193**, 4277–4298. 23, 24

BLENKINSOP, P.A. (1993). Titanium alloys. advances in alloys, processes, products and applications. *Journal de Physique IV*, **3**, 161–169. 72

BOOTHROYD, G. (1963). Temperatures in orthogonal metal cutting. *Proceedings of the Institution of Mechanical Engineers*, **177**, 789–810. 59

BROWN, C.A. (1987). Strain analysis in machining using metallographic methods. *Metallography*, **20**, 465–483. 58

CALAMAZ, M., COUPARD, D. & GIROT, F. (2008). A new material model for 2D numerical simulation of serrated chip formation when machining titanium alloy Ti-6Al-4V. *International Journal of Machine Tools and Manufacture*, **48**, 275 – 288. 30, 83, 164

CERETTI, E., LUCCHI, M. & ALTAN, T. (1999). FEM simulation of orthogonal cutting: serrated chip formation. *Journal of Materials Processing Technology*, **95**, 17–26. 8

CHILDS, T.H.C. (1998). Material property needs in modeling metal machining. *Machining Science and Technology*, **2**, 303–316. 32

CHILDS, T.H.C., MAEKAWA, K., OBIKAWA, T. & YAMANE, Y. (2000). *Metal machining: theory and applications*. Arnold, London. 1, 12, 24

CHOU, Y.K. & SONG, H. (2004). Tool nose radius effects on finish hard turning. *Journal of Materials Processing Technology*, **148**, 259–268. 9

COTTERELL, M. & BYRNE, G. (2008). Dynamics of chip formation during orthogonal cutting of titanium alloy Ti–6Al–4V. *CIRP Annals-Manufacturing Technology*, **57**, 93–96. 8

DAVIES, E.D.H. & HUNTER, S.C. (1963). The dynamic compression testing of solids by the method of the split hopkinson pressure bar. *Journal of the Mechanics and Physics of Solids*, **11**, 155–179. 64

DAVIM, J.P. & MARANHÃO, C. (2009). A study of plastic strain and plastic strain rate in machining of steel AISI 1045 using FEM analysis. *Materials & Design*, **30**, 160–165. 58

DONACHIE, M.J. (2000). *Titanium: a technical guide*. ASM International, Materials Park, Ohio. 70, 71

DONACHIE, M.J. & DONACHIE, S.J. (2002). *Superalloys: a technical guide*. ASM International, Materials Park, Ohio. 70, 71

DURRENBERGER, L. & MOLINARI, A. (2009). Modeling of temperature and strain-rate effects in metals using an internal variable model. *Experimental mechanics*, **49**, 247–255. xix, 34

ERNST, H. (1938). *Physics of metal cutting*. Cincinnati Milling Machine Company. 12

ERNST, H. & MERCHANT, M.E. (1941). Chip formation, friction, and high quality machined surfaces. In *Surface treatment of metals*, 299–378, ASM, New York. 9, 12, 14

FERREIRA, J.R., COPPINI, N.L. & MIRANDA, G.W.A. (1999). Machining optimisation in carbon fibre reinforced composite materials. *Journal of Materials Processing Technology*, **92**, 135–140. 1

FLANAGAN, D.P. & BELYTSCHKO, T. (1981). A uniform strain hexahedron and quadrilateral with orthogonal hourglass control. *International Journal for Numerical Methods in Engineering*, **17**, 679–706. 42

FLETCHER, R. (1971). A modified Marquardt subroutine for nonlinear least squares. Report No. R-6799. *Theoretical Physics Division, AERE Harwell*. 141, 145

FLUHRER, J. (2004). DEFORM user's manual. *Scientific Forming Technologies Corporation*. 20

GALASSI, M., DAVIES, J., THEILER, J., GOUGH, B., JUNGMAN, G., BOOTH, M. & ROSSI, F. (2002). *GNU scientific library*. Network Theory Ltd. 141, 143

GENTE, A. (2002). *Merkmale der Spanbildung von TiAl6V4 und Ck45 bei sehr hohen Schnittgeschwindigkeiten*. Ph.D. thesis, PhD thesis, Technische Universität Braunschweig. 94

GNANAMANICKAM, E.P., LEE, S., SULLIVAN, J.P. & CHANDRASEKAR, S. (2009). Direct measurement of large-strain deformation fields by particle tracking. *Measurement Science and Technology*, **20**, 095710. 58

GORHAM, D.A. (1989). Specimen inertia in high strain-rate compression. *Journal of Physics D: Applied Physics*, **22**, 1888. 65

GORHAM, D.A. (1991). The effect of specimen dimensions on high strain rate compression measurements of copper. *Journal of Physics D: Applied Physics*, **24**, 1489. 65

GORHAM, D.A. & WU, X.J. (1996). An empirical method for correcting dispersion in pressure bar measurements of impact stress. *Measurement Science and Technology*, **7**, 1227. 64

GOTO, D.M., GARRETT, R.K., BINGERT, J.F., CHEN, S.R. & GRAY, G.T. (2000). The mechanical threshold stress constitutive-strength model description of HY-100 steel. *Metallurgical and Materials Transactions A*, **31**, 1985–1996. xix, 34

GRAY, G.T.R. (2000). Classic split-hopkinson pressure bar technique. In H. Kuhn & D. Medlin, eds., *ASM Handbook, Vol 8, Mechanical Testing and Evaluation*, 462–476, ASM International, Materials Park, Ohio. 61, 64, 65

GÜNAY, M., ASLAN, E., KORKUT, I. & SEKER, U. (2004). Investigation of the effect of rake angle on main cutting force. *International Journal of Machine Tools and Manufacture*, **44**, 953–959. 8

GUO, Y.B., WEN, Q. & HORSTEMEYER, M.F. (2005). An internal state variable plasticity-based approach to determine dynamic loading history effects on material property in manufacturing processes. *International Journal of Mechanical Sciences*, **47**, 1423–1441. 66

HALLE, T. & MEYER, L.W. (2004). Influence of different material models on the result of numerical high speed cutting simulations. In *Proceedings of the 1st International Conference on High Speed Forming*, Institut für Umformtechnik-Technische Universität Dortmund. 33

HARGRAVE, B., GONZALEZ, M., MASKOS, K., SKOGSBERG, J. & GRAUMAN, J. (2010). Titanium alloy tubing for HPHT OCTG applications. *Corrosion 2010*. 72

HASTINGS, W.F., MATHEW, P. & OXLEY, P.L.B. (1980). A machining theory for predicting chip geometry, cutting forces etc. from work material properties and cutting conditions. *Proceedings of the Royal Society of London. A. Mathematical and Physical Sciences*, **371**, 569–587. 58

HEBDEN, M.D. (1973). An algorithm for minimization using exact second derivatives. Report TP515. Tech. rep., Atomic Energy Research Establishment, Harwell, England. 141, 145

HEMBUCH, J. (2012). Finite-Element-Modell des Zerspanprozesses mit einem Euler-Ansatz. *Studienarbeit, Institut für Werkstoffe, Technische Universität Braunschweig, Germany.* 207

HOFFMEISTER, H.W. & KSIEZYK, D. (2010). High speed cutting of Ti 15V 3Cr 3Al 3Sn and Alloy 625. In *Proceedings of the 2nd MAMINA Conference in the 20th International Workshop on Computational Mechanics of Materials*, 37–49, Loughborough, UK. 74

HOFFMEISTER, H.W., GENTE, A. & WEBER, T.H. (1999). Chip formation at titanium alloys under cutting speed of up to 100m/s. In *2nd International Conference on High Speed Machining. PTW Darmstadt University*, 21–28. 94

HOKKA, M., LEEMET, T., SHROT, A., BAEKER, M. & KUOKKALA, V.T. (2012a). Characterization and numerical modeling of high strain rate mechanical behavior of ti-15-3 alloy for machining simulations. *Materials Science and Engineering: A.* 5, 75

HOKKA, M., LEEMET, T., SHROT, A., BAKER, M. & KUOKKALA, V.T. (2012b). Dynamic behavior and numerical modeling of titanium 15-3-3-3 alloy. In *Proceedings of the SEM XII International Congress & Exposition on Experimental and Applied Mechanics*, Costa Mesa, USA. 5

HOKKA, M., LEEMET, T., SHROT, A., BÄKER, M. & KUOKKALA, V.T. (2012c). Modelling of the dynamic behaviour of hard-to-machine alloys. *EPJ Web of Conferences*, **26**, 04009. 5

HOLLOMON, J.H. (1945). Tensile deformation. *Transactions AIME*, **162**, 268–290. 29

HORTIG, C. & SVENDSEN, B. (2007). Simulation of chip formation during high-speed cutting. *Journal of materials processing technology*, **186**, 66–76. 40

JASPERS, S. & DAUTZENBERG, J.H. (2002). Material behaviour in conditions similar to metal cutting: flow stress in the primary shear zone. *Journal of Materials Processing Technology*, **122**, 322–330. 66

JASPERS, S.P.F.C. (1999). *Metal cutting mechanics and material behaviour*. Ph.D. thesis, Technische Universiteit Eindhoven. 33

JIA, D. & RAMESH, K.T. (2004). A rigorous assessment of the benefits of miniaturization in the kolsky bar system. *Experimental mechanics*, **44**, 445–454. 66

JOHNSON, G.R. & COOK, W.H. (1983). A constitutive model and data for metals subjected to large strains, high strain rates and high temperatures. In *Proceedings of the 7th International Symposium on Ballistics*, 541–547, The Hague, Netherlands. 29

KAKINO, Y. (1971). Analysis of the mechanism of orthogonal machining by the finite element method. *Journal of the Japan Society for Precision Engineering*, **37**, 503–508. 20

KASSNER, M.E., WANG, M.Z., PEREZ-PRADO, M.T. & ALHAJERI, S. (2002). Large-strain softening of aluminum in shear at elevated temperature. *Metallurgical and Materials Transactions A*, **33**, 3145–3153. 83

KECECIOGLU, D. (1958). Shear strain rate in metal cutting and its effect on shear flow stress. *Transactions of American Society of Mechanical Engineers*, **80**, 158–168. 135

KILIÇASLAN, C. (2009). *Modelling and simulation of metal cutting by finite element method*. Master's thesis, Izmir Institute of Technology. 33

KOCH, P. (1964). Wood machining processes. 1

KOMANDURI, R., ZHANG, B. & VISSA, C.M. (1991). Machining of fiber reinforced composites. In *Processing and Manufacturing of Composite Materials*, vol. 1, 1–36. 1

LALWANI, D.I., MEHTA, N.K. & JAIN, P.K. (2009). Extension of Oxley's predictive machining theory for Johnson and Cook flow stress model. *Journal of Materials Processing Technology*, **209**, 5305–5312. 17

LEE, E.H. & SHAFFER, B.W. (1951). The method of plasticity applied to a problem of machining. *Transactions of the ASME*, **18**, 405–413. 7

LEE, S., HWANG, J., SHANKAR, M.R., CHANDRASEKAR, S. & DALE COMPTON, W. (2006). Large strain deformation field in machining. *Metallurgical and Materials Transactions A*, **37**, 1633–1643. 59

LEOPOLD, J. (1999). *Werkzeuge für die Hochgeschwindigkeitsbearbeitung*. Hanser. 22, 23

Leopold, J., Hoyer, K. & U., S. (2001). Simulation of chip forming process in high speed machining using eulerian finite element analysis. In H. Schulz, ed., *Scientific fundamentals of HSC*, 92–102, Carl Hanser Verlag, Munich. 22, 23

Levenberg, K. (1944). A method for the solution of certain problems in least squares. *Quarterly of applied mathematics*, **2**, 164–168. 141, 143

Leyens, C. & Peters, M. (2003). *Titanium and titanium alloys*. Wiley Online Library. 71, 72

Lira, F. & Thomsen, E.G. (1967). Metal cutting as a property test. *ASME Journal of Engineering for Industry*, **89**, 489–493. 135

Liu, M., Takagi, J. & Tsukuda, A. (2004). Effect of tool nose radius and tool wear on residual stress distribution in hard turning of bearing steel. *Journal of Materials Processing Technology*, **150**, 234–241. 9

Lo, S.P. (2000). An analysis of cutting under different rake angles using the finite element method. *Journal of materials processing technology*, **105**, 143–151. 8

Ludwik, P. (1909). *Elemente der technologischen Mechanik*. Springer. 29

Mabrouki, T. & Rigal, J.F. (2006). A contribution to a qualitative understanding of thermo-mechanical effects during chip formation in hard turning. *Journal of materials processing technology*, **176**, 214–221. 68

Mabrouki, T., Girardin, F., Asad, M. & Rigal, J.F. (2008). Numerical and experimental study of dry cutting for an aeronautic aluminium alloy (A2024-T351). *International Journal of Machine Tools and Manufacture*, **48**, 1187–1197. 21, 39, 43

Mackerle, J. (1998). Finite-element analysis and simulation of machining: a bibliography (1976–1996). *Journal of Materials Processing Technology*, **86**, 17–44. 20

Mackerle, J. (2003). Finite element analysis and simulation of machining: an addendum:: A bibliography (1996-2002). *International Journal of Machine Tools and Manufacture*, **43**, 103–114. 20

MADHAVAN, V., CHANDRASEKAR, S. & FARRIS, T.N. (2000). Machining as a wedge indentation. *Journal of Applied Mechanics*, **67**, 128–139. 58

MAEKAWA, K. & OHHATA, H. (1997). Simulation analysis of three-dimensional continuous chip formation processes.(part 3) – Influence of physical properties of work and tool materials. *International journal of the Japan Society for Precision Engineering*, **31**, 103–108. 40

MAEKAWA, K., SHIRAKASHI, T. & USUI, E. (1983). Flow stress of low carbon steel at high temperature and strain rate. II: Flow stress under variable temperature and variable strain rate. *Bulletin of the Japan Society of Precision Engineering*, **17**, 167–172. 32

MAEKAWA, K., SHIRAKASHI, T. & OBIKAWA, T. (1996). Recent progress of computer aided simulation of chip flow and tool damage in metal machining. *Proceedings of the Institution of Mechanical Engineers, Part B: Journal of Engineering Manufacture*, **210**, 233–242. 24

MAMALIS, A.G., HORVATH, M., BRANIS, A.S. & MANOLAKOS, D.E. (2001). Finite element simulation of chip formation in orthogonal metal cutting. *Journal of Materials Processing Technology*, **110**, 19–27. 60

MARQUARDT, D.W. (1963). An algorithm for least-squares estimation of nonlinear parameters. *Journal of the society for Industrial and Applied Mathematics*, **11**, 431–441. 141, 143

MARUSICH, T.D. & ORTIZ, M. (1995). Modelling and simulation of high-speed machining. *International Journal for Numerical Methods in Engineering*, **38**, 3675–3694. 58, 59, 60

MATHEW, P. & OXLEY, P.L.B. (1982). Predicting the effects of very high cutting speeds on cutting forces, etc. *CIRP Annals-Manufacturing Technology*, **31**, 49–52. 58

MATLAB (2010). *version 7.10.0 (R2010a)*. The MathWorks Inc., Natick, Massachusetts. 74

MAUREL, A., FONTAINE, M., THIBAUD, S., MICHEL, G. & GELIN, J.C. (2008). Experiments and FEM simulations of milling performed to identify material parameters. *International Journal of Material Forming*, **1**, 1435–1438. 136

MERCHANT, M.E. (1945a). Mechanics of the metal cutting process. I. orthogonal cutting and a type 2 chip. *Journal of applied physics*, **16**, 267–275. 9, 14, 15

MERCHANT, M.E. (1945b). Mechanics of the metal cutting process. II. plasticity conditions in orthogonal cutting. *Journal of Applied Physics*, **16**, 318–324. 14, 15

METSÄJOKI, J. (2011). Mamina final report – ESR S2. Tech. rep., Institut für Werkzeugmaschinen und Fertigungstechnik, Braunschweig. xx, 93

METSÄJOKI, J. & HOFFMEISTER, H.W. (2012). Chip formation mechanism of advanced ti-alloys during high speed cutting at 20 to 30 m/s. In *Proceedings of the 9th international conference on high speed machining*, San Sebastian, Spain. 74

MILANI, A.S., DABBOUSSI, W., NEMES, J.A. & ABEYARATNE, R.C. (2009). An improved multi-objective identification of Johnson-Cook material parameters. *International Journal of Impact Engineering*, **36**, 294–302. 80

MONEIM, M.E. *et al.* (1981). Effect of the clearance angle on the wear of high speed steel tools. *Wear*, **72**, 1–11. 9

MORÉ, J. (1978). The Levenberg-Marquardt algorithm: implementation and theory. *Numerical analysis*, 105–116. 141, 144, 145

NAGARAJ, B., CARROLL, D. & DIEHL, T. (1999). Ball drop simulation on two-way radio lens using Abaqus/Explicit. In *Proceedings of the 1999 Abaqus Users' Conference*. 45

NELDER, J.A. & MEAD, R. (1965). A simplex method for function minimization. *The computer journal*, **7**, 308–313. 147

NG, E.G. & ASPINWALL, D.K. (2002). Modelling of hard part machining. *Journal of materials processing technology*, **127**, 222–229. 21

OSTROUSHKO, D., SAKSL, K., SIEMERS, C. & RIHOVA, Z. (2012). Chips of Ti-6Al-2Sn-4Zr-6Mo alloy – A detailed geometry study. In *Proceedings of the International Conference on Materials Science and Engineering 2012 (ICMSE 2012)*, Paris, France. 73

OXLEY, P.L.B. (1989). *The mechanics of machining: An analytical approach to assessing machinability*. Ellis Horwood, UK. 12, 15, 16, 17, 58, 135

OXLEY, P.L.B. & STEVENSON, M.G. (1967). Measuring stress/strain properties at very high strain rates using a machining test. *Journal of the Institute of Metals*, **95**, 308–313. 135

OXLEY, P.L.B. & WELSH, M.J.M. (1963). Calculating the shear angle in orthogonal metal cutting from fundamental stress, strain, strain-rate properties of the workpiece material. In *Proceedings of the Fourth International Machine Tool Design and Research Conference*, 73–86, Pergamon, Oxford. 9, 15, 99

ÖZEL, T. (2006). The influence of friction models on finite element simulations of machining. *International Journal of Machine Tools and Manufacture*, **46**, 518–530. 40

ÖZEL, T. & ALTAN, T. (2000). Determination of workpiece flow stress and friction at the chip-tool contact for high-speed cutting. *International Journal of Machine Tools and Manufacture*, **40**, 133–152. 135

ÖZEL, T. & KARPAT, Y. (2007). Identification of constitutive material model parameters for high-strain rate metal cutting conditions using evolutionary computational algorithms. *Materials and manufacturing processes*, **22**, 659–667. 136

PEARSALL, G.W. & BACKOFEN, W.A. (1963). Frictional boundary conditions in plastic compression. *Journal of Engineering for Industry-Transactions of the ASME*, **85**, 68–76. 65

PETTERSEN, T. & NES, E. (2003). On the origin of strain softening during deformation of aluminum in torsion to large strains. *Metallurgical and Materials Transactions A*, **34**, 2727–2736. 83

PIISPANEN, V. (1948). Theory of formation of metal chips. *Journal of Applied Physics*, **19**, 876–881. 9

PRESS, W.H., TEUKOLSKY, S.A., VETTERLING, W.T. & FLANNERY, B.P. (1993). *Numerical Recipes in FORTRAN; The Art of Scientific Computing*. Cambridge University Press, New York, USA, 2nd edn. 101, 141, 142, 143

PROIX, J.M., LAURENT, N., HEMON, P. & BERTRAND, G. (2000). Code Aster, manuel de référence. *Fascicule R*, **8**. 21

PUJANA, J., ARRAZOLA, P.J. & VILLAR, J.A. (2008). In-process high-speed photography applied to orthogonal turning. *Journal of materials processing technology*, **202**, 475–485. 58, 59

RAKOTOMALALA, R., JOYOT, P. & TOURATIER, M. (1993). Arbitrary lagrangian-eulerian thermomechanical finite-element model of material cutting. *Communications in Numerical Methods in Engineering*, **9**, 975–987. 23

RAMESH, A. & MELKOTE, S.N. (2008). Modeling of white layer formation under thermally dominant conditions in orthogonal machining of hardened AISI 52100 steel. *International Journal of Machine Tools and Manufacture*, **48**, 402–414. xix, 21, 35, 39

RAMESH, K.T. (2008). High rates and impact experiments. In W.N. Sharpe, ed., *Springer Handbook of Experimental Solid Mechanics*, 929–960, Springer US. xiv, 62, 64, 65

RAMM, A.G. & SMIRNOVA, A.B. (2001). On stable numerical differentiation. *Mathematics of computation*, **70**, 1131–1154. 146

REED, R.C. (2006). *The superalloys: fundamentals and applications*. Cambridge University Press. 71

RODNEY, B., GERHARD, W. & COLLINGS, E.W., eds. (1994). *Materials properties handbook: Titanium alloys*. ASM International, Materials Park, Ohio. 71, 72

ROKICKI, P., SPOTZ, Z., FUSOVA, L., SAKSL, K., SIEMERS, C. & ZAHRA, B. (2010). Chip formation process of Ti-15V-3Al-3Sn-3Cr alloy. In *Proceedings of the 19th international conference on metallurgy and materials*, Roznov pod Radhostem, Czech Republic. 74

RÖSLER, J., BÄKER, M. & SIEMERS, C. (2005). Mechanisms of chip formation. In H.K. Tönshoff & C. Hollmann, eds., *Hochgeschwindigkeitsspanen metallischer Werkstoffe*, 492–514, Wiley-VCH Verlag GmbH & Co. KGaA, Weinheim, Germany. 12

SAMANTARAY, D., MANDAL, S. & BHADURI, A.K. (2009). A comparative study on Johnson Cook, modified Zerilli-Armstrong and Arrhenius-type constitutive models to predict elevated temperature flow behaviour in modified 9Cr-1Mo steel. *Computational Materials Science*, **47**, 568–576. 76

SARTKULVANICH, P., KOPPKA, F. & ALTAN, T. (2004). Determination of flow stress for metal cutting simulation – a progress report. *Journal of materials processing technology*, **146**, 61–71. 136

SEKHON, G.S. & CHENOT, J.L. (1993). Numerical simulation of continuous chip formation during non-steady orthogonal cutting. *Engineering Computations*, **10**, 31–48. 58

SEO, S., MIN, O. & YANG, H. (2005). Constitutive equation for Ti-6Al-4V at high temperatures measured using the SHPB technique. *International Journal of Impact Engineering*, **31**, 735–754. 66

SEVIER, M., YANG, H.T.Y., LEE, S. & CHANDRASEKAR, S. (2007). Severe plastic deformation by machining characterized by finite element simulation. *Metallurgical and Materials Transactions B*, **38**, 927–938. 59

SHATLA, M., KERK, C. & ALTAN, T. (2001a). Process modeling in machining. part I: determination of flow stress data. *International Journal of Machine Tools and Manufacture*, **41**, 1511–1534. 136

SHATLA, M., KERK, C. & ALTAN, T. (2001b). Process modeling in machining. part II: validation and applications of the determined flow stress data. *International Journal of Machine Tools and Manufacture*, **41**, 1659–1680. 136

SHAW, M.C. (1984). *Metal cutting principles*. Clarendon Press, Oxford. 1, 12

SHI, B., ATTIA, H. & TOUNSI, N. (2010a). Identification of material constitutive laws for machining – part I: An analytical model describing the stress, strain, strain rate, and temperature fields in the primary shear zone in orthogonal metal cutting. *Journal of Manufacturing Science and Engineering*, **132**, 051008. 138

SHI, B., ATTIA, H. & TOUNSI, N. (2010b). Identification of material constitutive laws for machining – part II: Generation of the constitutive data and validation of the constitutive law. *Journal of Manufacturing Science and Engineering*, **132**, 051009. 138

SHIH, A.J. (1995). Finite element analysis of the rake angle effects in orthogonal metal cutting. *International journal of mechanical sciences*, **38**, 1–17. 8

SHIRAKASHI, T. & USUI, E. (1976). Simulation analysis of orthogonal metal cutting process. *Journal of the Japan Society for Precision Engineering*, **42**, 340–345. 20, 24

SHIRAKASHI, T., MAEKAWA, K. & USUI, E. (1983). Flow stress of low carbon steel at high temperature and strain rate. I: Propriety of incremental strain method in impact compression test with rapid heating and cooling systems. *Bulletin of the Japan Society of Precision Engineering*, **17**, 161–166. 31

SHROT, A. & BÄKER, M. (2010). Is it possible to identify Johnson-Cook law parameters from machining simulations? *International Journal of Material Forming*, **3**, 443–446. 5

SHROT, A. & BÄKER, M. (2011a). Determination of Johnson-Cook parameters from machining simulations. *Computational Materials Science.* xiv, 5, 54, 55

SHROT, A. & BÄKER, M. (2011b). How to identify Johnson-Cook parameters from machining simulations. In *AIP Conference Proceedings*, vol. 1353, 29. 5

SHROT, A. & BÄKER, M. (2011c). Inverse identification of Johnson-Cook material parameters from machining simulations. *Advanced Materials Research*, **223**, 277–285. 5

SHROT, A. & BÄKER, M. (2011d). Johnson-Cook parameter identification from machining simulations using an inverse method. In E. Oñate & D.R.J. Owen, eds., *XI International Conference on Computational Plasticity, Fundamentals and Applications*, CIMNE, Barcelona. 5

SHROT, A. & BÄKER, M. (2012a). Material parameter identification from machining simulations using inverse techniques. *Key Engineering Materials*, **504**, 1281–1286. 5

SHROT, A. & BÄKER, M. (2012b). A study of non-uniqueness during the inverse identification of material parameters. *Procedia CIRP*, **1**, 72–77. 5

SIEMERS, C., ZAHRA, B., KSIEZYK, D., ROKICKI, P., SPOTZ, Z., FUSOVA, L., RÖSLER, J. & SAKSL, K. (2011). Chip formation and machinability of nickel-base superalloys. *Advanced Materials Research*, **278**, 460–465. 74

Sima, M. & Özel, T. (2010). Modified material constitutive models for serrated chip formation simulations and experimental validation in machining of titanium alloy Ti-6Al-4V. *International Journal of Machine Tools and Manufacture*, **50**, 943 – 960. 31, 83

Strenkowski, J.S. & Carroll, J.T. (1985). A finite element model of orthogonal metal cutting. *Journal of Engineering for Industry Transactions of the ASME*, **107**, 253–267. 58

Strenkowski, J.S. & Moon, K.J. (1990). Finite element prediction of chip geometry and toolworkpiece temperature distributions in orthogonal metal cutting. *Journal of Engineering for Industry*, **112**, 313–318. 23

Sutter, G. & Ranc, N. (2007). Temperature fields in a chip during high-speed orthogonal cutting – an experimental investigation. *International Journal of Machine Tools and Manufacture*, **47**, 1507–1517. 59

Taljat, B., Radhakrishnan, B. & Zacharia, T. (1998). Numerical analysis of GTA welding process with emphasis on post-solidification phase transformation effects on residual stresses. *Materials Science and Engineering: A*, **246**, 45–54. xiii, 34, 35

Tounsi, N., Vincenti, J., Otho, A. & Elbestawi, M.A. (2002). From the basic mechanics of orthogonal metal cutting toward the identification of the constitutive equation. *International Journal of Machine Tools and Manufacture*, **42**, 1373–1383. 137

Trent, E.M. & Wright, P.K. (2000). *Metal cutting*. Butterworth-Heinemann. 68

Treppmann, C. (2001). *Fließverhalten metallischer Werkstoffe bei Hochgeschwindigkeitsbeanspruchung*. Ph.D. thesis, RWTH Aachen. 66

Umbrello, D., Hua, J. & Shivpuri, R. (2004). Hardness-based flow stress and fracture models for numerical simulation of hard machining AISI 52100 bearing steel. *Materials Science and Engineering: A*, **374**, 90–100. 31

Westerberg, C. (2002). Finite element simulation of crash testing of self-piercing rivet joints, peel specimen. *Master's dissertation, Division of Structural Mechanics, LTH, Lund University, Sweden*. 45

WORTHINGTON, B. (1975). The effect of rake face configuration on the curvature of the chip in metal cutting. *International Journal of Machine Tool Design and Research*, **15**, 223–239. 8

XU, Z. & HUANG, F. (2012). Comparison of physically based constitutive models characterizing armor steel over wide temperature and strain rate ranges. *Modelling and Simulation in Materials Science and Engineering*, **20**, 015005. 32

YAMASHITA, N. & FUKUSHIMA, M. (2001). On the rate of convergence of the Levenberg-Marquardt method. *Topics in numerical analysis*, 239–249. 146

YANG, J.B., WU, W.T. & SRIVATSA, S. (2011). Inverse flow stress calculation for machining processes. *Advanced Materials Research*, **223**, 267–276. 190

YANG, W., CAO, W., CHUNG, T.S. & MORRIS, J. (2005). *Applied numerical methods using MATLAB*. Wiley Online Library. 146

YEN, Y.C., JAIN, A. & ALTAN, T. (2004). A finite element analysis of orthogonal machining using different tool edge geometries. *Journal of Materials Processing Technology*, **146**, 72–81. 9

ZERILLI, F.J. & ARMSTRONG, R.W. (1987). Dislocation-mechanics-based constitutive relations for material dynamics calculations. *Journal of Applied Physics*, **61**, 1816–1825. 32

ZERILLI, F.J. & ARMSTRONG, R.W. (1997). Dislocation mechanics based analysis of material dynamics behavior: enhanced ductility, deformation twinning, shock deformation, shear instability, dynamic recovery. *Le Journal de Physique IV*, **7**, 3–3. 33

ZIENKIEWICZ, O.C. (1971). *The finite element method in engineering science*. McGraw-Hill. 20

ZIENKIEWICZ, O.C. & TAYLOR, R.L. (2005). *The finite element method for solid and structural mechanics*, vol. 2. Butterworth-Heinemann. 20, 24, 25